Volume 35 No. 1 | JNSChE Mar/Apr 2020 | ISSN 0794-6759

JOURNAL OF THE NIGERIAN SOCIETY OF CHEMICAL ENGINEERS

Published by,
THE NIGERIAN SOCIETY OF CHEMICAL ENGINEERS
National Secretariat: Infinite Grace House, Plot 4, Oyetubo Street,
Off Obafemi Awolowo Way, Ikeja, Lagos State, Nigeria.
E-mail: nationalhqtrs@nsche.org, nsche_headquarters@yahoo.com
Website: http:www.nsche.org.ng
Submission of Manuscripts: nschejournal@yahoo.com and copy: stevmomoh@yahoo.com

JOURNAL OF THE NIGERIAN SOCIETY OF CHEMICAL ENGINEERS
A Publication on the Science and Technology of Chemical Engineering

EDITORIAL BOARD

2020 BOARD OF DIRECTORS AND OFFICIALS

CHAPTER CHAIRMEN

SUBSCRIPTION

a.	**Individual Member**	₦3,000.00
b.	**Overseas Subscribers**	US$100.00
c.	**Institution, Libraries, etc**	₦5,000.00

STUDY OF CORN HUSK AS SORBENT FOR OIL SPILL CLEANUP

***Olawale, A. S., Olakunle, M. S. and Ajayi, O. A.**
Chemical Engineering Department, Ahmadu Bello University
Zaria. Nigeria
*Corresponding author: +2348036862485; asolawale@abu.edu.ng

ABSTRACT

The use of lignocellulosic wastes as sorbents in oil spill cleanup is becoming of interest due to their ready availability, cheapness and biodegradability. In this study corn husk was used to remove Escravos crude oil from seawater. The investigations were carried out using five different particle size ranges (4000-1000, 1000-500, 500-105, 105-53 and <53 µm) of corn husk on three oil layer thicknesses (3, 4.5 and 6 mm) over water. The oil and water sorption characteristics of the lignocellulosic particles were obtained. The initial sorption rates of the sorbent in the first ten minutes were the highest with the three oil layer thicknesses investigated. The maximum sorption capacity for oil and water were recorded with 3mm oil layer by particle B (1000-500µm), at 40 minutes as 9.9719 g oil/g sorbent and 2.220 g water/g sorbent respectively. The 9.9719g/g maximum oil sorption capacity recorded is indicative of crude oil sorption potential of corn husk as it falls within the 6 to 30 g/g range commonly recorded for natural sorbents like sugar cane bagasse, raw cotton, kapok, hog moss and barley straw. When 4.5 and 6 mm oil layer thickness were used, the maximum sorption capacity obtained were 6.7272g/g and 5.3386g/g respectively. No water sorption was recorded by the sorbent on 4.5 and 6 mm oil layers. The oil sorption kinetic model of raw corn husk particle was of inverse (decaying) exponential form ($q = a\ (1 - e^{-t})$); this indicates a diffusion sorption mechanism.

Keywords: *Particle sizes, oil sorption, Escravos oil, lignocellullosics, biodegradable*

1 INTRODUCTION

There have been many incidents of oil spill from 1907 till date with dire consequences to marine lives as well as human environment and health (Saidu, 2011; Jain, 2017). When crude oil spills on water it destroys the habitats of many bottom dwelling organisms and it has toxicological effects on the aquatic life and hence on human beings (Rene *et al.*, 1993). Oil spills may occur due to accident, leakages (pipeline and flow station), failure (over pressure line and hose), overflow of process equipment components and sabotage to flow lines (Egwaikhide *et al*., 2007).

Spilled crude oil can be cleaned from the water surfaces through mechanical/physical recovery (using booms, skimmers and sorbents), chemical treatment (using dispersing materials, sinking materials, emulsion breaker, gelling agents, solidifiers and neutralizing agents),bioremediation and burning (Choi and Cloud, 1992). Sorption is a common method of cleaning up oil spill from water areas that cannot be easily accessed by booms or skimmers; sorbents are used to achieve this operation. Utilisation of porous materials as sorbents in oil spill clean-up has been reviewed and several studies on different types of sorbents have been conducted (Choi and Moreau 1993; Reynolds *et al.*, 2001; Toyoda and Inagaki 2003; Teas *et al*., 2001; Reynolds *et al.*, 2001; Adebajo *et al.*, 2003; Pinto *et al.*, 2016).).

The types of sorbents that are used to remove oil from sea and other waterways are natural/modified organic, synthetic organic and natural inorganic materials. Synthetic sorbents have good hydrophobic and oleophilic properties but are non-biodegradable (Choi and Cloud, 1992; Deschamps *et al.*, 2003). Biodegradable materials, such as lignocellulosic agricultural products and wastes with excellent sorption properties would be useful substitutes in this respect. The advantages of using these natural materials include local availability, cheapness, and biodegradability; in addition, reuse of the waste materials would result in disposal fee savings. Many of these plant materials are available abundantly in Nigeria and other tropical countries (Odedokun, 2014 and Sanni *et al*., 2017).

In the recent past there has been a growing interest in studying the use of agricultural materials for crude oil sorption. Such works have been done with rice straw and cotton (Teas *et al*., 2001), cotton (Choi *et al.*, 1993; Choi,1996), kapok (Huang and Lim, 2005; Hori *et al*., 2000), pith bagasse (Amer *et al*., 2007), groundnut husk (Olawale and Saidu, 2010), barley straw (Hussein *et al*., 2009), rice hull/straw (Bayat *et al*., 2004; Sun *et al.*, 2002), kapok and aquatic plants like *Pistia stratiotes* and *Salvinia molesta* (Zeigler *et al.*, 2015) and wool (Radetic *et al*., 2003), among others.

Despite the many works on oil sorption performance of biomass, there are still substantial number of these

natural organic materials that are yet to be studied. Therefore, there is the need to carry out investigations into oil and water sorption characteristics of more lignocellulosic materials such as corn husk which have not been reported in the literature before now. These efforts would make it possible to identify more of these lignocellusic wastes having sorption potentials and also improve our understanding of their sorption mechanism.

In this work the sorption characteristics of the corn husk particles on Escravos crude oil spill on sea water were investigated at 26 ± 1^0C.

2 METHODOLOGY

2.1 Pretreatment of Sorbents

Corn husks were collected from a farm settlement in Zaria (Kaduna State) Nigeria. They were cleansed to remove particles and other foreign materials and then sun dried. The husks were then screened for wax deposition, buoyancy and toxicity to marine life. Information were obtained from literature on wax content and toxicity of the cellulosic material. The buoyancy test was carried out as described in Section 2.2.1.

The husks were subjected to size reduction and separated into different sizes with Gallenkamp^R sieves (SB 40), of varying mesh sizes to obtain the following particle size ranges: 4000-1000, 1000-500, 500-105, 105-53 and <53 µm. The samples of the indicated particle size ranges were respectively labelled A, B, C, D and E. These lignoccellulosic particulates were subjected to analysis and sorption tests.

2.2 Tests and Analyses of Sorbents

2.2.1 Buoyancy test

Buoyancy of corn husk was determined by filling a 250 ml beaker with sea water to 200 ml mark. The sea water was sourced from the Atlantic Ocean shore in Lagos and its density was determined as described in Section 2.2.3. The pH and temperature of the system were taken. Thereafter, 1g corn husk (in its native form) was gently placed on the water surface and the times for partial and complete immersions of the husk in water were recorded.

2.2.2 Composition and morphology of corn husk

The composition of corn husk was determined using the method described by Van Soest *et al*. (1991). Scanning electron microscopic (SEM) analysis of the husk was carried out with Zeiss scanning electron microscope at an accelerated voltage of 15 kV. The FTIR analysis was done with Shimadzu-8400S Fourier transform infrared (FTIR) spectrophotometer within spectra range of 4000–500 cm^{-1}.

2.2.3 Density

The method described by Kopecky (1999) was used to determine the apparent and real densities of the husk using pycnometer. The weights of glassware, corn husk particles and water were measured with digital weighing balance (Adam, PW 184).

2.3 Analyses of Crude Oil

Escravos crude oil was collected from Kaduna Refining and Petrochemical Company (KRPC), Kaduna. Nigeria. The crude oil was weathered for 24 h inside a fume cupboard in order to remove the lighter components of the oil.

2.3.1 Density of crude oil

The density of the oil was measured using the method described by Kopecký (1999).

2.3.2 Viscosity of the crude oil

The viscosity of the crude oil was determined with Brookfield digital viscometer (DV-E) as follows. The crude oil was mixed thoroughly at room temperature for 24 h. The guard leg was mounted on the DV-E viscometer; a spindle size 4 was attached to the shaft. The shaft was slightly lifted, held firmly and screwed to the spindle with the other hand. The crude oil was poured into a 250ml beaker to about 200 ml marks. The spindle was inserted at the centre of the crude oil contained in the beaker and the viscometer was then turned on until the crude oil level gets to the immersion groove in the spindle shaft. The two-spindle digit number and desired speed setting were entered into the key pad of the viscometer and the motor was turned on. Time was allowed for the indicated speed reading to stabilize before recording the viscosity measurement. Average of five readings was used to determine the final value which was recorded in Pa.s.

2.4 Determination of Sorption Capacity

Half a litre (500 mL) seawater was placed in 1 L glass beaker which contained a cylindrical cell made of wire gauze (12cm x 7cm). Forty (40) grams of crude oil was introduced into the beaker to form oil (6 mm) layer on top of sea water. After measuring the oil layer's thickness 1 g corn husk particles (<53µm) was evenly spread on the oil surface. The cylindrical wire gauze was suspended such that its base is located within the water layer and below it was placed a magnetic bar at the bottom of the beaker.

A mild whirl movement of the liquid inside the beaker was achieved with magnetic stirring device (Stuart Heat Stir SB 162). After 10 min, the wire gauze cell was raised to recover the soaked sorbent particles. The recovered mass was left to drain for 5 min and the total weight of soaked sorbent and the cell (M_T) was obtained using a digital weighing balance (Adam, PW 184). The amount of liquid sorbed by the sorbent ($_{Mso}$) was determined by subtracting the initial sorbent and cell weight from the total weight of the wetted sorbent (M_T) as given in Equations 1 and 2. A known quantity of the sorbed liquid (oil/water) was recovered with the aid of 5-10 mL petroleum ether (40-60^{0}C). Petroleum ether contained in the recovered liquid was driven off over water bath at 45^{o}C. This was done to obtain the proportion of water (if any) that was sorbed along with the crude oil. The steps described were repeated at 20, 30, 40, 50 and 60 min. The experiments were carried out at 26 ± 1^{0}C.

The procedure described above was repeated on setups containing 4.5 and 3 mm oil layer over sea water. This was done using the five particle sizes already mentioned and the sorption capacity of the particles for oil and water was calculated using Equations 1 and 2 respectively.

$$SC_o = \frac{Mo}{Ms} \quad 1$$

$$SC_W = \frac{Mw}{Ms} \quad 2$$

$$M_{so} = M_T - (M_c + M_s) \quad 3$$

$$M_o = M_{so} - M_W \quad 4$$

where SC_o and SC_w are oil sorption capacity (g oil/g sorbent) and water sorption capacity (g water/ g sorbent) respectively. M_{so} is the mass of sorbate, M_T is the mass of the soaked sorbent and cell, M_c is the mass of cell, M_s is the mass of sorbent, M_o is the mass of oil and M_w is the mass of water (based on water proportion of the recovered sorbate and M_{so})

3.1.2 SEM Analysis

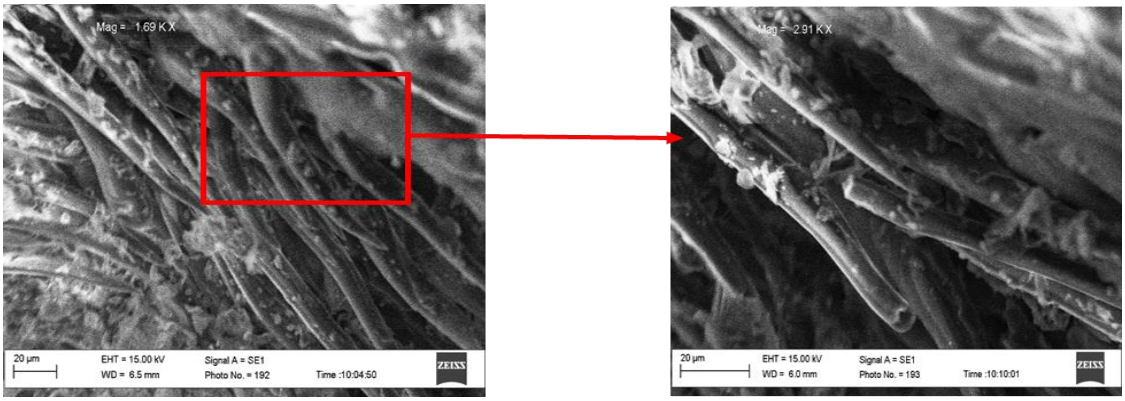

Figure 1: SEM images of corn husk

The data obtained from the sorption experiments over different time durations were fitted by DataFit 9.0^R software to obtain the oil sorption kinetic model of the corn husk particles investigated.

3 RESULTS AND DISCUSSION

3.1 Properties of Materials

3.1.1 Physicochemical property

The dried corn husk was found to contain 48.40% cellulose, 34.31% hemicelluloses, 3.20% lignin and 14.09% others. These values agree with those reported by De Carvalho Mendes *et al*. (2015). In addition, the FTIR result also indicates the presence of cellulose, hemicellulose and lignin within the moiety of the corn husk studied. The real and apparent densities of the husk were 0.160 and 0.179 g/m^3 respectively. The density value compares well with that reported by Kaiser (2013). Corn husk is not toxic to marine life and has no oil/fat deposit.

Buoyancy test on the husk showed that partial immersion in sea water (pH = 6.85 at 29^{o}C) occurred after 24 h and the husk was still partially floating after one week of introduction into the salty water which had a density of 1.0462 g/cm^3. Corn husk sorbed water but did not sink in the water due to its low density and hydrophilic characteristics; the latter might be linked to its high combined cellulose/lignin content. These buoyancy characteristics would make the husk float on water (Lee *et al*., 1999) and this is indicative of its good hydrophobic property and sorption potential for oil spill clean-up

The density, specific gravity, dynamic viscosity and kinematic viscosity of the crude oil were determined as 0.9002 g/cm^3 (28.4 ^{0}API), 0.885, 5 cP and 6.2 cSt respectively.

The scanning electron micrographs of the corn husk (Figure 1) show longitudinal section of fibres and a large number of microfibrils which are randomly distributed. The SEM images confirm that corn husk fibre has an irregular cross-section, non-uniform surface, some impurities and shallow grooves, with apparent minute crevices, which are typical of raw natural fibres. The fibre structure comprises of dense hollows (called *lumina*) inside the fiber bundles. This lumina structure helps in sorption duty of the corn husk. The amount and the size of lumens, which are correlated to the voids in the structure, affect the fibre's sorption behaviour. The larger the lumens are, the more the absorption capacity for liquid but lower the fibre's tensile strength may be.

3.1.3 FTIR analysis

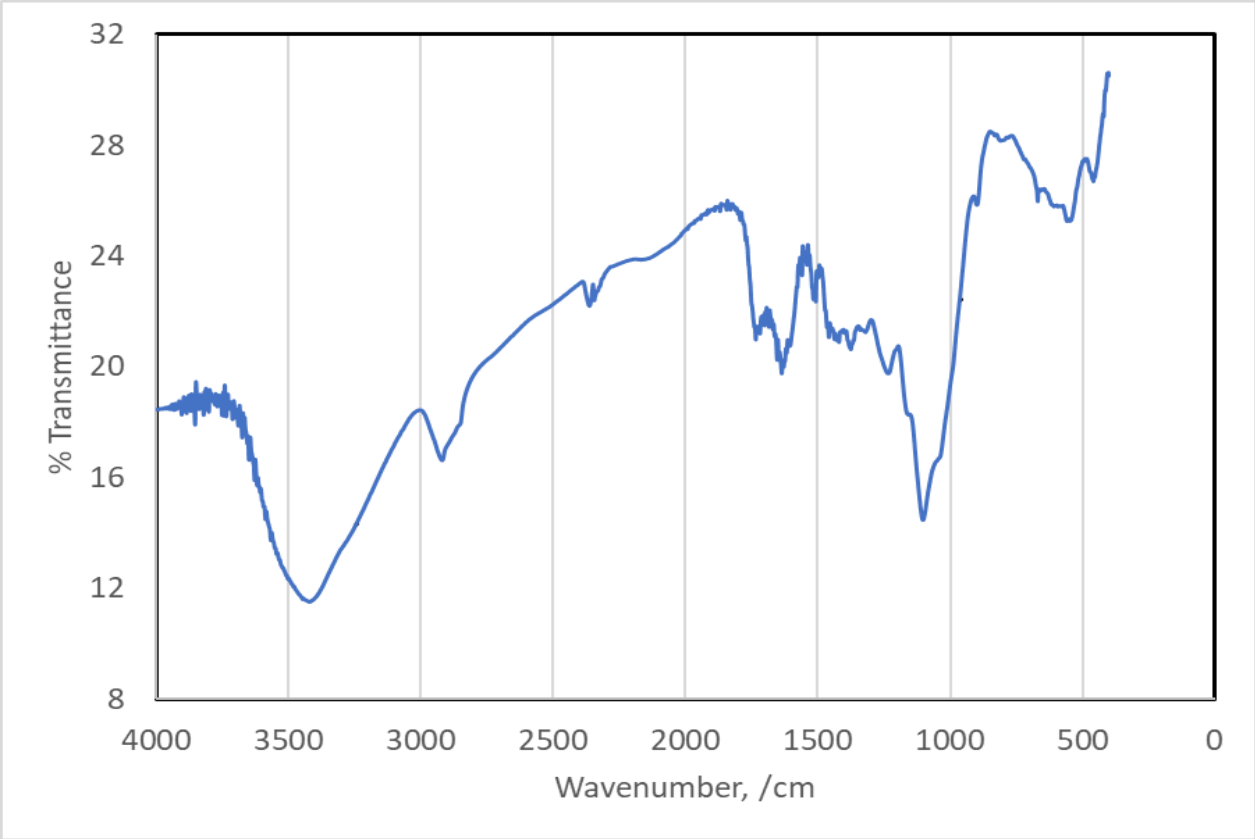

Figure 2: FTIR spectra of corn husk

The strong bands in the region of 3421cm^{-1} (Figure 2) indicate the presence of a strong hydroxyl groups in cellulose, hemicellulose and the lignin of the corn husk (Behnod *et al*, 2013; Yeasmin and Mondal, 2015 and El-Din *et al, 2017*). The bands at 2920cm^{-1} and shoulder at 2850cm^{-1} were assigned to C-H asymmetric stretching and symmetric stretching of C-H of CH_2-groups respectively (Sathasivam *et al, 2005*). The bands at 1735cm^{-1} and 1631cm^{-1} were attributed to H-O-H bending of absorbed water, C=O stretching (hemicellulose band) and carbonyl stretching of

aromatic ring (lignin). The band at 1233cm^{-1} corresponds to C-O stretching (lignin and hemicellulose) while the one at 1103cm^{-1} corresponds to C-O-C antisymmetric bridge stretching (Yeasmin and Mondal, 2015).

3.2 Sorption Capacity and Behaviour

The variation of the sorption capacity with time for corn husk particles spread on 3mm, 4.5mm and 6mm oil layer thicknesses (on water surface) are given in Figures 3, 4 and 5 respectively.

3.2.1 Oil sorption capacity

The maximum oil sorption capacity of the sorbent recorded was 9.9719 g oil/g sorbent with particle B (400-1000 µm) at about forty min on 3 mm oil layer thickness while the least was 4.8958 g oil/g sorbent with particle D (105-53 µm) at forty minutes. Particle A recorded equilibrium sorption value similar to particle D. Particle B gave the highest initial uptake rate and particle D (105-53 µm) gave the lowest rate. As seen in Figure 3 particles C and D gave an unusual sorption trend. The initial sorption rate was low before sudden increase in sorption capacity were observed at 30

minutes for particle C and 40 minutes for particle D. This might be due to desorption arising from fibrils' pores destruction.

From Figure 4, it is seen that the maximum oil sorption capacity of corn husk (on 4.5 mm oil layer) was 6.8901 g oil/g sorbent with particle B (1000-500 µm) at about twenty min while the minimum equilibrium capacity was 5.4879 g oil/g sorbent with particle A (4000-1000 µm) at ten minutes. Particle B (1000-500 µm) recorded the highest initial uptake rate and particle A (4000-1000µm) gave the lowest rate.

Figure 5 indicates that the maximum oil sorption capacity of the sorbent over 6mm oil layer thickness was 5.3386 g oil/g sorbent with particle D (105-53 µm) at forty minutes and the lowest was 2.9258 g/g with particle A (4000-1000 µm) at twenty minutes. Even then, the sorption capacity of particle B can be seen to be among the highest here. Particle B (1000-500 µm) gave the highest initial uptake rate and particle E (<53 µm) gave the lowest rate, though that of particle A was not too different. The sorption of particle E decreased at forty and fifty minutes and this may be due to effect of particles clogging the fibril pores (Hussein *et al.* 2009).

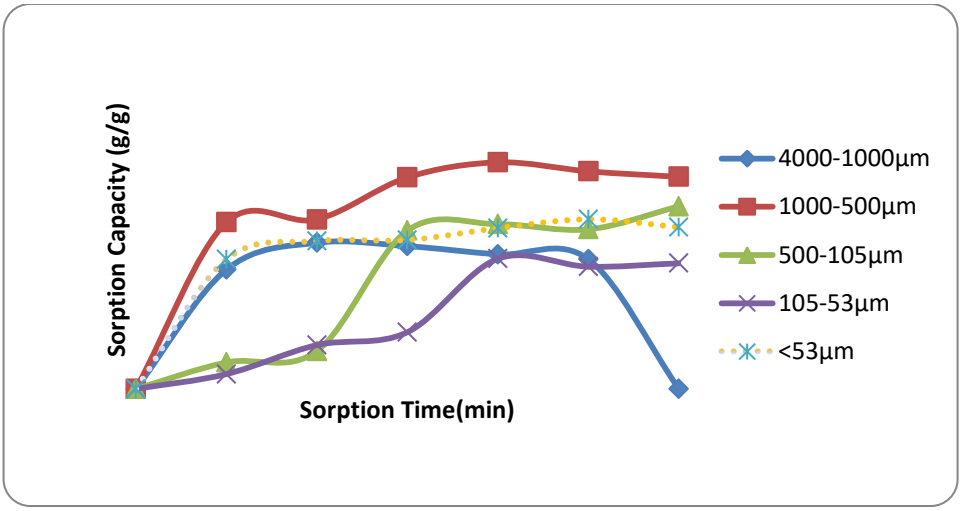

Figure 3: Variation of oil sorption capacity with time for corn husk particles (on 3 mm oil layer)

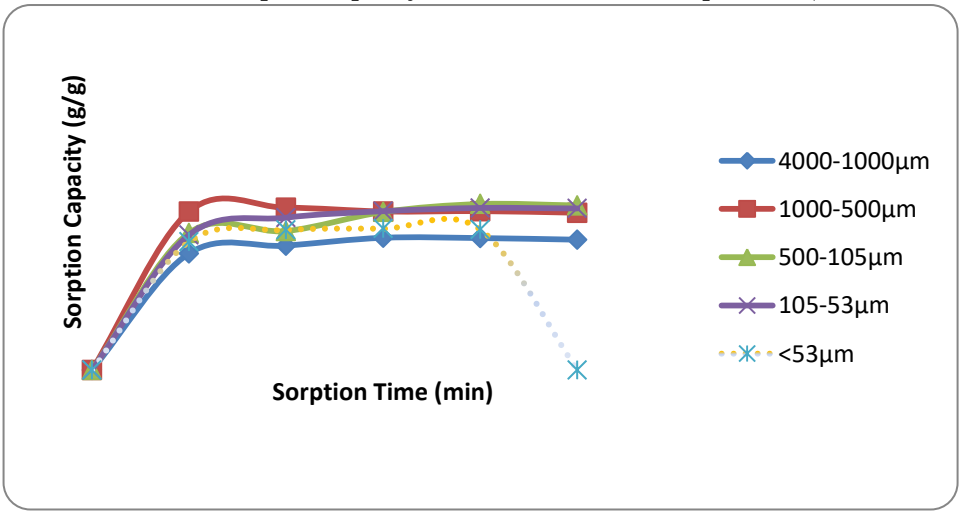

Figure 4: Variation of oil sorption capacity with time for corn husk particles (on 4.5 mm oil layer)

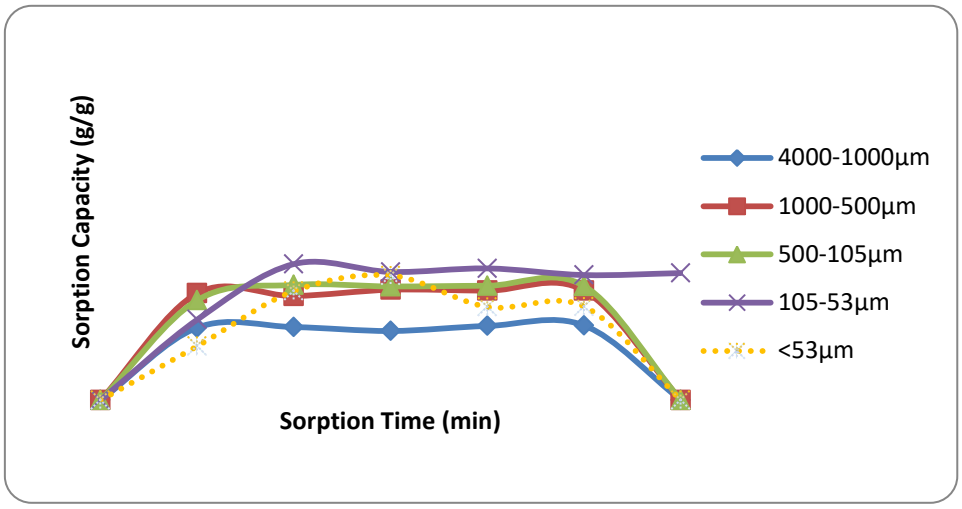

Figure 5: Variation of oil sorption capacity with time for corn husk particles (on 6 mm oil layer)

Particle B (1000-500µm) appears to give the maximum equilibrium sorption when exposed to the three oil layers, while particle A (4000-1000µm) sorbed the least. The relative prominence of particle B in term of the equilibrium sorption capacity increased as the oil layer thickness, which the sorbent was exposed to, decreased; an opposite trend was observed with particles D.

The sorption capacity initially increased with contact time but the equilibrium sorption was reached in less than thirty minutes as shown in Figures 3 – 5. This implies that the crude oil is trapped fast and indicates a

potential for quick cleanup of oil spill, which would prevent fast dispersal of the spilled oil (Shashwat *et al.*, 2006). The exponential decay trend displayed by the particles in oil sorption rate may be due to blockage of the fibrils' pores by the particles and/or the oil. This phenomenon might have led to the stoppage of capillary filling after a period of time.

The oil sorption capacity was observed to decrease with oil layer thickness over water for the different particle size ranges investigated, as shown in Figures 6 - 8. This might be due to the effect of the up thrust forces originating from the water layer within the water-oil-sorbent system. The thicker the oil layer over the water the less would the convective force per area of the oil layer that is available to enhance oil transport, by capillary action (Choi and Moreau, 1993), into the particles' pores, other factors being held constant.

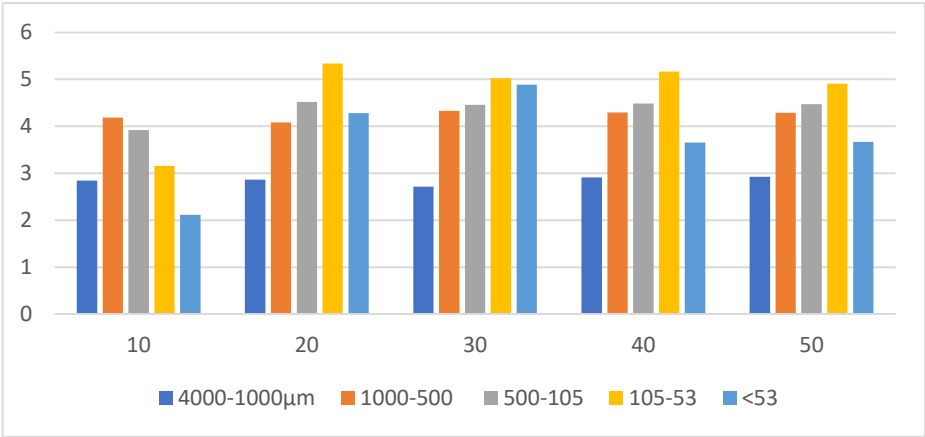

Figure 6: Sorption capacities of different particle sizes over 6mm oil layer thicknesses

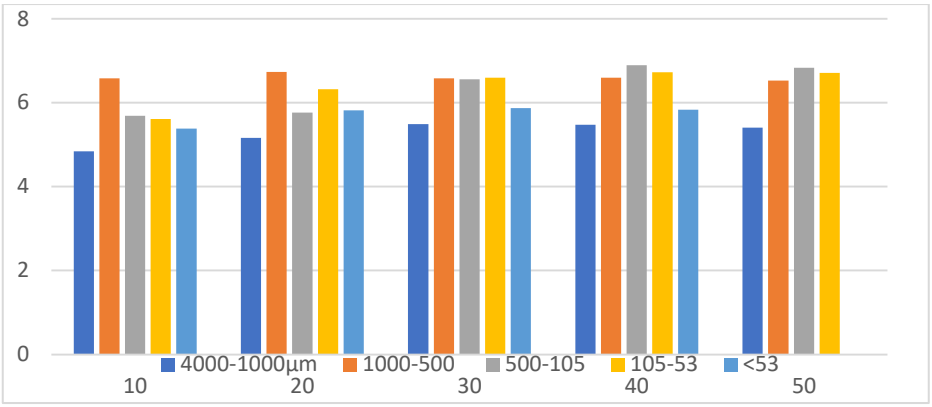

Figure 7: Sorption capacities of different particle sizes over 4.5mm oil layer thicknesses

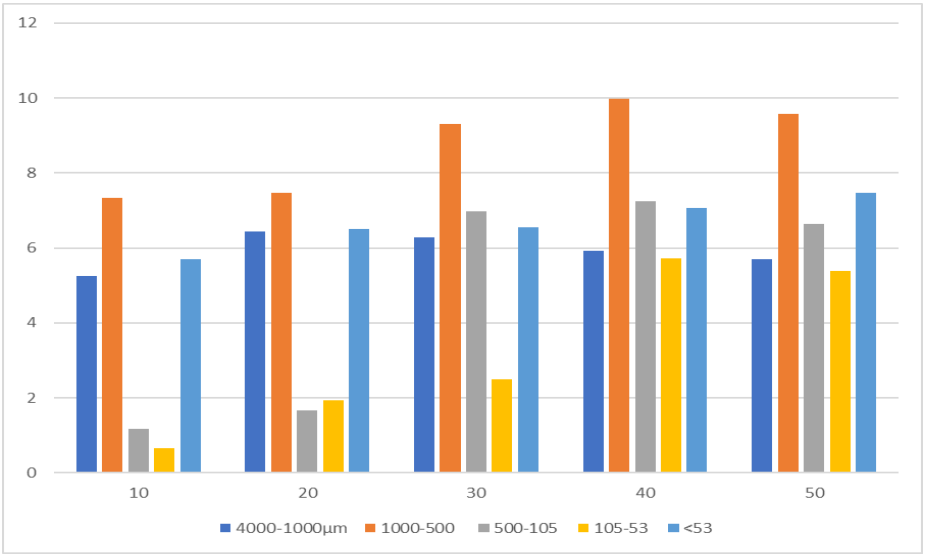

Figure 8: Sorption capacities of different particle sizes over 3mm oil layer thicknesses

A cursory look at Figures 3 – 8 does not establish any discernible trend in relation between oil sorption capacity and particle size ranges utilized in this study. This appears to suggest that other phenomena aside particle size related ones (such as adsorption) are involved in oil sorption by the biomass particles. Blockage of the pores by particles of smaller sizes than the pores' might have occurred just as the destruction of the fibre pores in the course of size reduction (Benhood *et al.*, 2014). These factors, in addition to others such as size and viscosity of the crude oil and, pH of the medium, could affect oil absorption/retaining capacity of the particles. Further investigations are needed to correctly situate the effects of these factors in the oil sorption characteristics of biomass particles.

3.2.2 Water sorption characteristics

Water was sorbed only with the sorbents exposed to 3mm oil layer thickness on water. The highest water sorption capacity by corn husk was 2.2022 g water /g sorbent with particle B (1000-500 µm) at thirty minutes and the minimum equilibrium capacity was 0.4726 g water/g sorbent with particle C (500-105 µm) at fifty minutes. This is probably due to the relatively high cellulose/lignin content of corn husk as seen from the reported composition of the husk. Corn husk sorbed water but did not sink in the water due to its low density and hydrophilic characteristics which might be linked to its high combined cellulose/lignin content. Thus its buoyancy (density and hydrophilicity) would make it float on water (Lee *et al*., 1999a).

3.3 Comparison of Sorption Capacity of Corn Husk and Commercial Sorbents

The maximum sorption capacity of 9.9719 g/g recorded by corn husk was comparable to that of the commercial sorbents (Adsorb-IT filtration Fabric gray sheet) which recorded 10.15 g/g (Hussein *et al*., 2008). The sorbent used in this research was in its natural form, thus if this sorbent was modified to increase its surface area and oleophilic properties, its sorption capacity would improve.

3.4 Sorption Kinetics

From the results presented in Figures 3 – 5, it is seen that oil sorption by the different particle sizes of corn husk displayed decaying exponential trends with time. The model of oil sorption kinetics of corn husk was obtained by fitting the data of Figures 3 to 5 using DataFit 9.0^R software. The best fit was obtained with the function given by Equation 5.

$$q = a(1 - e^{-t}) \quad 5$$

where **q** is sorption capacity, **a** is the model (fit) parameter and **t** is time.

The parameters for kinetic model given by Equation 5 for the five particle size ranges employed for sorption over three oil layer thicknesses are presented in Table 1. The coefficient of determination (R^2) recorded in all cases were higher than 0.98 except for samples D and E when used on 6 mm oil layer thickness when R^2 fell between 0.71 and 0.85. The values of the model parameters, as shown in Table 1, follow the trend obtained for oil sorption capacities of the corn husk particles; this parameter could therefore be regarded as sorption coefficient. The sorption kinetic model which is an inverse exponential form, appears to indicate a diffusion mechanism for oil sorption by the raw corn husk particles.

Table 1: Model parameters of corn husk's oil sorption kinetics for 3 oil layer thicknesses over sea water

Oil layer thickness, mm	Particle Size Range Labels				
	A	B	C	D	E
3	6.2959	7.6249	7.4128	7.41296	6.9331
4.5	5.2743	6.6033	6.3470	6.3913	5.9115
6	2.8512	4.2367	4.3713	4.7626	3.9312

4. CONCLUSION

The oil sorption characteristics of corn husk wastes was evaluated for dynamic conditions at 27^{o}C on Escravos crude of 3mm, 4.5 and 6 mm oil layer thickness on water. The oil sorption by corn husk particles followed the exponential decay pattern. It was observed that as oil layer thickness increased, the sorption capacity decreased. Sorption capacity of corn husk particles was good, especially with those in size range of 1000 – 500 µm. crude oil sorption capacity in excess of 9 g/g was obtained for corn husk particle.

REFERENCES

Adebajo, M. O., Frost, R. L., Kloprogge, J. T., Carmody, O. and Kokot, S. (2003). Porous materials for oil spill clean-up: a review of synthesis and absorbing properties. *Journal of Porous Material*. 10, 159-170.

Amer, A. A., El Maghraby, A., Malash, G. F. and Nahla, T. A. (2007). Extensive characterization of raw barley straw and study the effect of steam pretreatment, *Journal of Applied Science Research. 3* (11): 1336-1342.

Bayat, A., Aghamiri, S. F., Moheb, A. and Vakili-Nezhaad G. R. (2004). *Chemical Engineering and Technology*, 28 (12): 1525 – 1528

Choi, H. M. (1996). Needle punched cotton nonwoven and other natural fibers as oil clean- up sorbents. *Environmental Science Health,* A. 31, 1441-1457.

Choi, H. M., Kwon, H. and Moreau, J. (1993a). Cotton nonwovens as oil spill clean- up sorbents. *Textile Research Journal*. 63 (4): 211-218.

Choi, H., and Cloud, R.M. (1992). Natural sorbents in oil spill cleanup. *Environmental Science and Technology*. 26 (4): 772 – 776.

Choi, H., and Moreau, J.P. (1993). Oil spill sorption behaviour of various sorbents studied by sorption capacity measurement and environmental scanning microscope. *Microscopy Research and Technique*. 25 (5): 447- 455.

De Carvalho Mendes, C. A., De Oliveira Adnet, F. A., Leite, M. C. A. M., Furtado, C. R. G. and Furtado de Sousa, A. M. (2015). Chemical, physical, mechanical, thermal and morphological characterization of corn husk residue. *Cellulose Chemistry and Technology.* 49(9): 727-735)

Deschamps, G., Caruel, H., Borredon, M. E., Bonnin, C. and Vignoles, C. (2003). Oil removal from water by sorption on hydrophobic cotton fibers. Study of

sorption properties and comparison with other cotton fiber-based sorbents. *Environmental Science Technology*. 37 (5): 1013-1015.

Egwaikhide, P.A., Akporhonor, E.E. and Okieimen, F.E. (2007). Utilization of coconut fibre in the removal of soluble petroleum fraction polluted water. *International Journal of Sciences.* 2 (2): 047-049.

Hori, K., Flavier, M. E., Kuga, S, Lam, T.B.T. and Liyama, K. (2000). Excellent oil absorbent kapok (*Ceiba pentandra* (L.) *Gaertn*.) Fiber structure, chemical characteristics and application., *Wood Science*, 46 (5): 401- 404.

Huang, X. and Lim, T. (2005). Experimental evaluation of a natural hollow hydrophobic-oleophilic fiber for its potential application in NAPL cleanup. *Proceedings of International Oil Spill Conference*, Singapore.

Hussein, M., Amer, A. A. and Sawsan, I. I. (2008). Oil spill sorption using carbonized pith bagasse: trial for practical application. *International Journal of Environmental Science and Technology, 5* (2): 233-242.

Hussein, M., Amer, A. A., El-Maghraby, A. and Taha, N. A. (2009). Availability of barley straw application on oil spill clean- up. *International Journal of Environmental Science and Technology, 6* (1): 123-130.

Jain, A. (2017). Oil sorption behavior of fibrous substrates, M.Sc. Thesis, Texas tech University, Texas.

Kaiser P. (2013). Usability of agricultural residues out of the corn harvest in the panel production. *9th International Conference on Production Engineering: Development and Modernization of Production*, Sprungbrett, pp 689-694

Karan C. P., Rangasamy R. S. and Das D. (2011). Oil spill cleanup by structured fibre assembly. *Indian Journal of Fibre and Textile Research*, 36, 190 – 200.

Kopecký, F. (1999). *Physics for Students of Pharmacy,* edited by I. Bratislava, UK. (In Slovak).

Lee, B. G., Han, J. S. and Rowell, R. M. (1999). In: Kenaf properties, processing and products: Oil sorption by lignocellulosic fibre. Mississippi State University, *Agricultural. and Biological Engineering,* pp. 423-433.

Odedokun, O. V. (2014). Economic analysis of cotton production and supply trend estimation in Zamfara State, Nigeria. A Ph.D. Dissertation. Department of Agricultural Economics and Rural Sociology, Ahmadu Bello University, Zaria. Nigeria.

Olawale, A. S. and B. B. Saidu (2010). Oil Sorption Characteristics of Lignocellulosics Particulates. Conference paper: 3rd *International Conference on Engineering Research and Development: Advances in Engineering Science and Technology,* Pg. 63; 10184

Pinto, J., Athanassiou, A. and Fragouli, D. (2016). Effects of the porous structure of polymer foams on the remediation of oil spills. *Journal of Physics D. (Applied Physics)*. Vol 49, 145601 (8 pp)

Radetic, M., Jocic, D., Jovancic, P., Petrovic, Z. and Thomas, H. (2003). Recycled wool-based nonwoven material as an oil sorbent., *Environmental Science and Technology.* 37 (5): 1008-1012.

Rene, P. S., Philip M. G., and Dieter M. I. (1993). *Environmental Organic Chemistry*, John Wiley and Sons, Inc., U.S.A.,

Reynolds, J. G., Coronado, P. R. and Hrubesh, L. W. (2001). Hydrophobic aerogels for oil-spill cleanup–intrinsic absorbing properties. *Energy Source*. 23 (9): 831-843.

Saidu, B. B. (2011). Study of oil spill clean-up by selected natural organic sorbents., M.Sc. Thesis, Department of Chemical Engineering, Ahmadu Bello University, Zaria. Nigeria. pp 46, 66.

Sanni, A., Olawale A. S. and Sani Y. M. (2017). Techno-economic analysis of agricultural wastes as feedstocks for bioethanol production in Nigeria. Proceedings of the 13th Conference/AGM of Material Science and Technology Society of Nigeria (MSN), Kaduna State Chapter. 4th November. Zaria. Nigeria

Shashwat, S. B., Milind V. J and Radha V. J. (2006). Treatment of oil spill by sorption Techniques using fatty acid grafted saw dust. *Chemosphere.* 64 (6): 1026-1031.

Sun, X. P., Sun, R. and Sun, J. X. (2002). Acetylation of rice straw with or without catalysts and its characterization as a natural sorbent in oil spill clean-up. *Journal for Agricultural and Food Chemistry.* 50, 6428-6433.

Teas, C., Kalligeros, S., Zanikos, F., Stournas, S., Lois, E. and Anastopoulos, G. (2001). Investigation of the effectiveness of absorbent materials in oil spills clean-up. *Desalination.* 140 (3): 259-264.

Toyoda, M.; Inagaki, M., (2003). Sorption and recovery of heavy oils by using exfoliated graphite. *Spill Science Technology Bulletin*. 8 (2): 467- 474.

Van Soest, E. P. J., Robertson, J. B. and Lewis, B. A. (1991). Methods for dietary fiber, neutral detergent fiber and non-starch polysaccharides in relation to animal nutritive. *Journal of Diary Science.* 74:3583–3597.

Zheng, Y., Wang, J., Zhu, Y. and Wang, A. (2015). Research and application of kapok fibre as an absorbing material: A mini review. *Journal of Environmental Sciences*. 27, 21 – 32.

Zeigler, C., da Silva, I. C. R., Mail, M., Kavalenka, M. N., Barthlott, W. and Holscher H. (2016). Microstructure of superhydrophobic plant leaves-inspiration for efficient oil spill cleanup materials. *Bioinspiration and Biomimetic*. Vol 11, 10pp.

SYNTHESIS, CHARACTERIZATION AND APPLICATION OF KAOLIN-BASED ZSM-5 ZEOLITE FOR WATER DESALINATION

[*]Aliyu, U. M.[1], Rathilal, S.[1], and Isa, Y. M.[1]
Chemical Engineering Department
Durban University of Technology,
P.O. Box 1334, Durban 4000, South Africa.
Corresponding Author: usmanaliyumohammed@gmail.com

ABSTRACT

ZSM-5 was produced after the metakaolinization of Graham town clay deposit of Eastern Cape province South African and the use of NaOH, TPABr, $Na_2SiO_3.9H_2O$ solution and deionized water with a molar composition of $50SiO_2:Al_2O_3:20Na_2O:2TPABr:2000H_2O$. The synthesized product was characterized by XRD, SEM, TGA and BET surface area. The characterization results confirmed that the sample produced was of ZSM-5 phase. The product has a specific surface area, pore size and pore volume of 179.9 m^2/g, 49.262A and 0.05 cm^3/g respectively. The effect of zeolite dosage, (1.0, 2.5, 4.0, and 6.0g/100ml) on salinity reduction of seawater was investigated via adsorption study. The result revealed that effectiveness salinity (ES) increases with the increase of the sorbent dose. At 1.0g dose, the salt removal value is 1.04 ppt (SR) which is 3.64% effectiveness salt removal. At ZSM-5 dose of 2.5, 4.0, and 6.0 g, the SR values are 3.29, 6.46, and 8.12 ppt which correspond with ES value of 9.40, 18.40, and 23.20%. ZSM-5 zeolite synthesized from kaolin of South African origin has shown great prospect as natural abundant sorbent material for desalination of synthetic seawater.

Keywords: *Kaolin, ZSM-5 zeolite, Seawater, Desalination, Salinity*

INTRODUCTION

Global water shortage has progressively become a great opposition to human exploit, agricultural growth and industrial activities (Zhu *et al.*, 2016). Availability of potable water is vital for human needs and it scarcity is threatened in many areas across the globe more especially in developing countries and arid regions (Shannon *et al.*, 2008; Zhao *et al.*, 2014). Oceans and seas water comprises of more than 71% of earth surface and 97% of it is saline and cannot be used as potable water, industries as well as agricultural purposes (Von-kiti, 2012). To curb and subdue this salinity problem and ensure the accessibility of freshwater a right strategy has to be adapted. South Africa is located between two great oceans, Atlantic and Indian and water crisis is usually emanating in some part of cape town province. Therefore, seawater desalination is a choice and potential technology to subjugate the water crisis in the future (Wibowo *et al.*, 2017).

Desalination of seawater is a process whereby dissolved salts and minerals are removed to produce fresh potable water (Zhao *et al.*, 2013; Wang *et al.*, 2016; Wenten *et al.*, 2016). Nowadays, there are many types of seawater desalination technologies – including reverse osmosis (RO) (Greenlee *et al.*, 2009) and thermal processes like multi-effect distillation (MED) (Abu-Zeid *et al.*, 2015), membrane vacuum distillation (MVC) (Pérez-González *et al.*, 2012) and multi-stage flash distillation (MSF)(Khawaji *et al.*, 2008). These processes produce potable water but the technology is expensive to operate, therefore, some cheaper alternative methods is required.

Sorption is a process in which one substance takes up or holds another by either absorption or adsorption. Sorption technique is the potential presume process for seawater desalination. Sorption technology is coherence and highly productive with a varied range of materials which influence its potentiality and less expensive method of desalination of seawater (Wibowo *et al.*, 2017). The adsorption process is considered as the most sufficient technology for desalination of seawater environmentally and economically. Many sorbent materials such as eggshell, fly ash and clay mineral (Aliyu *et al.*, 2017) and natural zeolites were applied to treat saline water (Wibowo *et al.*, 2017). Kaolin-based zeolite is appraised as cheap and abundant sorbent material (Lijalem Ayele Regassa, 2016). In this study, kaolin-based zeolite was synthesized and applied as an absorbent for the desalination of seawater. The salinity reduction (RS) and the effectiveness of salinity reduction (ES) of seawater after treatment were determined and the effect of the seawater salinity reduction with an increase of zeolite dosage was evaluated.

MATERIALS AND METHODS.

As received kaolin from G&W minerals resources located in the Eastern Cape region of South Africa calcined at 650℃ for 2h with Si/Al ratio 2.91 was used as a source of silica and alumina (66.58% SiO_2 and 22.81 % Al_2O_3 respectively). Seawater solutions (0.35 w%) used for the adsorption studies were prepared from analytical seawater (Na, K, Ca, and Mg) salts from Sigma-Aldrich. Sodium silicate 26.5% SiO_2 and 10.6% Al_2O_3 composition solution and TPABr. All the chemicals were purchased from Sigma Aldrich except Nitric acid 55% which is sourced from Ace enterprises chemical association. The chemicals were applied as received with no additional purification.

SYNTHESIS OF KAOLIN-BASED ZSM-5 ZEOLITE.

In the preparation of kaolin-based ZSM-5, the required amount of G&W metakaolin and sodium hydroxide were dissolved in deionized (DI) water and TPABr were also mixed separately with the required amount of DI water. The solution of NaOH/Kaolin and sodium silicate solution were added simultaneously to the solution of the TPABr while stirring. Nitric acid was used to control the pH until the solution mixture is homogenous. The synthesized gel was transferred to stainless steel Teflon lined autoclave cup and was hydrothermally treated at 180℃ for two days. The resulting product was washed with DI until the pH is less than 8. The sample was dried overnight at 80℃ and calcined for 5 hours at 550℃. The resulting powder was characterized.

CHARACTERIZATION.

X-ray diffraction (XRD) patterns and average crystallite size were collected with Bruker AXS, D8 Advance equipped with Tube (Cu-Ka radiation (lKa_1=1.5406Å) and Detectors Lynx Eye (Position sensitive detector) at 40kV, 40mA and V20 variable slit. The measurements were carried out with a step width of 0.5° to 130° 2θ with an increment (Δ2θ of 0.034° and a scan rate of 0.5 sec per step. The diffraction data were analyzed using OriginPro 2018 software to give the estimation of the amount of each phase in the sample. The morphology was characterized by using scanning electron microscopy FEI Nova NanoSEM 230 with a field emission gun equipped with a high-resolution immersion lens. The EDS detector is an Oxford X-Max, using INCA software. Surface area, pore size, and pore volume measurements and analysis were determined by BET machine. Thermal analysis was done using thermogravimetric analyzer/differential scanning calorimetry (TGA/DSC 1) STAR System Mettle Toledo.

BATCH ADSORPTION STUDIES

The adsorption of Na, Ca, K and Mg from the synthetic seawater containing NaCl, $CaCl_2$, KCl, and $MgSO_4$ with an average salinity of 35g/L or 35,000mg/L were conducted in the laboratory using linear shaker 262 apparatus experiment. The experimental runs were conducted by dispersing a required amount of kaolin-based ZSM-5 into a 100mL synthetic seawater solution. The sorbent material (kaolin-based ZSM-5) dosage was varied at 1, 2.5, 4.0, and 6.0g and dispersed in the seawater sample using a linear shaker apparatus for 180 min at room temperature and 7.8 pH in order to determine the optimum dosage and salt reduction. The adsorbent was filtered out with Whitman filter paper No. 5 after each run and the salinity of the water after adsorption was estimated by **YSI** Pro Plus Multi-Parameter Water Quality Meter. The effectiveness of salt removal (*ES*), salt removal (*SR*), and adsorbent dosage was analyzed.

Study by the school of ocean science and technology, (2015) table 1. shows the major salt ions found in seawater of salinity 35g/L and their respective percentage total and mass concentrations. Chlorine (Cl^-) has the highest percentage of 55.29% and 19.353gms/kg while potassium (K^+) has the least with 1.14% and 0.399gms/kg. other ions in descending order of percentage total and concentrations are sodium (Na^+): 30.74% and 10.76gms/kg, Sulphate (SO_4^{2-}): 17.75% and 2.712gms/kg, Magnesium (Mg^{2+}): 3.69% and 1.292gms/kg, Calcium (Ca^{2+}): 1.18% and 0.412gms/kg.

Table 1. Major ions in seawater of salinity 35g/L

Symbol	Name	% of total	mmoles	gms/kg
Cl^-	Chlorine	55.29	546	19.353
Na^+	Sodium	30.74	469	10.76
Mg_{2+}	Magnesium	3.69	53	1.292
SO_4^{2-}	Sulphate	7.75	28	2.712
Ca_{2+}	Calcium	1.18	10.3	0.412
K^+	Potassium	1.14	10.2	0.399

(School of Ocean Science and Technology, 2015)

The amount of salt ion adsorbed (RS) at equilibrium was evaluated in equation 1.

$$RS = c_i - c_e \qquad (1)$$

Where C_i and C_e are initial and equilibrium adsorbate concentration respectively. The percentage of salt ions removal (%ES) was evaluated using equation 2.

$$\% ES = \frac{Ci - Ce}{Ci} * 100 \qquad (2)$$

RESULTS AND DISCUSSION

X-ray diffraction (XRD) studies

The XRD pattern of ZSM-5 synthesized at 180℃ for 2days using metakaolin that calcined at 650℃ for 2hour is shown in Fig. (1a). The characteristic peaks of ZSM-5 are in the ranges of 7.9 to 23.1^o 2θ which show nucleation with a sizable amount of quartz as an impurity at 20.9 and 26.6^o 2θ clearly confirmed the formation of crystalline ZSM-5 phase (Salou *et al.*, 2001; Mohiuddin *et al.*, 2016). The percentage (%) crystallinity and the average crystal (grain) size was evaluated using OriginPro 2018 version and found to be 87% crystallinity and 28 nm respectively. The two parameters are key to the sorption process. The specific surface area, pore size and pore volume of 179.9 m^2/g, 49.262A and 0.05 cm^3/g respectively were deduced using BET surface area analyzer. The crystal size of the sorbent rises the specific surface area and intense surface porosity increases the outer surface area of the zeolite (Wibowo *et al.*, 2017). The incorporation of the two parameters together influences the effective surface area. This shows that the synthesized kaolin-based ZSM-5 with a good surface area would promote high sorption potential and proficiency. Consequently, it will be applied as a sorbent medium in seawater desalination.

Scanning electron microscopy (SEM) studies

SEM is a technique used to interpret the morphology and distribution of crystals size of the zeolite phase. Typically, the configuration, formation, and structure of ZSM-5 crystals were highly controlled and depend on synthesis parameters such as crystallization temperature, time and aging. Mohiuddin (2015), conducted a study on the synthesis of ZSM-5 using impure kaolin under various parameters resulting in different morphologies. The image of kaolin-based ZSM-5 nanocrystals synthesized under 180℃, 48hr and 48hr crystallization temperature, time and aging respectively were performed in this study and presented in Fig. 1(b). It can be seen clearly that the kaolin-based ZSM-5 is obviously orthogonal shape and highly crystallized with an average crystals size of 28 nm indicated that there is an intergrown crystal with some amorphous material presence. The orthogonal nanocrystals are as a result of the aggregation of their high surface Gibbs free energy (Wu *et al.*, 2013). The TGA results depicted in Fig. 1(c). show the stability of the synthesized kaolin-based ZSM-5. The graph demonstrated that water and other volatile material are removed from the sample at around 45 to 180℃ and the material became stable through the ranges of temperature until it is about 950°C from where phase change was noticed as it's approaching its melting point which is 1000°C (Arbad *et al.*, 2010).

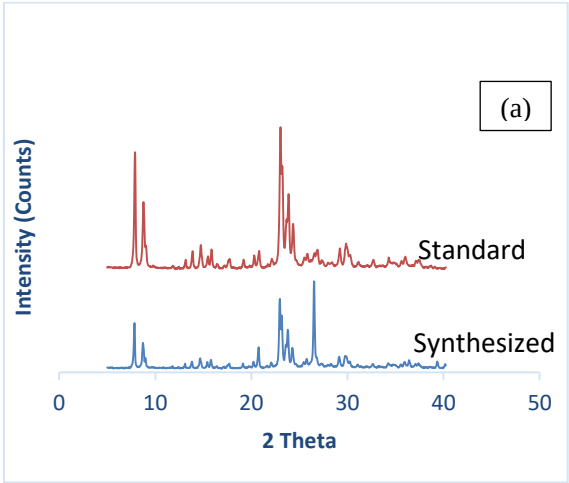

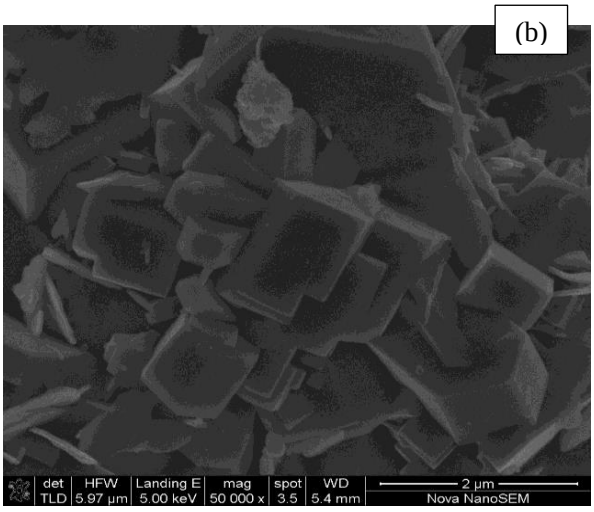

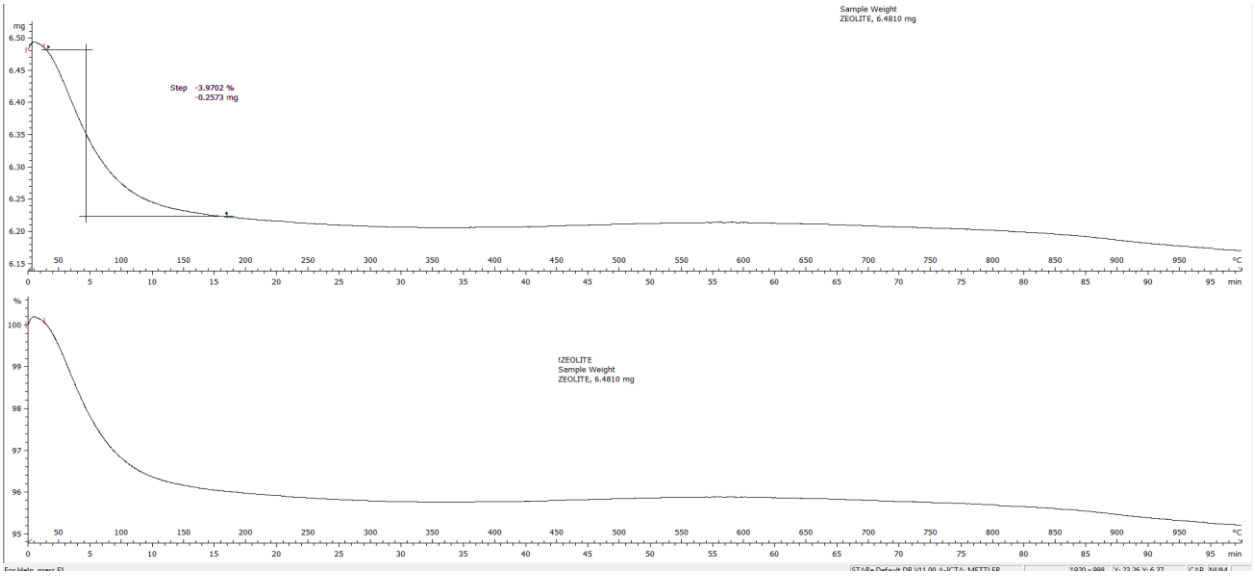

Figure 1(a). XRD pattern of standard and kaolin-based ZSM-5 zeolite and (b). SEM image of synthesized kaolin-based ZSM-5 zeolite (c)TGA of the synthesized kaolin-based ZSM-5.

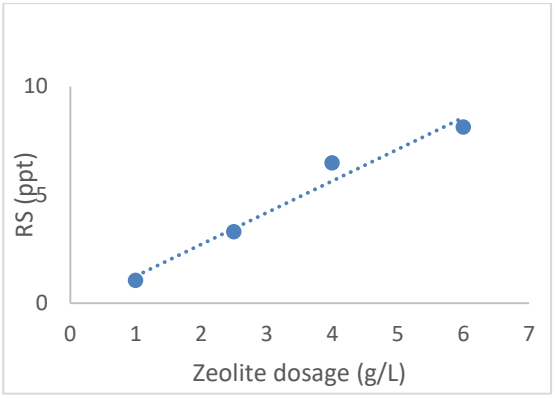

Figure 2. Salinity reduction with an increase of zeolite dosage.

Effect of Adsorbent Dosage.

The effect of adsorbent dose on the adsorption of salt from seawater onto kaolin-based ZSM-5 zeolite revealed that the seawater was desalinated and there is a reduction of salinity after treatment as shown in Fig. 2. The salinity reduction (effectiveness) rises with an increase in an adsorbent dose which shows that the adsorption sites are capable of absorbing more salt ions. By increasing the adsorbent dose, the sorption active area is adequately accessible for the adsorbate to utilize. The effectiveness of the adjusted ZSM-5 zeolite dosage for the desalination process is depicted in Figure 2. We applied different zeolite dosage of 1.0, 2.5, 4.0, and 6.0g to investigate the salinity reduction of seawater after treatment with the different dosage of the adsorbent. At 1.0g dose, the salt removal effectiveness value is 1.04 ppt which is 3.64% salt removal (SR). At ZSM-5 dose of 2.5, 4.0, and 6.0 g, the ES values are 3.29, 6.46, and 8.12 ppt which correspond with RS value of 9.40, 18.40, and 23.20%. However, It was reported by Mekonnen et al (2015) that adsorption of Cr(VI) onto some selected adsorbents shows that, adsorbent dosage above the equilibrium stage does not ameliorate adsorption due to the accessibility of surplus adsorption sites than that of sorbent considering that the adsorption sites per unit mass of adsorbent remain constant. They reported that with an increase in sorbent dosage, removal is increasing exponentially rather than linearly. The behavior of kaolin-based ZSM-5 presents a different tendency. This shows that the desalination of seawater using synthesized ZSM-5 is a function of sorbent dosage. The interaction of seawater-ZSM-5 zeolite reveals that desalination performance was better with an increase of adsorbent dosage. Therefore, it can be concluded that the behavior of sorbent is a result of sorbate-sorbent interaction. This implies that each sorption materials have a different characteristic reaction (Wibowo *et al.*, 2017).

CONCLUSION

Kaolin-base ZSM-5 from south African local kaolin with specific surface area, pore size and pore volume of 179.9 m^2/g, 49.262A and 0.05 cm^3/g, respectively were successfully synthesized and applied as sorbent material to desalinate synthetic seawater. The values of *RS* are found to increase as dosage increases 1.0, 2.5, 4.0, and 6.0 as 1.04, 3.29, 6.40, and 8.12 ppt respectively. whereas *ES* values are 3.64, 9.40, 18.40, and 23.20 % at

1.0, 2.5, 4.0, and 6.0 g. ZSM-5 zeolite synthesized from kaolin of South African origin has shown great prospect as low-cost sorbent material for desalination of synthetic seawater.

Acknowledgment: The authors wish to appreciate and acknowledged the financial support from Umgeni water, Durban, KZN South Africa and the Durban University of Technology.

REFERENCES

Abu-Zeid, M. A. E. R., Zhang, Y., Dong, H., Zhang, L., Chen, H. L. and Hou, L. 2015 A comprehensive review of vacuum membrane distillation technique, *Desalination*. Elsevier B.V., **356**, pp. 1–14. doi: 10.1016/j.desal.2014.10.033.

Aliyu, A., Abdulkareem, A., Kovo, A., Abubakre, O., Tijani, J. and Kariim, I. 2017 Synthesize multi-walled carbon nanotubes via catalytic chemical vapour deposition method on Fe-Ni bimetallic catalyst supported on kaolin, *Carbon letters*, **21**, pp. 33–50. doi: 10.5714/CL.2017.21.033.

Arbad, B. R. and Lande, M. K. 2010 ZnO-beta zeolite mediated simple and efficient method for the one-pot synthesis of quinoxaline derivatives at room temperature, **8**(2). doi: 10.2478/s11532-009-0151-7.

Greenlee, L. F., Lawler, D. F., Freeman, B. D., Marrot, B. and Moulin, P. 2009 Reverse osmosis desalination: Water sources, technology, and today's challenges,

Water Research. Elsevier Ltd, **43**(9), pp. 2317–2348. doi: 10.1016/j.watres.2009.03.010.

Khawaji, A. D., Kutubkhanah, I. K. and Wie, J. M. 2008 Advances in seawater desalination technologies, *Desalination*, **221**(1–3), pp. 47–69. doi: 10.1016/j.desal.2007.01.067.

Lijalem Ayele Regassa 2016 Synthesis and Characterization of Zeolite A from Kaolin of Ethiopia : Studies of its application as detergent builder and in tannery wastewater treatment Lijalem Ayele Regassa A Thesis Submitted to Department of Chemistry Presented in Fulfillment of the R.

Mekonnen, E., Yitbarek, M. and Soreta, T. R. 2015 Kinetic and Thermodynamic Studies of the Adsorption of Cr (VI) onto Some Selected Local Adsorbents, *South African Journal of Chemistry*, **68**, pp. 45–52. doi: 10.17159/0379-4350/2015/v68a7.

Mohiuddin, E., Isa, Y. M., Mdleleni, M. M., Sincadu, N., Key, D. and Tshabalala, T. 2016 Synthesis of ZSM-5 from impure and beneficiated Grahamstown kaolin: Effect of kaolinite content, crystallisation temperatures and time, *Applied Clay Science*, **119**(November), pp. 213–221. doi: 10.1016/j.clay.2015.10.008.

Pérez-González, A., Urtiaga, A. M., Ibáñez, R. and Ortiz, I. 2012 State of the art and review on the treatment technologies of water reverse osmosis concentrates, *Water Research*, **46**(2), pp. 267–283. doi: 10.1016/j.watres.2011.10.046.

Salou, M., Kooli, F., Kiyozumi, Y. and Mikamizu, F. 2001 Effect of aluminium source and content on the synthesis of zeolite ZSM-5 from kanemite solid-state transformation, *Journal of Materials Chemistry*, **11**(5), pp. 1476–1481. doi: 10.1039/b008126o.

School of Ocean Science and Technology 2015 Chemical composition of seawater, *Chemical Oceanography*, p. 26. Available at: http://www.soest.hawaii.edu/oceanography/courses/OCN623/Spring2012/Salinity2012web.pdf.

Shannon, M. A., Bohn, P. W., Elimelech, M., Georgiadis, J. G., Marinas, B. J. and Mayes, A. M. 2008 Science and technology for water purification in the coming decades, *Nature (London, U. K.)*, **452**(March), pp. 301–310. doi: 10.1038/nature06599.

Von-kiti, E. 2012 *SYNTHESIS OF ZEOLITES AND THEIR APPLICATION TO THE, Msc.thesis Knust*.

Wang, Q., Li, N., Bolto, B., Hoang, M. and Xie, Z. 2016 Desalination by pervaporation: A review, *Desalination*, **387**, pp. 46–60. doi: 10.1016/j.desal.2016.02.036.

Wenten, I. G. and Khoiruddin 2016 Reverse osmosis applications: Prospect and challenges, *Desalination*. Elsevier B.V., **391**, pp. 112–125. doi: 10.1016/j.desal.2015.12.011.

Wibowo, E., Sutisna, Rokhmat, M., Murniati, R., Khairurrijal and Abdullah, M. 2017 Utilization of Natural Zeolite as Sorbent Material for Seawater Desalination, *Procedia Engineering*. The Author(s), **170**, pp. 8–13. doi: 10.1016/j.proeng.2017.03.002.

Wu, G., Wu, W., Wang, X., Zan, W., Wang, W. and Li, C.

2013 Nanosized ZSM-5 zeolites: Seed-induced synthesis and the relation between the physicochemical properties and the catalytic performance in the alkylation of naphthalene, *Microporous and Mesoporous Materials*. Elsevier Inc., **180**, pp. 187–195. doi: 10.1016/j.micromeso.2012.11.011.

Zhao, L., Chang, P. C. Y. and Ho, W. S. W. 2013 High-flux reverse osmosis membranes incorporated with hydrophilic additives for brackish water desalination, *Desalination*. Elsevier B.V., **308**, pp. 225–232. doi: 10.1016/j.desal.2012.07.020.

Zhao, L. and Ho, W. S. W. 2014 Novel reverse osmosis membranes incorporated with a hydrophilic additive for seawater desalination, *Journal of Membrane Science*. Elsevier, **455**, pp. 44–54. doi: 10.1016/j.memsci.2013.12.066.

Zhu, Y., Gupta, K. M., Liu, Q., Jiang, J., Caro, J. and Huang, A. 2016 Synthesis and seawater desalination of molecular sieving zeolitic imidazolate framework membranes, *Desalination*. Elsevier B.V., **385**, pp. 75–82. doi: 10.1016/j.desal.2016.02.005.

IMPROVED SELECTIVITY EFFECT OF COBALT, NICKEL CO-METAL IMPREGNATION WITH ZINC ON ZSM-5 FOR AROMATIZATION OF PROPANE

***Oseke, G.G[1], Atta, A. Y.[1], Mukhtar, B.[1], El-Yakubu, B. J.[1] and Aderemi, B. O.[1]**

[1]Chemical Engineering Department, Ahmadu Bello University, Zaria.

**Corresponding author:* osechemtechy@gmail.com

Sub-theme: Research Development and innovation in chemical engineering

ABSTRACT

Conversion of light alkanes catalytically to aromatic compounds is an important research area of interest. This is because aromatic compound are the major feedstocks for petrochemical industries. Zn/ZSM-5 has been found to improve aromatic selectivity of HZSM-5 but unstable. Hence the need for stabilizing Zn with another metal. The interaction of Zn with Co and Ni on ZSM-5 shows a higher selectivity towards aromatics over 85%. This improved Zinc stability on ZSM-5 as compared to only Zinc with dwindling selectivity to 50% and HZSM-5 of 10% at ten hours TOS. Catalyst physicochemical properties were analysed with XRD, BET, N_2-adsorption, FTIR, FTIR-Pyridine, SEM, and TEM. The XRD and FTIR characterization showed that the modified catalysts were still crystalline after metal impregnation. The products distribution also showed reduced light gases formation and formation of more aromatics. The synergistic interaction between Ni and Co with Zn metal improved the catalytic performance of Zn-Co/ZSM-5 and Zn-Ni/ZSM-5 catalysts by promoting and sustaining the dehydrogenation step and suppressing protolytic cracking step in the reaction series resulting in the recorded significant improvement in aromatic yield over the monometallic Zn/ZSM-5 catalyst.

Keywords:

Propane conversion, bimetallic, toluene selectivity, co-impregnation, Metal modified Zn/ZSM-5

1. INTRODUCTION

The conversion of propane to aromatics has been a subject of interest to industrialists and academia within the last two decades. This is closely related to increasing demand for aromatic compounds (mainly, benzene, toluene, ethylbenzene and xylene) which are used as feedstocks for the production of chemicals, polymers, detergents, pharmaceuticals, agricultural inputs and explosives from petrochemical industries. Nigeria among many nations has been declared to be more of gas rich nation which are substrates for production of aromatic compounds. It is becoming more important and imperative to start considering ways to transform these abundant gas resources (light alkanes such as propane) to aromatic compound which are building block and feedstock to petrochemical and chemical process industries. Propane exists in large deposits in natural gas reservoirs, gas condensate, and refinery gases (Derouane *et al.,* 2006: Asaftei *et al.,* 2009).

A number of researches have been conducted over time to understudy the kinetics and mechanism of propane transformation to aromatics (Fechete *et al.,* 2012: Armor, 2011). It was found that reaction steps majorly includes: Protolysis, hydride transfer, beta-scission, alkylation-dealkylation, dehydrogenation, oligomerization, olefin adsorption and desorption, alkanes adsorption and desorptions, cyclization and aromatization. Most related researches from kinetic and thermodynamic views have revealed that propane protolytic cracking step is the rate limiting step and the hydride transfer which is recombination of the abstracted hydrogen with the radical intermediates further limits the progression of the reaction to form aromatics (Lindström and Lars, 2003: Bhattacharya and Sivasanker, 1996: Rane *et al.,* 2006: Xu *et al.,* 2013).

Modification of catalyst by metal anchoring on ZSM-5 catalyst had made up part of the efforts applied to produce aromatic compounds as parent HZSM-5 had been found to be low on aromatic selectivity. These include developments of monometallic zeolitic catalysts i.e. Pt/ZSM-5, Ga/ZSM-5, Zn-ZSM-5, Mo/ZSM-5 aimed at promoting protolytic scission over C=C cracking and improve cyclization to aromatization (Bhan and Nicholas, 2008: Choudhary *et al*., 1996: Choudhary *et al*., 2006: Guisnet *et al.,* 1992: He, 2015)

Zn/ZSM-5 emerged as the most promising catalyst considering cost effectiveness, selectivity toward

aromatics, minimization of light gases production and environmental friendliness when compared to Ga or Pt based ZSM-5. Also, all attempts to correct this ZSM-5 Zn-based catalyst modification can only help to enhance aromatic selectivity, but cannot inhibit severe coke formation on the catalyst which is another challenge that can be generated rather than improving the whole reaction process. These put limit to industrial application and commercialization of the process.

The need to enhance Zn/ZSM-5 catalyst stability and activity at reaction operating condition thus call for the introduction of the second metal to make bimetallic stable and active catalysts. Other approaches to mitigate this challenge include incorporating the Zn into the zeolite intra-framework or create hierarchical structure in the zeolite (Ogunronbi *et al*., 2015).

Therefore, this work studied the effect of co-impregnation of cobalt and nickel as a second metal with zinc on ZSM-5 due to their atomic size similarity, same oxidation states and closer electronegativity to improve zinc activity, aromatic selectivity and catalyst lifespan on stream on bimetallic catalyst for propane aromatization.

2. METHODOLOGY

2.1. Catalyst Preparation

NH_4-ZSM5 (Si/Al=50) was sourced commercially from Sigma Aldrich and calcined to HZSM-5 at 550 ^oC for five hours. Aqueous solutions containing 2 wt. % of ZnO from $Zn(NO_3)_2$ as precursor 2 wt. % of Co_3O_4 from $(Co_3(NO_3)_2$ as precursor and 2 wt. % of NiO from $Ni(NO_3)_2$ as precursor were co-impregnated by introducing them at the same time dropwise on solution of H-ZSM5 catalysts while stirring for effective mixing, and dried at 70 ^oC. The samples were further dried at 80 ^oC for 16 hours and then calcined by temperature programmed furnace at 550 ^oC (4 ^oC per minute ramping) for five hours. The nitrates decomposition during heating leaves the oxides of the metals on ZSM-5 catalyst surface.

2.2 Catalyst Characterization

The metallic content in the catalyst were determined by a handheld XRF machine, Thermofisher Scientific NITON XL3t Waltham, Massachusetts USA. FTIR spectra measurements were performed using Shimadzu FTIR-8400s (Shimadzu, Japan) spectrophotometer instrument with a MCT detector (64 scans, $4cm^{-1}$) at National Research Institute of Chemical Technology, Zaria. Pyridine-adsorbed Fourier Transform Infrared Spectroscopy (Py-FTIR) was used to determine the amount of Brønsted and Lewis acid sites using Shimadzu FTIR-8400s Spectrophotometer equipment. 20 mg of each catalyst was degassed at 200 ^oC in an oven and then put in a desiccator for pyridine adsorption at atmospheric temperature. The suction was allowed for about thirty minutes after which the catalyst were re-weighed to measure the increment in mass due to pyridine adsorption and then pressed into a regular wafer and put in an infrared cell, and this spectrum was used as background for the 95 adsorbed pyridine experiments. Pyridine was then adsorbed to a 5.0×10^{-2} Pa equilibrium pressure at 30 °C. FTIR spectra were recorded.

The powder X-ray diffraction (XRD) patterns were obtained on a Siemens D500 X-ray Powder Diffraction (XRD) using Cu Kα. The anode was operated at 40 kV and 40 mA. X-Ray. The catalysts were scanned in continuous mode at wavelength K_{alpha1}= 1.540598, K_{alpha2}= 1.544426 and K_{beta}=1.392218 $2\theta=10^o$-80^o at scanning speed of 12°/min°.

Nitrogen adsorption and BET analyses were performed at 77 K using Micromeritics ASAP-2020 unit at Jubilee Campus University of Nottingham, UK. Catalyst samples were vacuum-degassed at 300 ^oC for 10 hours to remove surface humidity and pre-adsorbed gases before exposure to adsorption gas. The specific surface areas of the catalyst samples were calculated from the Nitrogen isotherm data using the Brunauer–Emmett–Teller (BET) model. The micropore volumes and micropore areas were measured using t-plot analysis (Brunauer, *et al*., 1938: Lippens *et al.,* 1964: Ahmad *et al.,* 2016).

Morphology of the catalyst samples surface were obtained using Scanning Electron Morphology Machine Hitachi S-4800. Resolution : 1.0 nm （15KV). Transmission electron morphology TEM images of the catalyst samples were obtained on a FEI Tecnai G2 Spirit STEM.

2.3 Performance Test

Performance tests of the prepared catalysts were carried out in a stainless-steel fixed bed continuous flow reactor with internal diameter of 9 mm. 0.5 g of the catalyst samples was mixed with 0.5g of silica glass beads. The catalysts were degassed under inert nitrogen flow environment as the temperature rose through the reactor to 540^oC for two hours before the flowing in propane into the reactor. Propane was introduced to flow through the reactor. Aromatization reaction was carried out at

540°C and Gas Hourly Space Velocity (GHSV) of 1200 mL/g-h, pure propane and nitrogen of ratio 1:2 under atmospheric pressure. The gaseous products were analysed in-situ by an online Buck Scientific GC 910 gas chromatograph equipped with a Thermal Conductivity Detector TCD having a Molsieve 13X packed column for hydrogen, nitrogen and hydrogen detection and a flame ionization detector (FID) connected to Restek MTX1 and HAYESEP D oven packed column for hydrocarbon and aromatics detection analysis. Aromatic and other hydrocarbon selectivity were calculated based on the total carbon moles with a unit of Carbon-mole, that is ratio of each product with respect to the total moles of Carbon-containing products and carbon balance.

3. RESULTS AND DISCUSSIONS

3.1 Characterizations

Figure 1 shows the FTIR spectra of the catalyst sample. Peak intensities at 450 and 550 cm^{-1} wave number show pentasil ring of ZSM-5 while 1100 and 1225 cm^{-1} which correspond to bridged silanol Brönsted acid sites (Si-OH-AL) and Lewis acid sites (AL-OH) respectively. The bands at 3400 and 1700 cm^{-1} = stretching and bending vibration of hydroxyl (OH^{-}) group correspond to physically absorbed water on ZSM-5 surface. The spectra wave number in the OH stretching region suggested that HZSM-5 contained Brönsted acid groups also on 3610 cm^{-1} associated with the framework aluminium [Si(OH)Al], isolated external silanol groups (3740 cm^{-1}), free internal silanol groups (3730 cm^{-1}), and delocalized hydrogen-bonded groups (3500 cm^{-1}) of lattice defects. For Zn/HZSM-5, the introduction of Zn species has little effect on the OH groups associated with 3500 and 3740 cm^{-1}. The silanol groups characterized by 3730 cm^{-1} decreased slightly, which was attributed to the interaction between the internal silanol groups and Zn (OH)+ and other loaded metal cations located in cationic positions of the zeolites. The Brönsted acid peak (3610 cm^{-1}) decreased obviously, suggesting the replacement of the zeolite protons by the impregnated Zn and other metals (Ni and Co).

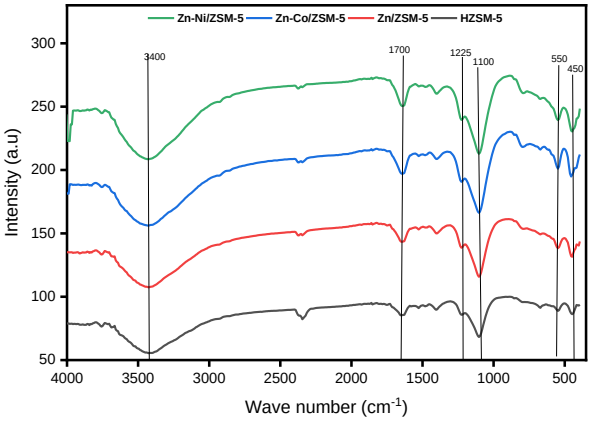

Figure 1: FTIR spectra of the catalyst samples

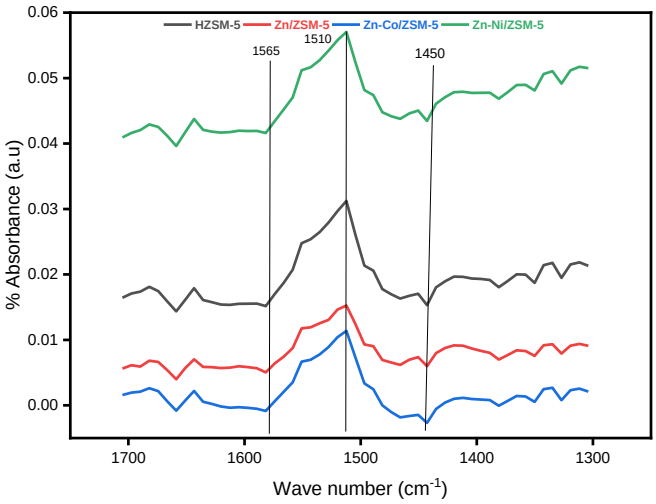

Figure 2: Pyridine-IR spectra of catalyst sample

Figure 2 shows the Pyridine-FTIR spectra of zeolitic catalysts. Three characteristic peaks around 1450,1540 and 1490 cm^{-1} are observed in all of the catalyst though there were little shifts, they represent the amount of Lewis acid sites, Bronsted acid sites and both Bronsted and Lewis acid sites respectively (He *et al.*, 2015). Lewis acid sites enhance the process of dehydrogenation and aromatization (Ni *et al.*, 2014: Cihanoglu *et al.*, 2015)

Figure 3 shows the XRD patterns of the synthesized catalysts together with ZSM-5 as control catalyst. This analysis revealed that the loading of Zn, Ni and Co oxides in accessible positions inside the zeolite matrix had no influence on its crystallinity. However, intensities of characteristic peaks were changed due to filling of metallic oxides into the zeolite matrix of ZSM-5. The characteristic peak intensities were suppressed as the X-ray absorption was fevered by the presence of Zn Co and Ni oxide particles (Wu *et al.*, 2009: Li *et al.*, 2009:

El-Shall *et al*., 2009: Yanming *et al*., 2016).

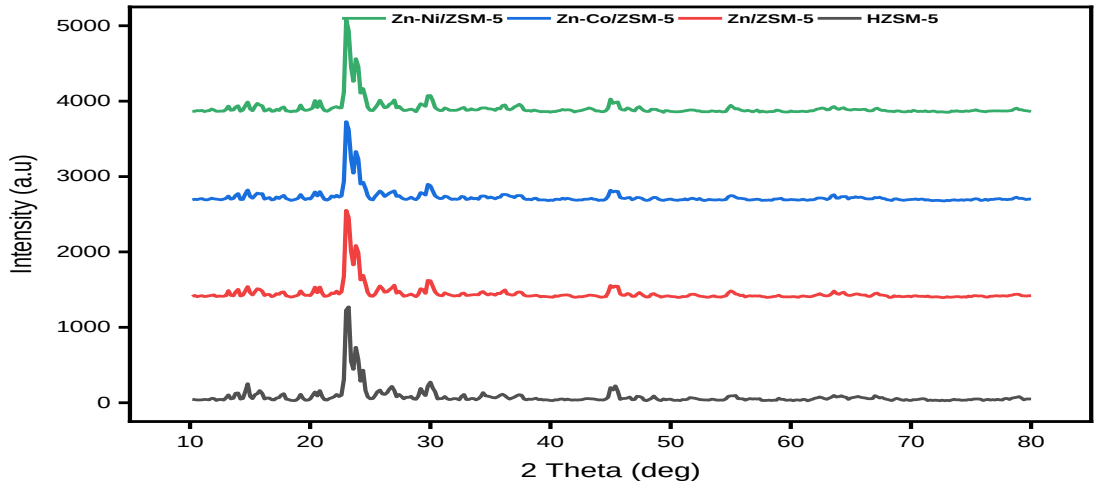

Figure 3: XRD analysis of parent and metal cation-loaded ZSM-5 zeolites

The Textural physical properties of the catalyst samples are provided in Table 1. Addition of metal oxides via co-impregnation of their precursor and their thermal decomposition during calcination had a little effect of specific surface area reduction. This decrease is attributed to the filling of the metallic oxides inside the pores and also on the surface of the matrix and decreased the pore volume, and specific area in turn. Metal co-impregnation on ZSM-5 did not affect the micro porosity of the zeolite structure (Wu *et al*., 2005).

Thus, from the XRD and BET results of the metal incorporated catalysts compared to the parent HZSM-5, it follows that the oxides of Zn, Co and Ni might have been deposited on the outer surface of the zeolite.

Nitrogen adsorption and desorption isotherm plots are shown in Figure 4 for all the prepared catalysts. All the plots for the catalysts represent a Type I isotherm with high level microporosity as revealed in the BET surface area. The summary of the surface area and micropore analysis is shown in Table 1. Addition of Zn to the parent HZSM-5 decreased the total surface area, including the micropore area and the external (mesopore) surface area of the catalyst. As Co was added to Zn/ZSM-5 further decrease in the external surface area resulted. However, their micropore area did change slightly compared to Zn/ZSM-5, suggesting that the Co metal particles did not diffuse much into the micropore structure of the zeolite. The addition of Ni to the Zn/ZSM-5 catalyst showed increased surface area. This may suggest that some Ni particles occupy sideway attachment to the external acid sites on the ZSM-5 structure while some on the surface.

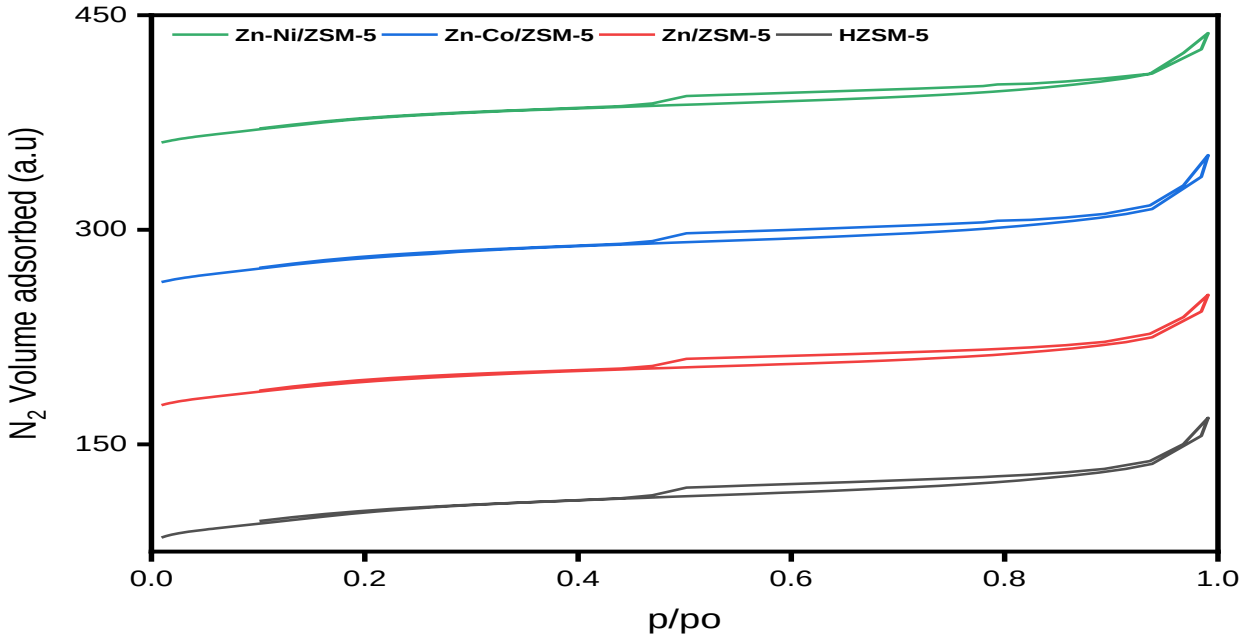

Figure 4: N_2-adsorption of parent and metal cation-loaded ZSM-5 zeolites

The SEM and TEM study of synthesized catalyst are presented in Figure 5. The morphology of the parent ZSM-5 Figure 5 a and b was significantly changed after the addition of metallic oxides and as the loading increased as seen in a, b, c and d. The evenness of metallic oxide dispersion could be observed clearly in images in Figure 5 a-h.

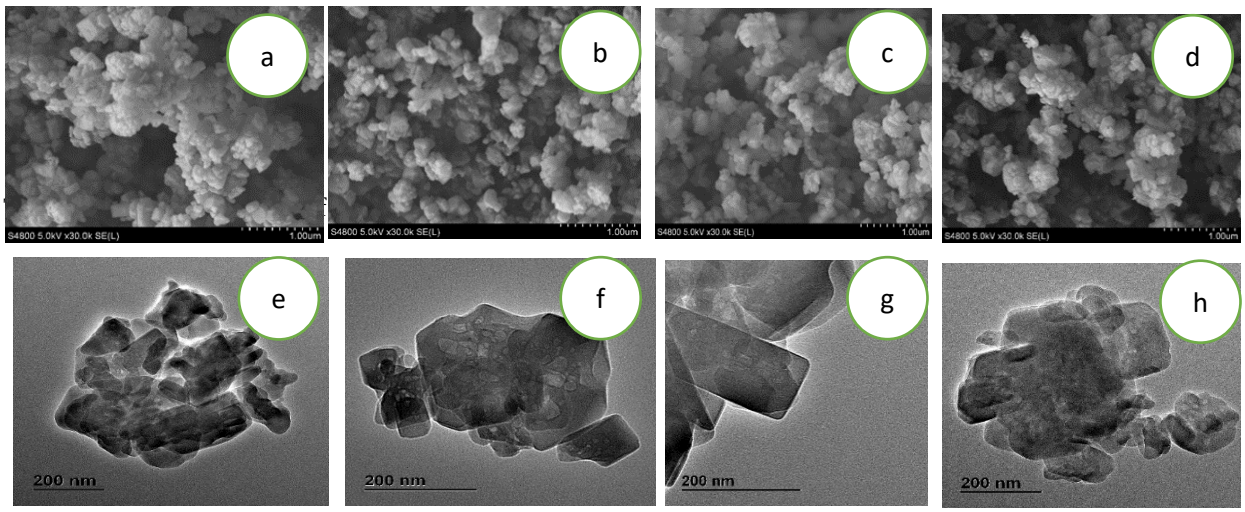

Figure 5: SEM (a–d) and TEM (e-h) images of HZSM-5, Zn/ZSM-5, Zn-Co/ZSM-5 and Zn-Ni/ZSM-5.

Table 1: Textural properties of catalyst

Catalyst(s)	S_{BET}a (m^2/g)	S_{micro}c (m^2/g)	S_{meso}c (m^2/g)	V_{total}b (cm^3/g)	V_{micro}c (cm^3/g)	Pore width(nm)
HZSM-5	373.223	333.360	39.867	0.261	0.106	2.793
Zn/Z	361.081	323.096	37.984	0.254	0.141	2.778
Co-Zn/Z	359.185	324.452	34.733	0.246	0.145	2.735
Ni-Zn/Z	362.020	324.719	37.301	0.246	0.145	2.719

.

3.2 Catalytic performance

Catalytic conversion of propane to aromatic was investigated and shown in Figure 6. Aromatic compounds require strong acid sites of parent HZSM-5. Impregnation of metals to HZSM-5 did not really have much effect on propane activation which could have probably caused some blockages reason for some levels of reduction in the conversion when compared to the conversion on HZSM-5. As it can be observed on Figure 7, HZSM-5 has lowest selectivity because of cracking. On addition of Zn, selectivity was highly improved largely because of improved dehydrogenation ascribed to the production of $ZnOH^+$ species. Selectivity kept dropping with time on stream. This was tentatively ascribed to already established acid sites coke deactivation and zinc instability at operating condition. The effect of the second metal Ni and Co addition stabilized aromatic selectivity, minimized formation of light gases through cracking and enhanced stable production of aromatics.

This also has been explained that large amount of Zn-Lewis acid sites ($ZnOH^+$ species) for dehydrogenation and aromatization, are produced more than ZnO with the introduction of Ni and Co species. This enhanced effective dispersion of the active $ZnOH^+$ as shown by TEM and SEM images thereby bringing it to tighter interaction of $ZnOH^+$ with the zeolite framework making it difficult to drain it out from the surface of zeolite as compared to ZnO. This made more sites available for dehydrogenation and aromatization thus improving the catalysts' selectivity towards aromatics and stability.

Zn-Ni/ZSM-5 has greater stable and sustain selectivity towards aromatics because of its unique properties of same oxidation state similar atomic size and electronegativity with Zinc. Zn-Co/ZSM-5 has improved selectivity toward toluene among other aromatics in the product distribution. This is attributed to more alkylation of toluene from methane dehydrogenation. Figures 8, 9 and 10 show the effect of Ni and Co on product distribution.

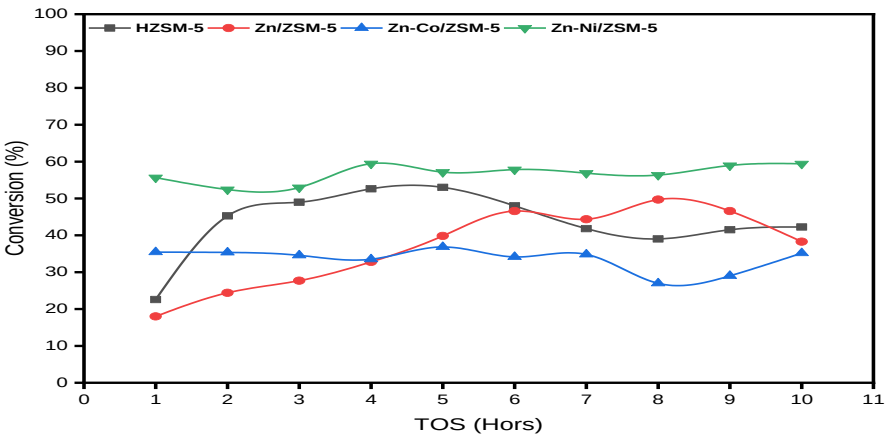

Figure 6: Propane conversions over catalyst samples.

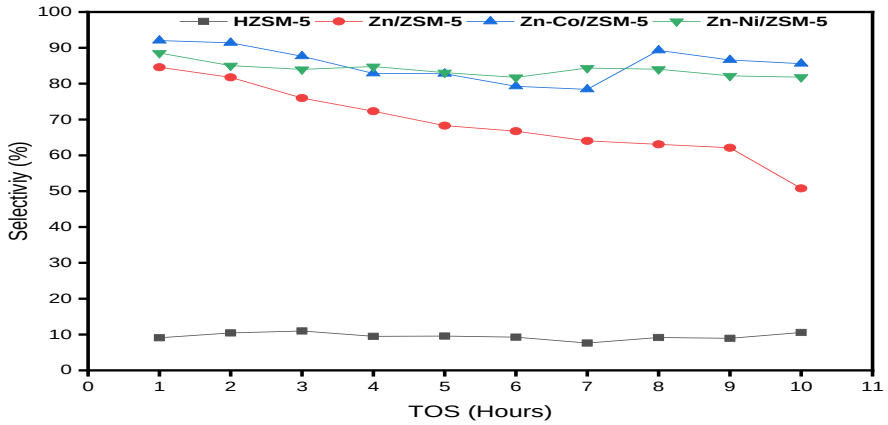

Figure 7: Aromatic selectivity over parent and metal cation-loaded ZSM-5 zeolite.

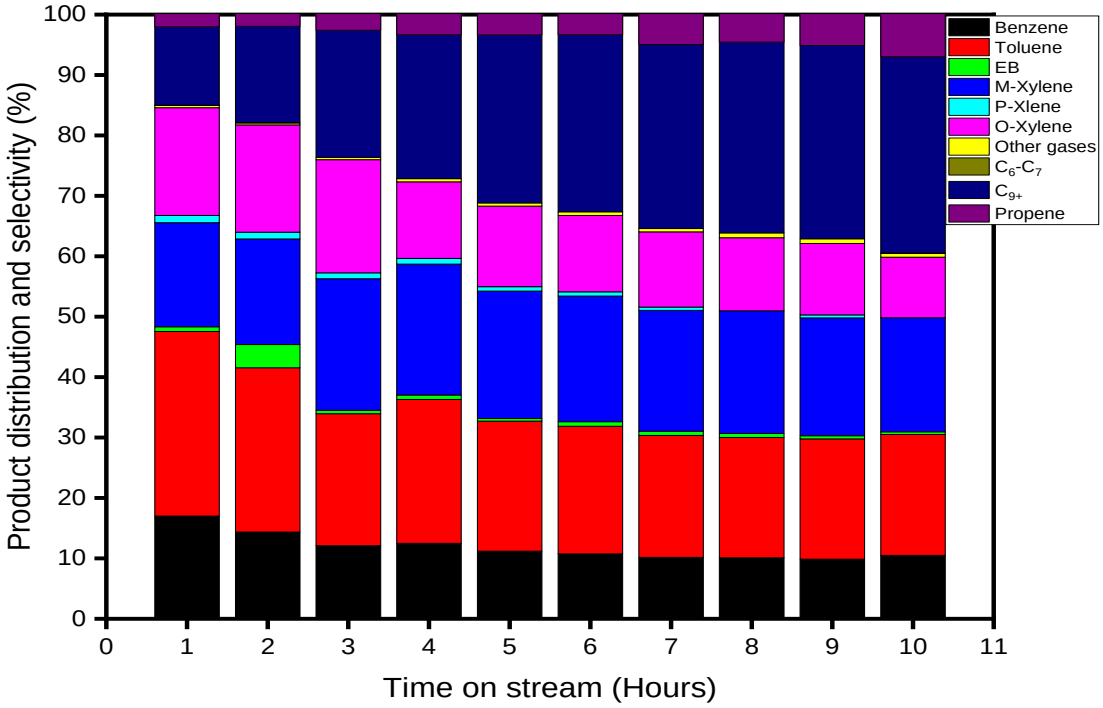

Figure 8: Product distribution of propane aromatization over Zn/ZSM-5

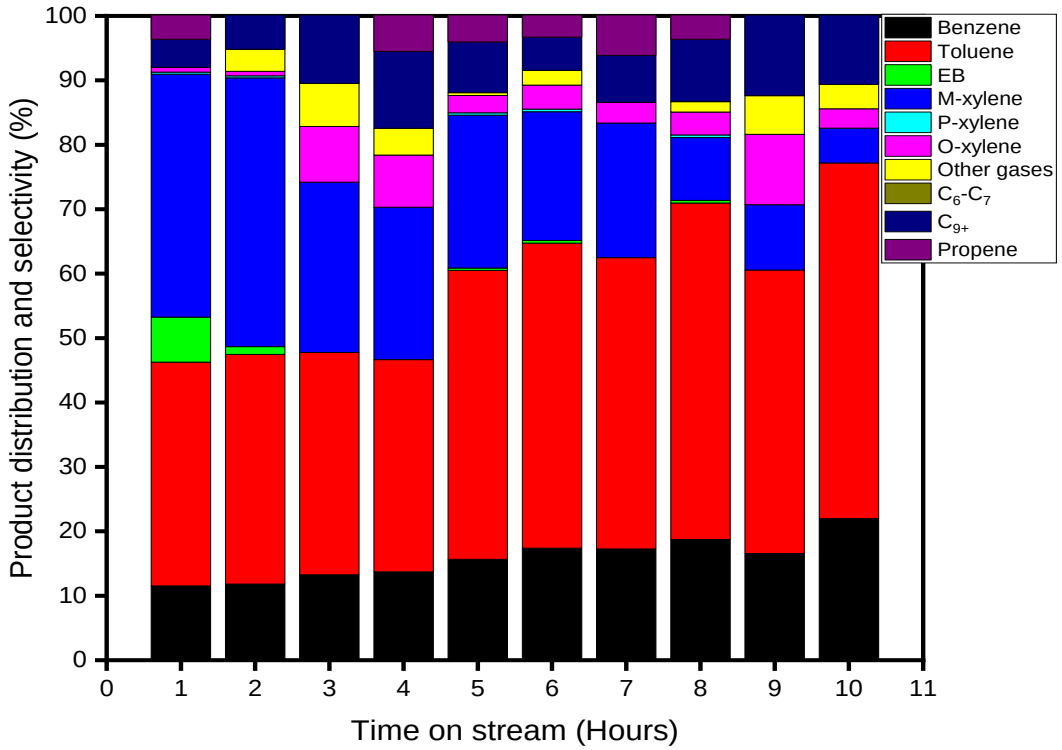

Figure 9: Product distribution of propane aromatization over Zn-Co/ZSM-5

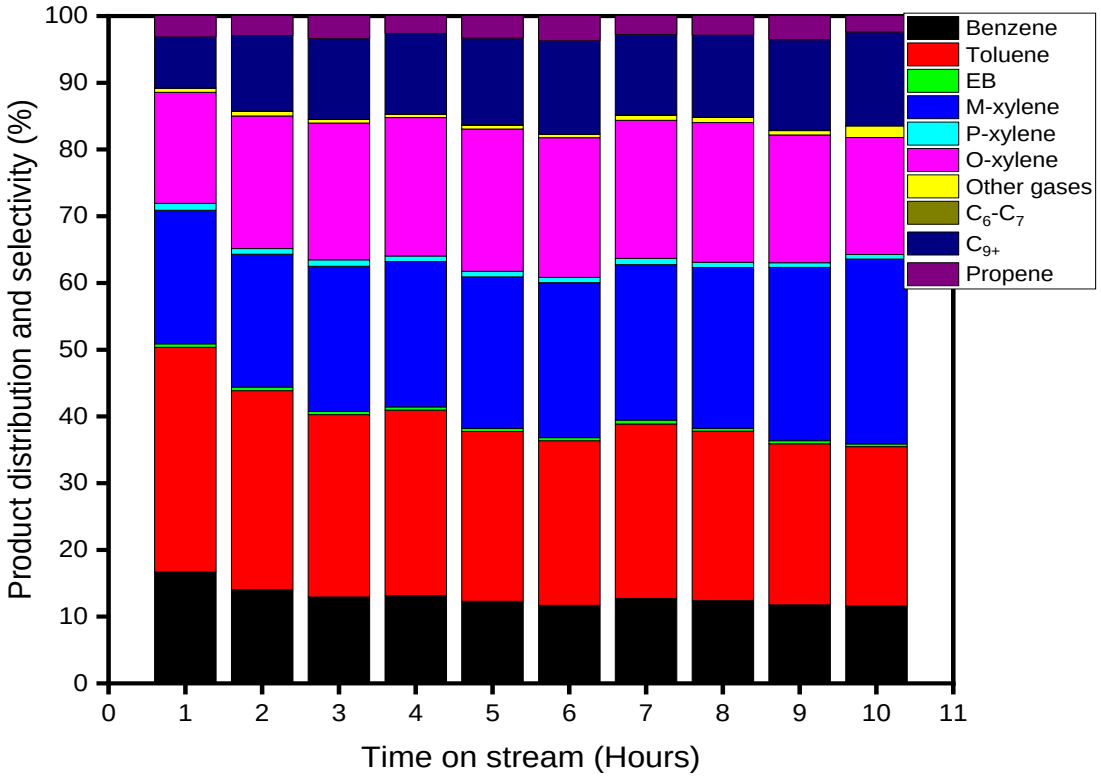

Figure 10: Product distribution of propane aromatization over Zn-Ni/ZSM-5

The remarkable increase and sustained selectivity towards aromatics as seen in Figure 9 and 10 are as a result of enhanced primary aromatization through dehydroaromatization as well as suppressed cracking and subsequent H-transfer reaction.

4. CONCLUSION

In summary, Zinc based bimetallic catalyst containing Cobalt and Nickel were prepared and tested for propane aromatization. All physicochemical properties in characterizations revealed that the crystallinity and structure of the zeolite were preserved. The modified catalysts had strong influence on activity, aromatic selectivity and product distribution with minimized undesired products when compared to already existing catalyst. The promotional and stabilizing effects of Cobalt and Nickel on Zinc instability were observed with sustained improved and sustained selectivity towards aromatics. The introduction of these metals help to disperse zinc making more sites available for dehydrogenation reaction step and as a result improving aromatic selectivity and minimize catalyst deactivation. The developed bimetallic catalyst will contribute to the development industrial catalysts with high activity and superior stability for desired aromatic production for petrochemical and chemical process industries.

ACKNOWLEDGMENT

The authors would like to appreciate PTDF for the fund provided through her Annual Oil and Gas Research Grant Competition.

REFERENCE

Abdelsayed, V., Shekhawat, D., Poston Jr, J. A., & Spivey, J. J. (2013). Synthesis, characterization, and catalytic activity of Rh-based lanthanum zirconate pyrochlores for higher alcohol synthesis. Catalysis today, 207, 65-73.

Ahmad, M., Farhana, R., Raman, A. A. A., & Bhargava, S. K. (2016). Synthesis and activity evaluation of heterometallic nano oxides integrated ZSM-5 catalysts for palm oil cracking to produce biogasoline. Energy conversion and management, 119, 352-360.

Armor, John N. "A history of industrial catalysis." Catalysis Today 163.1 (2011): 3-9.

Asaftei, I. V., Bilba, N., Birsa, L. M., & Iofceab, G. (2009). Aromatization of industrial feedstock mainly with butanes and butenes over HZSM-5 and Zn/HZSM-5 catalysts. Acta Chennica Lasi, 17, 5-34.

Bhattacharya, D., and S. Sivasanker. "Aromatization of n-hexane over H-ZSM-5: Influence of promoters and added gases." Applied Catalysis A: General 141.1-2 (1996): 105-115.

Brunauer, S., Emmett, P. H., & Teller, E. (1938). Adsorption of gases in multimolecular layers. Journal of the American chemical society, 60(2), 309-319.

Derouane, E. G., Parmon, V., Lemos, F., & Ribeiro, F. R. (Eds.). (2006). Sustainable Strategies for the Upgrading of Natural Gas: Fundamentals, Challenges, and Opportunities: Proceedings of the NATO Advanced Study Institute, held in Vilamoura, Portugal, July 6-18, 2003 (Vol. 191). Springer Science & Business Media.

Fechete, I, Ye W, and Jacques C. V. (2012) "The past, present and future of heterogeneous catalysis." Catalysis Today 189.1: 2-27.

Lindström, Bård, and Lars J. Pettersson. "A brief history of catalysis." Cattech 7.4 (2003): 130-138.

Lippens, B. C., Linsen, B. G., & De Boer, J. H. (1964). Studies on pore systems in catalysts I. The adsorption of nitrogen; apparatus and calculation. Journal of Catalysis, 3(1), 32-37.

Ogunronbi, K. E., Al-Yassir, N., & Al-Khattaf, S. (2015). New insights into hierarchical metal-containing zeolites; synthesis and kinetic modelling of mesoporous gallium-containing ZSM-5 for propane aromatization. Journal of Molecular Catalysis A: Chemical, 406, 1-18.

Rane, N., Overweg, A. R., Kazansky, V. B., Van Santen, R. A., and Hensen, E. J. M. (2006). Characterization and reactivity of Ga+ and GaO+ cations in zeolite ZSM-5. Journal of Catalysis, 239(2), 478-485.

Wu, X. N., Zhao, H. T., Li, J., Schlangen, M., & Schwarz, H. (2014). Highly regioselective hydride transfer, oxidative dehydrogenation, and hydrogen-atom abstraction in the thermal gas-phase chemistry of $ZnOH^+/C_3H_8$. Physical Chemistry Chemical Physics, 16(48), 26617-26623.

Xu, Yuebing, Yoshizo Suzuki, and Zhan-Guo Zhang. "Comparison of the activity stabilities of nanosized and microsized zeolites based Fe–Mo/HZSM-5 catalysts in the non-oxidative CH4 dehydroaromatization under periodic CH_4–H_2 switching operation at 1073 K." Applied Catalysis A: General 452 (2013): 105-116

Zhao, Y., Liu, X., & Han, Y. (2015). Microporous carbonaceous adsorbents for CO_2 separation via selective adsorption. RSC Advances, 5(38), 30310-30330.

THEORETICAL PREDICTION OF BIOGAS FROM SOLID WASTE GENERATED IN UNIVERSITY OF LAGOS, NIGERIA

***Salami, L.[1], Patinvoh, R.J.[2], Folami N.A.[3] and Salami, K.B.[4]**

[1]Environmental Engineering Research Unit, Department of Chemical and Polymer Engineering, Lagos State University, Lagos State, Nigeria.

[2]Department of Chemical and Polymer Engineering, Lagos State University, Lagos State, Nigeria.

[3]Department of Chemical Engineering, Lagos State Polytechnic, Ikorodu, Lagos State, Nigeria.

[4]Department of Mechanical Engineering, Federal University of Technology, Akure, Ondo State, Nigeria.

*Corresponding author: SalamiLukumon@yahoo.com; Lukumon.salami@lasu.edu.ng

ABSTRACT

The management of solid waste especially in a developing country like Nigeria is a challenge. There is a possibility of biogas recovery from solid waste generation. This study was carried out to predict the amount of biogas and methane from solid waste generated in University of Lagos, Nigeria. The composition of solid waste generated in University of Lagos was used to establish the chemical formulas for the solid waste. The model of Buswell and Muller was used to generate the reaction for the solid waste from which the theoretical and actual amount of biogas and methane were predicted. The chemical formulas with and without sulphur for organic portion of solid waste generated in University were $C_{187}H_{377}O_{137}N_7S$ *and* $C_{26.71}H_{53.88}O_{19.57}N$ *respectively. The theoretical and actual amount of biogas were found to be 0.847 and 0.678* m^3/kg *respectively while that of methane were 0.469 and 0.375* m^3/kg *respectively. The biogas from solid waste generated in University of Lagos can be used for domestic purposes and electricity generation to promote energy security and sustainability.*

Keywords*: Biogas, generated, prediction, solid waste, theoretical and university of Lagos.*

1.0 INTRODUCTION

Solid wastes can be a blessing or a curse depending on the way they are managed. Solid wastes are wastes generated from human activities which are solid and are discarded as useless or unwanted (Olafadehan and Salami, 2011). According to Robert (1999) as cited by Salami et al., 2011, the generation of solid waste varies by source, season, geography and time. As urbanization continues in developing countries, Nigeria inclusive, generation of solid wastes is a major public health and environmental concern (Olafadehan and Salami, 2011). Nigeria generates more than 32 million tons of solid waste annually (Adeniran *et al*., 2017). This is a huge challenge as there have not been proactive measures in the management of solid wastes in Nigeria. Solid wastes can be managed by digestion of the organic portion of the waste anaerobically to produce biogas and a stabilized solid residue which is the digestate (Roati*et al*., 2012).

Biogas is made of carbondioxide, methane, ammonia, hydrogen sulphide, water vapour and other minor components whose volume distribution is a function of substrate characteristics and the process operating conditions (Roati *et al*., 2012). Many scholars have worked on solid wastes (Salami et al., 2011; Olafadehan and Salami, 2011;Adeyinka et al., 2014; Uwadiegwu and Chukwu, 2013, Nwachukwu, 2010; Olukanni and Ugwu, 2013; Nathaniel *et al*., 2012; Arazon, 2015; Coker *et al*., 2015 and Peretomode *et al*., 2019). Okeniyi and Anwan (2012) researched on solid waste generated in Covenant University, Ota, Nigeria. The researched provided the percentage composition of average waste generation per day in the institution. The energy content of the waste was not considered. Amori *et al*., (2013) worked on waste generation and management practices in residential areas in three institutions in Southwest, Nigeria but neglected the energy content analysis.

Arazo (2015) studied the compositions of solid wastes generated from Misamis Oriented State College of Agriculture and Technology, Philippins. The study revealed that the major components of the waste stream from the institution are organics but the amount of biogas recoverable from the organic waste was not considered. Adeniran *et al*., 2017 characterized the solid waste generated in University of Lagos for sustainable waste management. The work revealed the various compositions of the solid waste components but neglected the exergy and energy content analysis of the waste. Salami et al., 2018 studied the exergy and the energy content analysis of the solid waste generated in University of Lagos, Nigeria. The study presented the numerical value of heat which would be released during incineration of the solid waste and the thermal exergy of the waste. The quantification of biogas potential of the solid waste was ignored.

It is evident from the available literature that the prediction of biogas potential from solid waste generated in University of Lagos, Nigeria has not been carried out. Therefore, the aim of this study is to predict theoretically the quantity of biogas potential from solid waste generated in University of Lagos, Nigeria. The recovery and use of biogas from solid waste promote energy security, enhance economic growth and improve

local air quality and public health (Global Methane Initiative, 2016). If the biogas content especially methane of solid waste is known, it will help the University authority in policy formulation to reduce greenhouse gas emissions, improve the health of the people on campus and its environ and produces renewable source of energy which justifies the work.

2.0 THEORY AND QUANTIFICATION OF BIOGAS

Table 1 shows a trend of component and composition of solid waste generation in University of Lagos, which was obtained from the work of Adeniran *et al*. (2017). Table 2 presents the typical values on moisture content and ultimate analysis of the organic portion of solid waste generated in University of Lagos, adapted from the work of Tchobanoglous *et al*., 1972 cited by Salami *et al.*,2011 and Singh and Neclancherry, 2014. Polyethylene bag and sanitary waste were excluded in Table 2 because they cannot be broken down by microorganisms and will also reduce the amount of biogas that can be produced.

Table 1. Waste component and composition of solid waste generated in University of Lagos

(Adeniran*et al*., 2017)

Component	% by mass
Organic waste	15
Paper	15
Plastic	9
Sanitary waste	7
Textile	7
Polyethylene bag	24
Metals	3
Leather	4
Glass	2
Soil and stone	8
Dirty	6

Table 2. Typical values on moisture content and ultimate analysis of organic portion of solid waste generated in the University of Lagos (Tchobanoglous*et al*., 1972 cited by Salami *et al*., 2011 and Singh and Neclancherry, 2014).

Component	Typical moisture (%)	% by mass (dry mass)				
		C	H	O	N	S
Organic waste	25	48.50	6.50	37.50	2.20	0.30
Paper	6	43.50	6.00	44.00	0.30	0.20
Plastic	2	60.00	7.20	22.80	0.00	0.00
Textile	10	55.00	6.60	31.20	4.60	2.45
Leather	10	60.00	8.00	11.60	10.00	0.40

With a basis of 100 kg of waste, Equation (1) was applied to arrive at the dry mass of the organic portion of the solid waste. The dry mass of the organic portion of the solid waste was obtained to be 44.07 kg as shown in Table 3.

$$M_d = \sum \left(\frac{100 - C_i}{100} \right) d_i \qquad (1)$$

Where M_d = dry mass solid waste; C_i = percentage of typical moisture content of each component; d_i = percentage by mass of each component.

Table 3 depicts the composition, wet and dry mass of organic portion of the waste. The mass of moisture in the organic portion of the waste sample = (52 – 44.07) kg = 7.93 kg

The mass of moisture content was converted to hydrogen and oxygen to yield:

Hydrogen = *2 x 7.93 / 18 = 0.88 kg*

Oxygen = *16 x 7.93 / 18 = 7.05 kg*

Total mass of hydrogen = *(2.93 + 0.88) kg = 3.81 kg*

Total mass of oxygen = *(7.05 + 14.82) kg = 21.87 kg*

Table 3.Composition, wet and dry mass of organic portion of the solid waste.

Component	Wet mass (kg)	Dry mass (kg)	Composition (kg)				
			C	H	O	N	S
Organic waste	25.00	11.25	5.46	0.73	4.22	0.25	0.03
Paper	6.00	14.10	6.13	0.85	6.20	0.04	0.03
Plastic	2.00	8.82	5.29	0.64	2.01	0.00	0.00
Textile	10.00	6.30	3.47	0.42	1.97	0.29	0.15
Leather	10.00	3.60	2.16	0.29	0.42	0.36	0.01
Total	52.00	44.07	22.51	2.93	14.82	0.94	0.22

To get the chemical formulas for the organic portion of the waste sample with and without sulphur, the mole ratios were normalized as shown in Table 4. Hence the chemical formulas for the organic portion of solid waste generated in University of Lagos were obtained to be $C_{187}H_{377}O_{137}N_7S$ and $C_{26.71}H_{53.88}O_{19.57}N$ respectively. With the establishment of chemical formular of the waste sample, the quantity of methane can be predicted from the equation proposed by Buswell and Neave shown in Equation (2), cited by Tchabanoglous *et al.* (1993), which shows the stoichiometric balance between the quantity of organic portion and gaseous products.

Table 4. The normalized mole ratios

Element	Mass (kg)	Molar mass (kg/mol)	Mole	Mole ratio	
				Sulphur = 1	Nitrogen = 1
C	22.51	12.01	1.87	187.00	26.71
H	3.81	1.01	3.77	377.00	53.86
O	21.87	16.00	1.37	137.00	19.57
N	0.94	14.01	0.07	7.00	1
S	0.22	32.06	0.01	1.00	-

$$C_aH_bO_cN_d+\left(a-\frac{b}{4}-\frac{c}{2}+\frac{3d}{4}\right)H_2O\rightarrow\left(\frac{4a+b-2c-3d}{8}\right)CH_4+\left(\frac{4a-b+2c+3d}{8}\right)CO_2+d\,NH_3 \quad (2)$$

Buswell and Hatfield (1936) developed an equation to predict the quantity of methane from waste as depicted in Equation (3) cited Murphy and Thamsiriroj, 2013 and Achinas and Euverink, 2017. The products in this case are a binary mixture of methane and carbondioxide.

$$C_aH_bO_c+\left(a-\frac{b}{4}-\frac{c}{2}\right)H_2O\rightarrow\left(\frac{a}{2}+\frac{b}{8}-\frac{c}{4}\right)CH_4+\left(\frac{a}{2}-\frac{b}{8}+\frac{c}{4}\right)CO_2 \quad (3)$$

The reaction of Buswell and Muller, 1952 cited by Deubiein and Steinhauser, 2008 included nitrogen and sulphur to obtain the fraction of ammonia and hydrogen sulphide in the produce biogas as presented in Equation (4).

$$C_aH_bO_cN_dS_e+\left(a-\frac{b}{4}-\frac{c}{2}+\frac{3d}{4}+\frac{e}{2}\right)H_2O\rightarrow\left(\frac{4a+b-2c-3d-2e}{8}\right)CH_4+\left(\frac{4a-b+2c+3d+2e}{8}\right)CO_2+d\,NH_3+eH_2S$$

(4)

Using the chemical formular with sulphur and applying Equation (4), it gives:

$C_{187}H_{377}O_{137}N_7S + 38\ H_2O \rightarrow 103.5\ CH_4 + 83.5\ CO_2 + 7\ NH3 + H_2S$ (5)

The theoretical amount of methane (M_{th}) of the solid waste can be predicted using Equation (6) with the following assumption (Feng *et al*., 2013):

- Constant temperature and perfect mixing;
- No accumulation of ashes;
- Ideal bacterial condition meaning full digestion;
- Input waste comprises only C, H, O, N and S;
- Products of reaction include only CH_4, CO_2, NH_3 and H_2S.

$$M_{th} = \frac{22.4\left(\frac{4a - b + 2c + 3d + 2e}{8}\right)}{12a + b + 16c + 14d + 32e} \quad (6)$$

Using Equation (6), M_{th} = 22.4 *x* 103.5 /4943 = 0.469 m^3/kg of waste

The theoretical amount of biogas (B_{th}) can be predicted using Equation (7) (Roati *et al*., 2012),

$$B_{th} = \frac{22.4\ x\,a}{12a + b + 16c + 14d + 32e} \quad (7)$$

Applying Equation (7), B_{th} = 187 *x* 22.4 / 4943 = 0.847 m^3/kg of waste

The assumptions made affect the amount of biogas produce and as a result, a limiting factor (f) was used to give a reliable value and eradicate the discrepancy between the theoretical and actual biogas quantity. With f = 80 % (Feng*et al*., 2013);

Actual amount of biogas predicted = 0.8 *x* 0.847 = 0.678 m^3/kg of waste

Actual amount of methane predicted = 0.8 *x* 0.469 = 0.375 m^3/kg of waste.

3.0 RESULTS AND DISCUSSION

The compositions of carbon, hydrogen, oxygen, nitrogen and sulphur shown in Table 3 were obtained by multiplying the dry mass of each component in Table 3 by the percentage by mass presented in Table 2. In Table 3, carbon has the highest composition of 22.51 kg while sulphur has the least composition of 0.22 kg. The dry mass and of moisture content of the organic fraction of the waste were 44.07 and 7.93 kg respectively. The normalized mole ratios were shown in Table 4 and the chemical formulas for the organic portion of the waste generated in University with and without sulphur were obtained to be $C_{187}H_{377}O_{137}N_7S$ and $C_{26.71}H_{53.88}O_{19.57}N$ respectively.

Salami et al. (2011) obtained the chemical formulas for organic portion of solid waste generated in Lagos State with and without sulpur to be $C_{597.24}H_{872.26}O_{496.02}N_{15.12}S$ and $C_{26.71}H_{53.88}O_{19.57}N$ respectively. The composition of organic waste, paper and plastic in the solid waste generated in Lagos State were 62, 10 and 15 % respectively (Salami *et al*., 2011). The composition of organic waste, paper and plastic in the waste generated in University of Lagos were 15, 15 and 9 % respectively (Adeniran*et al*., 2017). In the chemical formular with sulphur, the number of carbon, hydrogen, oxygen and nitrogen atoms in the waste generated in Lagos State were 597.24, 872.26, 496.02 and 15.12 respectively while that of the waste generated in the University of Lagos were 187, 377, 137 and 7 respectively. This is attributed to the composition of organ waste generated in Lagos State and University of Lagos which were 62 and 15 % respectively. This clearly indicates that a waste with higher composition of organic waste will have a higher carbon, hydrogen and nitrogen atoms. This was also the case in the chemical formula without sulphur for waste generated in Lagos State and University of Lagos except for nitrogen atom.

Biogas is made of carbondioxide, methane, ammonia, hydrogen sulphide, water vapour and other minor components whose volume distribution is a function of the substrate characteristics and on the process operating conditions (Roati*et al*., 2012). It is considered as a clean energy source for those who need an alternative energy (Achinas and Euverink, 2016). The theoretical biogas from the solid waste generated in the University of Lagos was 0.847 m^3/kg of waste while the actual amont of biogas was 0.678 m^3/kg of waste. Davidson *et al*. (2007) gave the yield of biogas from organic fraction of municipal solid waste in an anaerobic digester to vary between 0.4 and 0.6 m^3/kg of waste.The actual amount of biogas predicted from waste generated in University of Lagos (0.678 m^3/kg) was considered to be in li ne with the work of Davidson *et al*. (2007).

The theoretical methane predicted from the solid waste generated in University of Lagos was 0.469 m^3/kg of waste while the actual amount of methane predicted was 0.375 m^3/kg of waste which was 55.31 % of the amount biogas predicted. Global Methane Initiative (2016) gave the methane composition of biogas to range between 50 and 75 %. The 55.31 % methane composition of biogas predicted in this work was in agreement with the Global Methane Initiative (2016). Moreover, Davidson *et al*. (2007) gave the yield of methane from organic fraction of municipal solid waste to vary between 0.1 and 0.4 m^3/kg. This is an indication that the amount of methane predicted in this work was reasonable and acceptable.

This work has provided an insight on the amount of biogas recoverable in solid waste generated in University of Lagos. This biogas especially methane can be used as a clean source of energy for electricity generation and domestic use for the University sustainability. According to Adeniran *et al*. (2017), the importance of Universities in promoting sustainable development has been highlighted in a number of significant declarations including the Talloires Declaration (1990), the Halifax Declaration (1991, Swansea Declaration (1993) and Students for a Sustainable Future (1995). It is imperative for the authority of University of Lagos to tap the biogas recoverable from solid waste generated in the University as this promote energy security and improve local air quality.

4.0 CONCLUSION

The quantification of biogas from solid waste generated in the University of Lagos has been predicted. The chemical formulas for the organic portion of solid waste generated in the University with and without sulphur were $C_{187}H_{377}O_{137}N_7S$ and $C_{26.71}H_{53.88}O_{19.57}N$ respectively. The theoretical and actual amounts of biogas predicted from the solid waste generated in the University were 0.847 and 0.678 m^3/kg of waste respectively. Moreover, the theoretical and actual amounts of methane predicted from the solid waste generated in the University were 0.469 and 0.375 m^3/kg of waste respectively. The actual amount of methane accounted for 55.31 % of the actual amount of biogas. This work has provided a platform for the University authority to look inward and tap the biogas recoverable from the solid waste generated in the University to promote energy security and sustainability as well as improving local air quality.

ACKNOWLEDGEMENT

The authors appreciate the efforts of the anonymous reviewers whose comments enhanced the manuscript.

REFERENCES

Achinas, S. and Euverink, G.J.W. (2016). Theoretical analysis of biogas potential prediction from agricultural waste. Resource – Efficient Technology, 2: 143 – 147.

Adeniran, A.E., Nubi, A.T. and Adelopo, A.O (2017).Solid waste generation and characterization in the University of Lagos for a sustainable waste management. Waste Management, 67: 3 – 10.

Adeyinka, S.Y., Wasiu, J., Oluwashola, O. and Adebayo, A. (2014).Pyhsico-chemical composition and energy content analysis of solid waste: A case of Castlereagh district, Northern Ireland. American Journal of Engineering Science and Technology Research, 2(1): 1 – 9.

Amori, A.a, Fatile, B.O., Ihuoma, S.O. and Omoregbe, H.O. (2013). Waste generation and management practices in residential areas of Nigerian tertiary institutions. Journal of Education and Social Research, 3(4): 45 – 51.

Arazon, R.O. (2015). Composition of solid wastes generated from a school campus. Internation Journal of Research in Engineering and Technology, 4(10): 263 – 267.

Buswell, A.M. and Muller, H.F. (1952).Mechanism of methane fermentation. Industrial Engineering Chemistry, 44: 550 – 552.

Buswell, A.M. and Hatfield, W.D. (1936).Anaerobic fermentations, State of Illinois Department of Rigistration and Education, Division of the State Water Survey, Urbana, Illinois.

Buswell, A.M. and Neave, S.l.(1930). Laboratory studies of slude digestion. Department of Registration and Education.

Coker, A.O., Achi, C.G., Sridhar, M.K.C. and Donnett, C.J. (2016). Solid waste management practices at a private institution of higher learning in Nigeria. Procedia Environmental Sciences, 35: 28 – 39.

Davidson, A., Gruvberger, C., Christensen, T.H., Hansen, T.L. and Jansen, J.L.C. (2007).Methane yield in source – sorted organic fraction of municipal solid waste. Waste Management, 27: 406 – 414.

Deublein, D. and Steinhauser, A. (2008). Energy supply in the future scenarios, chapter 2, in: Biogas from waste and Renewable Resources, Wiley – VCH Verlag GmbH and Co. KGaA, Weinbeim: 7 – 26.

Feng, L., Li, Y., Chen, C., Liu, X., Xiao, X. and Ma, X. (2013).Boigas from vinegar residue. Bioresources, 8(2):2487 – 2498.

Global Methane Initiative (2016).Overview of anaerobic digestion for municipal solid waste.

Murphy, J.D. and Thamsiririroj, T. (2013). Fundamental Science and Engineering of the Anaerobic Digestion process for Biogas Production, in Wellinger, A., Murphy, J.P. and Baxtex, D. (Eds.), The biogas handbook, WoodheadPublishinh Series in Energy: 104 – 130.

Nathaniel, U.E., Romanus, U.E. and Glasys, A.C. (2012).Minimizing the negative externality from sachet water consumption in Nigeria. European Journal of Business Management, 4: 118 – 125.

Nwachukwu, M.U. (2010). Solid waste generation and disposal in Nigeria city: An empirical analysis in Onitsha metropolis. Journal of Enviromental Management, 1: 180 191.

Okeniyi, J.O. and Awan, E.U. (2012). Solid waste generation in Covenant University, Ota, Nigeria: Characvterisation and implication for sustainable waste

management. Journal of Material and Environmental Science, 3(2): 419 – 424.

Olafadehan, O.A. and Salami, L. (2011). Proactive solid waste management and control: A way of environmental sustainability in Nigeria. Nigerian Journal of Engineering Management, 12(1): 26 – 32.

Olukanni, D.O. and Ugwu, N.C. (2013). Analysis of municipal solid waste management in Ota, Nigeria: Potential for wealth generation. International Journal of Water Resources, 5: 262 – 271.

Peretomode, O.V., Eyenubo, O.B. and Bulouebibo, L. (2019).Evaluation of solid wastes generation in Abraka, Delta State, Nigeria. Nigerian Research Journal of Engineering and Environmental Sciences, 4(1): 174 – 183.

Roati, C., Fiore, S. and Ruffino, B. (2012).Premilinary evaluation of the potential biogas production of food processing industrial waste. American Journal of Environmental Science, 8(3): 291 – 296.

Robert, A.C. (1999). Standard handbook of Environmental Engineering, McGraw – Hill Company, U.S.A.

Salami, L., Odunlami, M.O. and Keleola, O. (2018).Exergy content analysis of solid waste generation in University of Lagos, Nigeria. Nigerian Research Journal of Engineering and Environment Sciences, 3(1): 273 – 279.

Salami, L., Susu, A.A., Patinvoh, R.J. and Olafadehan, O.A. (2011). Charaterisation study of solid wastes: A case of Lagos State. International Journal of Applied Science and Technology, 1(3): 47 – 52.

Singh, A. and Neelancharry, R. (2014). Solid waste management: Acase study of ultimate analysis and landfill design for NIT Calicut. International Journal of Scientific and Engineering Research, 5(7): 174 – 180.

Tchabanoglous, G., Theissen, H, and Vigil, S.A. (1993).Integrated Solid Waste Management: Engineering Principles and Management Issues, McGraw – Hill, New York.

Tchobanoglous, G., Theisen, H. and Eliassen, R. (1972). Solid Wastes: Engineering Principle and Management Issues, McGraw – Hill, New York.

Uwadiegwu, B.O. and Chukwu, K.E. (2013).Strategies for effective urban solid waste management in Nigeria. European Science Journal, 98: 296 – 308.

KINETIC COEFFICIENTS OF SUBSTRATE UTILIZATION AND BIOMASS GROWTH IN THE BIO-DEGRADATION OF PETROLEUM REFINERY WASTEWATER IN AN ACTIVATED SLUDGE PROCESS

***Momoh, O. J.[1], Okonkwo, P.C[1] and Edomwonyi-Otu, L.C [2]**

[1]Department of Chemical Engineering, Ahmadu Bello University, Zaria

[2]Department of Chemical and Petroleum Engineering, Delta State University, Abraka

[*]Corresponding author: ojamesmomoh@gmail.com

ABSTRACT

A study of the kinetics of petroleum refinery wastewater biodegradation in an activated sludge process was carried out in a 25 L bio-reactor, for a time range of 2-10 hours hydraulic retention. Substrate utilization and microbial growth rate were monitored at various hydraulic retention time which shows corresponding increase in microbial growth and coliform count with substrate utilization. Analysis of the results obtained using the Monod and the modified Monod kinetic model gave the following bio-kinetic parameters: Maximum Substrate Utilization Rate= 4.4 day^{-1}, Half Saturation Constant=275 mg/L, Yield Coefficient=0.5083 mgVSS/mgBOD and Endogenous Decay Constant=0.003 day^{-1}.

1. INTRODUCTION

The ever-increasing world population and industrial development have led to the introduction of different types of chemical substances to the environment, leading to considerable deterioration in environmental quality (Taghreed and Muftah, 2018). Petroleum refinery generates enormous wastewater that requires effective treatment before discharge into the environment. A typical petroleum refinery generates wastewater 0.4-1.6 times the volume of crude oil processed (Coelho *et al.*, 2006) which is potentially harmful to man and the environment if not well treated before discharge. According to Qin *et al.* (2007) biological treatment of petroleum refinery wastewater by an activated sludge process is viable, as it is generally the most economical method for reducing both wastewater toxicity and dissolved organic constituents, although the process is faced with challenges in terms of performance. Earlier, activated sludge process designs were not based on kinetic data but recently, a more rational solution for the design of activated sludge process has been under studies. Process modeling of the activated sludge process as it is currently conceived requires experimental assessment of kinetic and stoichiometry coefficients, these coefficients vary for different wastewater (Tchobanoglous *et al*., 2003).

Previously Ambreen *et al*. (2013) used a laboratory-scale reactor to obtain the following kinetic coefficients for diary wastewater: maximum specific growth rate (μ_{max}) =4.46 day^{-1}, saturation constant (Ks) =534 mg/l, yield coefficient (Y) =0.714 mgVSS/mgCOD and decay coefficient (Kd) =0.038. Similarly Haydar and Aziz (2009) used a laboratory scale completely mixed continuous flow reactor to generate the following kinetic data for tannery wastewater: maximum substrate utilization rate, half velocity constant, cell yield coefficient and decay coefficient of 3.125 day-^{1}, 488 mg/L, 0.64 and 0.035 day^{-1}, respectively.

For petroleum refinery wastewater, Carlos *et al.* (2013) reported rate constant (*k*) values of 0.055 and 0.059 L mg^{-1} VSS day^{-1}, with and without biomass recirculation, respectively for the removal of organic matter in petroleum refinery wastewater treatment in activated sludge process (ASP). Fazel (2016) treated a simulated petroleum refinery wastewater in an aerobic film bioreactor integrated with a UV reactor and obtained saturation constant (K_B) and maximum utilization rate (U_{max}) of 110.67 g/Lday and 90.90 g/Lday respectively.

In the present work actual petroleum refinery wastewater was treated in ASP to obtain maximum substrate utilization rate, half saturation constant, yield coefficient and Endogenous decay constant. The determinations of these kinetic parameters are helpful in understanding the kinetics of substrate utilization, sludge production and design of activated sludge process for wastewater treatment (Haydar and Aziz, 2009).

Mechanism and Kinetics of Activated Sludge Process

The mechanism of the activated sludge process is such that microorganism takes in oxygen and feed on the organic materials in the wastewater which enables reproduction of more microorganisms. According to Tchobanoglous *et al.* (2003), reaction (1), (2) and (3) represent the biochemical reaction in the activated sludge

process which involves bacterial cell respiration and synthesis using organic pollutants as substrate. Reaction (3), the endogenous respiration stage is the last phase in the process; it takes place when new cells begin to consume their own cell tissue to obtain energy for their cells maintenance and simultaneously release carbon dioxide and water.

Oxidation (Catabolism)

$$Organics + O_2 \xrightarrow{Micro-organism} CO_2 + H_2O\ Energy \quad (1)$$

S**ynthesi**s (Anabolism)

$$Organics + O_2 + Nutrients \xrightarrow{Micro-organism} New\ Cells + H_2O + CO_2 \quad (2)$$

Endogenous Respiration (Endogenous metabolism)

$$Cell\ matter + O_2 \xrightarrow{Micro-organism} CO_2 + H_2O + Nutrient + Energy \quad (3)$$

Generally substrate utilization and cell growth rate in an activated sludge process can be related as described by Sperling (2007) in Equations 4 to 16.

$$r_{su} = \frac{kSX}{K_s+S} \quad (4)$$

Where r_{su}= rate of substrate concentration change due to utilization, S=substrate concentration, k=maximum specific substrate utilization rate, X=biomass (microorganism) concentration, K_s = half saturation coefficient.

The bacteria growth rate is dependent on the rate at which the substrate is utilized; making the bacterial growth rate maximum at maximum substrate utilization rate as shown in Equation 5.

$$u_{max} = kY \quad (5)$$

Where, μ_{max} = maximum specific growth rate, Y is the yield coefficient. Therefore,

$$k = \frac{u_{max}}{Y} \quad (6)$$

The rate of substrate utilization can be further expressed as:

$$r_{su} = \frac{\mu_{max}SX}{Y(K_s+S)} \quad (7)$$

The specific growth rate is related to substrate utilization rate as follows:

$$\mu = Y\frac{r_{su}}{X} \quad (8)$$

Therefore, $\mu = \mu_{max}\frac{S}{K_s+S}$ (9)

Equation (9) is the Monod kinetic model which relates the microbial growth with the substrate concentration. Considering microbial death rate, r_d.

$$r_d = -(k_d)(X) \quad (10)$$

Where k_d =endogenous decay coefficient, the endogenous decay coefficient accounts for the loss in cell mass. Growth rate of biomass is proportional to the substrate utilization rate by the synthesis yield coefficient, and biomass decay is proportional biomass present (Sperling, 2007).

Net rate of growth can be obtained as follows:

$$r_g = -(Y)(r_{su}) - (k_d)(X) \quad (11)$$

Therefore equation (9) becomes:

$$r_g = \frac{(\mu_{max})(S)(X)}{K_s+S} - (K_d)(X) \quad (12)$$

Or as $r_g = Y\frac{kSX}{K_s+S} - K_dX$ (13)

Specific biomass growth rate, $\mu = \frac{r_g}{X}$ (14)

The corresponding expression for the net specific growth rate is written as:

$$\mu = \mu_{max}(\frac{S}{K_s+S}) - (K_d) \quad (15)$$

Or in terms of Y as

$$\mu = Y\frac{kS}{K_s+S} - K_d \quad (16)$$

Equation (4), (9), (10) and (15) are useful equations to obtain the following kinetic coefficients data: k, K_s, K_d and Y, which can be used in the prediction of the rate of substrate utilizations and biomass growth rate in an activated sludge process (Haydar and Aziz, 2009). Understanding of the dynamic nature of substrate utilization and microbial growth rate in ASP is essential, as it can be used as diagnostics tool to improve process performance.

2. METHODOLOGY

Petroleum refinery wastewater sample was collected from the wastewater treatment plant of Kaduna Refining and Petrochemical Company (KRPC) Kaduna. The study was carried out in a 25 L activated sludge process reactor shown in Figure 1. The reactor was seeded with 2 L sludge obtained from the bio-filter unit of KRPC wastewater treatment plant. An air compressor was used to supply air at a rate of 10 L/min into the reactor for aeration and to maintain intimate contact between the influent wastewater and the microbes.

The process was operated at a hydraulic retention time (HRT) of 2,4,6,8 and 10 hrs, at the end of each HRT, effluent was taken for BOD, biomass growth and coliform count analysis using the America Public Health Association (APHA) Standard Method for the Examination of Water (APHA, 2017).

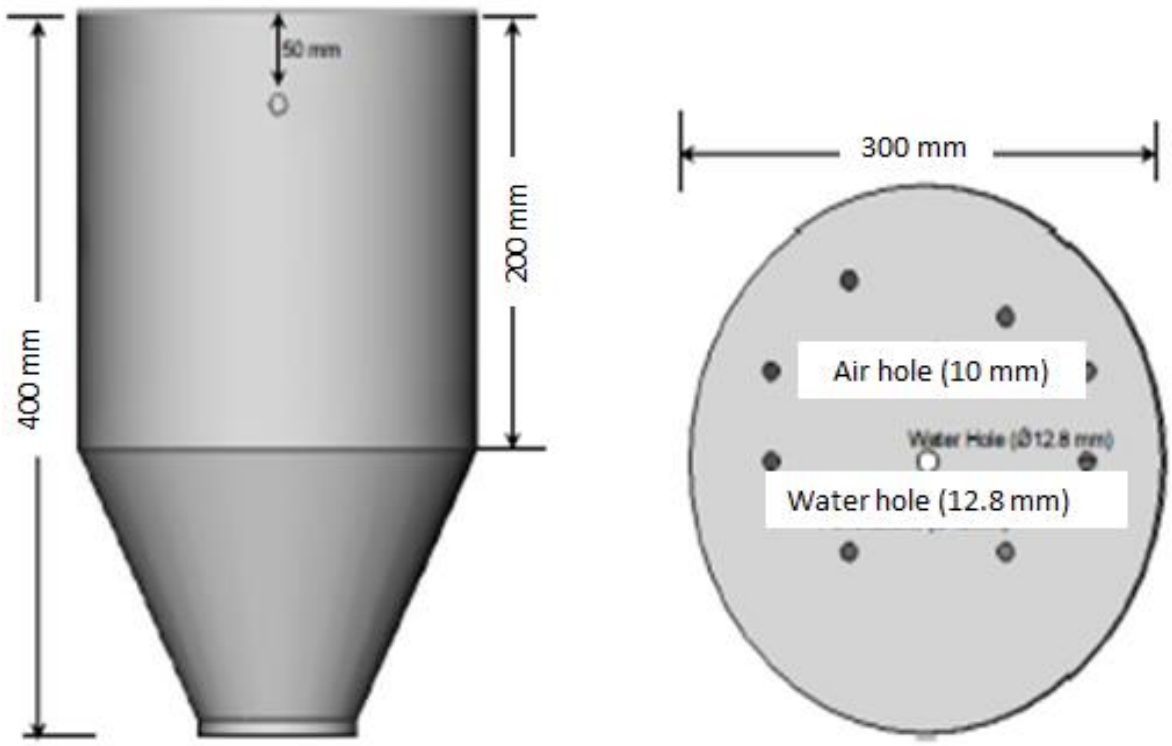

Figure 1: Activated Sludge Bio-reactor

Equation (4) and (16) were linearized to obtain Equation (17) and (18) as shown in Table 1, which were plotted to arrive at the kinetic coefficients (Haydar and Aziz (2009) and Ambreen *et al.* (2013)).

$$\frac{X\theta}{So-S} = \frac{Ks}{k}\frac{1}{S} + \frac{1}{k} \quad (17)$$

$$\frac{1}{\theta} = \frac{So-S}{X\theta}Y - K_d \quad (18)$$

Table 1: Monod and modified Monod Kinetics

S/N	Rate Expression	Kinetics	Integrated Form	Plot
1	$\frac{ds}{dt} = \frac{KsX}{(Ks+S)}$	Monod Kinetics	$\frac{X\theta}{So-S} = \frac{Ks}{K}\frac{1}{S} + \frac{1}{K}$	Plot of $\frac{X\theta}{So-S}$ versus $\frac{1}{S}$
2	$\frac{dX}{dt} = Y\frac{dS}{dt} - K_dX$	Modified Monod	$\frac{1}{\theta} = \frac{So-S}{X\theta}Y - kd$	Plot of $\frac{1}{\theta}$ versus $\frac{So-S}{X\theta}$

Where X is mass of microorganisms, S is mass of organic matter used as food by the microorganisms (BOD), and Y is the cell yield coefficient, which is the ratio of the mass of cells formed to the mass of substrate consumed. K_d represents the proportion of the total mass of microorganisms that self-degrades (endogenous respiration) per unit time, K is the maximum rate of substrate utilization per unit mass of microorganisms, and K_s is the half saturation constant, which is the substrate concentration at one half of the maximum growth rate, mass per unit volume.

3. RESULTS AND DISCUSSION

3.1 Cell growth and substrate utilizations

Figure 2 shows that cell growth rate is proportional to the cell concentration X with gradual utilization of the substrate. Bacteria growth count also shows in Figure 2 that there is a steady increase in bacteria growth from 1.1×10^5 to 6.4×10^5 cfu after 10 hours of aeration.

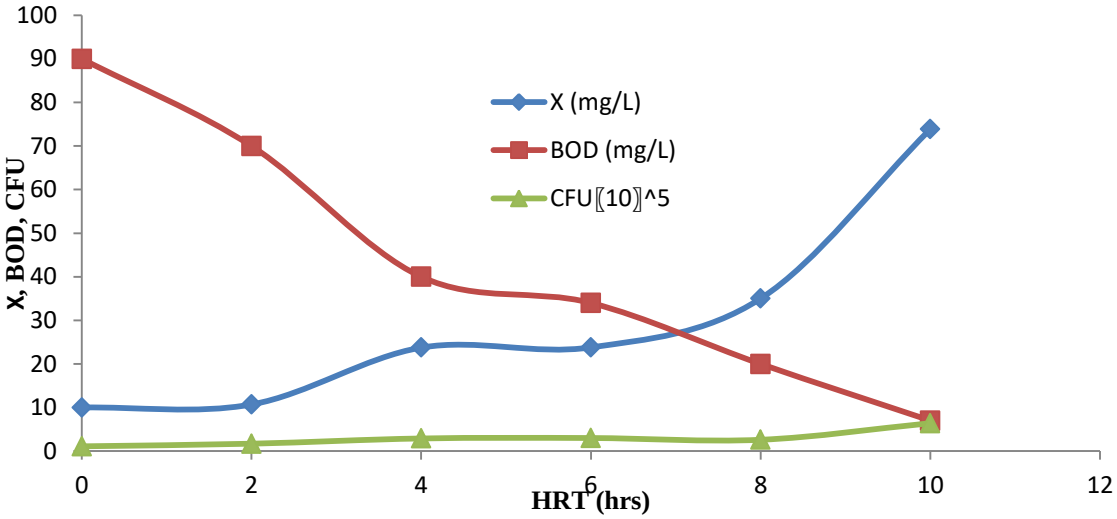

Figure 2: Cell Growth and Substrate Utilization

Figure 3 is the Food-to-Microorganism Ratio (F/M) obtained at various HRT; this indicates how much food is available at a particular time for microorganism to consume. An appropriate F/M ratio is necessary to obtain proper performance from the activated sludge process.

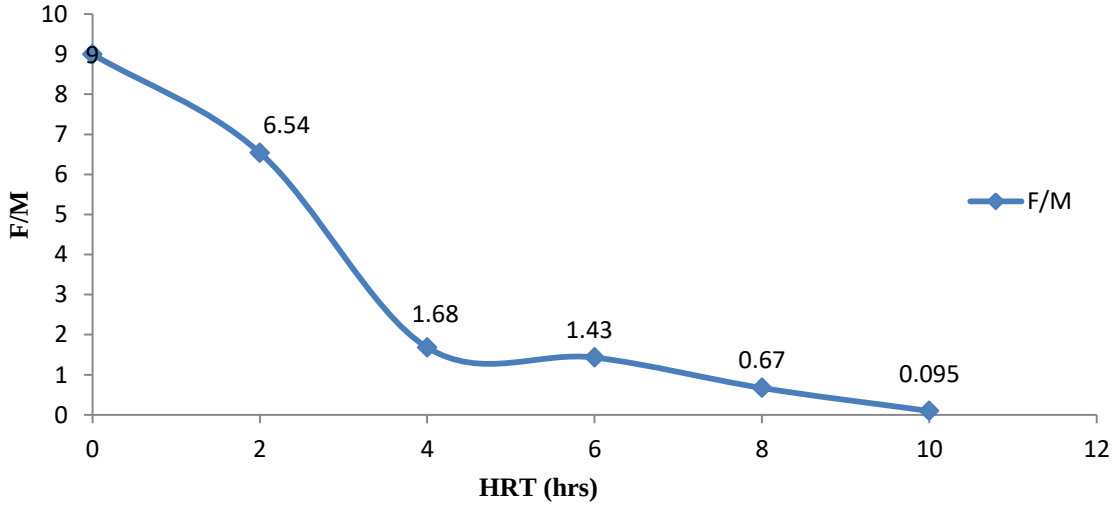

Figure 3: Food-to-Micro-organism ratio

The highest value of 9.0 was obtained at the start of the process when the food (BOD) was very high but it gradually reduces as treatment progresses and more food has been used up for metabolism by the microorganism.

3.2 Determination of bio-kinetic coefficients

Figure 4 and 5 is the plots of the linearized Monod and modified Monod equations in Table 1 which were used to determine the bio-kinetic coefficients for petroleum refinery wastewater bio-degradation in the activated sludge process. Using the Line-Weaver approach, a linear regression line is fitted to the plotted data. The intercept on the y-axis and the slope of this line is used to find K andK_s. From the linearized Equation 17 and Figure 4, K = 4.4 day^{-1}, Ks =275 mg/L.

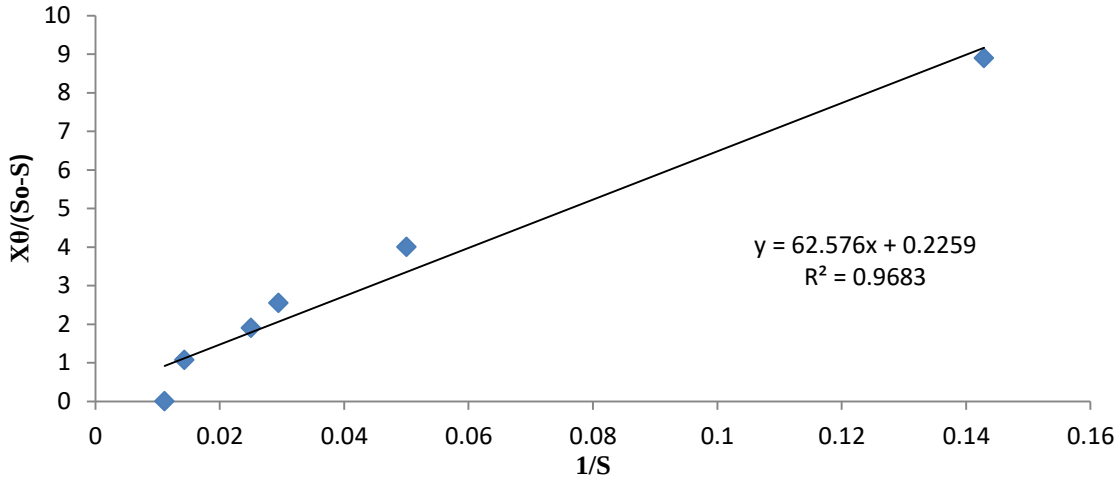

Figure 4: Determination of K and K_s

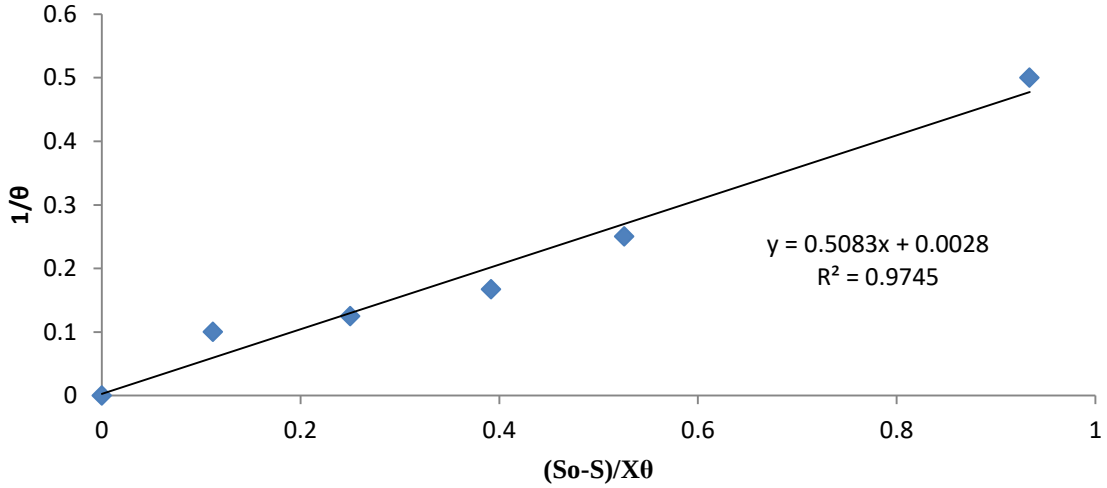

Figure 5: Determination of K_d and Y

Figure 5 is the plot of the linearized form of the modified Monod equation which was used to obtain K_d and Y. A plot of 1/θ against (So-S)/Xθ, gives an intercept which represents K_d, while the slope represents Y. Therefore, an Endogenous Decay Constant (K_d) and Yield Coefficient (Y) of 0.0028 and 0.5083 respectively were obtained for this study as seen in Figure 5.Kinetic parameters vary for different industrial wastewater based on the nature of raw materials processed and the nature of wastewater effluent. Table 2 shows a fit of the obtained kinetic coefficients in Equation (4), (5), (9), (10) and (15) for substrate utilization rate, maximum bacterial growth rate, bacterial growth rate, microbial death rate and net biomass production rate respectively.

Table 2: Parameters for Substrate Utilizations and Biomass Growth Prediction

	Parameter	Equation	Predictive Equation
1	Substrate utilization rate	$r_{su} = \frac{kSX}{K_s + S}$	$r_{su} = \frac{4.4SX}{275 + S}$
2	Maximum bacterial growth rate	μ_{max}=kY	u_{max}=4.4×0.5083= 2.236

	Parameter	Equation	Predictive Equation
3	Bacterial growth rate	$\mu = \mu_{max}\frac{S}{K_s + S}$	$\mu = 2.236\frac{S}{275 + S}$
4	Microbial death rate	$r_d = -(k_d)(X)$	$r_d = -(0.003)(X)$
5	Net biomass production rate	$r_g = Y\frac{kSX}{K_s+S} - K_dX$	$r_g = 0.5083\frac{4.4SX}{275 + S} - 0.003X$

Table 3 presents summary of the kinetic parameters for petroleum wastewater bio-degradation in an activated sludge process obtained in this work in comparison with previous works.

Table 3: Obtained Kinetic Coefficients and Previous Works

S/N	Author	Wastewater	K (day^{-1})	K_s (mg/l)	Y mgVSS/mgCOD	K_d (day^{-1})
1	**This work**	**Petroleum**	**4.4**	**275**	**0.5083** mgVSS/mgBOD	**0.003**
2	Ambreen, *et al*.(2013)	Dairy	4.46	534	0.714	0.038
3	Zhong, *et al.* (2003)	Petrochemicals	0.185 h^{-1}	154	-	-
4	Andress, *et al*., (2011)	Petroleum	0.274	165.8	0.424	0.01
5	Mardani, *et al*. (2011)	Municipal	0.95-0.98	52-71	0.48-0.8	0.0189-0.026
6	Haydar and Aziz (2009)	Tannery	3.125	488	0.64 mgVSS/mgBOD	0.035
7	Prakash and Sockan (2014)	Tannery	1.66	1132	0.22	0.05

3.3 Kinetic parameters obtained and their significance

3.3.1 Maximum Rate of Substrate Utilization (K)

K represents the maximum rate of substrate utilization per unit mass of microorganisms. K was obtained as 4.4 day^{-1} in the present study. Maximum substrate utilization rate has significance in the design of the volume of reactor for biological system, the greater the value of K, the smaller will be the size of the reactor (Benefield and Randall, 1980).

The value obtained in this study falls within the general range of 2-10 day^{-1} for wastewater treatment reported by Tchobanoglous, *et al.* (2003). A value as low as 0.216 day^{-1} was reported for fertilizer industry wastewater by Gupta and Sharma (1996), while Haydar and Aziz (2009) obtained 3.125 day^{-1} for tannery wastewater. Ambreen, *et al*. (2013) reported 4.46 day^{-1} for diary wastewater, which is close to that obtained in this work.

These variations may be attributed to the characteristics nature of the various wastewaters studied. Industrial wastewater varies in nature depending on an industry manufacturing processes (Sharma, 2011). In addition, bio-kinetics depends on the actual environment and the biological metabolic activities in a system (Prakash and Sockan, 2014). Petroleum refinery wastewater often contains oil, ammonia, sulfides, chlorides, mercaptans, phenols and other hydrocarbons (Jou and Huang, 2003).

3.3.2 Half Saturation Constant (K_s)

The substrate concentration at which specific substrate utilization rate is half of maximum substrate utilization rate is called half saturation constant, it is analogues to the half velocity constant (V_{max}) in the Michealis-Menten model. K_s was obtained as 275 mg/L in the present study which is large compare to 165.8 mg/L obtained by Andress, *et al*., (2011) for an onsite study of petroleum refinery wastewater treatment plant located in the Midwestern United State, to establish site-specific bio-kinetic constants for the existing wastewater treatment facility. Zhong, et al. (2003) reported 154 mg/L for petrochemicals wastewater.

As reported by Ambreen *et al.*, (2013) large value of K_s shows that the maximum specific yield of bacteria occurs at high substrate concentration. Therefore, the relatively high value obtained in the present study is an indication

that the process bacteria yield occurred at higher substrate concentration. K_s has no direct application in the process design, its significance is of theoretical nature and gives an idea about change in specific growth rate of bacteria with more a change in the concentration of growth limiting substrate (Benefield and Randall, 1980).

3.3.3 Biomass Yield (Y)

Yield Coefficient or Biomass Yield is the mass of cells produced per unit of substrate utilized which may be measured as mgVSS/mgCOD, it may also be described as how biomass is produced against substrate utilized. A value of 0.5083 mgVSS/mgBOD was obtained in this study, which is within the typical range of 0.4-0.8 reported by Sperling (2007). Previously, Andress, *et al*., (2011) obtained 0.424 mgVSS/mg COD for an onsite study for an existing petroleum refinery wastewater treatment plant. Yield coefficient of 0.714 mgVSS/mgBOD was reported by Ambreen *et al.* (2013). Haydar and Aziz (2009) reported 0.64 for tannery wastewater treatment in activated sludge process.

These differences may be attributed to the variations in the wastewater compositions. According to Tchobanoglous, *et al* (2003) bio kinetic coefficients depend on the kind of wastewater and its contents. The significance of Y in process design is that it gives an estimate of the sludge produced as a result of wastewater treatment. The greater the value of Y, the greater will be the amount of sludge, and the size of sludge handling facility. Preliminary cost estimates for sludge handling can be found out once the size is known (Ambreen, *et al.*, 2013).

3.3.4 Endogenous Decay Coefficient (K_d)

Endogenous decay coefficient represents the fraction of the cells oxidized by endogenous respiration per unit of time. An endogenous decay coefficient of 0.003 d^{-1} was obtained in this study. The range of K_d generally for wastewater treatment is 0.06-0.100 d^{-1} (Sperling, 2007). Andress, *et al*., (2011) obtained 0.01 d^{-1} in another study of petroleum refinery wastewater. Haydar and Aziz (2009) reported 0.035 d^{-1} for tannery wastewater while Ambreen *et al* (2013) also reported another close value of 0.038 d^{-1} for diary industry wastewater.

The very low value of K_d obtained in this study is an indication of low bacterial decay rate, on the other hand the yield coefficient, Y was observed to be relatively high above the general minimum of 0.3 reported by Tchobanoglous, *et al*. (2003).The higher value of yield coefficient (Y) and lower value of organism decay (K_d) obtained shows that there is extremely higher production of excess sludge in the process. This implies that optimum sludge removal at frequent intervals has to be designed and sludge disposal mechanism has to be developed (Ashwin and Ramakrishaniah, 2014). K_d has reasonable significance in the design of activated sludge process as it is used in the evaluation of net sludge production in activated sludge process. According to Benefield and Randall (1980), it can be used to fine-tune the size of sludge handling facilities resulting in some economic benefits in the cost reduction.

4. CONCLUSION

Petroleum refinery wastewater biodegradation in an activated sludge process gave the following kinetic coefficients: Maximum Substrate Utilization Rate=4.4 day^{-1}, Half Saturation Constant=275 mg/L, Yield Coefficient=0.5083 mgVSS/mgBOD and Endogenous Decay Constant=0.003 day^{-1}. These kinetic coefficients are useful as predictive and diagnostic tool for further design and control of activated sludge process for optimal process performance.

REFERENCES

Ambreen, L., Muhammad , N.C and , Shazia, I. (2013). Biological treatment of dairy wastewater using activated Sludge. *Science Asia, 29*, 179-185.

Andres, H., Kujawski, D., Schraa, O., Lin, Che-Jen., Wong, A. (2011). Process Optimization of Petroleum Refinery Wastewater Treatment Facility Using Process Modeling and Site Specific Biokinetic Constants. *Proceedings of the Water Environment Federation*. 2011. 1712-1726.

APHA (2017) *Standard Methods for the Examination of Water and Wastewater*. 21st Edition, American Public Health Association/American Water Works Association/Water Environment Federation, Washington DC.

Ashwin, H. V., Ramakrishaniah, C. R. (2014). Determination of bio-kinetic parameters for sequencing batch reactor type sewage treatment plant. *International Journal of Civil Engineering Research and Developmen*t. 4. 51-58.

Benefield, L.D, Randall, C.W (1980). *Biological Process Design for Wastewater Treatment*, Prentice Hall, Inc., Englewood Cliffs.

Carlos, E. Santo, Vítor J.P. Vilar, Amit Bhatnagar, Eva Kumar, Cidália M.S. Botelho & Rui A.R. Boaventura (2013) .Biological treatment by activated sludge of petroleum refinery wastewaters, *Desalination and Water Treatment*, 51:34-36, 6641-6654.

Coelho, A., Castro, A.V., Dezotti, M., & Sant'Anna Jr., G.L. (2006). Treatment of Petroleum Refinery Sourwater by Advanced Oxidation Processes. *J. Hazard. Mater*. 137, 178–184.

Fazel, D. (2016). Kinetics Study of Organic Removal in a Biological Treatment of Refinery Wastewater by Activated Sludge, *6th Conference 0n Energy Management and the Environment*, Iranian Scientific Society of Thermal Engineering, Energy Seminar Kimia, 2016,Volume 6.

Gupta, S.K., Sharma, R. (1996). Biological oxidation of high strength nitrogenous wastewater. *Water Resources*, 30, 593–600.

Haydar, S., and Aziz, J.A. (2009). Kinetic Coefficients for the Biological Treatment of Tannery Wastewater using Activated Sludge Process. *Pak. J. Engg & Appl. Sci., 5*, 39-43.

Jou, C.G. and Huang, G., (2002). A Pilot Study for Oil Refinery Wastewater Treatment Using a Fixed Film Bioreactor. *Advance Environmental Resource*, 7, 463–469.

Mardani, Sh., Mirbagheri, A., Amin, M.M and Ghasemian, M. (2011). Determination of Biokinetic Coefficients for Activated Sludge Processes on Municipal Wastewater ., 2011, Vol. 8, No. 1, pp. 25-34. *Iran. J. Environ. Health. Sci. Eng, Vol. 8,* (No. 1), 25-34.

Prakash, N. B. and Sockan, V. (2014). BioDecomposition and Bio-Kinetic Characterization of Tannery Effluent Treatment", *American International Journal of Contemporary Research*, 2014, 4(9), 85-93.

Qin, J.-J., Oo, M.H., Tao, G., Kekre, K.A. (2007). Feasibility study on petrochemical wastewater treatment and reuse using submerged MBR. *Journal of Membrane Science* 293, 161-166.

Sharma, B.K (2011). *Industrial Chemistry* (16th Ed). Krishna, Meerut, India.

Sperling, M. V. (2007). *Activated Sludge and Aerobic Biofilm Reactor* (Vol. 5). London, U.K: IWA Publishing, Alliance House.

Taghreed A and Muftah, H. E (2018). Organic Contaminants in Refinery Wastewater: Characterization and Novel Approaches for Bio-treatment. *Recent Insights in Petroleum Science and Engineering.*

Tchobanoglous, G., Burton, F. L., Stensel, H. D., & Metcalf & Eddy. (2003). *Wastewater engineering: Treatment and reuse*. Boston: McGraw-Hill

Zhong J, Sun X, Wang C. (2003).Treatment of oily wastewater produced from refinery processes using flocculation and ceramic membrane filtration, *Separation Purification Technology* 2003; (3)2:93-8.

ASSESSMENT OF SOYA BEAN HUSK FOR CRUDE OIL SPILL CLEANUP

***Olawale, A. S., Olakunle, M. S. and Ajayi, O. A.**
Chemical Engineering Department, Ahmadu Bello University
Zaria. Nigeria
*Corresponding author: +2348036862485; asolawale@abu.edu.ng

ABSTRACT

Soya bean husk, a readily available, cheap and biodegradable lignocellulosic wastes was used in this study as a sorbent material for the removal of Escravos crude oil from seawater in order to assess its oleophilicity and hydrophobicity. The oil and water sorption performance of the sorbent was investigated using five different particle size ranges (4000-1000, 1000-500, 500-105, 105-53 and <53 µm) of soya bean husk on different thickness of oil layer (3, 4.5 and 6 mm) over the seawater. The morphology, functional groups, density and buoyancy of the husk were determined as a prelude to assessing the oil and water sorption of the biomass. The highest oil sorption capacity rate was recorded by 105 – 53 µm particle size range (particle D) on 3 mm oil. The maximum oil sorption capacity obtained over 4.5 and 6 mm oil layer thicknesses were 7.4383 g oil/g sorbent with particle D (105 – 53 µm) at forty minutes and 4.8189 g oil/g sorbent with particle B (1000 – 500 µm) also at forty minutes, respectively. Particles in the five size ranges recorded highest sorption rates within the first ten minutes on the three oil layer thicknesses investigated in this work. The oil sorption capacity of the sorbent is moderate; it was higher than 7 g/g. The oil sorption kinetic model fitted fairly well to the inverse exponential function, which is indicative of diffusion mechanism for the oil sorption process.

Keywords: *Particle sizes, oil sorption, Escravos oil, lignocellullosics, biodegradable*

1 INTRODUCTION

Oil spill on water bodies usually cause a great deal of damage to the marine lives and environment and, humans. The spill could be caused by accident on the oil production rigs, leakages and failures in pipelines and crude transporting barges and ships as well as sabotage to flow lines (Egwaikhide *et al*., 2007, Agida *et al*., 2017). This environmental and ecological nuisance occurs in the course of exploration, production, transportation and processing of crude oil. Crude oil pollution effect is felt all over the world because of the key role oil play in global economy as the principal energy source. Whenever oil spill and pollution occurs in the marine and adjoining habitats, it is usually difficult to carry out recovery and remediation steps and, the damaging effects on the ecosystem could take long to recede (Rene *et al.*, 1993; Ifelebuegu and Johnson, 2017; Agida *et al.*, 2017)

Oil recovery is sometimes carried out by sorption of the spilled crude on water; this method is especially preferable on cost consideration or when the oil spill occurs on water body that is not easily accessible to booms and skimmers (Ifelebuegu and Johnson, 2017; Olawale *et al*., 2019). Other methods used for remediation include burning, dispersal, emulsification, bioremediation may present safety and environmental challenges (Olawale *et al.*, 2019, Agida *et al.*, 2017). Sorption methods utilizes sorbents as the mass agent for recovery of the spilled hydrocarbon and remediation of the impacted sites.

The three classes of sorbents used in spilled oil sorption are synthetic, natural inorganic and natural organic materials (Deschamps *et al*., 2003). Many works have been reported on these three classes of sorbents in oil spill removal from water bodies (Choi and Moreau 1993; Reynolds *et al.,* 2001; Toyoda and Inagaki 2003; Choi and Cloud, 1992; Deschamps *et al.,* 2003, Zeigler *et al*., 2016, Agida *et al*., 2017; Pinto *et al*., 2016).

The natural organic materials which are mostly agricultural products and residues have the advantages of availability, cheapness and biodegradability over synthetic and inorganic natural materials. For these reasons, there have been interests in utilization of natural organic materials, which are majorly lignocellulosic agricultural waste, as oil spill cleanup sorbents. Some of the sorbents studied included rice straw and cotton (Teas *et al*., 2001), cotton (Choi *et al.*, 1993; Choi,1996), kapok (Huang and Lim, 2005; Hori *et al*., 2000), pith bagasse (Amer *et al*., 2007), groundnut husk (Olawale

and Saidu, 2010), barley straw (Hussein *et al*., 2009), rice hull/straw (Bayat *et al*., 2004; Sun *et al.*, 2002), kapok and aquatic plants like *Pistia stratiotes* and *Salvinia molesta* (Zeigler *et al.*, 2015, 2016), wool (Radetic *et al*., 2003) and corn husk (Olawale, *et al.*, 2020) among others

Many plant wastes are available abundantly in the tropics, Nigeria inclusive (Odedokun, 2014 and Sanni *et al*., 2017). Soya bean husk is a byproduct of the high valued commodity crop which is available in abundance in the tropics. There is the need to carry out investigations into oil and water sorption characteristics of more lignocellulosic materials such as soya bean husk which is yet to be studied properly. With this investigation, it would be possible to establish the potentials of soya bean husk - a lignocellusic wastes - for oil spill cleanup.

In this work the sorption characteristics of the soya bean husk particles on Escravos crude oil spill on sea water were investigated at 26 ± 1^0C.

2 METHODOLOGY

2.1 Pretreatment of Sorbents

Soya bean husks were collected from a farm settlement in Zaria (Kaduna State) Nigeria. They were cleansed to remove particles and other foreign materials and then sun dried. The husks were then screened for wax deposition, buoyancy and toxicity to marine life. Data were obtained from literature to establish wax deposition and toxicity levels in the cellulosic material. The buoyancy test was carried out as described in section 2.2.1.

The husks were subjected to size reduction and separated into different sizes with Gallenkamp^R sieves (SB 40), of varying mesh sizes to obtain the following particle size ranges, namely: 4000-1000, 1000-500, 500-105, 105-53 and <53 µm. The particle size ranges were respectively labelled A, B, C, D and E. The lignoccellulosic particulates so obtained were subjected to analysis and sorption tests.

2.2 Tests and Analyses of Sorbents

2.2.1 Buoyancy test

Buoyancy of soya bean husk was determined by filling a 250 ml beaker with sea water to 200 ml mark. The sea water was sourced from the Atlantic Ocean shore in Lagos and its density was determined as described in Section 2.2.3. The pH and temperature of the system were taken. Thereafter, 1 g soya bean husk (in its native form) was gently placed on the water surface and the times for partial and complete immersions of the husk in water were recorded.

2.2.2 Composition and morphology of soya bean husk

The composition of soya bean husk was determined by the method described by Van Soest *et al*. (1991). Scanning electron microscopic (SEM) analysis of the husk was carried out with Zeiss scanning electron microscope at an accelerated voltage of 5 kV and FTIR analysis was done with Shimadzu-8400S Fourier transform infrared (FTIR) spectrophotometer within spectra range of 4000–500 cm^{-1}.

2.2.3 Density of husk

The method described by Kopecky (1999) was used to determine the apparent and real densities of the husk using pycnometer. The weights of glassware, soya bean husk particles and water were measured with digital weighing balance (Adam, PW 184).

2.3 Analyses of Crude Oil

Escravos crude oil was collected from Kaduna Refining and Petrochemical Company (KRPC), Kaduna. Nigeria. The crude oil was weathered for 24 h inside a fume cupboard in order to remove the lighter components of the oil.

2.3.1 Density of crude oil

The density of the oil was measured using the method described by Kopecký (1999).

2.3.2 Viscosity of the crude oil

The viscosity of the crude oil was determined with Brookfield digital viscometer (DV-E) as follows. The crude oil was mixed thoroughly at room temperature for 24 h. The guard leg was mounted on the DV-E viscometer; a spindle size 4 was attached to the shaft. The shaft was slightly lifted, held firmly and screwed to the spindle with the other hand. The crude oil was poured into a 250ml beaker to about 200 ml marks. The spindle was inserted at the centre of the crude oil contained in the beaker and the viscometer was then turned on until the crude oil level gets to the immersion groove in the spindle shaft. The two spindle digit number and desired speed setting were entered into the key pad of the viscometer and the motor was turned on. Time was allowed for the indicated speed reading to stabilize before recording the viscosity measurement. Average of five readings was used to determine the final value which was recorded in Pa.s.

2.4 Determination of Sorption Capacity

Half a litre (500 mL) seawater was placed in 1 L glass

beaker which contained a cylindrical cell made of wire gauze (12cm x 7cm). Forty (40) grams of crude oil was introduced into the beaker to form oil (6 mm) layer on top of sea water. After measuring the oil layer's thickness 1 g soya bean husk particles (<53µm) was evenly spread on the oil surface. The cylindrical wire gauze was suspended such that its base is located within the water layer and below it was placed a magnetic bar at the bottom of the beaker.

A mild whirl movement of the liquid inside the beaker was achieved with magnetic stirring device (Stuart Heat Stir SB 162) at 27°C. After 10 minutes, the wire gauze cell was raised to recover the soaked sorbent particles. The recovered mass was left to drain for 5 minutes and the total weight of soaked sorbent and the cell (M_T) was obtained using a digital weighing balance (Adam, PW 184). The amount of liquid sorbed by the sorbent ($_{Mso}$) was determined by subtracting the initial sorbent and cell weight from the total weight of the wetted sorbent (M_T) as given in Equations 1 and 2. A known quantity of the sorbed liquid (oil/water) was recovered with the aid of 5-10 mL petroleum ether (40-60^{0}C). Petroleum ether contained in the recovered liquid was driven off over water bath at 45°C. This was done to obtain the proportion of water (if any) that was sorbed along with the crude oil. The steps described were repeated at 20, 30, 40, 50 and 60 min. The experiments were carried out at 26 ± 1^{0}C.

The procedure described above was repeated on setups containing 4.5 and 3 mm oil layer over sea water. This was done using the five particle sizes already mentioned and the sorption capacities of the particles for oil and water were calculated using Equations 1 and 2 respectively.

$$SC_o = \frac{Mo}{Ms} \quad 1$$

$$SC_W = \frac{Mw}{Ms} \quad 2$$

$$M_{so} = M_T - (M_c + M_s) \quad 3$$

$$M_o = M_{so} - M_W \quad 4$$

where SC_o and SC_w are oil sorption capacity (g oil/g sorbent) and water sorption capacity (g water/ g sorbent) respectively. M_{so} is the mass of sorbate, M_T is the mass of the soaked sorbent and cell, M_c is the mass of cell, M_s is the mass of sorbent, M_o is the mass of oil and M_w is the mass of water (based on water proportion of the recovered sorbate and M_{so}).

The data used in Figures 3 to 5 were fitted with DataFit 9.0^R software to obtain the oil sorption kinetic model of the soya bean husk particles investigated.

3 RESULTS AND DISCUSSION

3.1 Properties of Materials

3.1.1 Physicochemical properties

Soya bean husk was determined to contain 32.20, 14.43, 7.40 and 45.97% cellulose, hemicellulose, lignin and other components respectively. These values are within the ranges given in the literature (Mullin *et al.*, 2001; Batra, 1985; Hurter, 1988; Eman, 2005; Reddy *et al.*, 2004 and Bilba *et al.*, 2007). The real and apparent densities of the husk were obtained as 124.14 and 164.5 kg/m^3 respectively. Buoyancy test on soya bean showed that it took 1 h and 42 min for the biomass to start sinking into the sea water while the complete immersion of the hull occurred after 7.5 h.

The density, specific gravity, dynamic viscosity and kinematic viscosity of the crude oil were determined as 0.9002 g/cm^3 (28.4 ^{0}API), 0.885, 5 cP and 6.2 cSt respectively. This result indicate that the Escravos crude oil used in the work is a light crude.

3.1.2 SEM analysis

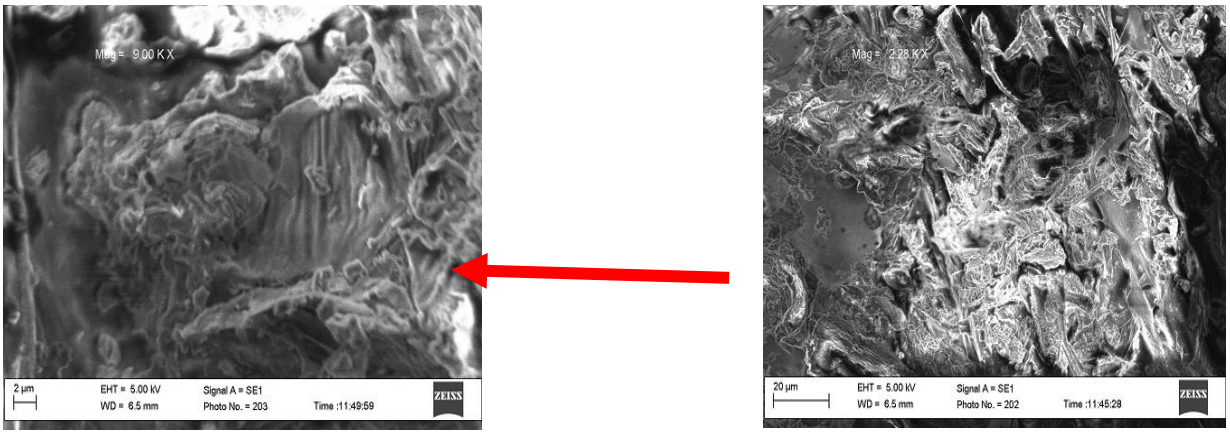

Figure 1: SEM images of soya bean husk

The SEM image (Figure 1) shows that soya bean husk possesses an inner non-smooth epidermis consisting of interlaced reticulated fibres, with little, twisty lacuna and leathery layer. The hole in the outer epidermis are the

stomata of the pod as shown in the enlarge section of the micrograph in Figure 1 (Ashori *et al.*, 2014). It is surrounded by guard cells which controls the opening and closing of the aperture as well as support for the cells. According to Raven et al. (2005) and Zhu et al. (2008) these structural characteristics of husk controls the transportation and distribution of water, air and nutrition within and between the pod and husk. This constitutes the route for transport of liquid (oil and water) in the biomaterial when used as sorbent.

3.1.3 **FTIR analysis**

The FTIR spectra of soya bean husk, shown in Figure 2, is similar to those reported in literature (Schmidt *et al.*, 2005; Mondal *et al.*, 2015). The characteristic major absorption peaks of soya bean husk were observed at 3421.43, 2921.99, 1735.09, 1624.41 and 1034.04 cm^{-1} which confirmed the presence of hemicellulose, cellulose and lignin in the soya bean husk structure. The broad absorption band at 3421.43 cm^{-1} corresponds to the characteristic O–H stretching vibration and hydrogen bond of the hydroxyl groups, (Spinace *et al*., 2009). The sharp peak band at 2921.99 cm^{-1} may represent the C–H stretching vibration from CH and CH_2 in cellulose and hemicellulose (Essabir *et al.*, 2013; Sanusi *et al.*, 2018). The band at 1735.09 cm^{-1} belongs to the carbonyl C=O stretching vibration of linkage of carboxylic acid in lignin or ester group in hemicellulose (Doulati *et al.*, 2008; Essabir *et al*., 2013). The band at 1624.41 cm^{-1} represents the carbonyl group stretching (Mondal *et al*., 2015), and the band observed at 1420.07 cm^{-1} in the spectrum indicate the bending vibration of C–H and C–O groups of the aromatic ring in polysaccharides (Mondal *et al*., 2015). The strong absorbance band at 1034.04 cm^{-1} is ascribed to the C–O and O–H stretching vibration of the polysaccharide in cellulose (Zheng *et al*., 2009). The finger-print region of the spectra shows the same characteristic bands as those of the cellulose obtained from different sources (Chen *et al*., 2012).

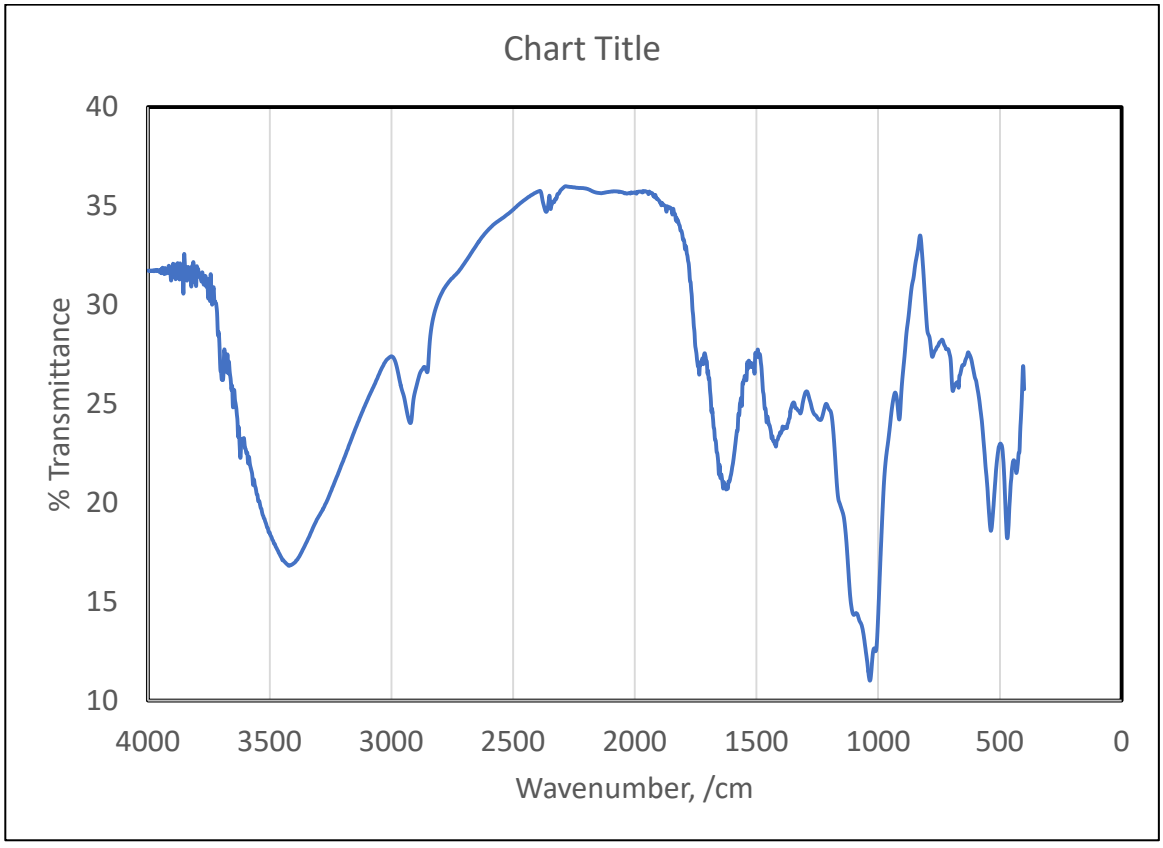

Figure 2: FTIR spectra of soya bean husk

3.2 Sorption Capacity and Behaviour

The variation of the sorption capacity with time for soya bean husk particles spread on 3mm, 4.5mm and 6mm oil layer thicknesses (on water surface) are given in Figures 3, 4 and 5 respectively.

3.3.1 Oil sorption capacity

Figure 3 shows the time variability of oil sorption capacity of soya bean husk on 3 mm (20g) oil layer thickness over water (20g). The maximum oil sorption capacity was 7.6802 g oil/g sorbent with particle D (105-53µm) at twenty minutes and the lowest

equilibrium capacity was 4.0253g oil/g sorbent with particle E (<53µm) at thirty minutes. This performance by particle E is not too different from those of C, B and A. Particle D (105-53µm) gave the highest initial sorption rate and particle B (1000-500µm) gave the lowest rate.

From Figure 4, it is seen that with 4.5mm oil layer thickness on water (30g), the highest oil sorption capacity of soya bean husk was 7.4383g oil/g sorbent with particle D (105-53µm) at forty minutes and the minimum equilibrium capacity was 4.6762g oil/g sorbent with particle B (1000-500µm) at fifty minutes. This is not too different from those of particles C and E. Particle A (4000-1000µm) gave the highest initial rate closely followed by particle D. Particle B (1000-500µm) and C (500-105µm) gave the lowest rate.

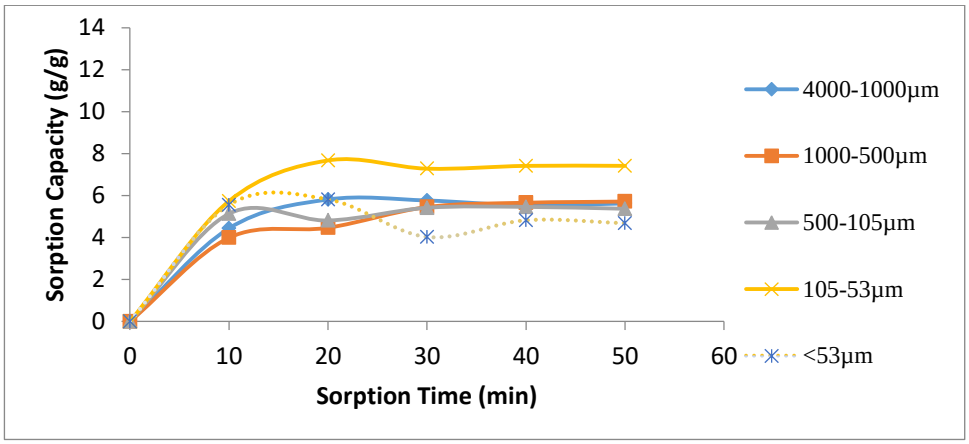

Figure 3: Variation of oil sorption capacity with time for soya bean husk particles (on 3 mm oil layer)

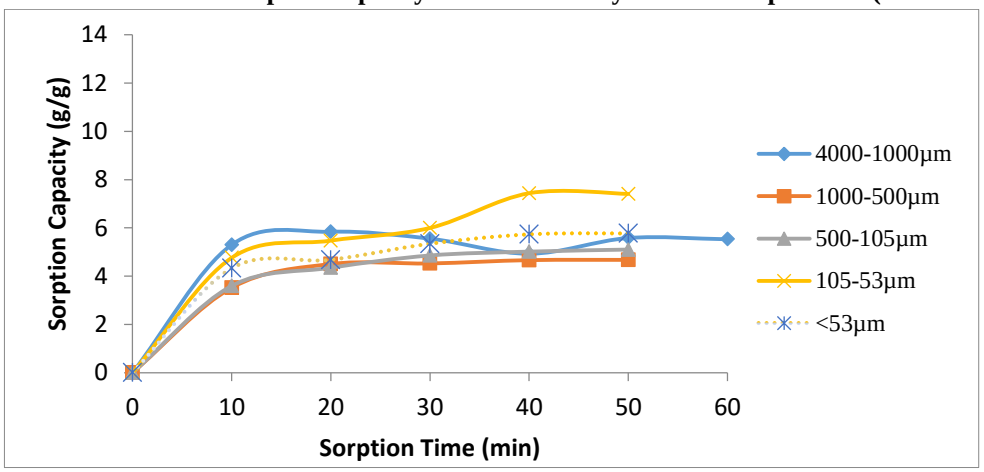

Figure 4: Variation of oil sorption capacity with time for soya bean husk particles (on 4.5 mm oil layer)

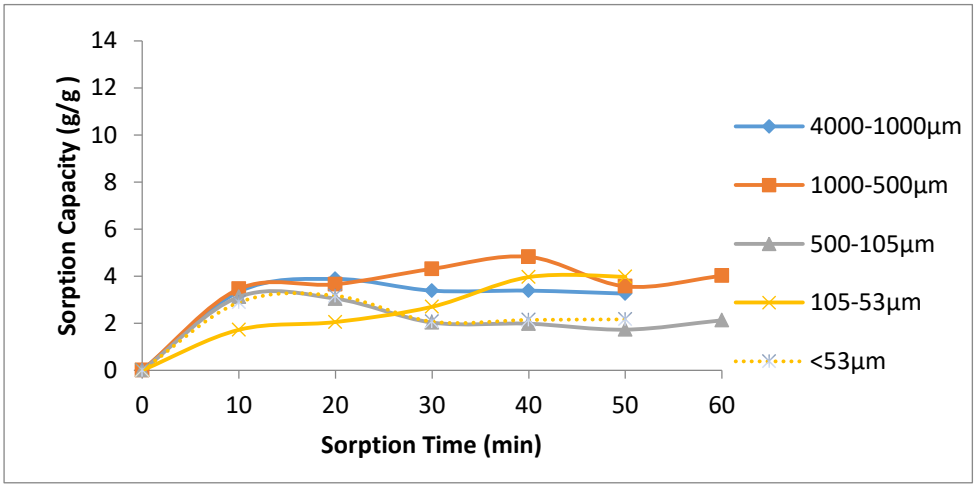

Figure 5: Variation of oil sorption capacity with time for soya bean husk particles (on 6 mm oil layer)

With 6mm oil layer thickness (40g), Figure 5 indicates that maximum oil sorption capacity of soya bean husk was 4.8189g oil/g sorbent with particle B (1000-500µm) at forty minutes though particle D recorded high sorption as well. The minimum equilibrium capacity was 2.8818goil/g sorbent with particle C (500-105µm) at fifty minutes. Particle B (1000-500µm) gave the highest initial uptake rate and particle D (105-53µm) gave the lowest initial uptake rate.

From the results presented in Figures 3 - 5, it is observed that particle D gave maximum sorption of the oil over 3 and 4.5 mm oil layer thickness. The sorption capacity initially increased with contact time but the equilibrium sorption was reached between 20 and 40 minutes as shown in Figures 3 – 5. The decaying exponential trend displayed by the particles in oil sorption rate may be due to blockage of the pores by the particles and/or the oil. This phenomenon might have led to the stoppage of fibrils' capillary filling after a period of time as observed by Olawale *et al.* (2019).

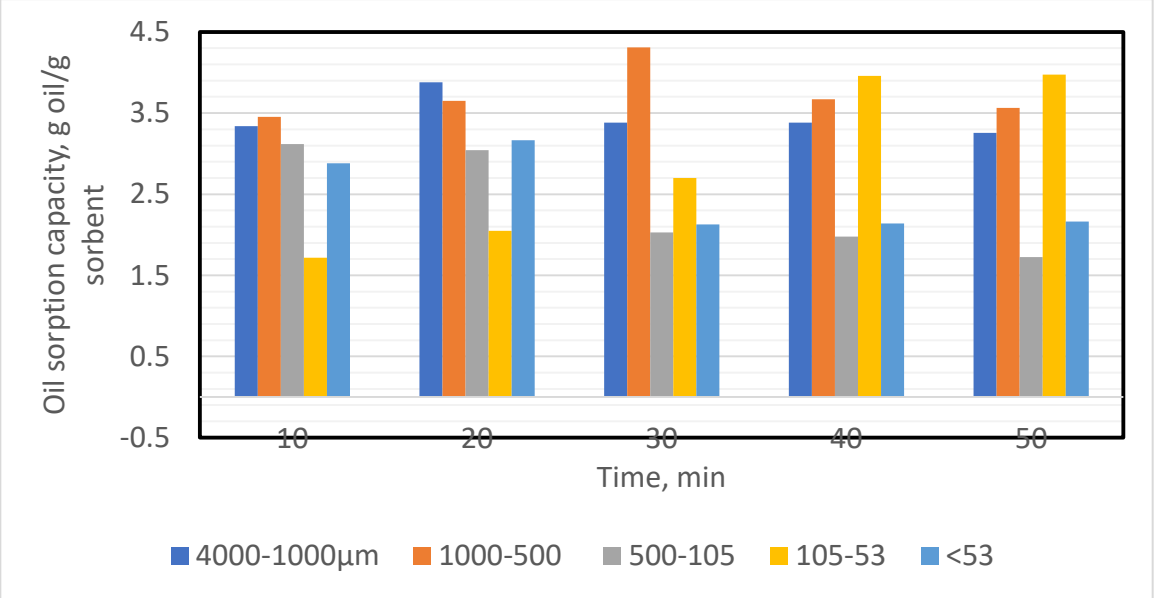

Figure 6: Sorption capacities of different particle sizes over 6 mm oil layer thicknesses

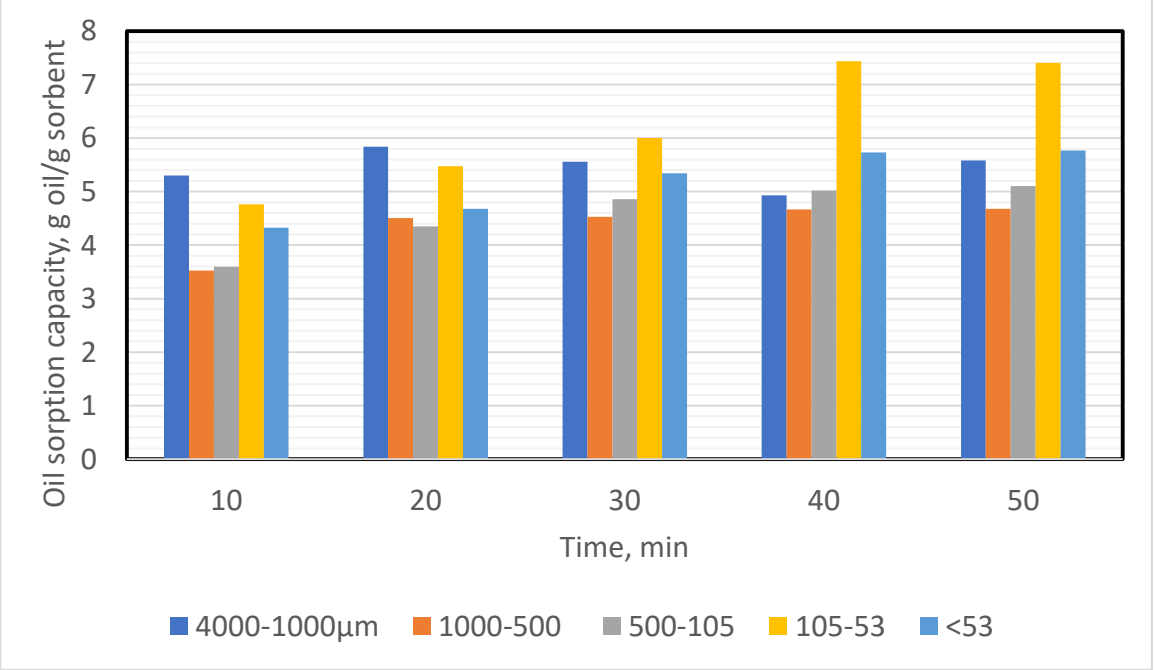

Figure 7: Sorption capacities of different particle sizes over 4.5 mm oil layer thicknesses

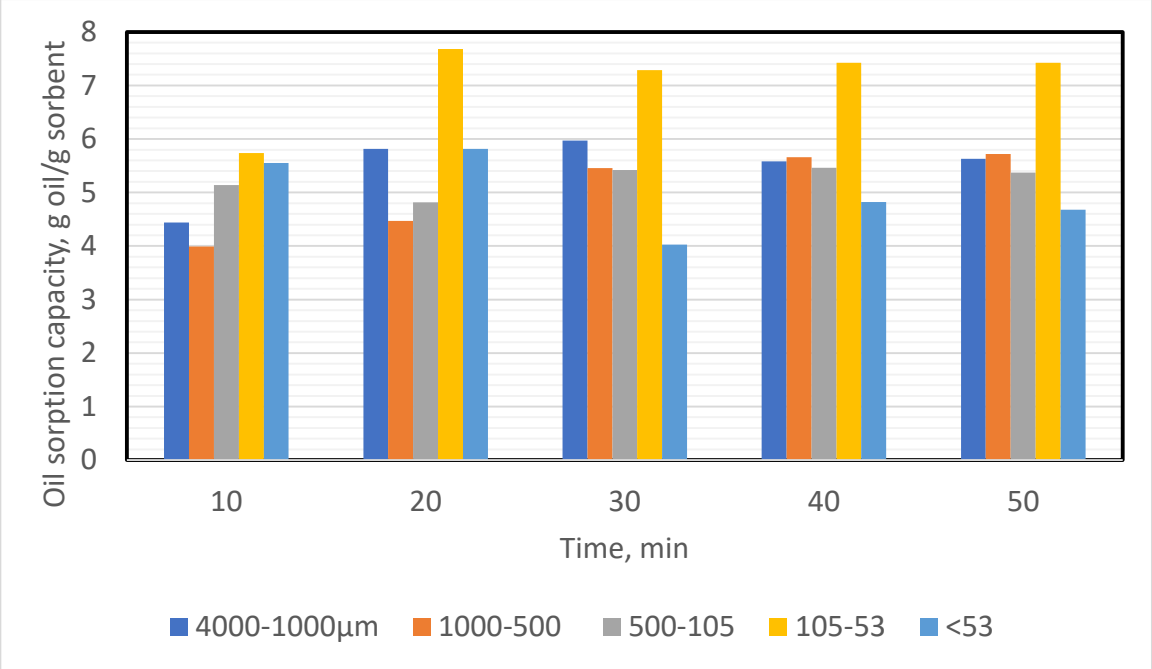

Figure 8: Sorption capacities of different particle sizes over 3 mm oil layer thicknesses

The oil sorption capacity of particle D was observed to decrease with oil layer thickness over water as shown in Figures 6 - 8. Similar trends were observed in the previous work on corn husk reported by Olawale *et al*. (2020); this observation was speculated to be caused by the forces originating from the water layer acting

vertically upward. The convective force that reaches the oil layer (to aid oil transport into the particles' pores) would be less, the thicker the oil layer over water.

No discernible trend in relation between oil sorption capacity and particle size could be established from the results presented in Figures 3 – 8. This appears to suggest that other phenomena aside particle size related ones (such as adsorption) are involved in oil sorption by the biomass particles. Blockage of the pores by particles of smaller sizes than the pores' might have occurred just as the destruction of the fibre pores in the course of size reduction (Benhood *et al.*, 2014). These factors, in addition to others such as size and viscosity of the crude oil and, pH of the medium, could affect oil absorption/retaining capacity of the particles as already stated by Olawale *et al*. (2009).

3.2.2 Water sorption characteristics

Water was sorbed only with the sorbents exposed to 3mm oil layer thickness on water as observed with corn husk (Olawale *et al*., 2020). The highest water sorption capacity recorded by soya bean husk was 8.4009 g water /g sorbent with particle D (105-53µm) at thirty minutes and the minimum equilibrium capacity recorded was 0.5865 g water /g sorbent with particle B (1000-500µm) at fifty minutes. This result would appear to correlate with the buoyancy test result which showed soya bean husk sank in water after 7.5 h. The trend of water affinity of the major components of lignocellulosic materials is: lignin < cellulose < hemicellulose (Olesen, 1997). Therefore, the composition of the materials influences the oil/water sorption capacity of the sorbents.

3.3 Comparison of Sorption Capacity of Soya bean husk and Commercial Sorbents

The maximum sorption capacity of 7.6802 g recorded by soya bean husk is far less than that of the commercial sorbents (Adsorb-IT filtration Fabric gray sheet) which recorded 10.15 g (Hussein *et al*., 2008). Since the sorbent used in this research was in its natural form, chemical and or physical modification would improve the oil sorption capacity of this biomass.

3.4 Sorption Kinetics

From the results presented in Figures 3 – 5, it is seen that oil soption by the different particle sizes of soya bean husk displayed inverse (decaying) exponential trends with time. The best fit to the sorption capacity data of the husk was obtained with the function given by Equation 5.

$$q = a\,(1 - e^{-t}) \qquad 5$$

where **q** is sorption capacity, **a** is the model (fit) parameter and **t** is time.

Table 1: Model parameters of soya bean husk's oil sorption kinetics for 3 oil layer thicknesses over sea water

Oil layer thickness, mm	Particle Size Range Labels				
	A	B	C	D	E
3	0.7998	6.1059	5.2427	5.2427	4.9793
4.5	5.4567	4.3795	4.7430	6.2165	5.1684
6	3.6368	3.9681	2.3358	2.7535	2.4832

The parameters of the kinetic model (Equation 5) for the five particle sizes employed for sorption over three oil layer thicknesses are presented in Table 1. The coefficient of determination (R^2) varied between 0.81 and 0.99 for sorption over 3 and 4.5 mm oil layer thicknesses while for 6 mm oil layer thickness, R^2 values were between 0.57 and 0.91. The R^2 values are indicative of the closeness between the empirical data and the sorption kinetic model given by Equation 5. The model fitted the oil sorption characteristics of soya bean husk fairly well but not as good as reported for corn husk particles by Olawale *et al.* (2020).

4. CONCLUSION

The oil sorption characteristics of soya bean husk wastes was evaluated for dynamic conditions at 27^{o}C on Escravos crude of 3mm, 4.5 and 6 mm oil layer thickness over water. The oil sorption by soya bean husk particles followed the exponential decay pattern. It was observed that as oil layer thickness increased, the sorption capacity decreased. Sorption capacity of soya bean husk particles was fairly good in sorption performance, especially those in the size range of 105 – 53 µm. A sorption performance higher than 7 g/g was obtained with particles in this size distribution range.

REFERENCES

Amer, A. A., El Maghraby, A., Malash, G. F. and Nahla, T. A. (2007). Extensive characterization of raw barley straw and study the effect of steam pretreatment, *Journal of Applied Science Research, 3* (11): 1336-1342.

Agida I. R., Olawale A. S. and Isa M. T. (2017). Prospects of biosorbents development for oil spill cleanup in Nigeria. Proceedings of the 13th Conference/AGM of Material Science and Technology Society of Nigeria (MSN), Kaduna State Chapter. 4th November. Zaria. Nigeria

Ashori, A., Hamzeh, Y. and Ziapour, A. (2014). Application of soybean stalk for the removal of hazardous dyes from aqueous solutions. *Polymer Engineering Science* 54(1), 239-245. DOI:10.1002/pen.23695

Batra, S.K. (1985). Other long vegetable fibres, In: Fibre Chemistry (Ed) *Hand Book of Fibre Science and Technology.* 4, 727-808.

Bayat, A., Aghamiri, S. F., Moheb, A. and Vakili-Nezhaad G. R. **(**2004). *Chemical Engineering and Technology*, 28 (12**): 1525 – 1528**

Behnood, R., B. Anvaripour, Fard, N.J.H and Farasati, M (2014). Crude oil layer sorption from saline water surface by raw and acetylated sugarcane bagasse. *Science International* (Lahore), 26 (3), 1157-1161 ISSN 1013-5316

Bilba, K., Arsene, M.A. and Ouensanga, A. (2007). Study of banana and coconut fibers: botanical composition, thermal degradation and textural observations. *Bioresource Technology*, 98, 58-60.

Choi, H. M. (1996). Needle punched cotton nonwoven and other natural fibers as oil clean- up sorbents. *Environmental Science Health,* A, 31, 1441-1457.

Choi, H. M., Kwon, H. and Moreau, J. (1993). Cotton nonwovens as oil spill clean- up sorbents. *Textile Research Journal,* 63 (4): 211-218.

Choi, H., and Cloud, R.M. (1992). Natural sorbents in oil spill cleanup. *Environmental Science and Technology*, 26 (4): 772 – 776.

Choi, H., and Moreau, J.P. (1993). Oil spill sorption behaviour of various sorbents studied by sorption capacity measurement and environmental scanning microscope. *Microscopy Research and Technique*, 25 (5): 447- 455.

Chun, K. S., Salmah, H., and Osman, H. (2012). "Mechanical and thermal properties of coconut shell powder filled polylactic acid biocomposites: Effect of the

filler content and silane coupling agent," *Journal of Polymer Research.* 19(5), 1-8

Deschamps, G., Caruel, H., Borredon, M. E., Bonnin, C. and Vignoles, C. (2003). Oil removal from water by sorption on hydrophobic cotton fibers. Study of sorption properties and comparison with other cotton fiber-based sorbents. *Environmental Science Technology*, 37 (5): 1013-1015.

Doulati, A. F., Badil, K., Yousefi Limaee, N., Shafael, S. and Mirhabibi, A.R. (2008). Adsorption of direct red 80 dye from aqueous solution onto almond shells: Effect of pH, initial concentration and shell type. *Journal of Hazardous Materials*; 15(1): 730-737

Egwaikhide, P. A., Akporhonor, E.E. and Okieimen, F.E. (2007). Utilization of coconut fibre in the removal of soluble petroleum fraction polluted water. *International Journal of Sciences,* 2 (2): 047-049.

Eman, A. A. (2005). An Investigation on the feasibility of peanut hull as an adsorbent. *Alexandria Engineering Journal*, 44, 129- 139.

El-Din, G.A., Amer, A. A., Malsh, G and Hussein, M. (2017). Study on the use of banana peels for oil spill removal. Alexandria Engineering Journal (Article in Press).

Essabir, H., Nekhlaoui, S., Malha, M., Bensalah, M.O., Arrakhiz, F.Z., Qasis, A. and Bouhfid, R. (2013). Bio-composites based on polypropylene reinforced with Almond Shells particles: Mechanical and thermal properties. *Materials and Design* 51: 225-230;

Hori, K., Flavier, M. E., Kuga, S, Lam, T.B.T. and Liyama, K. (2000). Excellent oil absorbent kapok (Ceiba pentandra (L.) Gaertn.) Fiber structure, chemical characteristics and application., *Wood Science*, 46 (5): 401- 404.

Huang, X. and Lim, T. (2005). Experimental evaluation of a natural hollow hydrophobic-oleophilic fiber for its potential application in NAPL cleanup. *Proceedings of International Oil Spill Conference*, Singapore.

Hurter, A.M. (1988). Utilization of annual plants and agricultural residues for the production of pulp and paper. *Proceedings of Tappi Pulping Conference, (TPC'88), New Orleans, LA. USA*. pp. 139-160.

Hussein, M., Amer, A. A. and Sawsan, I. I. (2008). Oil spill sorption using carbonized pith bagasse: trial for practical application. *International Journal of Environmental Science and Technology, 5* (2): 233-242.

Hussein, M., Amer, A. A., El-Maghraby, A. and Taha, N. A. (2009). Availability of barley straw application on oil spill clean- up. *International Journal of Environmental Science and Technology, 6* (1): 123-130. http://dx.doi.org/10.1016/j.matdes.2013.04.031

Ifelebuegbu A and Johnson A. (2017). Non-conventional low-cost cellulose and keratin based biopolymeric sorbents for oil/water separation and spill cleanup - A review. *Critical Reviews in Environmental Science and Technology.* Vol 47 (no. 11), 964 - 1001

https://dx.doi.org/10.1080/10643389.2017.1318620

Kopecký, F. (1999). *Physics for Students of Pharmacy,* edited by I. Bratislava, UK. (In Slovak).

Mondal, I.H., Yeasmin, S. and Rahman, S. (2015). Preparation of food grade carboxymethyl cellulose from u agrowaste. International Journal of Biological Macromolecules; 79:144-150. http://dx.doi.org/10.1016/j.ijbiomac.2015.04061

Mullin, W. J. and Weili Xu. (2001). Study of Soybean Seed Coat Components and Their Relationship to Water Absorption. *Journal of Agricultural and Food Chemistry*, 49, 5331-5335.

Odedokun, O. V. (2014). Economic analysis of cotton production and supply trend estimation in Zamfara State, Nigeria. A Ph.D. Dissertation. Department of Agricultural Economics and Rural Sociology, Ahmadu Bello University, Zaria. Nigeria.

Olawale, A. S. and Saidu B. B. (2010). Oil Sorption Characteristics of Lignocellulosics Particulates. Conference paper: 3rd *International Conference on Engineering Research and Development: Advances in Engineering Science and Technology,* Pg. 63; 10184

Olawale, A. S., Olakunle M. S. and Ajayi O. A. (2020). Study of corn husk as sorbent for oil spill cleanup. Journal of the Nigeria Society of Chemical Engineers Vol ,(35), No. 1 pp 1

Olesen, P. O. and Plackett, D. V. (1997). *Perspective on the performance of natural plant fibres*. Plant Fibre Laboratory, Royal Veterinary and Agricultural University, Coperhagen. Denmark.

Pinto, J., Athanassiou, A. and Fragouli, D. (2016). Effects of the porous structure of polymer foams on the remediation of oil spills. *Journal of Physics D. (Applied Physics)*. Vol 49, 145601 (8 pp)

Radetic, M., Jocic, D., Jovancic, P., Petrovic, Z. and Thomas, H. (2003). Recycled wool-based nonwoven material as an oil sorbent., *Environmental Science and Technology,* 37 (5): 1008-1012.

Raven, H.P., Evert, F.P and Eichhorn, E.S (2005). Biology of Plants. W.H. Freeman and Company Publishers, New York. pp. 427-600

Reddy, N and Yang, Y. (2004). Structure of Novel Cellulosic Fibres from Corn Husks. *Polymer Preprints (American Chemical Society, Division of Polymer Chemistry,* 45, 411.

Rene, P. S., Philip M. G., and Dieter M. I. (1993). *Environmental Organic Chemistry*, John Wiley and Sons, Inc., U.S.A.,

Reynolds, J. G., Coronado, P. R. and Hrubesh, L. W. (2001). Hydrophobic aerogels for oil-spill cleanup–intrinsic absorbing properties. *Energy Source*. 23 (9): 831-843.

Sanni, A., Olawale A. S. and Sani Y. M. (2017). Techno-economic analysis of agricultural wastes as feedstocks for bioethanol production in Nigeria. Proceedings of the 13th Conference/AGM of Material Science and Technology Society of Nigeria (MSN), Kaduna State Chapter. 4th November. Zaria. Nigeria

Sanusi, K.A., Sunday, N.S., Hassan, M.S. and Abdulqadir, T.A. (2018). The effect of operational parameters on biosorption of Cd^{2+}, Ni^{2+} and Cr^{6+} using *Glycine max* pod (Soya Bean). *Environ Risk Assess Remediat*; 2(2): 26-34

Schmidt, V., Giacomelli, C., and Soldi, V. (2005). "Thermal stability of films formed by soy protein isolate-sodium dodecyl sulphate," *Polym. Degrad. Stabil.* 87(1), 25-31.

Sathasivam, K and Haris, M.R.H.M (2010). Adsorption kinetics and capacity of fatty acid-modified banana trunk fibers for oil in water. Water, Air and Soil pollution-An *International Journal of Environmental Pollution.* 213, 413-423

Spinace. M.A.S., Lambert, C.S., Fermoselli, K.K.G. and De Paoli, M.A. (2009). Characterization of lignocellulosic curaua fibers. *Carbohyd Polym*; 77:47-53.

Sun, X. P., Sun, R. and Sun, J. X. (2002). Acetylation of rice straw with or without catalysts and its characterization as a natural sorbent in oil spill clean-up. *Journal for Agricultural and Food Chemistr.* 50, 6428-6433.

Teas, C., Kalligeros, S., Zanikos, F., Stournas, S., Lois, E. and Anastopoulos, G. (2001). Investigation of the effectiveness of absorbent materials in oil spills clean -up. *Desalination.* 140 (3): 259-264.

Toyoda, M.; Inagaki, M., (2003). Sorption and recovery of heavy oils by using exfoliated graphite. *Spill Science Technology Bulletin*. 8 (2): 467- 474.

Van Soest, E. P. J., Robertson, J. B. and Lewis, B. A. (1991). Methods for dietary fiber, neutral detergent fiber and non-starch polysaccharides in relation to animal nutritive. *Journal of Diary Science.* 74:3583–3597.

Yeasmin, S and Mondal, I.H (2015). Synthesis of highly substituted carboxymethyl cellulose depending on cellulose particle size. *International Journal of Biological Macromolecules*. 80, 725-731

Zeigler, C., da Silva, I. C. R., Mail, M., Kavalenka, M. N., Barthlott, W. and Holscher H. (2016). Microstructure of superhydrophobic plant leaves-inspiration for efficient oil spill cleanup materials. *Bioinspiration and Biomimetic*. Vol 11, 10pp.

Zheng, J.C., Feng, H.M., Lam, M.H., et al. (2009). Removal of Cu(II) in aqueous media by biosorption using water hyacinth roots as a biosorbent material. *Journal of Hazardous Materials*. 17(1): 780-785

Zhu, B., Fan, T.X and Zhang, D. (2008). Adsorption of copper ions from aqueous solution by citric acid modified soybean straw. *Journal of Hazardous Materials*. 153(1-2), 300-308.

THE EFFECT OF SYNTHESIZED NPK LOADED SURFACTANT MODIFIED ZEOLITE A BASED FERTILIZER IN TOMATO *(Lycopersycum esclentum)* CULTIVATION

Salako. O. [1], *Kovo, A.S.[1], Abdulkareem, A.S. [1], Yusuf, S.T. [2], Afolabi, E.A. [1] and Auta, M.[1]

[1]Department of Chemical Engineering, Federal University of Technology, Minna

[2]Department of Crop Production, Federal University of Technology, Minna

*corresponding author: Kovo@futminna.edu.ng, 08094059107

ABSTRACT

The surface of zeolite A synthesised from Ahoko kaolin was optimally modified by quaternary ammonium compound, HDTMA and used as fertilizer carrier. Characterization techniques such as FTIR and BET were used to characterise the zeolite A and modified zeolite A samples. Zeolite A's maximum adsorption capacity of 7.55mg/g was obtained with initial concentration of 162.6 mmol/L, contact time of 16 h, and temperature of 25 ^oC. The initial HDTMA concentration was the most significant term that influenced the adsorption capacity of zeolite A. The interactive effect that contributed significantly to the maximum adsorption capacity (6.27 mg/g) of the zeolite occurred with initial HDTMA concentration (243.80 mmol/L) and adsorption temperature of 25.21^oC as predicted by the Design Expert software version 7 used for the work. The surfactant modification of the surface of zeolite A reversed the negative charges on the framework to positive and allowed the adsorption of oxyanions such as nitrates and phosphates. The results indicated a reduction in the BET surface area of HDTMA modified zeolite A from 65 to 46.72 m^2/g and 62.27 m^2/g for phosphate loaded zeolite A and nitrate loaded zeolite A based fertilizers respectively. Conventional NPK 15:15:15 and the NPK loaded zeolite A based fertilizer were applied on tomato crop. The result of a higher leaf count (growth parameter) of zeolite A based fertilizer with mean (54.2) compared with NPK 15:15:15 with mean (25.7) at 11 WAT indicated the slow release property and nutrient retention of zeolite A based fertilizer. The zeolite A based fertilizer treated plants had a higher fruit yield with mean (84.69) compared with NPK 15:15:15 fertilizer with mean (69.34).

Keywords: Zeolite A, Surfactant Modified Zeolite A, Optimization, Zeolite A based slow release fertilizer, Plant growth, fruit yield.

INTRODUCTION

The application of excessive high soluble inorganic fertilizers has resulted to agronomic and pollution problems (Rahman and Zhang, 2018). Zeolite based slow release fertilizers signify an endeavour to answer the drawback of low nutrient retention capacity and nutrient leaching which causes low crop yields and soil contamination. Zeolites are hydrated crystalline aluminosilicates of alkali and alkaline earth cations with 3 – dimensional framework channelled by pores and channels (Notario del Pino *et al*., 1995). The negative charge framework of zeolites creates the prospect for surface modification of zeolites by functional groups such as cationic surfactants. This surface functionalization of zeolites improves its activity in the sorption of anionic species (Thirunavukkarasu and Subramanion, 2014). Baniswal *et al*. (2006) reported the use of modified synthetic zeolite in environmental applications especially for the adsorption of anionic nutrients such as phosphate, nitrate and nitrite. Surfactant modified zeolites (SMZ) have been known for high sorption capacity for phosphates, nitrates, sulphates, and chromates (Li *et al*., 1988). Studies on zeolites are increasing because of their high cation exchange capacity which subsequently increases the fertility of the soil. They are also used as inexpensive carriers of plant nutrients because of their slow release property (Ramesh *et al*., 2015). Baniswal *et al*. (2006) observed that the phosphorous released from fertilizer loaded SMZ was available even after 1080 h of continuous percolation whereas phosphorous release from KH_2PO_4 was exhausted in 264 h. The result suggests that SMZ could be used as carriers for slow release fertilizers (SRF) to control phosphate release.

Jakkula *et al*. (2011) reported that synthetic phillipsite had a high affinity for ammonium ion when it was used as a soil amendment compared to natural phillipsite.

Synthetic phillipsite could be a potential slow release fertilizer due to its high selectivity and high affinity for ammonium ion.

Li (2003) also reported using surfactant-modified zeolite (SMZ) as fertilizer carrier to control nitrate release. Results indicated that the adsorption of nitrate by SMZ increased as the HDTMA loading on SMZ increased. The result further showed that 30 – 40 % of adsorbed nitrate still remained on SMZ after 100 pore volumes of distilled water was used to desorb the nitrate from SMZ. The result indicate that slow release of nitrate is achievable.

Li and Zhang (2010) reported the practicality of using SMZ as fertilizer additives to control sulphate release in batch and column leaching experiments. Batch results indicated an almost instantaneous and partially reversible sulphate release while 70 % and 85 % of the loaded sulphate was still remaining on SMZ modified to 150 % and 200 % external cation exchange capacity (ECEC) respectively. The initial sulphate concentration of leachate was reduced by a factor of three.

Tomato is grown in low fertile soils in Nigeria because of continuous cropping with no added inputs to enhance soil fertility (Mofuka *et al*., 2007). FAO (2012) reported the yield level of tomato in Nigeria with a mean of 3.91 t ha^{-1} in comparison to producing countries like Ethiopia and Niger Republic with a mean yield of 7.11 t ha^{-1}. Past researches on the effect of NPK zeolite based SRF on plant growth, fruit yield and soil nutrient efficiency on tomato crops focused only on the natural forms of zeolite, natural zeolite use as soil amendment and the use of one variable at a time (OVAT) experimental design in the synthesis of zeolite from kaolin. However, this paper reports the optimized surfactant modified zeolite A synthesis from kaolin and the effects of NPK loaded zeolite A based SRF on tomato growth and fruit yield.

MATERIALS AND METHODS

Preparation of hexa-decytrimethyl ammonium bromide (HDTMA) modified zeolite

Zeolite A was produced from Ahoko kaolin through a process of metakaolization, gel formation and zeolitization by hydrothermal method as reported by Salako *et al*. (2017). The surfactant modified zeolite A samples were prepared according to a procedure described by Schick *et al*. (2010) by treating 5 g of raw zeolite A by 25 mL of 25 – 299 mmol/L surfactant (HDTMA) solution at temperature between 60 to 120 ^{o}C for a period of 8 to 24 h using a central composite design. The mixture was continuously stirred at 150 rpm to achieve equilibrium. After filtration, the sample was washed with 50ml distilled water to remove the excess HDTMA and it was thereafter dried at 70 ^{o}C overnight. Table 1 shows the experimental design matrix for the adsorption of HDTMA on zeolite A.

Table 1: Experimental design matrix of the adsorption of HDTMA on zeolite A

Std	HDTMA conc mmol/ kg	Temperature ^{o}C	Contact time (h)	Adsorption Capacity (q) mg /kg
1	81.3	25	8	3.75
2	243.9	25	8	5.95
3	81.3	65	8	0.5
4	243.9	65	8	2
5	81.3	25	24	0.5
6	243.9	25	24	5.25
7	81.3	65	24	0.35
8	243.9	65	24	2
9	25.87	47.5	16	1.95
10	299.33	47.5	16	5.85
11	162.6	25	16	7.55
12	162.6	85.34	16	1.3

Std	HDTMA conc mmol/ kg	Temperature ^{o}C	Contact time (h)	Adsorption Capacity (q) mg /kg
13	162.6	47.5	2.55	0
14	162.6	47.5	29.45	0.6
15	162.6	47.5	16	1.1
16	162.6	47.5	16	0.7
17	162.6	47.5	16	1.35
18	162.6	47.5	16	0.6
19	162.6	47.5	16	1
20	162.6	47.5	16	1.25

The central composite design which is significant for its five factor levels is a tool in Response Surface Methodology obtained from Design Expert software version 7, Stat-Ease Incorporation, Minneapolis, USA. The experimental matrix was generated from three independent variables comprising of concentration of HDTMA, adsorption temperature and contact time to give a total of 20 experimental runs in a standard order as shown in Table 1. Response surface methodology is a statistical approach used to maximize the adsorption process by optimization of operational variables. The interactive effects of the adsorption process were also determined by this statistical technique.

Phosphate and nitrate loading on surfactant modified zeolite A

KH_2PO_4 was used as the reagent to carry out ion exchange for phosphate on surfactant modified zeolite A. 25 mL of KH_2PO_4 solution was added to 5 g of surfactant modified zeolite A and stirred continuously at 150 rpm in a conical flask for 16 h at room temperature as also reported by Jakkula *et al*. (2011). 1 mole of ammonium nitrate solution was added to 5 g for of HDTMA modified zeolite A in a 250 ml conical stoppered flask. The mixture was placed in a mechanical shaker and agitated at 150 rpm for 16 h. Each of the solutions was filtered and washed with 50 ml of distilled water to wash off the excess soluble nutrients loaded on the extra lattice framework and dried at temperature of 40 ^{o}C for 24 h (Zhaohu *et al*., 2013). The phosphate and nitrate loaded zeolite A were blended to give the NPK loaded zeolite A based slow release fertilizer.

Samples of zeolite A and HDTMA modified zeolite A were analysed with the Perkin Elmer 100 Fourier Transform Infra-red (FTIR) Spectrometer model "Spectrum Two" to identify functional groups. 0.005 g of each sample was placed directly under the FTIR probe and scanned. Spectra corresponding to each individual sample were collected after the peaks were smoothened.

The zeolite A and the modified zeolite A samples for the Brunnauer, Emmett and Teller (BET) analysis were degassed under vacuum at 250 ^{o}C for 3 h to remove any residual moisture. They were then placed in a sample holder for the adsorption of nitrogen gas on the surface of the solid at 77 K. Surface areas were estimated using the multipoint BET fit at relative pressures < 0.1.

Evaluation of the effects of zeolite A based slow release fertilizer application on growth and fruit yield of tomato (Lycopersycum esculentum) in pot experiment.

A pot experiment was conducted to evaluate the efficacy of the synthesized zeolite A based fertilizer on the growth and fruit yield of two cultivars of tomato (Roma VF and UC82B). Treatment consists of four levels each of the synthesized zeolite A based fertilizer, and NPK 15:15:15 fertilizer laid out in completely randomized design (CRD) with three replications. Soil samples were initially collected from a depth of 0 - 20 cm, processed and subjected to physico-chemical analysis. The tomato seeds were initially sown in germination trays and later transplanted into pots 3 week after sowing the seeds. Application of the synthesized zeolite A based fertilizers and NPK 15:15:15 at four levels of treatment (Soil alone 0 % as control, 0.66 g, 1.33 g, 2.66 g which is equivalent to 0, 150, 300 and 600 kg/ha) took place 5 weeks after transplanting. At 6 weeks after transplanting (6 WAT), data were recorded on growth parameters viz; number of leaves, plant height, number of fruits and fruit yield on a

weekly basis. At crop maturity and following the ripening of the tomato fruit, harvesting were carried out and fruit yields on treatment basis were determined accordingly.

All data generated through the experiment were subjected to statistical analysis engaging statistical analysis software (SAS). The means were separated by Duncan's Multiple Range Test (DMRT) at 5 % level of probability.

RESULTS AND DISCUSSION

Analysis of zeolite A and HDTMA modified zeolite A.

The Fourier transform infra-red spectroscopy (FTIR) was employed to understand the interaction between the zeolite and the cationic surfactant. The spectrum of the synthesized zeolites in Figures 1 and 2 showed vibrational bands with different types of functional groups present. The overall spectrum of FTIR is divided into two general regions: 4000 –1300 cm^{-1} (the functional group region) and 1300 – 400 cm^{-1} (the fingerprint region). The frequency assignment approach was used for the interpretation of the spectrum. The FTIR spectrum demonstrated that HDTMA had completely adsorbed on zeolite A surface as observed from HDTMA-Modified zeolite A in Figure 2. The absorption bands near 3488 cm^{-1} represent OH groups for the surfaces of zeolite A and HDTMA-modified zeolite A. This showed that zeolites are hydrated materials. The OH group in Figure 2 also suggests that HDTMA only adsorbs on partial surface of the zeolites. The weak absorbance of the signal near 1000 cm^{-1} for the zeolite A and HDTMA modified zeolite A in Figures 1 and 2 indicate the presence of asymmetric stretching vibration modes of internal T-O bonds in TO_4 tetrahedral (T = Si and Al) on the surface. The strong absorbance signal near 1000 cm^{-1} for the HDTMA modified zeolite A is considered as the CN group on the zeolite surface. The absorbance of the HDTMA modified zeolite located in the region below 1000 cm^{-1} might have resulted from the alkyl groups of HDTMA on the zeolite surface. It is important to note that HDTMA molecules adsorb on the external surface of the zeolite and do not react completely with all the surface hydroxyl groups because HDTMA molecules are too big to enter the internal pores of zeolite A. The net effect leads to HDTMA modified zeolite A having the positive charge on the external surface and also the negative charge on the internal pore surface.

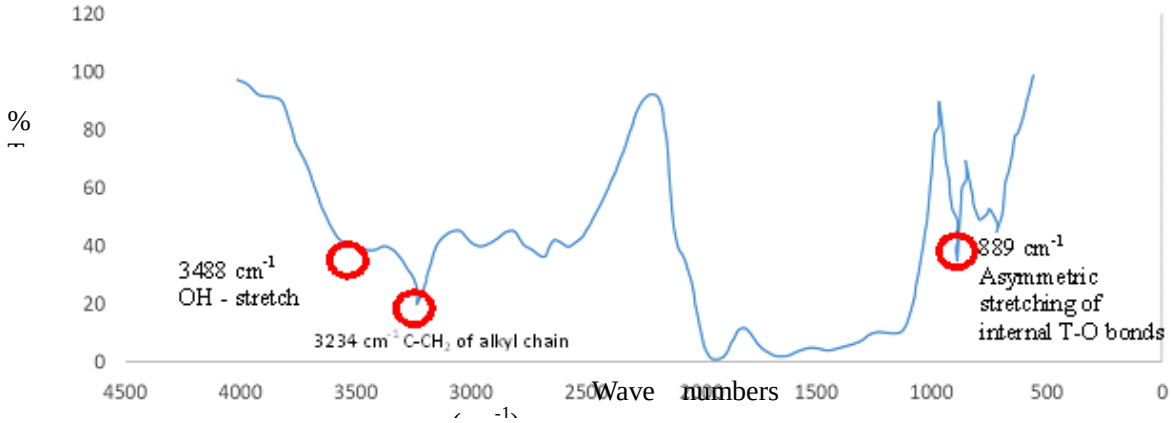

Figure 1: FTIR spectrum of the synthesized zeolite A

The bands observed at 3488 cm^{-1} and 2978 cm^{-1} in Figure 2 were attributed to symmetrical stretching vibration of C-CH_2 of alkyl chain while the band around 1404 cm^{-1} was assigned to the trimethylammonium quaternary group vibration C-N$(CH_3)_3$ (Aroke and El-Nafaty, 2014; Maina, 2016). These spectra bands could be correlated with antisymmetric and symmetric C-H stretching of the methylene group. The extra peaks suggest that the HDTMA surfactant successfully modified the zeolite surface. There was no change in band positions after modification in Zeolite A and this showed that the basic zeolite structure was kept unchanged (Aseidu, 2016).

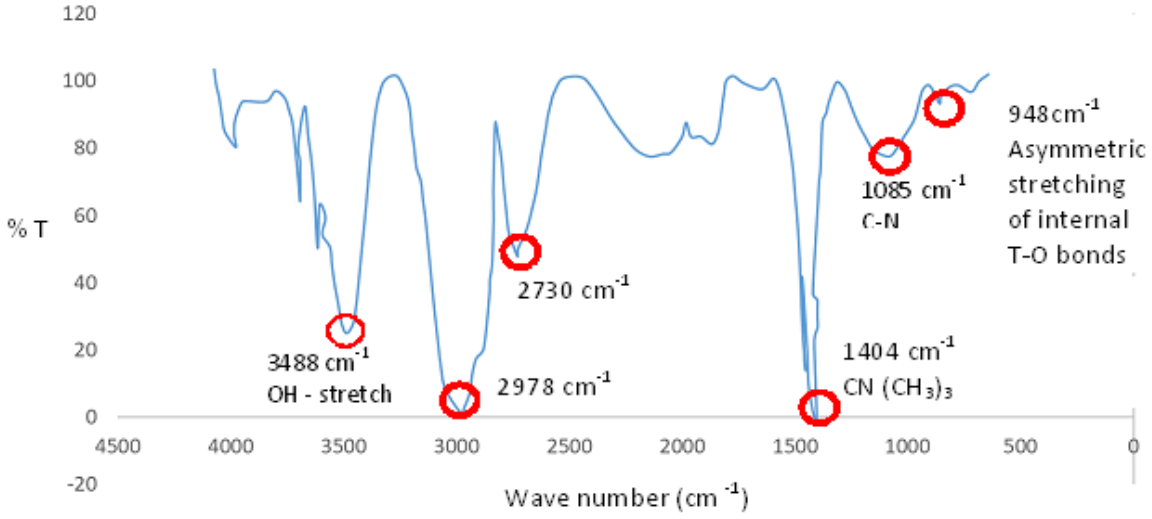

Figure 2: FTIR spectra of the HDTMA modified Zeolite A

Textural analysis by Nitrogen adsorption

Surface areas, pore volumes and pore sizes are important characteristics responsible for the description of the adsorption process in zeolites. The BET surface area analysis was performed on the synthesized zeolite A and its modification as shown in Table 2. It was observed that the specific surface areas of zeolite A reduced with HDTMA modification. Subsequent loading of phosphate ions (KH_2PO_4) and nitrate ions (NH_4NO_3) on the HDTMA-zeolite A modification reduced the surface areas further. This result is similar to the trend observed by Fungaro and Magdalena (2014) that the modified zeolites show lower total BET surface area than the unmodified zeolite. The authors further reported that the addition of the external surface area and micropore surface area gave the total BET surface area. The internal area of the zeolites was blocked and the micropore surface area decreased when the bulky molecules of the HDTMA are adhered on the external surface and pore openings of the zeolites.

Table 2: BET results of Specific surface area, Pore volume and Pore size

	Specific Surface Area (m^2/g)	**Pore Volume (cm^3/g)**	**Pore Size (nm)**
Zeolite A	296.178	0.137	0.4523
Modified Zeolite A	65.257	0.017	0.3488
Phosphate loaded Zeolite A	46.724	0.014	0.3469
Nitrate loaded Zeolite A	62.272	0.018	0.3423

Adsorption optimization using Response Surface Methodology (RSM*)*

The process of occluding oxyanions (phosphates and nitrates) in zeolite pores require reverting the negative surface charge of the zeolite A to positive by ion exchange mechanism to cause an intense attraction between the surfactant (HDTMA) and the zeolite A adsorbent. This adsorptive process requires optimization in the development of a zeolite based slow release fertilizer. Table 1 showed zeolite A with maximum adsorption capacity of 7.55mg/g at an initial HDTMA concentration of 162.6 mmol/kg, adsorption temperature of 25 ^oC and contact time of 16 h. The statistical significance as inferred from the p- values of the model terms further provides information concerning the relationship between the adsorption capacity of zeolite A and the adsorption process variables as shown in Table 3.

Table 3: Analysis of variance (ANOVA) for HDTMA adsorption on Zeolite A

Source	Sum of Squares	Degrees of freedom	Mean square	F value	P- value	
Model	89.97	9	10.00	22.85	<0.0001	significant
A-conc.	20.32	1	20.32	46.46	< 0.0001	
B-Temp.	32.63	1	32.63	74.61	< 0.0001	
C- Contact time	0.70	1	0.70	1.60	0.2347	
AB	1.80	1	1.80	4.13	0.0696	
AC	0.91	1	0.91	2.08	0.1795	
BC	1.80	1	1.80	4.13	0.0696	
A^2	12.47	1	12.47	28.50	0.0003	
B^2	17.94	1	17.94	41.01	< 0.0001	
C^2	1.69	1	1.69	3.87	0.0775	
Residual	4.37	10	0.44			
Lack of Fit	3.93	5	0.798.83	0.0160		

The model F-value of 22.85 implies the model is significant. There is only a 0.01 % chance that a "Model F-Value" this large could occur due to noise. The values of "Prob > F" less than 0.0500 indicate that the model term significantly influence the adsorption capacity of zeolite A. Table 3 shows A, B, A^2, B^2 as significant model terms. The p-values greater than 0.0500 indicate the model terms do not significantly influence the adsorption capacity**.** The "Lack of Fit, F-value" of 8.83 implies the Lack of Fit is significant which indicates that the model does not fit all the experimental data. There is only a 1.60 % chance that a "Lack of Fit F-value" this large could occur due to noise. The guiding rule is that lack of fit should be low for a model to fit. The coefficients in Equation 1 were evaluated and the p-values showed that linear coefficients A and B were more significant than their quadratic terms and interractive terms. The regression model representing the adsorption process of HDTMA on zeolite A was found to fit into the second order polynomial equation as shown in Equation 1.

$$q = 1.01 + 1.22A - 1.55B - 0.23C - 0.48AB + 0.34AC + 0.48BC + 0.93A^2 + 1.12B^2 - 0.34C^2 \quad (1)$$

where q is the adsorption capacity.

Given that A = HDTMA concentration, B = Adsorption temperature and C = Contact time. Equation 1 is valid within the range of HDTMA concentration of 25.87 to 299.33 mmol/kg, Adsorption temperature of 25 – 65 ^oC and contact time of 2.55 to 29.45 h

The adequate precision measures the signal to noise ratio. Patil and Deng (2009a and b) reported a statistical analysis that showed a ratio greater than 4 was desirable. The ratio of 15.194 obtained with the model indicated an adequate signal. The model can therefore be used to navigate the design space. The coefficient of determination (R^2) with value 0.9536 obtained for the model indicated that only 95.36 % of the experimental data are well represented within the range of the study. The optimized conditions obtained from the Design Expert software were suitable for the various types of adsorption process carried out. The value of coefficient of variation (CV) of 30.37 indicated a better precision and reliability of the experimental runs (Karmakar and Ray, 2011).

Table 4: Statistical model parameters for the adsorption of HDTMA on Zeolite A

Standard deviation	**Mean**	**C.V. %**	**PRESS**	**Pred R-Squared**	**Adj R-Squared**	**R-Squared**	**Adeq Precision**
0.66	2.18	30.37	31.59	0.6652	0.9119	0.9536	5.194

The "Predicted R-Squared of 0.6652 is not as close to the Adjusted R-Squared of 0.9119 as one might normally expect. This may indicate a large block effect with the model.The smaller the value of the predicted error sum of squares (PRESS) with value of 31.59, the better the model's precision in predicting responses in a

new experiment (Musyoka *et al*., 2012).

The main effects of HDTMA concentration, temperature and contact time on adsorption capacity of Zeolite A

The observation shown in Figure 3a revealed that as the concentrations of HDTMA increased from 81.3 - 243.90 mmol/kg, the adsorption capacity of zeolite A also increased from 0.72 – 3.16 mg/g indicating a positive effect on adsorption capacity. This trend is similar to Demircvi and Saygili (2014) who reported that HDTMA sorption percentages on vermiculite, perlite, and zeolite clays increased with increasing initial concentration of HDTMA. It was also observed in Figure 3b that as temperature increased from 25 to 65 ^{o}C, the adsorption capacity of zeolite A decreased from 3.68 to 0.58 mg/g. Thus increase in temperature had a negative effect on adsorption capacity of zeolite A. This trend is similar to that of Jin *et al*. (2008) who reported that though the optimum temperature was found to be 25 ^{o}C, there was variation of adsorbed methylene blue with increasing temperature for SDS – modified zeolite. Figure 3c showed the plot of adsorption capacity and contact time. It was observed that there was a slight increase in adsorption from 8 to 13.78 h and thereafter a noticeable decrease in adsorption capacity as contact time increased from 16 to 24 h. The reduced adsorption capacity at higher HDTMA concentration may have been as a result of excess, loosely bound HDTMA from admicelles on the organo-zeolite into the aqueous solution (Haggerty and Bowman, 1994).

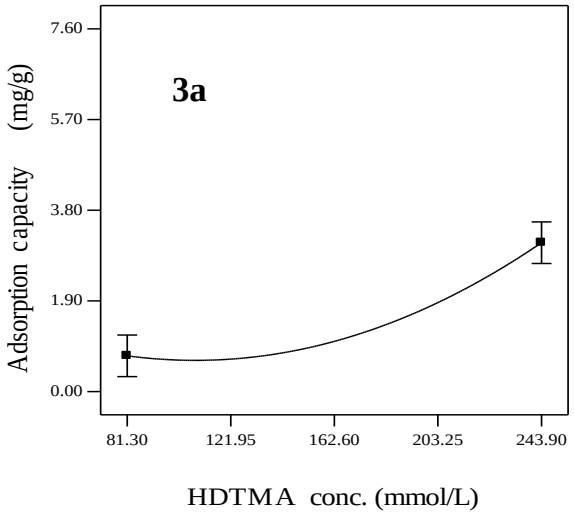

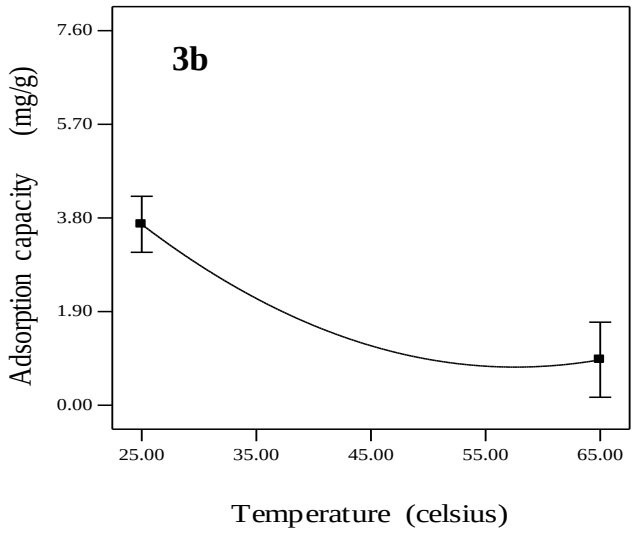

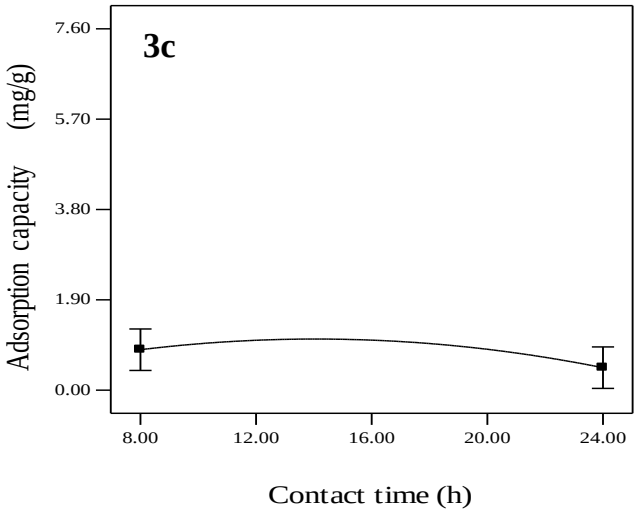

Figure 3(a, b and c): Main effects of HDTMA concentration, Temperature and Contact time on adsorption capacity of zeolite

Effect of interactive variables on adsorption capacity of zeolite A

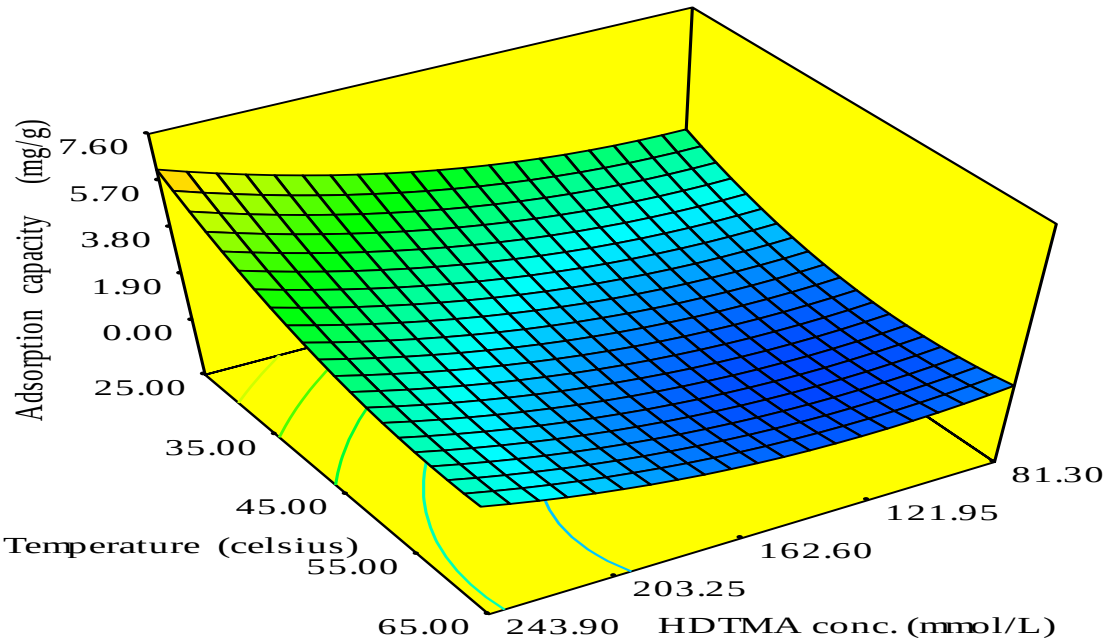

Figure 4a: 3D response surface plot of the interactive effect of temperature and HDTMA concentration on the adsorption capacity of zeolite A

Figure 4a shows the relationship between adsorption capacity, temperature and concentration of HDTMA on zeolite A. The 3D plot showed that as temperature increased from 25 to 65 ^{o} C and concentration of HDTMA increased from 81.30 to 243.90 mmol/L, there was a general increase in the adsorption capacity of zeolite A. The maximum adsorption capacity was 6.27 mg/g when the HDTMA concentration was 243.80 mmol/L and temperature was 25.21 ^{o} C.

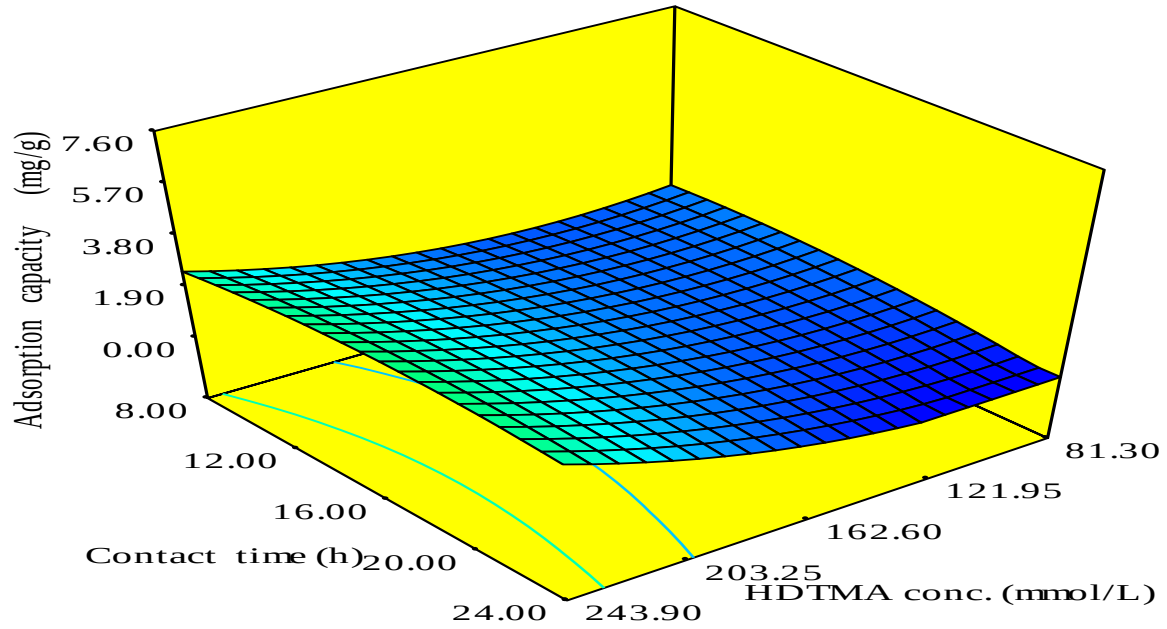

Figure 4b: 3D response surface plot of contact time and concentration of HDTMA on the adsorption capacity of zeolite A

Figure 4b showed the interactive effects of contact time and HDTMA concentration on adsorption capacity of zeolite A. The response surface plot shows that as contact time increased from 8 to 24 h, the adsorption capacity of zeolite A decreased simultaneously as the HDTMA concentration increased from 81.30 – 243.90 mmol/L. The maximum effect of these two variables resulted to an adsorption capacity of 2.59 mg/g when HDTMA concentration was 243.75mmol/l and contact time was 8.15 h.

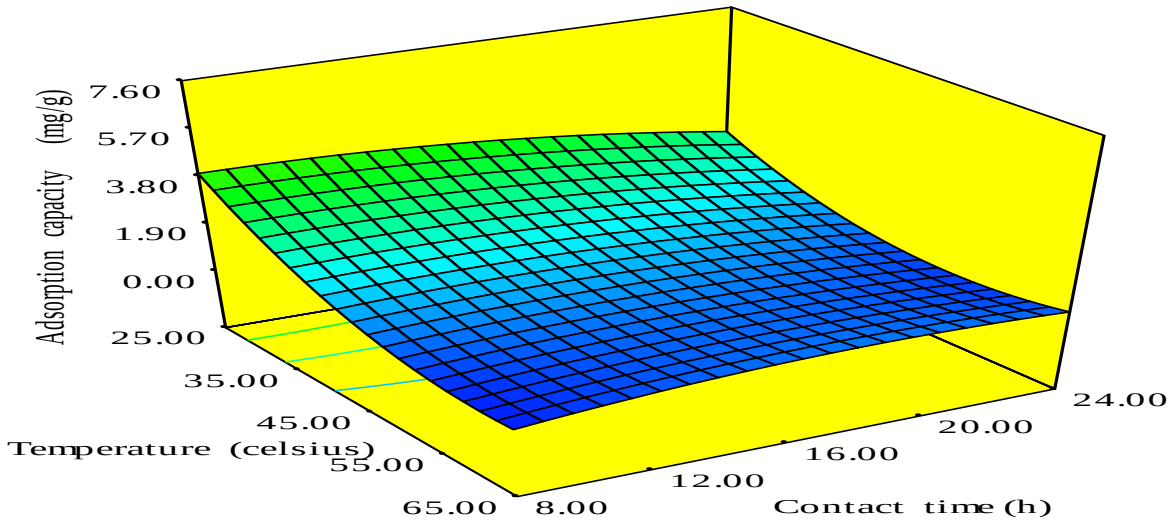

Figure 4c: 3D response surface plot of the interactive effect of contact time and temperature on the adsorption capacity of zeolite A

Figure 4c shows the interactive effects of constant time and temperature on the adsorption capacity of zeolite A. It was observed that as temperature increased from 25 to 65 ^{o}C, the adsorption capacity reduced as contact time increased from 8 to 24 h. However, it was observed that the maximum interactive effect of the two variables gave an absorption capacity of 4.02 mg/g when contact time was 8.05 h and temperature was 25.09 ^{o}C.

Evaluation of the effects of zeolite A based slow release fertilizer on growth and fruit yield of tomato.

The evaluation of the synthesized NPK-loaded-surfactant-modified zeolite A based fertilizer on two varieties of tomato crop in a completely randomized design to determine their effects on the growth parameters such as the leaf count, plant height, fruit count and fruit yield as presented in Tables 5 to 8.

Effect of varieties, fertilizer sources and rates of fertilizer application on the leaf count of tomatoes for 5 -11 weeks after transplanting (WAT)

In Table 5, it was generally observed that the mean of UC82b variety were higher than the Roma VF variety in the leaf counts from 5 to 10 weeks after transplanting. However, there was no significant difference between the leaf counts of the two varieties. There was generally an increase in the number of leaves from week 5 to 9 with respect to the two fertilizer sources; however, there was generally a drop in the leaf counts from 10 and 11 WAT. This trend might be traceable to the fact that the plant diverts nutrients to the development of the fruits. Interestingly, at the 11 WAT, the zeolite A based fertilizer treated plants were observed to have greener leaves than the plants treated with NPK fertilizer. The mean values of zeolite A based fertilizer treated plants were found to be significantly different from the mean values of the plants treated with NPK fertilizer. It was further observed that the leaves of the plant treated with NPK fertilizer were wilting and dying. The greener leaves on the plants with zeolite A based fertilizer application indicated the presence of more nutrients retained in the soil by the zeolite A carrier in the fertilizer. The zeolite A based fertilizer released their nutrients slowly for a longer period of time than the conventional fertilizers. In the conventional NPK fertilizer, nutrient carriers or fillers have no adherence to the plant nutrients and therefore nutrients leach easily beyond the root zone with percolated water. The consequence is the cutting off of the supply of nutrients to the leaves. The rates of application were not significantly different at 150, 300 and 600 kg/ha at 11 WAT.

Table 5: Effect of varieties, fertilizer sources and rates of application on the leaf count of tomatoes for 5 -11 weeks after transplanting (WAT)

	WAT						
Treatment	**5**	**6**	**7**	**8**	**9**	**10**	**11**
Variety(V)							
UC82b	98.70a	124.92a	131.85a	137.56a	124.54a	80.35a	41.6a
Roma Vf	96.12a	120.94a	128.39a	133.54a	123.16a	79.19a	32.2a
SE±	5.53	5.74	5.55	5.53	5.00	1.84	5.65
Fertilizer Source							
Zeolite A based fertilizer	78.33b	99.56b	107.76b	113.17a	104.38b	81. 35a	54.2a
NPK15:15;15	93.75a	122.22a	128.07a	133.19a	120.47a	82.36a	25.7b
SE±	4.51	3.36	3.25	3.13	2.94	2.37	7.44
Rate (kg/ha)							
0	86.45b	111.54b	118.29b	123.67b	110.67b	78.45abc	31.5a
150	103.04a	129.83ab	137.88a	143.17a	130.14a	83.87ab	46.58a
300	94.63a	119.38ab	127.04a	131.79ab	122.05ab	72.53c	32.21a
600	105.54a	130.96a	137.29a	143.37a	132.43a	84.25a	37.29a
SE±	6.75	7.36	7.04	6.92	6.66	2.52	6.43
Interactions							
V*F	NS	NS	NS	NS	NS	NS	NS
V*L	NS	NS	NS	NS	NS	NS	NS
F*L	NS	NS	NS	NS	NS	NS	NS
V*F*L	NS	NS	NS	NS	NS	NS	NS
CV (%)	22.92	19.03	17.43	16.60	16.86	14.51	15.09

Means with unlike letter(s) in columns or rows are significantly different at $p \leq 0.05$ by Duncan's Multiple Range Test (DMRT), NS stands for not significant

The effect of varieties, fertilizer sources, rates of fertilizer application on the plant height of tomato for 5 -10 weeks after transplanting (WAT)

The analysis of variance for plant height did not significantly differ for the two varieties (Roma VF and UC82b) from 5 – 10 WAT in Table 6 though Roma VF variety had a higher mean of 64.8 than UC82b with 63.3. The effect of the NPK fertilizer source on the plant height of tomato showed it was statistically significant only at 5 and 9 WAT and not statistically significant for 6, 7, 8, and 10 WAT. However, it was observed that at 5 WAT, zeolite A based fertilizer was not statistically different. The maximum plant height with mean of 69.53 was recorded at 7 WAT with NPK 15:15:15 beyond which the plant height decreases. The minimum plant height with mean of 44.13 was recorded at 5 WAT for zeolite A based fertilizer. The effect on plant height with rate of application showed no statistical difference at 5, 6, and 7 WAT while statistical difference was recorded at 8, 9 and 10 WAT. Generally, there was a growing trend in the plant heights from 5 -10 WAT with increase in rates of the different fertilizer application. This is expected because the proportion of fertilizers that was added per level of application was also increasing.

Table 6: Effect of fertilizer sources, rates and varieties on the Plant height of tomato for 5 -10 weeks after transplanting (WAT)

	Week After Transplanting (WAT)					
Treatment	**5**	**6**	**7**	**8**	**9**	**10**
Variety (V)						
Uc82b	45.03a	52.26a	59.15a	62.14a	62.83a	63.33a
Roma VF	45.56a	53.05a	60.64a	63.94a	64.66a	64.85a
SE±	0.83	1.04	0.96	0.83	0.98	0.85
Fertilizer Source						

	Week After Transplanting (WAT)					
Treatment	**5**	**6**	**7**	**8**	**9**	**10**
Zeolite A based fertilizer	44.13a	52.73a	58.56a	61.55a	67.87a	63.06a
NPK15:15:15	45.83a	50.67a	69.53a	62.03a	62.67b	62.82a
SE±	0.92	1.21	1.45	1.32	1.36	1.23
Rates (kg/ha)						
0	45.83a	53.13a	58.73a	60.97b	61.33b	61.55b
150	45.73a	53.15a	58.97a	62.34ab	63.00b	63.44ab
300	45.45a	51.84a	59.96a	63.44ab	64.48ab	65.13a
600	45.86a	52.76a	62.04a	65.42a	66.18a	66.57a
SE±	1.36	1.37	1.43	1.14	1.25	1.13
Interaction						
V*F	NS	NS	NS	NS	NS	NS
V*L	NS	NS	NS	NS	NS	NS
F*L	NS	NS	NS	NS	NS	NS
V*F*L	NS	NS	NS	NS	NS	NS
CV (%)	11.05	10.48	8.74	8.11	8.00	7.93

Means with unlike letter(s) in columns or rows are significantly different at p≤0.05 by Duncan's Multiple Range Test (DMRT)

The effect of varieties, fertilizer sources and rates of fertilizer application on tomato fruit count for 5 -10 weeks after transplanting (WAT)

It was observed from Table 7 that tomato variety, UC82b had the highest fruit count at 10 WAT with a mean value of 2.65 while Roma VF variety had a mean value of 2.53 at 10 WAT. There was no significant difference between the means of the two varieties from 5 – 10 WAT. Zeolite A based fertilizer produced the highest fruit count at 7 WAT with a mean of 2.48. The NPK fertilizer had its highest fruit count with a mean value of 2.12 at 9 WAT. The difference in mean values of the zeolite A based fertilizer to the conventional NPK fertilizers is traceable to the steady nature the zeolite A based fertilizer releases its nutrients to the plant. Leaching of plant nutrients beyond the root zone is reduced largely because the plant nutrients are occluded in the pores of the zeolite framework and they are not exposed easily as conventional NPK are mainly supported by fillers for handling purposes. It was also observed that the rate of application of 300 kg/ha which was the recommended rate for applying NPK 15: 15:15 produced the highest fruit count at 9 and 10 WAT (Isah *et al*., 2014).

Table 7 Effect of varieties, fertilizer sources and rates of fertilizer application on tomato fruit count for 5 -10 weeks after transplanting (WAT)

	Weeks after transplanting					
Treatment	**5**	**6**	**7**	**8**	**9**	**10**
Variety(V)						
UC82b	0.00a	1.02a	2.05a	2.57a	2.62a	2.65a
Roma VF	0.00a	0.32b	2.02a	2.54a	2.55a	2.53a
SE±	0.00	0.13	0.25	0.26	0.26	0.22
Fertilizer Source						
Zeolite based fertilizer	0.00a	0.59a	2.48a	2.26a	2.33a	2.36a
NPK15:15:15	0.00a	0.70a	1.83a	2.00a	2.12a	2.11a
SE±	0.00	0.24	0.26	0.22	0.27	0.23
Rates of application (kg/ha)						
0	0.00a	0.47a	1.83a	2.29a	2.22b	2.22b
150	0.00a	0.56a	2.16a	2.57a	2.52ab	2.54ab
300	0.00a	0.83a	2.17a	2.86a	3.06a	3.05a
600	0.00a	0.94a	2.24a	2.54a	2.56ab	2.53ab

	Weeks after transplanting					
Treatment	**5**	**6**	**7**	**8**	**9**	**10**
SE±	0.00	0.34	0.33	0.31	0.30	0.30
Interaction						
V*F	NS	NS	NS	NS	NS	NS
V*L	NS	NS	NS	NS	NS	NS
F*L	NS	NS	NS	NS	NS	NS
V*F*L	NS	NS	NS	NS	NS	NS
CV(%)	0.00	16.43	37.94	23.16	38.77	38.77

Means with unlike letter(s) in columns or rows are significantly different at p≤0.05 by Duncan's Multiple Range Test (DMRT)

The effect of varieties, fertilizer sources and rates of fertilizer application on tomato fruit yield for 5 -10 weeks after transplanting (WAT)

The mean values of the fruit yield of tomato variety shown in Table 8 illustrate that UC82b produced the highest fruit yield with mean value of 92.71 while Roma VF produced the lowest yield with mean value of 87.66. The mean values of the two varieties were not significantly different. It was observed that zeolite A based fertilizer produced the highest fruit yield with a mean value of 84.69. The fruit yield of NPK 15:15: 15 was lowest with a mean value of 69.34. The increase observed in zeolite A based fertilizer is traceable to its slow release property of the adsorption between the plant nutrients and the pores of the zeolite carrier. The rate of application of fertilizer (300 kg/ha) had the highest mean value of 103.57 and it was statistically different from rate of application (600kg/ha).

Table 8: Effect of varieties, fertilizer sources and rates of fertilizer application on tomato fruit yield for 5 -10 weeks after transplanting (WAT)

Treatment	**Fruit yield (g/pl**
Variety (V)	
UC82b	92.71a
Roma VF	87.66a
SE±	7.58
Fertilizer Source	
Zeolite A based fertilizer	84.69a
NPK15:15:15	69.34b
SE±	4.93
Rates of application (kg /ha)	
0	70.36b
150	97.57a
300	103.57a
600	89.25ab
SE±	12.19
Interaction	
V*F	NS
V*R	NS
F*R	NS
V*F*R	NS
CV (%)	25.30

Means with unlike letter(s) in columns or rows are significantly different at p≤0.05 by Duncan's Multiple Range Test (DMRT)

CONCLUSIONS

The study investigated the sorption of quaternary amine compound, HDTMA and oxyanions such as nitrates and phosphates on optimized zeolite A synthesised from an Ahoko kaolin using central composite design. The initial concentration of HDTMA (162.6 mmol/L) equivalent to its external cation exchange capacity (ECEC) was adsorbed to zeolite A surface by coulombic interactions. The study further evaluated the application of synthesized NPK loaded zeolite A based fertilizer and conventional NPK 15:15:15 fertilizer on the growth and fruit yield of tomato crop. Tomato crop treatments with NPK loaded zeolite A based fertilizer showed much greener leaves than the plants treated with NPK fertilizer with less green leaves at 11 weeks. This result indicates better retention of plant nutrients and the slow release property of the carrier, surfactant modified zeolite A. The fruit yield from plants treated with NPK loaded zeolite A based fertilizer also showed higher fruit yields than the plants treated with conventional NPK based fertilizer indicating that plant nutrients which might have leached beyond the root zone in the NPK fertilizer were utilized in the zeolite A based fertilizer to giver higher fruit yields.

ACKNOWLEDGEMENT

The authors appreciate the financial support of TETFUND through grant number

TETFUND/FUTMINNA/2016 – 2017/6th/BRT/21.

REFERENCES

Aroke, U. O. and El-Nafaty, U. (2014). XRF, XRD and FTIR properties and characterization of HDTMA-Br surface modified organo-kaolinite clay. *International Journal of Emerging Technology and Advanced Engineering, 4(4), 817-825*
.

Asiedu, O. (2016). Removal of fluoride from water using surfactant modified synthetic zeolites (Doctoral Dissertation), Kwame Nkrumah University of Science and Technology, Kumasi, Ghana.

Bansiwal, A. K., Rayalu, S. S., Labhasetwar, N. K., Juwarkar, A. A., and Devotta, S. (2006). Surfactant-modified zeolite as a slow release fertilizer for phosphorus. *Journal of Agricultural and Food Chemistry*, 54(1), 4773-4779.

Demirçivi, P. and Saygılı, G. (2014). Sorption isotherms and modelling studies of HDTMA for adsorption onto vermiculite, perlite and zeolite clays. *Sigma Journal of Engineering and Natural Sciences*, *32(2)*, 311-320

Food and Agricultural Organization FAO (2012). Faostat. Retrieved December 29th 2012 from http://faostat.fao.org/site/339/defalt.aspx

Fungaro, D. A. and Magdalena, C. P. (2014). Counter-ion effects on the adsorption of acid orange 8 from aqueous solution onto HDTMA-Modified nano-zeolite from fly ash. *Environment and Ecology Research*, *2*(2), 97-106

Haggerty, G.M., Bowman, R.S., (1994). Sorption of inorganic anions by organo-zeolites, *Environmental Science and Technology*, 28 (3), 452-458.

Isah, A. S., Amans, E.B., Odion, E. C. and Yusuf, A. (2014). Growth rate and yield of two tomato varieties (*Lycopersicon esculentum Mill*) under green manure and NPK Fertilizer rate, Samaru Northern Guinea Savanna, *International Journal of Agronomy,* (2014) 8.http://dx.doi.org/10.1155/2014/932759

Jin, X., Jiang, M. Q., Shan, X. Q., Pei, Z. G., and Chen, Z. (2008). Adsorption of methylene blue and orange II onto unmodified and surfactant-modified zeolite. *Journal of Colloid and Interface Science*, 328(2), 243-247.

Jakkula, V. S., Williams, C. D., Hocking, T. J., and Fullen, M. A. (2011). High selectivity and affinity of synthetic phillipsite compared with natural phillipsite towards ammonium (NH_4^+) and its potential as a slow release fertilizer. *Archives of Agronomy and Soil Science*, *57*(1), 47-60.

Jakkula, V.S. and Wani, S. P. (2018). Zeolites: Potential soil amendments for improving nutrient and water use efficiency and agriculture productivity, Scientific Reviews and Chemical Communications, 8 (1), 119 – 123.

Karmakar, M. and Ray, R. R. (2011). Current trends in research and application of microbial celluloses. *Journal of Microbiology Research*, 6(1), 41 - 46.

Li, Z., Roy, S. J., Zou, Y., and Bowman, R. S. (1998). Long-term chemical and biological stability of surfactant-modified zeolite. *Environmental Science and Technology*, 32(17), 2628-2632.

Li, Z. (2003). Use of surfactant-modified zeolite as fertilizer carriers to control nitrate release. *Microporous and Mesoporous Materials*, 61(1), 181-188

Li, Z., and Zhang, Y. (2010). Use of surfactant-modified zeolite to carry and slowly release sulfate. *Desalination and Water Treatment*, *21*(1-3), 73-78.

Maina, E. W. (2016). Studies on photo stabilization of pyrethrum flower extracts using clay, Master of Science (Chemistry), Jomo Kenyatta University of Agriculture and Technology, Kenya

Mofuka, M. M., Nsomb, M., Nkasa C., Ibwenzi, K and Taba, K. (2007).Effect of combining organic biomass and inorganic fertilizer on tomato yield and nematode control in Arenosal in Kinshasha. In: A Betonoed (ed)., Advances in Integrated Soil Fertility Management in sub-Saharan African. *Challenges and Opportunities*. 359-363 Springer.

Musyoka, N. M., Petrik, L. F., Balfour, G., Ndungu, P., Gitari, W. M., and Hums, E. (2012). Synthesis of zeolites from coal fly ash: Application of a statistical experimental design. *Research on Chemical Intermediates*, 38(2), 471-486.

Notario, P., Arteaga, J. S., Padron, I. J., Gonzalez M., M. M. and Garcia, H. (1995). Phosphorous and potassium release from phillipsite based slow release fertilizers.

Journal of Controlled Release, 34(1), 25 – 29

Rahman, K. M. and Zhang, D. (2018). Effects of fertilizer broadcasting on the excessive use of inorganic fertilizers and environmental sustainability. *Sustainability*, *10*(3), 759 - 763.

Ramesh, V., James G., Jissy S., Jyothi., and Shibli, S.M.A. (2015). Effect of zeolites on soil quality, plant growth and nutrient uptake efficiency in sweet potato. *Journal of Root Crops*, 41(1), 25 -31.

Salako, O., Kovo, A.S., Abdulkareem, A.S., Yusuf, S.T. (2017). Synthesis of LTA zeolite from Ahoko kaolin: Application of statistical analysis. Proceedings of 2nd International Engineering Conference, Federal University of Technology, Minna, Niger State, Nigeria, 17th -19th October, 2017, pp 39-47

Schick, J., Caullet, P., Paillaud, J. L., Patarin, J. and Mangold-Callarec, C. (2010). Batch-wise nitrate removal from water on a surfactant-modified zeolite. *Microporous and Mesoporous Materials*, 132(3), 395-400

Thirunavukkarasu, M. and Subramanian, K.S. (2014). Surface modified nano-zeolite used as carrier for slow release of sulphur. *Journal of Applied and Natural Science* 6 (1), 19-26.

Zhaohui, L., Yingpeng, Z and Yan, L. (2013). Zeolite as slow release fertilizer on spinach yields and quality in a greenhouse test, *Journal of Plant Nutrition*, 36(10), 1496-1505 DOI: 10.1080/01904167.2013.790429.

DELIGNIFICATION OF CORN COB FOR THE SYNTHESIS OF LACTIC ACID

***Alhafiz, H. A.[1*], Isa, M. T. [1], Sallau, A. B. [2] and Ameh, A. O. [1]**

[1]Department of Chemical Engineering, Ahmadu Bello University, Zaria, Nigeria

[2]Department of Biochemistry, Ahmadu Bello University, Zaria, Nigeria

*Corresponding Author: sadiyalhafeez@gmail.com. +2348038103443

ABSTRACT

Petroleum-based polymers are associated with environmental and sustainability issues such as environmental pollution and global warming. In view of these issues, corn cob was pretreated for the synthesis of lactic acid. Lactic acid is the base material for poly lactic acid production. The corn cob (Zea mays) which contains 79.73% holocellulose (cellulose+hemicellulose) and 16.24% lignin was subjected to oxalic acid pretreatment in order to remove lignin. With the aid of Central Composite Design (CCD) on Design-Expert 6.0.6 Software, the pretreatment was optimized at a temperature range of 25-120 ^{o}C and a time range of 30-60 min. Optimization studies revealed that the optimum temperature and time for oxalic acid treatment was 25 ^{o}C/30 min, holocellulose content improved from 79.73% to 85.565% and expectedly lignin content reduced from 16.24% to 9.91%. Fermentation with Bacillus coagulans at a temperature of 50 ^{o}C, a pH of 6.0 and a time of 48 hr produced lactic acid with a yield of 82%. This implies that oxalic acid pretreatment of corn cob is effective for the synthesis of lactic acid.

1.0 INTRODUCTION

Biodegradable and renewable polymers have drawn much interest owing to the environmental and sustainability issues associated with them. These issues include air pollution, production of hazardous substances, global warming and limited resources (fossil fuel) (Ren, 2010). Poly lactic acid (PLA) is a biodegradable and renewable polymer used in plastics for packaging and in medicine for implants (Averous, 2008). PLA is derived from lactic acid, a naturally occurring acid that is produced by chemical synthesis or by biochemical process. The chemical synthesis of lactic acid has a major drawback because it leads to a racemic mixture (Rafael, 2010). On the other hand, the biochemical process involves the use of microorgansms such as *Rhizopus oryzae*, *Lactobacillus delbruki* and *Lactobacillus casei* to ferment monomeric sugars. Another microorganism that has been used for lactic acid fermentation is *Bacillus coagulans*, it is a microorganism with thermophilic growth characteristic, a strong ability for pentose and hexose homofermentation and a robust tolerance to inhibitors (Maas *et al*., 2008). Figure 1 shows the conversion of glucose and xylose to lactic acid.

Monomeric sugars are found in carbohydrates such as cassava, rice, sweet potato, raw starch, sugar cane molasses as well as corn starch (Afolabi *et al.*, 2012; Lu *et al*., 2008; Panda and Ray 2008; Thongchul 2005). In addition to these carbohydrate sources, there exist lignocellulosic biomass also termed agro residue that can be employed in the production of lactic acid. These materials are abundant, cheap and do not compete as food source, thereby striking out the food versus raw material conflict that arise when carbohydrates are used (Hadar, 2014). Hence some agro residues have received attention in the production of lactic acid, these include: wheat straw, corn fiber, corn stover, cane molasses and corn cob (Maas *et al*., 2008; Bischoff *et al*., 2010; Zhao *et al*., 2013; Srivastava *et al*., 2014; Ali *et al*., 2006).

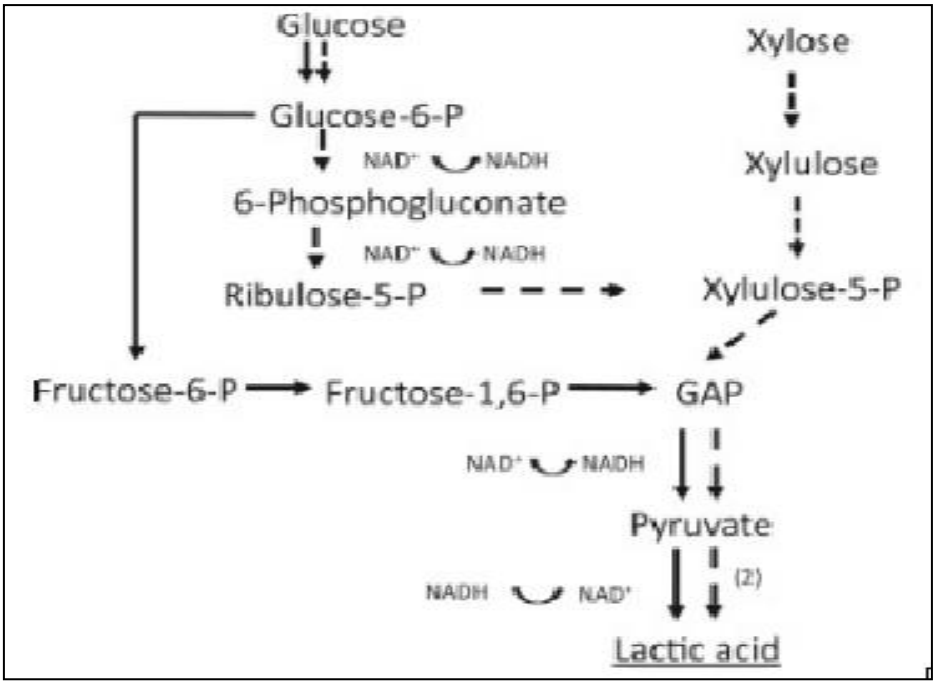

Figure 1: Conversion of Glucose and Xylose to Lactic Acid

Lignocellulosic materials are composed of cellulose and hemicellulose which are cemented together by lignin. This lignin component acts as a barrier that makes cellulose and hemicellulose inaccessible by microorganisms. In order to break this barrier, lignocellulosic materials have to undergo pretreatment prior to processing. This pretreatment which can be by physical, chemical, physicochemical or biological means decreases the crystallinity of cellulose as well as improves its porosity (Harmsen, 2010). Chemical pretreatment can be carried out using acids such as sulfuric acid and hydrochloric acid. These acids lead to corrosion of reaction vessel as well as production of inhibitory compounds that reduce lactic acid yield. In order to overcome these drawbacks, oxalic acid is used because it is odourless, produces low amounts of inhibitory products and does not disrupt glycolysis because it is less toxic to microorganisms (Lee and Jeffries 2011). The choice of pretreatment method relies on the raw material to be used and the by-products generated (Kumar *et al.*, 2009).

For the purpose of breaking down the lignin barrier in corn cob as a lignocellulosic biomass, this study focused on chemical pretreatment using oxalic acid pretreatment for the synthesis of lactic acid. Optimization studies were carried out to determine the optimum time and temperature for the pretreatment.

2.0 MATERIALS AND METHOD

2.1 Materials

The corn cob that was used for this study was obtained from a farm land in Dan-Alhaji, Lere local government, Kaduna State, Nigeria. It was identified at the Herbarium of the Department of Botany, Ahmadu Bello University as *Zea mays* with a voucher number 01824 belonging to the family Poaceae. The corn was harvested, dried and separated from the cob. The corn cob was cleaned to remove foreign materials, grinded to a particle size of 0.5 mm and dried at 103 ^{o}C until constant weight was achieved. Oxalic acid by Fizmerk India with 99% purity and a melting point of 101^{o}C was purchased from Emaco Chemicals Kaduna State. Sodium Hydroxide with 99% purity produced by Merck India was purchased from Hadis Chemicals Zaria Kaduna state. Design Expert 6.0.6 was used to carry out the experimental design and optimization. The holocellulose composition of the untreated and treated corn cob was based on the Technical Association of Pulp and Paper Industry (TAPPI) Standard 211 –om 85. The lignin content was estimated thus: 1 g of corn cob was treated with 72% sulfuric acid overnight at room temperature. It was filtered, weighed, ignited at 850 ^{o}C for 45 minutes. After the ignition, the weight of ash was subtracted from the weight of lignin to give the ash-free lignin in percentage.

2.2 Experimental design

This was carried out on design-expert 6.0.6 software. The design was with Central Composite Design (CCD) and a study type Response Surface Methodology (RSM) was adopted. Two factors (variables) and a response were considered. The factors were A (Time) in minutes and B (Temperature) in ^{o}C. The response was the holocellulose composition of corn cob in %. The lower and upper bounds for the time were 30 and 60 min respectively. While for the temperature, 25 and 120 ^{o}C were the lower and upper limits respectively. Eventually, 10 number of experimental runs were generated.

2.3 Pretreatment with Oxalic Acid

30 g of corn cob was immersed in 300 ml of oxalic acid solution with a concentration of 5 wt.%. Subsequently, the corn cob was washed with distilled water until a neutral pH was achieved and it was then dried at 103 ^{o}C for 10 hr.

2.4 Fermentation of Treated Corn cob

At the end of pretreatment with oxalic acid, the holcellulose content of the 10 experimental runs were fed back into design expert software in order to determine the optimum pretreatment condition. The determined optimum condition was used to pretreat corn cob that was subsequently used for the fermentation. The fermentation methodology by Hu *et al*. (2015) was adopted and modified. *Bacillus coagulans* inoculum (seed culture) was prepared in YEX medium containing 10 g/l xylose and 10 g/l yeast extract at a pH of 6.0, a temperature of 50 ^{o}C for a time span of 24 hr. Fermentation was carried out by introducing 10 % (w/w) oxalic acid treated corn cob, 10 g/l yeast extract and 10% (v/v) of the inoculum to 100 ml of the fermentation medium (50 g/l glucose and 10g/l yeast extract) in 150 ml Erlenmeyer flask. The fermentation was accomplished in an Incubator Shaker Water Bath at a temperature of 50 ^{o}C, pH of 6.0, agitated at 100 r.p.m for 48 hr. The fermentation process was maintained at a pH of 6.0 by charging 10 M NaOH solution. The concentration of lactic acid produced from the start to the end of the experiment was determined by spectrophotometry and the yield calculated using Equation 1.

$$LA\ Yield = \frac{[LA]\times V - [LA_o]\times V_o}{f \times Wcc \times 1.111} \times 100\% \qquad 1$$

Where LA = Lactic acid, [LA] = Lactic acid concentration at the end of the fermentation (g/L), [LAo] = Lactic acid concentration at the start of the fermentation (g/L), V = Volume of fermentation broth at the end of the fermentation (L), V_o = Volume of fermentation broth at the end of the fermentation (L), f = Cellulose fraction of dried corn cob (g/g), Wcc = Weight of dried corn cob used in fermentation (g), 1.111 = Conversion factor for cellulose to equivalent glucose.

2.5 Characterization of Lactic Acid Produced

The lactic acid produced was characterised using FTIR. The analysis was carried out with SHIMADZU FTIR-8400S. The spectra were documented between a range of 4000 and 650 cm^{-1} at a resolution of 8 cm^{-1}. In addition, Kelling's test using Iron (III) chloride was used to confirm the presence of lactic acid. Furthermore, the boiling point and specific gravity were determined to further confirm that lactic acid was produced.

3.0 RESULTS AND DISCUSSION

3.1 Composition of Untreated Corn Cob

Table 1 shows the composition of untreated corn cob. The corn cob used for this study had a holocellulose composition of 79.73% which is higher than that of Zhang (2016) and lower than that of Pointer *et al*. (2014). The variation in holocellulose is due to the fact that the composition of a lignocellulosic biomass depends on the location of growth, condition of the soil and fertilizers applied as well as the analytical procedure utilized (Kumar *et al.,* 2009).

Table 1: Composition of untreated corn cob

	Location	Cellulose (%)	Hemicellulose (%)	Holocellulose (%)	Lignin (%)
This Study	Kaduna, Nigeria	70.00	9.725	79.73	16.24
Pointer *et al*. 2014	Austria	38.80	44.40	83.20	11.90
Zhang 2016	Hubei, China	37.26	29.05	66.31	19.60

3.2 Composition of Corn Cob after Pretreatment

Table 2 shows the composition of corn cob in terms holocellulose and lignin after pretreating it with oxalic acid. There was a substantial increase in holocellulose and a corresponding decrease in lignin. A similar result was obtained in the work of Zhang *et al*. (2016) where the holocelluse content of corn cob increased after pretreatment. This increase in holocellulose implies the availability of more monomeric sugar for subsequent processing or for digestion by microorganisms. The holocellulose composition which is the response for the pretreatment was run on design expert 6.0.6 software in order to arrive at the optimum pretreatment conditions (time and temperature). Table 3 shows the Analysis of Variance (ANOVA) for the pretreatment. The model was a quadratic model with a 'prob>f' value of 0.001 which is less than 0.05. This implies that the model is significant and adequately fits the response.

Table 2: Composition of Oxalic Acid Treated Corn Cob

Time	Temperature	Holocellulose	Lignin
30	25.0	85.78	10.40
60	25.0	85.19	11.08
30	120.0	85.18	11.08
60	120.0	85.20	11.08
24	72.5	85.60	10.56
66	72.5	85.59	10.62
45	5.3	86.32	9.91
45	139.0	85.33	11.00
45	72.5	86.38	9.88
45	72.5	85.37	10.85

Figure 2 shows the parity plots for the pretreatment. This compares the actual experimental values with the values predicted by Design expert software. The R^2 value from the parity curve describes how well the model describes the process. It ranges from 0 to 1. An R^2 value of 1 means the model perfectly describes the process. The R^2 value for oxalic acid treatment is 0.9848, this means the model perfectly describes the process.

The result of the optimization is shown in Table 4. The optimum time and temperature for oxalic acid synthesis is 30 min and 25 ^oC respectively.

Table 3: Summary of Analysis of Variance (ANOVA) for Oxalic Acid Treated Corn Cob

Parameter Model	Prob > F	
Model	0.0010	Significant
A	0.8955	
B	0.0014	
A^2	0.2411	
B^2	0.0057	
AB	0.0002	

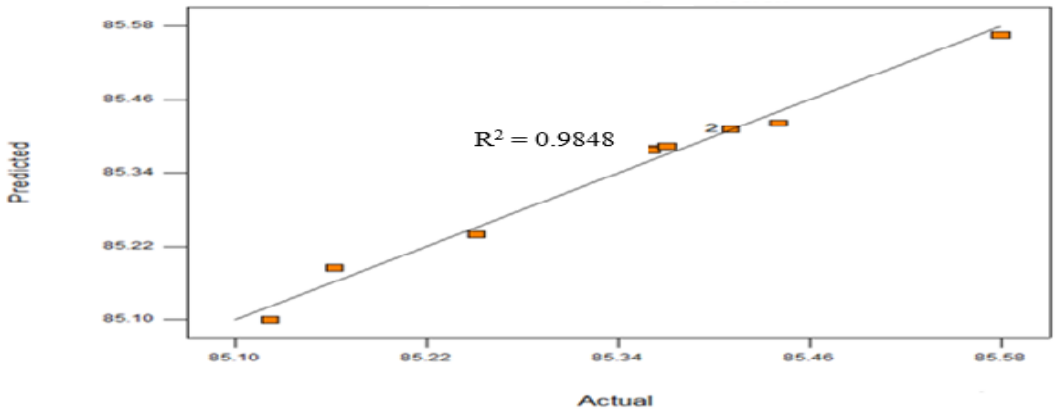

Figure 2: Predicted Versus Actual Holocellulose Values for Oxalic Acid Treated Corn Cob

Table 4: Optimization Result for Oxalic Acid Pretreatment of Corn Cob

Solution No.	Time (Minutes)	Temperature (^{0}C)	Holocellulose (%)	Desirability	
1	30.00	25.00	85.5646	0.967	Selected
2	30.79	25.00	85.5576	0.951	
3	60.00	106.65	85.4254	0.664	
4	60.00	107.02	85.4254	0.664	

3.3 Concentration and Yield of Lactic Acid after Fermentation

During the course of fermentation, the concentration of sugars (glucose and xylose) and lactic acid were determined. In addition, the concentration of acetic acid was determined. This is the most encountered inhibitor during pretreatment. Figure 3 shows the concentrations of glucose, xylose, lactic acid and acetic acid from the beginning to the end of fermentation. Also, the concentration of lactic acid during fermentation with oxalic acid treated corn cob increased from zero at the start of fermentation to 77.34 g/L at the end of the fermentation (48 hr). Glucose and xylose were utilized by *Bacillus coagulans* to produce lactic acid. Acetic acid was present in low amounts, the highest concentration throughout the 48 hours of fermentation was 0.015 g/L. The yield of lactic acid at the end of the fermentation was calculated as 82%.

3.4 Characterization of Lactic Acid

Figure 4 shows the FTIR spectrum of standard lactic acid and produced lactic acid. The spectrum of the lactic acid produced was similar to the spectrum of standard lactic acid. From the spectrum, the stretch between wavenumber 3000 and 3500 cm^{-1} indicates the presence of O-H bond. Furthermore, the stake-shaped bond located between wavenumber 1500 and 2000 cm^{-1} (1718.3 precisely) corresponds to C = O bond. The functional groups observed in the lactic acid produced matches those present in standard lactic acid spectrum as shown in Figure 3. Kelling's test with Iron (III) chloride gave a yellow colouration, indicating the formation of ferric lactate (Sood, 2006). The boiling point of the lactic acid produced was 125 ^{o}C. The specific gravity calculation revealed a value of 1.02. These values (boiling point and specific gravity) are close 122 ^{o}C and 1.12 as reported by Ren (2010).

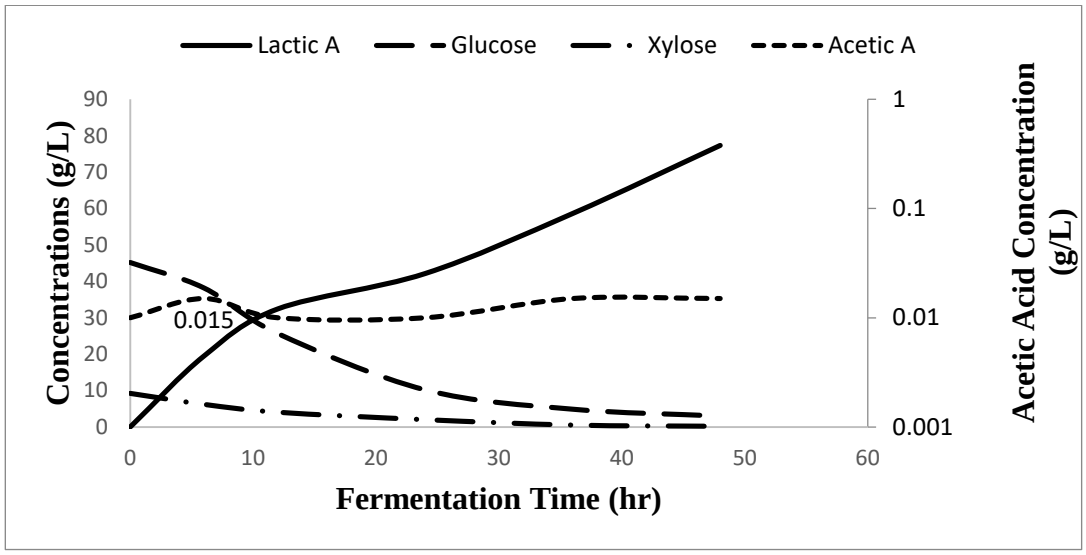

Figure 3: Concentrations of Sugars, Lactic Acid and Acetic Acid during Fermentation

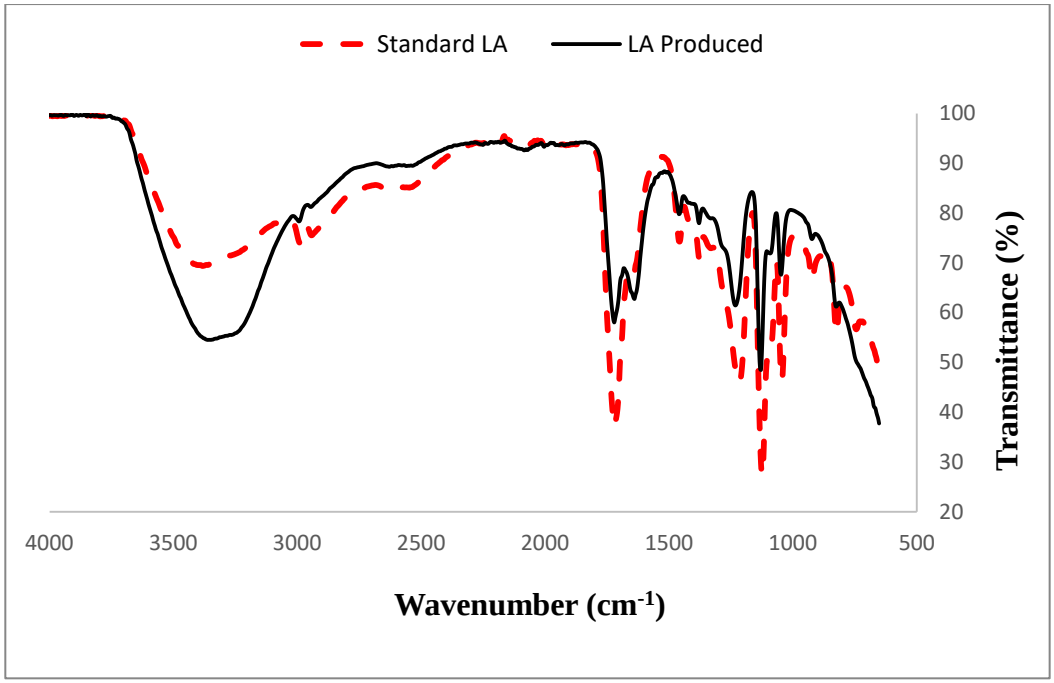

Figure 4: FTIR Spectrum of Lactic Acid Produced

4. CONCLUSION

The use of conventional sulfuric acid for the pretreatment of lignocellulosic biomass leads to corrosion of reaction vessel and production of inhibitory products. In this study, oxalic acid was used to treat corn cob which was subsequently used for the synthesis of lactic acid. The treatment was optimised leading to an optimum time and temperature of 30 min and 25 ^{o}C respectively. The treatment reduced lignin from 16.24% to 9.91% thereby making holocellulose increase from 79.73% to 85.565%. The fermentation with *Bacillus coagulans* produced lactic acid with a yield of 82% which is higher than what was obtained in studies where sulfuric acid pretreatment was carried out. Based on this, it can be concluded that oxalic acid is effective for the pretreatment of corn cob for use as substrate in lactic acid synthesis.

REFERENCES

Afolabi, A. S., Sosu-mobee, O., & Abdulkareem, A. S. (2012). Production of Lactic Acid from Cassava Starch Hydrolysate using Immobilized Lactobacillus Casei in a Fibrous Bed Bioreactor, *III*, 4–7.

Ali, Z., Anjum, F. M., & Zahoor, T. (2009). Production of lactic acid from corn cobs hydrolysate through fermentation by Lactobaccillus delbrukii. *African Journal of Biotechnology*, *8*(17), 4175–4178. https://doi.org/http://dx.doi.org/10.5897/AJB2009.000-9403

Bischoff, K. M., Liu, S., Hughes, S. R., & Rich, J. O. (2010). Fermentation of corn fiber hydrolysate to lactic acid by the moderate thermophile Bacillus coagulans. *Biotechnology Letters*, *32*(6), 823–828. https://doi.org/10.1007/s10529-010-0222-z

Hadar, Y. (n.d.). Sources for Lignocellulosic Raw Materials for the Production of Ethanol. https://doi.org/10.1007/978-3-642-37861-4_2

Harmsen, P. F. H., Huijgen, W., Bermudez, L., & Bakker, R. (2010). Literature review of physical and chemical pretreatment processes for lignocellulosic biomass. *Energy Research Centre of the Netherlands*, (September), 10–13.

Hu, J., Zhenting, Z., Yanxu, L., Shumiao, Z., Yuxia, M., Yunxiang, L. N. P. (2015). High-titer
lactic acid production from NaOH-pretreated corn stover by Bacillus coagulans LA204 using fed-batch simultaneous saccharification and fermentation under non-sterile condition, 182, 251-257.

Kumar, P., Barrett, D. M., Delwiche, M. J., & Stroeve, P. (2009). Methods for pretreatment of lignocellulosic biomass for efficient hydrolysis and biofuel production. *Industrial and Engineering Chemistry Research*, *48*(8), 3713–3729. https://doi.org/10.1021/ie801542g

Lu, Z. H., Peng, H. H., Cao, W., Tatsumi, E., & Li, L. T. (2008). Isolation, characterization and identification of

lactic acid bacteria and yeasts from sour Mifen, a traditional fermented rice noodle from China. *Journal of Applied Microbiology*, *105*(3), 893–903. https://doi.org/10.1111/j.1365-2672.2008.03814.x

Maas, R. H. W., Bakker, R. R., Jansen, M. L. A., Visser, D., & Jong, E. De. (2008). Lactic acid production from lime-treated wheat straw by Bacillus coagulans: neutralization of acid by fed-batch addition of alkaline substrate, 751–758. https://doi.org/10.1007/s00253-008-1361-1

Minmunin, J., Limpitipanich, P., & Promwungkwa, A. (2015). *Delignification of Elephant Grass for Production of Cellulosic Intermediate*. *Energy Procedia* (Vol. 79). Elsevier B.V. https://doi.org/10.1016/j.egypro.2015.11.468

Panda, S. H., & Ray, R. C. (2008). Direct conversion of raw starch to lactic acid by Lactobacillus plantarum MTCC 1407 in semi- solid fermentation using sweet potato (Ipomoea batatas L .) flour. *Industrial Research*, *67*(July), 531–537. Retrieved from http://www.scopus.com/inward/record.url?eid=2-s2.0-55349138790&partnerID=40

Pointner, M., Kuttner, P., Obrlik, T., Jäger, A., & Kahr, H. (2014). Composition of corncobs as a substrate for fermentation of biofuels, *12*(2), 391–396.

Rafael A. Auras, Loong-Tak Lim, Susan E. M. Selke, H. T. (2011). *Poly(lactic acid): Synthesis, Structures, Properties, Processing, and Applications*. *Bio-Based Plastics: Materials and Applications*. https://doi.org/10.1002/9780470649848

Ren, J. (2010). *Biodegradable Poly(Lactic Acid): Synthesis, Modification, Processing and Applications*. https://doi.org/10.1007/978-3-642-17596-1

Sanjay, A., Sinha, K., & Dhanraj, R. R. (2017). Response Surface Optimization of Rice Straw Treatment with Oxalic Acid For Production Of Xylose, Cellulose And Lignin, *9*(2), 163–174.

Sood (2006). Textbook of Medical Laboratory Technology. JaypeeBrothers Publishers. P.444. ISBN 978-81-8061-591-7.

Srivastava, A. K., & Tripathi, A. D. (2014). Production, optimization and characterization of lactic acid by Lactobacillus delbrueckii NCIM 2025 from utilizing agro-industrial byproduct (cane molasses). https://doi.org/10.1007/s13197-014-1423-6

Thongchul, N. (2005). Lactic acid production by immobilized Rhizopus oryzae in a rotating fibrus bed bioreactor, 265.

Wyman, C. E., Dale, B. E., Elander, R. T., Holtzapple, M., Ladisch, M. R., & Lee, Y. Y. (2005). Comparative sugar recovery data from laboratory scale application of leading pretreatment technologies to corn stover. *Bioresource Technology*, *96*(18 SPEC. ISS.), 2026–2032. https://doi.org/10.1016/j.biortech.2005.01.018

Zhang, Z., Xie, Y., He, X., Li, X., Hu, J., & Ruan, Z. (2016). Comparison of high-titer lactic acid fermentation from NaOH- and NH 3 -H 2 O 2 -pretreated corncob by Bacillus coagulans using simultaneous saccharification and fermentation. *Nature Publishing Group*, (April), 1–10. https://doi.org/10.1038/srep37245

Zhao, K., Qiao, Q., Chu, D., Gu, H., Dao, T. H., Zhang, J., & Bao, J. (2013). Bioresource
Technology Simultaneous saccharification and high titer lactic acid fermentation of corn stover using a newly isolated lactic acid bacterium Pediococcus acidilactici DQ2. *Bioresource Technology*, *135*, 481–489. https://doi.org/10.1016/j.biortech.2012.

THIN LAYER MODELLING OF OPEN SUN AND SOLAR DRYING KINETICS OF PULVERIZED MAIZE HUSKS

Agbede, O. O.[1], Ayanniyi, K. J.[1], Oke, E. O.[2], Babatunde, K. A[1], [*]Osuolale, F. N.[1], Ogunleye, O. O.[1] and Agarry, S. E.[1]

1. Department of Chemical Engineering, Ladoke Akintola University of Technology, Ogbomoso,Oyo State, Nigeria.
2. Department of Chemical Engineering, Michael Okpara University of Agriculture, Umudike, Abia State, Nigeria.

* Corresponding author: fnosuolale@lautech.edu.ng

ABSTRACT

The open sun and solar drying of maize husks were investigated. Husks obtained from freshly harvested maize were cut into pieces, pulverized and 5 – 20 mm deep beds of husks were dried in open sun and solar dryer. The drying data were fitted to twelve thin layer drying models. The drying time increased with increasing depth of husks for both open sun and solar drying. The solar drying was faster than open sun drying, however, both took place in the falling rate period. The effective moisture diffusivities for open sun dying were 1.65 x 10^{-9} - 9.39 x 10^{-9} m^2 s^{-1} while those for solar drying were 2.83 x 10^{-9} – 2.20 x 10^{-8} m^2 s^{-1} for bed depths of 5 - 20 mm. The Wang and Singh model best fitted the sun drying data, whereas it only fitted the solar drying data for the 15 and 20 mm samples. The time required for drying pulverized maize husks, by radiation from the sun, can be essentially shortened by using thinner layer of husks and drying in a solar dryer rather than in open sun. The data provided by this study can aid the design of solar dryers for agriculture residues.

Keywords: Maize husks, open sun drying, solar drying, effective moisture diffusivity, thin layer drying model

INTRODUCTION

Agricultural residues are biomass, a renewable source of energy which is easily replenished and environmentally benign (Saxena *et al.*, 2009; Ellabban *et al.*, 2014; Singh *et al.*, 2014). They can be converted to biofuels or bioenergy through physicochemical, biochemical and thermochemical processes (Kumar *et al*., 2009; Kumar *et al*., 2015).

Zea mays, maize or corn is an agricultural produce that is consumed globally as staple food, it is also processed into other forms of food as well as drink, animal feed and fuel (Eckhoff and Paulsen, 1996; Shiferaw *et al.*, 2011; Ranum *et al.*, 2014; Eckert *et al.*, 2018). Huge quantities of residues including husks usually remain after the harvest of maize which can be converted to biofuel and bioenergy by the thermochemical processes of pyrolysis, gasification and combustion (Nelson *et al.*, 2004; Schwietzke *et al.*, 2009; Scarlat *et al.*, 2010; Gregg and Smith, 2010; Zhang *et al.*, 2010; Görgens *et al.*, 2014; Okello *et al.*, 2013; Bentsen *et al.*, 2014; Hiloidhari *et al*., 2014). However, the efficiency of these thermochemical processes requires the removal of the large quantity of moisture that is usually present in the residues of freshly harvested agricultural produce (Bennion *et al*., 2015; Azizi, 2018).

Drying is a preservation method usually employed to reduce the moisture content of agricultural products and consequently decrease microbial and enzyme activities, thus enhancing product shelf-life and decreasing the packing and transportation cost (Mujumdar and Law 2010; Guine *et al*., 2012). Open sun drying or drying in direct sunlight is the traditional method of drying agricultural products, whereby the materials are simply spread outside or in the open to be dried by the sun radiation. Open sun drying is extremely weather dependent, takes a long time and materials are prone to contamination with dust, insect, etc. On the other hand, solar drying employs a solar dryer, an equipment which protects the material from direct exposure to rainfall, dust, insects, etc., but still uses energy from sun radiation to dry the material in a chamber heated up directly or indirectly by the sun radiation. The drying of several agricultural products including fruits, vegetables and staple foods have been reported in the literature (Davishi, 2017; Doymaz, 2010; Erbay and Icier, 2010; Ojediran and Raji, 2010; Rajkumar *et al*., 2007) but little has been reported on the drying of agricultural residues or agro-waste biomass for production of biofuel and

bioenergy.

Drying involves simultaneous coupled heat and mass transfer (Diamante *et al*., 2010), it is a complex process which requires effective mathematical models for process design, optimization and control as well as energy integration. The mathematical models employed for modelling drying processes can be either distributed or lumped parameter models. The distributed parameter models consider internal and external heat and mas transfer and predict temperature and moisture gradient whereas the lumped parameter models assume a uniform temperature distribution in the product which is the drying air temperature (Erbay and Filiz, 2010). For a uniform temperature to be correctly assumed for a lumped parameter model, the material must be dried as one layer of sample particles or slices, so that the material has a thin structure; this is generally known as thin layer drying (Akpinar, 2006a; Erbay and Filiz, 2010). The size, thickness or depth of the thin layer affects the rate of drying of the material (Ertekin and Yaldiz, 2004, Limpaiboon, 2011). Thin layer drying models are easy to use and require less data compared to complex distributed models, so they have been frequently applied in the study of the drying of foods, fruits and vegetables (Toğrul and Pehlivan, 2004; Akpinar and Bicer, 2008; Doymaz, 2010; Ojediran and Raji, 2010; Doymaz and Ismail, 2011; Tunde-Akintunde, 2011). They are useful for estimating drying times and so essential to the development and operation of drying processes (Akpinar and Bicer, 2008). Hence, this study investigated the thin layer modelling of open sun and solar drying of pulverized maize husks.

MATERIALS AND METHODS

2.1 Sample Collection and Preparation

Maize husks were obtained from freshly harvested maize collected from a farmland in Ogbomoso, Nigeria. The husks were cut into small pieces and then pulverized in a kitchen blender to increase the surface area of the material, prior to the drying operation.

2.2. Drying Equipment

A triangular prism-shaped natural convection direct solar dryer was used for the solar drying experiments. The drying chamber of the solar dryer has a height of 0.67 m while its rectangular base on which drying pans were placed has a dimension of 1.2 by 0.7 m. A schematic of the solar dryer is shown in Figure 1. A Citizen digital weighing balance which has an accuracy of 0.001 g was utilized for weighing the pulverized maize husks samples.

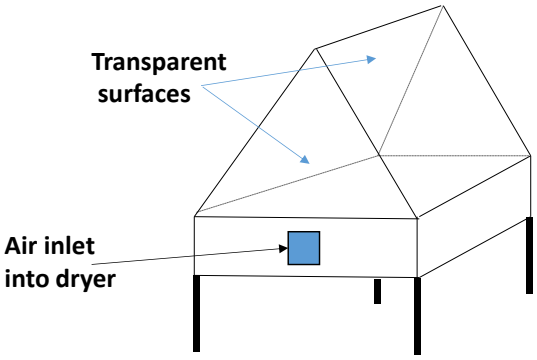

Figure 1: Schematic of a direct solar dryer

2.3 Experimental Procedure

The pulverized maize husk samples were spread in pre-weighed aluminium pans, of dimension 75 by 75 mm, which had been calibrated to depths of 5, 10, 15 and 20 mm for all the drying experiments. The initial mass of the pulverized maize husks in each of the pans was determined. A set of drying pans consisting of pulverized maize husks of depths 5, 10, 15 and 20 mm was placed in the solar dryer and at the same time, another set was placed in open sun or direct sunlight. The mass of the samples were measured at 30 min interval until constant mass was achieved (Akpinar, 2006b). The drying experiments were performed in triplicates, in the month of October, 2018 between 10 am and 6 pm. The total drying time was the period between the placement of drying pans, containing the samples, in open sun or solar dryer and the point when constant mass was observed. The ambient and solar dryer temperatures were monitored.

2.3 Determination of Drying Rate and Effective Moisture Diffusivity

The moisture content of the maize husks at time, t, X_t (g water. g dry matter^{-1}) was defined as:

$$X_t = \frac{m_t - m_d}{m_d} \quad (1)$$

where m_t (g) and m_d (g) are mass of sample at any time t and absolute dried mass of sample, respectively. The drying rate of the husks was computed from Equation (2):

$$D_R = \frac{X_{t+dt} - X_t}{dt} \quad (2)$$

where D_R (g water/g dry matter. min) is drying rate, X_{t+dt} (g water. g dry matter^{-1}) is moisture content at time $t+dt$ and dt (min) is time increment. The

moisture content can be expressed as dimensionless moisture ratio (M_R):

$$M_R = \frac{X_t - X_e}{X_i - X_e} \quad (3)$$

where X_i and X_e (g water/g dry matter) are initial and equilibrium moisture contents, respectively. For a long drying time the values of X_e are small compared with X_t and X_i , the moisture ratio may be simplified (Dissa *et al*., 2011; Perea-Flores *et al*., 2012):

$$M_R = \frac{X_t}{X_i} \quad (4)$$

The diffusion of moisture from the internal part of the maize husks to the surface during the falling rate drying period, when internal mass transfer is the controlling mechanism, may be described by Fick's second law of diffusion (Doymaz, 2008; Ruiz Celma *et al.*, 2008). The Fick's law in terms of M_R is expressed as (Vega-Galvez *et al.*, 2010):

$$\frac{dM_R}{dt} = D_{eff}\frac{d^2M_R}{dx^2} \quad (5)$$

where D_{eff} ($m^2 s^{-1}$) is the effective moisture diffusivity and x (m) is spatial dimension. The bed of maize husks in the drying pan had a slab geometry. Assuming a one dimensional transport of moisture in an infinite slab, negligible shrinkage, uniform initial moisture distribution, negligible external resistant and constant diffusivity; the mathematical solution of Equation (5) according to Crank (1975) is:

$$M_R = \frac{8}{\pi^2}\sum_{i=0}^{\infty}\frac{1}{(2i+1)^2}\exp\left[\frac{-(2i+1)^2 D_{eff}\pi^2 t}{4L^2}\right] \quad (6)$$

The first term in the series expansion of Equation (6) gives a good estimate of the solution for sufficiently long drying time (Di Scala and Crapiste, 2008):

$$M_R = \frac{8}{\pi^2}\exp\left[\frac{-D_{eff}\pi^2 t}{4L^2}\right] \quad (7)$$

where L (m) is half of the thickness of the slab and t (s) the time of drying. Equation (7) can be written in a linear form as:

$$In(M_R) = In\left(\frac{8}{\pi^2}\right) - \left(\frac{D_{eff}\pi^2 t}{4L^2}\right) \quad (8)$$

A plot of $In(M_R)$ versus t yields a straight line with slope (S_1) from which D_{eff} is calculated:

$$S_1 = \frac{D_{eff}\pi^2}{4L^2} \quad (9)$$

2.4. Thin Layer Modelling of Drying Kinetics

The moisture ratio-drying time data for both open sun and solar drying of pulverized maize husks were fitted to the twelve thin layer drying mathematical models shown in Table 1. These models have been identified as the most frequently suitable models by researchers for various products (Kucuk *et al*., 2014). They are Midilli-Kucuk, Page, Logarithmic, Two-term, Wang and Singh, Approximation of diffusion, Modified Henderson and Pabis, Modified Page, Henderson and Pabis, two-term exponential, Verma *et al*. and Weibull models.

Table 1: Thin layer drying models fitted to drying data

S/No	Model Name	Model	References
1	Midilli-Kucuk	$M_R = a\exp(-kt^n) + bt$	Midilli *et al.*, 2002
2	Page	$M_R = \exp(-kt^n)$	Page, 1949
3	Logarithmic	$M_R = a\exp(-kt) + c$	Chandra and Singh, 1995; Yagcioglu *et al*., 1999
4	Two-term	$M_R = a\exp(-k_0 t) + b\exp(-k_1 t)$	Henderson, 1974; Glenn, 1978
5	Wang and Singh	$M_R = 1 + at + bt^2$	Wang and Singh, 1978
6	Approximation of diffusion	$M_R = a\exp(-kt) + (1-a)\exp(-kbt)$	Kaseem, 1998

S/No	Model Name	Model	References
7	Modified Henderson and Pabis	$M_R = a\exp(-kt) + b\exp(-gt) + c\exp(-ht)$	Karathanos, 1999
8	Modified Page	$M_R = \exp(-(kt)^n)$	White *et al*., 1978
9	Henderson and Pabis	$M_R = a\exp(-kt)$	Henderson and Pabis, 1961
10	Two-term exponential	$M_R = a\exp(-kt) + (1-a)\exp(-kat)$	Sharaf-Eldeen *et al*., 1980
11	Verma et al.	$M_R = a\exp(-kt) + (1-a)\exp(-gt)$	Verma *et al*., 1985
12	Weibull	$M_R = a - b\exp(-kt^n)$	Weibull, 1951; Yi *et al.*, 2012

Non-linear regression analysis was employed to fit experimental data of moisture ratio (MR) versus drying time (t) to the thin layer drying models. Statistical Package for the Social Sciences (SPSS) version 20 (SPSS Inc., Chicago, Illinois), was the software used for the regression analysis. The coefficient of determination (R^2), sum of square error (SSE), root mean square error (RMSE) and Chi-square (χ^2) were the statistical parameter used as criteria to determine the model that best fit the moisture ratio – time data. The model that has the highest value of R^2 and lowest values of SSE, RMSE and χ^2 is the one that best fit the experimental drying data (Erbay and Icier, 2010; Kucuk *et al.*, 2014). The R^2 values were computed by SPSS while SSE, RMSE and χ^2 were calculated from equations 11, 12 and 13, respectively, using Microsoft Excel 2013.

$$R^2 = 1 - \left[\frac{\sum_{i=1}^{N} \left(M_{R_{\exp,i}} - M_{R_{pred,i}} \right)^2}{\sum_{i=1}^{N} \left(M_{R_{\exp,i}} - \bar{M}_R \right)^2} \right] \quad (10)$$

where $\bar{M}_R = \frac{1}{N} \sum_{i=1}^{N} M_{R_{\exp,i}}$

$$SSE = \frac{1}{N} \sum_{i=1}^{N} \left(M_{R_{\exp,i}} - M_{R_{pred,i}} \right)^2 \quad (11)$$

$$RMSE = \left[\frac{1}{N} \sum_{i=1}^{N} \left(M_{R_{pred,i}} - M_{R_{\exp,i}} \right)^2 \right]^{\frac{1}{2}} \quad (12)$$

$$\chi^2 = \frac{\sum_{i=1}^{N} \left(M_{R_{\exp,i}} - M_{R_{pred,i}} \right)^2}{N - z} \quad (13)$$

where $M_{R_{\exp,i}}$, $M_{R_{pred,i}}$, N and z are experimental moisture ratio, predicted moisture ratio, number of observations and number of constants, respectively.

RESULTS AND DISCUSSION

3.1 Open Sun Drying of Pulverized Maize Husks

The plot of moisture ratio versus drying time for open sun drying of pulverized maize husks of 5, 10, 15 and 20 mm depth is shown in Figure 2. The moisture ratio decreased progressively with time during the open sun drying of all samples of the pulverized maize husks of depths 5 – 20 mm considered, indicating that moisture was successfully removed from the maize husks by air heated through the sun radiation. As expected the drying time increased with increasing depth of maize husks in the pans, since the initial mass and moisture content of maize husks in the pans increased with increasing depth of husks in the pans. The drying time required for the 5, 10, 15 and 20 mm deep samples were 180, 240, 330 and 390 min, respectively. The moisture diffusion path increased with increasing depth of maize husks, so moisture was removed faster through thinner bed depths (Falade and Solademi, 2010; Doymaz and Özdemir, 2013). Hence, the drying time can be effectively reduced by decreasing the depth or thickness of the maize husks bed. A reduction in drying time of agricultural produce with decreasing bed depth or material thickness has been reported in the literature (Ertekin and Yaldiz, 2004, Limpaiboon, 2011).

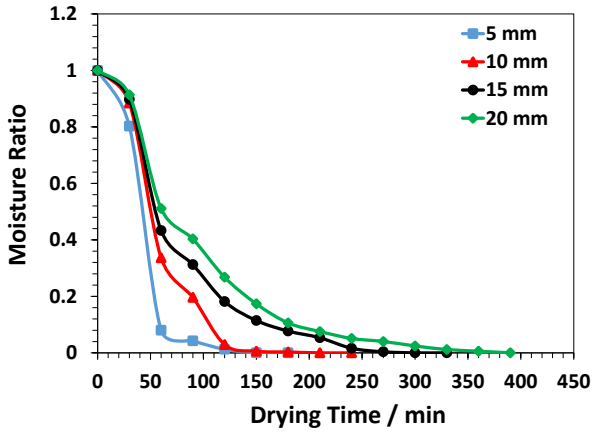

Figure 2: Plot of moisture ratio versus drying time for open sun drying of pulverized maize husks of 5, 10, 15 and 20 mm depth

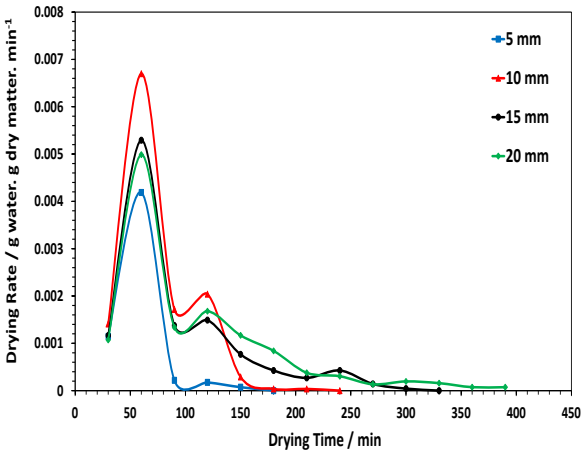

Figure 3: Plot of drying rate versus drying time for open sun drying of pulverized maize husks of 5, 10, 15 and 20 mm depth

The plot of drying rate versus drying time for open sun drying of pulverized maize husks of 5, 10, 15 and 20 mm depth is shown in Figure 3. The drying rate of each of the samples initially increased briefly, then largely decreased with drying time. There was no constant drying rate period, the drying took place mainly in the falling rate period. This means that the open sun drying of pulverized maize husks was controlled by the diffusion of moisture from the inner part of the maize husks bed to the outer surface (Doymaz, 2008; Ruiz Celma et al., 2008). A falling rate period has been reported for the open sun drying of basil, mint and parsley leaves (Akpinar, 2006b). The effective moisture diffusivity for open sun drying of maize husks of depths 5 – 20 mm is shown in Table 2. The effective moisture diffusivities of 1.65 x 10^{-9}, 6.01 x 10^{-9}, 7.18 x 10^{-9} and 9.39 x 10^{-9} were measured for bed depths of 5, 10, 15 and 20 mm, respectively. These values are within the range 10^{-12} – 10^{-6} m^2 s^{-1} previously reported for the drying of agricultural products (Erbay and Icier, 2010). The measured effective moisture diffusivity increased with increasing bed depth, this may be due to the rise in moisture activity associated with the increase in initial moisture of maize husks with increasing bed depth (Sadin *et al.*, 2013). An increase in effective moisture diffusivity with increasing thickness of material has been reported in the literature (Göğüş and Maskan, 2006; Falade and Solademi, 2010; Sadin *et al.*, 2013).

Table 2: Effective moisture diffusivity for open sun drying of pulverized maize husks

Depth (mm)	D_{eff} (m^2 s^{-1})
5	1.65 x 10^{-9}
10	6.01 x 10^{-9}
15	7.18 x 10^{-9}
20	9.39 x 10^{-9}

The statistical parameters obtained after the twelve thin layer models were fitted to the open sun drying data are shown in Tables 1 – 4. The Wang and Singh model best fitted the drying moisture ratio – time data for all the drying operations. This model had the highest R^2 and lowest SSE, RMSE and χ^2 compared to those of the other eleven models. The R^2, SSE, RMSE and χ^2 for open sun drying of pulverized maize husks of 5 mm depth were 0.996, 0.0111, 0.1052, and 0.0128, respectively. Similar high values of R^2 (>0.996) and low values of SSE (<0.02), RMSE (<0.15) and χ^2 (<0.025) were observed for the 10, 15 and 20 mm depth samples. The Wang and Singh model has also been reported to best fit the open sun drying of mint and parsley leaves (Akpinar, 2010; Akpinar, 2011).

Table 3: Statistical parameters for thin layer drying models for sun drying of 5 mm deep maize husks

Model	R^2	SSE	RMSE	χ^2
Wang and Singh	0.996	0.0111	0.1052	0.0128
Page	0.991	0.0435	0.2085	0.0502
Modified Page	0.991	0.0435	0.2085	0.0502
Verma *et al*.	0.986	0.0435	0.2085	0.0544
Approximation of diffusion	0.945	0.0435	0.2085	0.0544
Two-term exponential	0.945	0.0435	0.2085	0.0502
Logarithmic	0.547	0.0859	0.2931	0.1074
Weibull	0.547	0.0859	0.2931	0.1171
Midilli-Kucuk	0.428	0.0887	0.2978	0.1209
Two-term	0.415	0.0890	0.2983	0.1213
Modified Henderson and Pabis	0.415	0.0890	0.2983	0.1483
Henderson and Pabis	0.415	0.0890	0.2983	0.1027

Table 4: Statistical parameters for thin layer drying models for sun drying of 10 mm deep maize husks

Model	R^2	SSE	RMSE	χ^2
Wang and Singh	0.997	0.0093	0.0965	0.0107
Page	0.996	0.0624	0.2498	0.0720
Modified Page	0.996	0.0624	0.2498	0.0720
Verma *et al.*	0.996	0.0624	0.2498	0.0780
Approximation of diffusion	0.979	0.0624	0.2498	0.0780
Two-term exponential	0.979	0.0624	0.2498	0.0720
Logarithmic	0.470	0.0785	0.2801	0.0981
Weibull	0.470	0.0785	0.2801	0.1070
Midilli-Kucuk	0.281	0.0891	0.2985	0.1215
Two-term	0.260	0.0892	0.2986	0.1216
Modified Henderson and Pabis	0.260	0.0892	0.2986	0.1486
Henderson and Pabis	0.260	0.0891	0.2985	0.1028

Table 5: Statistical parameters for thin layer drying models for sun drying of 15 mm deep maize husks

Model	R^2	SSE	RMSE	χ^2
Wang and Singh	0.999	0.0128	0.1132	0.0148
Page	0.976	0.0765	0.2765	0.0882
Modified Page	0.976	0.0765	0.2765	0.0882
Henderson and Pabis	0.967	0.0643	0.2536	0.0742
Verma *et al.*	0.963	0.0765	0.2765	0.0956
Approximation of diffusion	0.893	0.0765	0.2765	0.0956
Two-term exponential	0.893	0.0765	0.2765	0.0882
Logarithmic	0.445	0.0903	0.3005	0.1129
Weibull	0.445	0.0903	0.3005	0.1231
Midilli-Kucuk	0.188	0.1053	0.3245	0.1436

Model	R^2	SSE	RMSE	χ^2
Two-term	0.151	0.1053	0.3245	0.1436
Modified Henderson and Pabis	0.151	0.1053	0.3245	0.1756

Table 6: Statistical parameters for thin layer drying models for sun drying of 20 mm deep maize husk

Model	R^2	SSE	RMSE	χ^2
Wang and Singh	0.998	0.0191	0.1382	0.0220
Page	0.974	0.0922	0.3036	0.1064
Modified Page	0.974	0.0922	0.3036	0.1064
Verma *et al.*	0.955	0.0922	0.3036	0.1152
Approximation of diffusion	0.866	0.0922	0.3036	0.1152
Two-term exponential	0.866	0.0922	0.3036	0.1064
Logarithmic	0.407	0.0977	0.3126	0.1221
Weibull	0.407	0.0977	0.3126	0.1332
Midilli-Kucuk	0.102	0.1185	0.3442	0.1616
Two-term	0.056	0.1185	0.3442	0.1616
Modified Henderson and Pabis	0.056	0.1185	0.3442	0.1975
Henderson and Pabis	0.056	0.1185	0.3442	0.1367

3.2 Solar Drying of Pulverized Maize Husks

The plot of moisture ratio versus drying time for solar drying of pulverized maize husks of 5, 10, 15 and 20 mm depth is shown in Figure 4. The moisture ratio decreased progressively with time during the solar drying of all samples of the pulverized maize husks of depths 5 – 20 mm investigated. This implies that moisture was also successfully removed from the pulverized maize husks by hot air within the solar dryer chamber.

Similar to the open sun drying, the drying time increased with increasing depth of maize husks in the pans because the initial mass and moisture content of the husks in the pans as well as the diffusion path increased with increasing depth of husks. The time required for drying of the 5, 10, 15 and 20 mm deep samples were 100, 120, 180 and 210 min, respectively; these drying times are shorter than those required for open sun drying of maize husks of similar depth. It was observed that the temperature in the solar drying chamber increased to about 31 – 51 ^{o}C (depending on the time of the day) compared to the ambient temperature of 30 - 39 ^{o}C, during the drying process, which consequently increased the thermal energy available for the removal of moisture from the maize husks. This resulted into a higher drying rate in the solar dryer compared to the open sun and consequently a shorter drying time in the solar dryer. Hence, the time required for drying pulverized maize husks, by radiation from the sun, can be essentially shorten by reducing the husks bed depth and by drying the material in a solar dryer rather than in open sun.

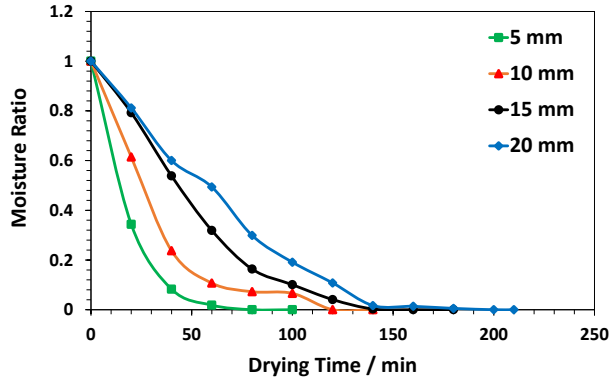

Figure 4: Plot of moisture ratio versus drying time for solar drying of pulverized maize husks of 5, 10, 15 and 20 mm depth

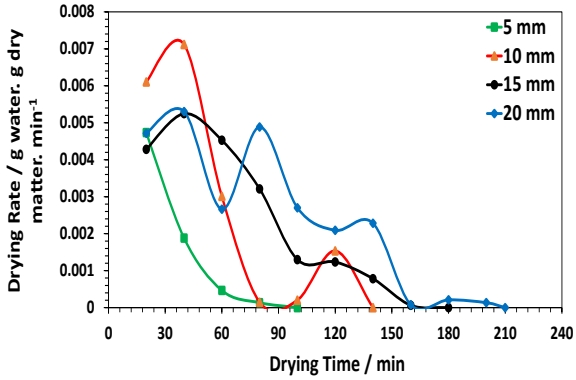

Figure 5: Plot of drying rate versus drying time for solar drying of pulverized maize husks of 5, 10, 15 and 20 mm depth

The plot of drying rate versus drying time for solar drying of pulverized maize husks of 5, 10, 15 and 20 mm depth is shown in Figure 5. The drying rate decreased with increasing drying time, no constant rate period was observed, the drying occurred entirely in the falling rate period. This implies that the solar drying of pulverized maize husks was also controlled by the diffusion of moisture from the inner part of the maize husk bed to the outer surface (Doymaz, 2008; Ruiz Celma et al., 2008). A falling rate period has also been reported for the solar drying of mint leaves and long green pepper (Akpinar, 2010; Akpinar and Bicer, 2008).

The effective moisture diffusivity for the solar drying of pulverized maize husks of 5, 10, 15 and 20 mm depth are presented in Table 7. The effective moisture diffusivities were 2.83 x 10^{-9}, 4.61 x 10^{-9}, 1.38 x 10^{-8} and 2.02 x 10^{-8} m^2 s^{-1} for the 5, 10, 15 and 20 mm deep husks beds, respectively. The moisture diffusivity also increased with increasing bed depth due to the rise in moisture activity associated with the increase in initial moisture of maize husks with increasing bed depth at (Sadin et al., 2013). The effective moisture diffusivities of 2.83 x 10^{-9} – 2.20 x 10^{-8} m^2 s^{-1} measured for the solar drying of pulverized maize husks, in this study, are also within the range of 10^{-12} – 10^{-6} m^2 s^{-1} previously reported for the drying of agricultural products (Erbay and Icier, 2010).

Table 7: Effective moisture diffusivity for solar drying of pulverized maize husks

Depth (mm)	D_{eff} (m^2 s^{-1})
5	2.83 x 10^{-9}
10	4.61 x 10^{-9}
15	1.38 x 10^{-8}
20	2.02 x 10^{-8}

The statistical parameters obtained after the twelve thin layer models were fitted to the solar drying data are shown in Tables 5 – 8. The R^2, SSE, RMSE and χ^2 for Wang and Singh model for the 5 mm deep pulverized maize husks sample were 0.998, 0.7317, 0.8554 and 0.8443, respectively; the corresponding values for the 10 mm deep sample were 0.997, 0.8473, 0.9205, and 0.9776, respectively. The Page and modified Page models had the lowest values of SSE (0.0083), RMSE (0.0914) and χ^2 (0.0096) compared to the other eleven models and R^2 value of 0.973, for the 5 mm deep sample whereas the Page model had the lowest values of SSE (0.0148), RMSE (0.1215) and χ^2 (0.0170) compared to the other eleven models and R^2 value of 0.985, for the 10 mm deep sample. Although the Wang and Sing model had the highest values of R^2, for the 5 and 10 mm deep samples, this same model also had the highest values of SSE, RMSE and χ^2, compared to the other eleven models.

Alternatively, the statistical parameters for the thin layer drying models fitted to the drying data for 15 and 20 mm deep samples of the pulverized maize husks, detailed in Table 7 and Table 8 show that the Wang and Singh model had high values of R^2 (>0.993) and lowest values of SSE (<0.011), RMSE (<0.15) and χ^2 (<0.012) compared to the other eleven models. The Weibull model had a slightly higher R^2 value of 0.999 compared to 0.996 for the Wang and Singh model but its SSE (0.4761), RMSE (0.6900) and χ^2 (0.6493) values were very high compared to those of Wang and Singh model, for the 15 mm sample. Similarly, the Midilli-Kucuk model had a slightly higher R^2 value of 0.995 compared to 0.994 for the Wang and Singh model but its SSE (0.4776), RMSE (0.6911) and χ^2 (0.6513) values are also much higher compared to those of Wang and Singh model, for the 20 mm sample. Hence, the Wang and

Singh model is considered to suitably describe the solar drying data for the 15 and 20 mm deep samples due to the high values of R^2 (>0.993) coupled with the lowest values of SSE (<0.011), RMSE (<0.15) and χ^2 (<0.012) compared to the other models. The Wang and Singh model has also been reported to best fit the solar drying of mint leaves (Akpinar, 2010) and parsley leaves (Akpinar, 2011).

Table 8: Statistical parameters for thin layer drying models for solar drying of 5 mm deep maize husks

Model	R^2	SSE	RMSE	χ^2
Wang and Singh	0.998	0.7317	0.8554	0.8443
Logarithmic	0.995	0.0565	0.2377	0.0706
Page	0.973	0.0083	0.0914	0.0096
Modified Page	0.973	0.0083	0.0914	0.0096
Verma *et al.*	0.964	0.0083	0.0914	0.0104
Modified Henderson and Pabis	0.924	0.0572	0.2392	0.0953
Approximation of diffusion	0.913	0.0083	0.0914	0.0104
Two-term exponential	0.913	0.0083	0.0914	0.0096
Weibull	0.890	0.0565	0.2377	0.0770
Midilli-Kucuk	0.846	0.0571	0.2389	0.0779
Two-term	0.839	0.0572	0.2392	0.0779
Henderson and Pabis	0.839	0.0572	0.2392	0.0660

Table 9: Statistical parameters for thin layer drying models for solar drying of 10 mm deep maize husks

Model	R^2	SSE	RMSE	χ^2
Wang and Singh	0.997	0.8473	0.9205	0.9776
Page	0.985	0.0148	0.1215	0.0170
Modified Page	0.985	0.0360	0.1896	0.0415
Verma *et al.*	0.974	0.0360	0.1897	0.0445
Approximation of diffusion	0.906	0.0360	0.1897	0.0445
Two-term exponential	0.906	0.0360	0.1897	0.0415
Logarithmic	0.646	0.0547	0.2339	0.0684
Weibull	0.646	0.0547	0.2339	0.0746
Midilli-Kucuk	0.458	0.0631	0.2512	0.0861
Two-term	0.417	0.0631	0.2512	0.0861
Modified Henderson and Pabis	0.417	0.0631	0.2510	0.1050
Henderson and Pabis	0.417	0.0631	0.2512	0.0728

Table 10: Statistical parameters for thin layer drying models for solar drying of 15 mm deep maize husks

Model	R^2	SSE	RMSE	χ^2
Weibull	0.999	0.4761	0.6900	0.6493
Wang and Singh	0.996	0.0101	0.1003	0.0112
Page	0.989	0.0706	0.2656	0.0814
Modified Page	0.989	0.0249	0.1578	0.0287
Verma *et al.*	0.963	0.0765	0.2765	0.0956
Approximation of	0.896	0.0706	0.2656	0.0882

Model	R^2	SSE	RMSE	χ^2
diffusion				
Two-term exponential	0.896	0.0706	0.2656	0.0814
Logarithmic	0.466	0.0749	0.2737	0.0936
Midilli-Kucuk	0.159	7589.7366	87.1134	10348.2771
Two-term	0.106	0.0936	0.3060	0.1277
Modified Henderson and Pabis	0.106	0.0935	0.3057	0.1558
Henderson and Pabis	0.106	0.0935	0.3058	0.1079

Table 11: Statistical parameters for thin layer drying models for solar drying of 20 mm deep maize husks

Model	R^2	SSE	RMSE	χ^2
Midilli-Kucuk	0.995	0.4776	0.6911	0.6513
Wang and Singh	0.994	0.0098	0.0991	0.0113
Page	0.993	0.0968	0.3112	0.1117
Modified Page	0.993	0.0968	0.3112	0.1117
Verma *et al*.	0.978	0.0968	0.3112	0.1210
Two-term	0.913	0.1134	0.3367	0.1546
Modified Henderson and Pabis	0.913	0.1134	0.3368	0.1890
Henderson and Pabis	0.913	0.1134	0.3368	0.1309
Approximation of diffusion	0.881	0.0968	0.3112	0.1210
Two-term exponential	0.881	0.0968	0.3112	0.1117
Logarithmic	0.393	0.0817	0.2858	0.1021
Weibull	0.393	0.0817	0.2858	0.1114

CONCLUSION

Maize husks were successfully dried in open sun and solar dryer. The drying time increased with increasing depth of pulverized maize husks for both sun and solar drying. The pulverized maize husks dried faster in the solar dryer than open sun. The open sun and solar drying of pulverized maize husks took place in the falling rate period and were controlled by the diffusion of moisture from the inner part of the husks bed to the outer surface. The effective moisture diffusivities for open sun dying were 1.65×10^{-9} - 9.39×10^{-9} $m^2 s^{-1}$ while those for solar drying were 2.83×10^{-9} – 2.20×10^{-8} $m^2 s^{-1}$ for bed depths of 5 - 20 mm. The time required for drying pulverized maize husks, by radiation from the sun, can be essentially shorten by reducing the husks bed depth and by drying the material in a solar dryer rather than in open sun. The Wang and Singh model best fitted the open sun drying data for all sample depths (5 – 20 mm) considered with highest values of R^2 (>0.993) and lowest values of SSE (<0.02), RMSE (<0.15) and χ^2 (<0.025), compared to the other eleven thin layer drying models. However, the Wang and Singh model only suitably described the solar drying data for the 15 and 20 mm deep samples. The data provided by this study are useful for the design of solar dryers for agriculture residues.

REFERENCES

Akpinar, E. K. (2006). Determination of suitable thin layer drying curve model for some vegetables and fruits. *Journal of Food Engineering*, 73, 75–84.

Akpinar, E. K. (2006). Mathematical modelling of thin layer drying process under open sun of some aromatic plants. *Journal of Food Engineering*, 77, 864–870.

Akpinar, E. K. (2010). Drying of mint leaves in a solar dryer and under open sun: Modelling, performance analyses. *Energy Conversion and Management*, 51, 2407–2418

Akpinar, E. K. (2011). Drying of parsley leaves in a solar dryer and under open sun: modeling, energy and exergy aspects. *Journal of Food Process Engineering*, 34, 27–48.

Akpinar, E. K. and Bicer, Y. (2008). Mathematical modelling of thin layer drying process of long green pepper in solar dryer and under open sun. *Energy Conversion and Management* 49, 1367–1375.

Azizi, K., Moravejia, M. K., and Najafabadi, H. A. (2018). A review on bio-fuel production from microalgal biomass by using pyrolysis Method. *Renewable and Sustainable Energy Reviews*, 83 (3), 3046-3059.

Bennion, E. P., Ginosar, D. M., Moses, J., Agblevor, F., and Quinn, J. C. (2015). Lifecycle assessment of microalgae to biofuel: comparison of thermochemical processing pathways. *Applied Energy*, 154, 1062–71.

Bentsen, N. S., Felby, C. and Thorsen, B. J. (2014). Agricultural residue production and potentials for energy and materials services. *Progress in Energy and Combustion Science*, 40, 59–73.

Chandra, P. K. and Singh, R. P. (1995). Applied Numerical Methods for Food and Agricultural Engineers, CRC Press, Boca Raton, FL.

Crank, J. (1975). The Mathematics of Diffusion, second ed. Oxford University Press, London.

Davishi, H. (2017). Quality, Performance Analysis, Mass Transfer Parameters and Modeling of Drying Kinetics of Soybean. *Brazilian Journal of Chemical Engineering*, 34 (1), 143 – 158.

Demirbas, A., Kabli, M., Alamoudi, R.H., Ahmad, W and Basahel, A. (2017). Renewable energy resource facilities in the Kingdom of Saudi Arabia: Prospects, social and political challenges. *Energy Sources, Part B: Economics, Planning, And Policy* 12 (1) 1, 8–16.

Diamante L. M., Ihns, R., Savage G. P., and Vanhanen, L. (2010). A new mathematical model for thin layer drying of fruits. *International Journal of Food Science and Technology,* 45 (9), 1956–1962.

Di Scala, K. and Crapiste, G. (2008). Drying kinetics and quality changes during drying of red pepper. *LWT – Food Science and Technology,* 41 (5), 789–795.

Dissa, A.O., Bathiebo, D.J., Desmorieux, H., Coulibaly, O. and Koulidiati, J. (2011). Experimental characterization and modelling of thin layer direct solar drying of Amelia and Brooks mangoes. *Energy*, 36, 2517–2527.

Doymaz, İ. (2008). Influence of blanching and slice thickness on drying characteristics of leek slices. *Chemical Engineering and Processing: Process Intensification*, 47(1), 41–47.

Doymaz, I. (2010). Evaluation of Mathematical Models for Prediction of Thin-Layer Drying of Banana Slices. *International Journal of Food Properties*, 13(3), 486–497.

Doymaz, I. and Ismail, O (2011). Drying characteristics of sweet cherry. *Food and Bioproducts Processing* 89, 31–38.

Doymaz, İ. and Özdemir, Ö. (2013). Effect of air temperature, slice thickness and pretreatment on drying and rehydration of tomato. *International Journal of Food Science & Technology,* 49(2), 558–564.

Eckert, C. T., Frigo, E. P., Albrecht, L. P., Albrecht, A. J. P., Christ, D., Santos, W. G., Berkembrock, E and Egewarth, V. A. (2018). Maize ethanol production in Brazil: Characteristics and perspectives. *Renewable and Sustainable Energy Reviews*, 82, 3907–3912.

Eckhoff, S.R. and Paulsen, M.R. (1996). Maize. In: Henry R.J., Kettlewell, P.S. (Eds.) Cereal Grain Quality. Springer, Dordrecht.

Ellabban, O., Abu-Rub, H. and Blaabjerg, F. (2014). Renewable energy resources: Current status, future prospects and their enabling technology. *Renewable and Sustainable Energy Reviews* 39, 748–764.

Erbay, Z. and Icier, F. (2010) A Review of Thin Layer Drying of Foods: Theory, Modeling, and Experimental Results. *Critical Reviews in Food Science and Nutrition* 50, 441–464.

Ertekin, C. and Yaldiz, O. (2004). Drying of eggplant and selection of a suitable thin layer drying model. *Journal of Food Engineering,* 63(3), 349–359.

Falade, K.O. and Solademi, O.J. (2010). Modelling of air drying of fresh and blanched sweet potato slices. *International Journal of Food Science & Technology,* 45(2), 278–288.

Glenn, T.L. (1978). Dynamic analysis of grain drying system. Ph.D. Thesis, Ohio State University, Ann Arbor,

MI (unpublished).

Göğüş, F. and Maskan, M. (2006). Air drying characteristics of solid waste (pomace) of olive oil processing. *Journal of Food Engineering*, 72(4), 378–382.

Görgens, J.F., Carrier, M. and García-Aparicio, M.P. (2014). Biomass Conversion to Bioenergy Products. In: Seifert T. (Eds.) Bioenergy from Wood. Managing Forest Ecosystems, Vol 26, Springer, Dordrecht.

Gregg, J. S. and Smith, S. J. (2010). Global and regional potential for bioenergy from agricultural and forestry residue biomass. *Mitigation and Adaptation Strategies for Global Change*, 15(3), 241–262.

Guine R. P. F., Francisca, H., and Barroca, M. J. (2012). Mass transfer coefficients for the drying of pumpkin (*Cucurbita moschata*) and dried product quality. *Food and Bioprocess Technology*, 5(1), 176–183.

Henderson, S.M. (1974). Progress in developing the thin layer drying equation. *Trans. ASAE*. **17**:1167–1172.

Henderson, S.M., and Pabis, S. (1961). Grain drying theory I: Temperature effect on drying coefficient. *Journal of Agricultural Engineering Research*. 6, 169–174.

Hiloidhari, M., Das, D., and Baruah, D. C. (2014). Bioenergy potential from crop residue biomass in India. *Renewable and Sustainable Energy Reviews*, 32, 504–512.

Karathanos, V.T. (1999). Determination of water content of dried fruits by drying kinetics. *Journal of Food Engineering*, 39, 337–344.

Kaseem, A.S. (1998). Comparative studies on thin layer drying models for wheat. In 13th International Congress on Agricultural Engineering, 2^{nd} - 6^{th} February, Morocco.

Kucuk, H., Midilli, A. Kilic, A and Dincer, I. (2014). A Review on Thin-Layer Drying-Curve Equations. *Drying Technology: An International Journal*, 32 (7), 757-773.

Kumar, A., Jones, D. D. and Hanna, M. A. (2009). Thermochemical Biomass Gasification: A Review of the Current Status of the Technology. *Energies*, *2*, 556-581;

Kumar, A., Kumar, N., Baredar, P. and Shukla, A. (2015). A review on biomass energy resources, potential, conversion and policy in India. *Renewable and Sustainable Energy Reviews*, 45, 530 – 539.

Limpaiboon, K. (2011). Effects of Temperature and Slice Thickness on Drying Kinetics of Pumpkin Slices. *Walailak Journal of Science and Technology*, 8 (2), 159-166.

Midilli, A., Kucuk, H., and Yapar, Z. (2002). A new model for single-layer drying. *Drying Technology*, 20, 1503–1513.

Mujumdar, A. S., and Law, C. L. (2010). Drying technology: trends and applications in post-harvest processing. *Food and Bioprocess Technology*, 3 (6), 843–85.

Nelson, R. G., Walsh, M., Sheehan, J. J. and Graham, R. (2004). Methodology for Estimating Removable Quantities of Agricultural Residues for Bioenergy and Bioproduct Use. *Applied Biochemistry and Biotechnology*, 113(1-3), 013–026.

Ojediran J. O. and Raji, A. O. (2010). Thin Layer Drying of Millet and Effect of Temperature on Drying Characteristics. *International Food Research Journal*, 17, 1095-1106.

Okello, C., Pindozzi, S., Faugno, S. and Boccia, L. (2013). Bioenergy potential of agricultural and forest residues in Uganda. *Biomass and Bioenergy*, 56, 515–525.

Page, G.E. (1949). Factors ınfluencing the maximum rate of air drying shelled corn in thin-layers. M.S.Thesis, Purdue University, West Lafayette, Indiana.

Panwar, N. L., Kaushik, S. C., and Surendra Kothari, S. (2011). Role of renewable energy sources in environmental protection: A review. *Renewable and Sustainable Energy Reviews*, 15 (3), 1513–1524.

Perea-Flores, M.J., Garibay-Febles, V., Chanona-Pérez, J.J., and Calderón-Domínguez, G., Méndez-Méndez, J.V., Palacios-González, E. and Gutiérrez-López, G.F. (2012). Mathematical modelling of castor oil seeds (Ricinus communis) drying kinetics in fluidized bed at high temperatures. *Industrial Crops and Products*, 38, 64–71.

Rajkumar, P., Kulanthaisami, S., Raghavan, G.S.V., Gariepy, Y. and Orsat, V. (2007). Drying kinetics of

tomato slices in vacuum assisted solar and open sun drying methods. *Drying Technology*, 25, 1349–1357.

Ranum, P., Pena-Rosas, J. P. and Garcia-Casal, M.N. (2014). Global maize production, utilization, and consumption. *Annals of the New York Academy of Sciences*, 1312, 105-112.

Ruiz Celma, A., Rojas, S. and Lopez-Rodriguez, F. (2008). Mathematical modelling of thin layer infrared drying of wet olive husk. *Chemical Engineering and Processing: Process Intensification*, 47 (9-10), 1810–1818.

Sadin, R., Chegini, G.-R. and Sadin, H. (2013). The effect of temperature and slice thickness on drying kinetics tomato in the infrared dryer. *Heat and Mass Transfer*, 50(4), 501–507.

Saxena, R.C., Adhikari, D.K. and Goyal, H.B. (2009) Biomass-based energy fuel through biochemical routes: A review. *Renewable and Sustainable Energy Reviews*, 13, 167–178.

Scarlat, N., Martinov, M., and Dallemand, J.-F. (2010). Assessment of the availability of agricultural crop residues in the European Union: Potential and limitations for bioenergy use. *Waste Management*, 30(10), 1889–1897.

Schwietzke S., Kim Y., Ximenes E., Mosier N. and Ladisch M. (2009). Ethanol Production from Maize. In: Kriz A.L., Larkins B.A. (Eds.) Molecular Genetic Approaches to Maize Improvement. Biotechnology in Agriculture and Forestry, Vol 63. Springer, Berlin, Heidelberg.

Sharaf-Eldeen, Y. I., Blaisdell, J.L., and Hamdy, M.Y. (1980). A model for ear corn drying. *Transaction of the ASAE*, 23, 1261–1271.

Shiferaw, B., Prasanna, B. M., Hellin, J. and Bänziger, M. (2011). Crops that feed the world 6. Past successes and future challenges to the role played by maize in global food security. *Food Security*, 3(3), 307–327.

Singh, N. B., Kumar, A. and Rai, S. (2014). Potential production of bioenergy from biomass in an Indian perspective. *Renewable and Sustainable Energy Reviews*, 39, 65–78.

Toğrul, I. T. and Pehlivan, D. (2004). Modelling of thin layer drying kinetics of some fruits under open-air sun drying process. *Journal of Food Engineering* 65, 413–425.

Tunde-Akintunde, T. Y. (2011). Mathematical modeling of sun and solar drying of chilli pepper. *Renewable Energy* 36, 2139- 2145.

Vega-Galvez, A., Miranda, M., Diaz, L. P., Lopez, L., Rodriguez, K. and Di Scala, K. (2010). Effective moisture diffusivity determination and mathematical modelling of the drying curves of the olive-waste cake. *Bioresource Technology*, 101 (19), 7265–7270.

Verma, L.R., Bucklin, R.A, Ednan, J.B., and Wratten, F.T. (1985). Effects of drying air parameters on rice drying models. *Transaction of the ASAE*. 28, 296–301.

Wang, C.Y., and Singh, R.P. (1978). A single layer drying equation for rough rice. ASAE Paper No. 3001.

Weibull, W. (1951). A statistical distribution of wide applicability. *Journal of Applied Mechanics*, 18, 293–297.

White, G.M., Bridges, T.C., Loewer, O.J., and Ross, I.J. (1978). Seed coat damage in thin layer drying of soybeans as affected by drying conditions. ASAE paper no. 3052.

Yagcioglu, A., Degirmencioglu, A., and Cagatay, F. (1999). Drying characteristics of laurel leaves under different conditions. Proceedings of the 7th international congress on agricultural mechanization and energy, ICAME'99, pp. 565–569, Adana, Turkey.

Yi, X.-K., Wu, W., Zhang, Y.-Q., Li, J.-X. and Hua-Ping, L. (2012). Thin-layer drying characteristics and modeling of Chinese jujubes. *Mathematical Problems in Engineering*, 2012, 1–18.

Zhang, L., Xu, C. and Champagne, P. (2010). Overview of recent advances in thermo-chemical conversion of biomass. *Energy Conversion and Management*, 51(5), 969–982.

DISPERSION MODELLING OF AIR EMISSION FROM A RICE MILLING PLANT

Akeredolu, F. A.[1], Sonibare, J. A.[1], *Fakinle, B. S.[2]and Jimoda, L. A.[3]

[1]Department of Chemical Engineering, Obafemi Awolowo University, Ile-Ife, Nigeria.
[2]Department of Chemical Engineering, Landmark University, Omu-Aran, Kwara State, Nigeria.
[3]Department of Chemical Engineering, Ladoke Akintola University of Technology, Ogbomoso, Nigeria.

Corresponding Author: Bamidele Sunday Fakinle, Email: xdales@yahoo.com, fakinle.bamidele@lmu.edu.ng.

ABSTRACT

*The study investigated the air quality impacts of Rice Mill using the ISC-AERMOD View. Contributions of steam boiler and electric power generators in the mill to ground level concentrations of criteria air emissions were established.The maximum ground level concentrations of air pollutants presently emitted by the steam boiler are 1-hour averaging period concentrations of 1.4 – 177.3 µg/m^3 with 24-hour level of 0.3 – 43.5 µg/m^3. Simultaneous operations of the steam boiler and electric power generators give 1-hour averaging period concentrations of 29.7 – 257.8 µg/m^3 with 24-hour levels of 8.8 – 95.8 µg/m^3 . The simultaneous operations of the steam boiler and the electric power generators add about 0.41 – 84.78% of the respective investigated air pollutants limits to the ambient air quality of the host environment. Occasionally the daily NO_X limits from ~~this~~ **scenario 2** could breach the ambient limit whenever all the three electric power generators are simultaneously operated with the steam boiler.*

Keywords: rice mill, criteria pollutants, dispersion modelling, air quality, rice husk.

1.0 INTRODUCTION

Rice is a very important staple food in Nigeria and the world at large. It is one of the major sources of Carbohydrate which is an essential element for energy, Human development and body growth (Adegun, 2012). In agricultural history, the domestication and cultivation of rice is one of the most important event. According to Okeke (2017) the raw material needed for commercial production of rice is the rice seeds or seedling.

Rice grain consist of husk and brown rice. The brown rice contains bran which comprises the outer layer and the edible portion. The rice mill operation is the removal of husk (dehusking) and bran to obtain the edible portion for consumption. The milling is wherein the rice grain is transformed into the form that is suitable for consumption. The extent of rice recovery during milling depends on many factors like variety of rice, degree of milling required, quality of equipment used and the operators (Poonam, 2014).

Due to increase population growth rate as well as consumers' demand of rice in Nigeria, the country has become the highest rice producing country in West Africa and the third largest in Africa. (WARDA, 1996). During rice processing, several streams of materials are generated which include the husks, the bran and the milled rice kernel. The rice kernel is further processed for consumption while the bran and the husk biomass waste generated are of environmental concern.

The availability of energy for rice processing is of outermost concern. One of the major sources of energy in Nigeria is the fossil fuel which it utilization has caused serious environmental impact such as global warming by greenhouse gases and acidification by SOx and NOx. In this study the environmental impact assessment of a rice milling facility located in Nigeria was carried out. This was with the view of determining the impact of the rice milling company activities on the ambient environment base on the source of energy used for its operation.

2.0 METHODOLOGY

2.1 Study Area Description

This Study is conducted in an Agro-allied Industries Limited which is an agricultural products processing company. The company currently owns and operates a 50 MT per day Rice processing Mill producing parboiled head rice and delivers to the final customer through its distributors. It is located in Kwara State, a location of about 7 km from Ajese-ipo and 4 km from Offa (Figure 1). The site accommodates the Factory, the administrative building and a warehouse which occupy about ten (10) hectares of the total land size (100 hectares). The Rice Mill has 2 x 1500 tonnes bulk storage silos with tempering bins. There is a Mechanical reception hopper that allows fast sack tipping before

movement to the Cleaning and destoning section in the Mill. Four soaking/steaming tanks are present with continuous flow drier and holding bin to rice mill and tempering bins. Inside the Double Flow, the parboiled paddy is dried carefully and efficiently with low, un-compacted, bed. There is also a low volume air that slowly cools the paddy in resting bins after which there follows distribution of paddy, water and steam to the tanks. In the multistage rice mill are husking, paddy separation, whitening, polishing, sifting, optical sorting and sacking. Also located in the mill is an air conditioned room on platform for optical sorter with overhead bins and sacking station. The husk fired steam boiler that assists in steam generation. It operates in the factory with husk store, ash settling chamber in brickwork and fan equipped with cyclone and chimney. The Rice Mill operates 2 - 3 shifts per day.

Figure 1: The Rice Mill Facility Site and Area of Influence

2.2 Emission Inventory

A very important step in air emission dispersion modelling is the air emission inventory. This is to identify sources of air emissions in a facility on which dispersion modelling is carried out. It was carried out in this study and with it sources of air emissions in the Rice Mill were identified. The identified major point sources of air emissions in the Rice Mill include the steam boiler where rice husk is used to generate steam for parboiling and utilities that consist of the three diesel-powered electric power generators where electricity is generated to meet its power requirements.

Criteria air pollutants of interest in this study are: carbon monoxide (CO), oxides of nitrogen (NO_X), suspended particulate matter (SPM), and sulphur dioxide (SO_2). Emission rates and stack parameters used as model input were obtained from project details. The emissions sources obtained in the study are as summarized in Table 1.

Table 1: Air Emission Source Characteristics of the Rice Mill Project

Air Emission Source	Coordinates		Exit Temp (°C)	Air Pollutant	Emission (g/s)	Release Height (m)	Stack Diameter (m)	Exit Velocity (m/s)
	Latitude (North)	Longitude (East)						
Husk fired steam boiler cyclone stack	08° 12.404'N	004° 46.432'E	750	PM*	0.5000	11.6	0.36	15
				NO_{X*}	0.0352			
				SO_{2*}	0.0204			
				CO*	2.6000			
500 kva Generator (1)	08° 12.410'N	004° 46.408'E	110	PM	0.0010	3.0	0.3	8.94
				NO_X	0.1182			
				SO_2	0.0136			
				CO	0.0086			
500 kva Generator (2)	08° 12.412'N	004° 46.410'E	110	PM	0.0010	3.0	0.3	8.94
				NO_X	0.1182			
				SO_2	0.0136			
				CO	0.0086			
200 kva Generator	08° 12.414'N	004° 46.412'E	100	PM	0.0004	2.5	0.2	6.40
				NO_X	0.0473			
				SO_2	0.0054			
				CO	0.0034			

Calculated from rice husk emission factors reported by Irfan et al., (2014) for gases and Mantananont and Patumsawad (2016) for particulates

2.3 Emission Modelling

The ISC-AERMOD View was used investigate the air emission dispersion modelling. It is a user-friendly interface for four U.S. EPA air dispersion models: ISCST3, ISC-PRIME, AERMOD and MET developed for Microsoft Windows which uses pathways consisting runstream file as basis for functional organization. Its version 8.2.0, serial number AER00005543, licensed to the Environmental Engineering Research Laboratory, Department of Chemical Engineering, Obafemi Awolowo University, Ile-Ife, Nigeria was used.

The identified point emission sources with all the parameters listed in Table 1 were considered as input parameters into the modelling while Table 2 was used to investigate their impacts on the ambient air quality.

From the identified sources of air emission in the Rice Mill project, two air emissions scenarios were considered to establish potential ground level concentrations of air pollutants within the site and surroundings. The operating scenarios investigated were Scenario 1 where process air emissions from the Rice Mill were considered where operation was assumed to be full with rice husk fired steam boiler in the Mill and Scenario 2 which assumed full operation of the rice-husk-fired steam boiler simultaneously in operation with the three diesel-fired electric power generators.

Table 2: Standards of Ambient Air Quality

Air Pollutants	Averaging Period	Maximum Concentration (µg/m^3)	
		FMENV[a]	World Bank[b]
CO	1 – Hr	-	30,000
	8 – Hr	22,800	10,000
	24 – Hr	11,400	-
NO_X	1-Hr	-	200
	24 – Hr	75 – 113	-
	Annual	-	40
PM	1-Hr	600	
	24-Hr	250	
SO_2	1-Hr	260	
	24-Hr	26	

[a]Source: FEPA (1991); [b]Source: World Bank (2007

2.4 Meteorological Parameters

Meteorological information is essential in ISCST air dispersion modelling. Both the surface and upper air observations were compiled using meteorological data from the Lakes Environmental meteorological observations on the study area (Met Data Order # MET 134283). It has winds having prevalence for a south-westerly direction (Figure 2).

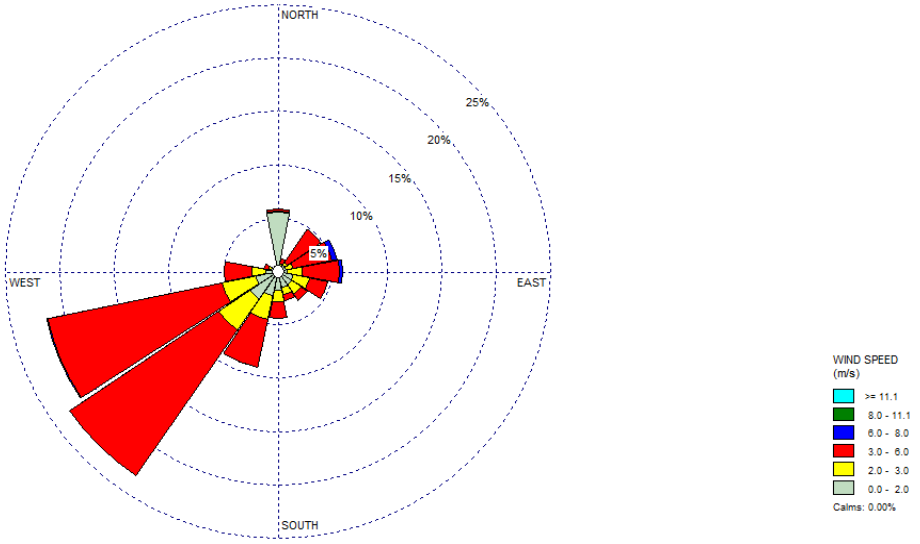

Figure 2: Generated Windrose from the Wind Data used for the Study

3.0 RESULTS AND DISCUSSION

3.1 Ground Level Concentrations of Criteria Pollutants

Presented in Figure 3 the present 1-hour averaging period CO concentrations from the Rice Mill Steam Boiler as investigated in ***scenario 1*** are 41.5 – 177.3 µg/m^3 while its 8-hour and 24-hour averaging period concentrations are 7.0 – 97.5 µg/m^3 (Figure 4) and 2.5 – 43.5 µg/m^3 (Figure 5). Its 1-hour ground level NO_X are 0.56 – 2.40 2.5 – 43.5 µg/m^3 (Figure 6) with 24-hour and annual averaging period concentrations of 0.03 – 0.59 2.5 – 43.5 µg/m^3 (Figure 7) and 0.0019 – 0.1814 2.5 – 43.5 µg/m^3 (Figure 8) respectively. While its 1-hour SPM are 7.99 – 34.09 µg/m^3 (Figure 9) the 24-hour levels are 0.47 – 8.37 µg/m^3 (Figure 10). This ***scenario 1*** emits 1-hour SO_2 concentrations of 0.33 – 1.39 µg/m^3 (Figure 11) with 24-hour levels of 0.02 – 0.34 µg/m^3 (Figure 12).

From the simultaneous operations of both the steam boiler and the diesel electric power generators in the Rice Mill as investigated in ***scenario 2***, the 1-hour

averaging period ground level CO are 43.5 – 185.1 µg/m^3 (Figure 13) with 8-hour and 24-hour levels of 7.1 – 99.3 µg/m^3 (Figure 14) and 2.5 – 46.8 µg/m^3 (Figure 15) respectively. Their 1-hour, 24-hour and annual NO_X averaging period concentrations are respectively 34.0 – 257.8 µg/m^3 (Figure 16), 2.0 – 95.8 µg/m^3 (Figure 17) and 0.2 – 21.0 µg/m^3 (Figure 18). Their 1-hour SPM are 8.2 – 35.0 µg/m^3 (Figure 19) with 24-hour levels are 0.48 – 8.75 µg/m^3 (Figure 20). Both their 1-hour and 24-hour SO_2 averaging period concentrations are respectively 3.95 – 29.67 µg/m^3 (Figure 21) and 0.2 – 11.0 µg/m^3 (Figure 22).

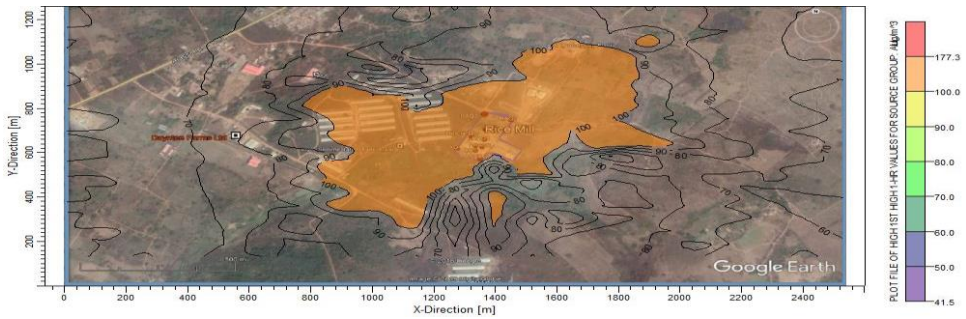

Figure 3: Isopleth of 1-Hour Ground Level CO from the Rice Mill Boiler (Scenario 1)

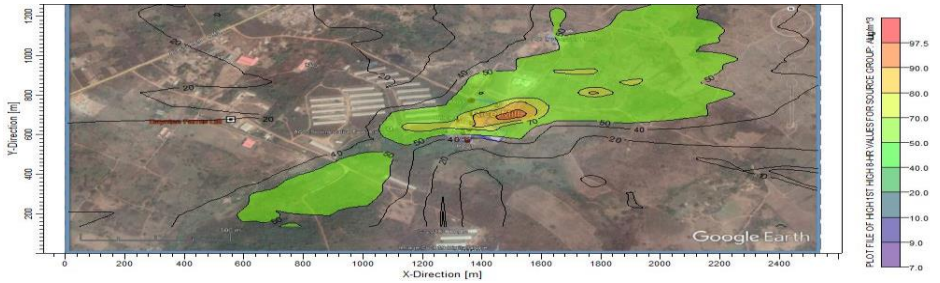

Figure 4: Isopleth of 8-Hour Ground Level CO from the Rice Mill Boiler (Scenario 1)

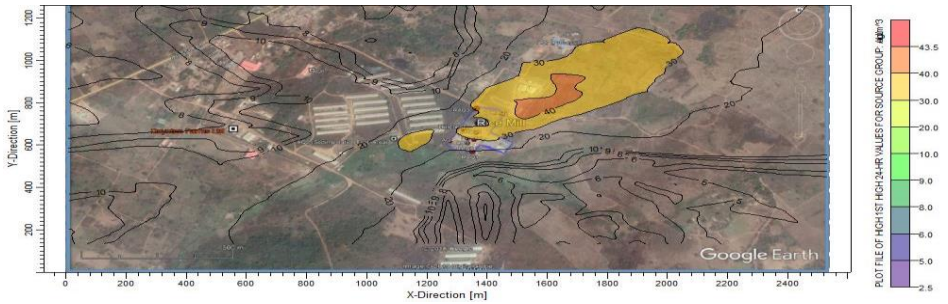

Figure 5: Isopleth of 24-Hour Ground Level CO from the Rice Mill Boiler (Scenario 1)

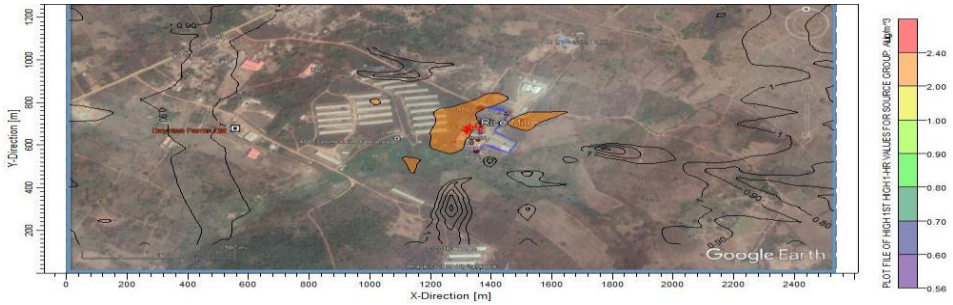

Figure 6: Isopleth of 1-Hour Ground Level NO_X from the Rice Mill Boiler (Scenario 1)

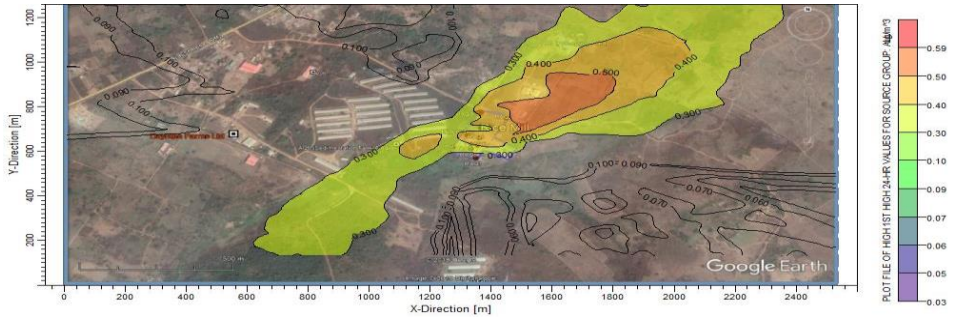

Figure 7: Isopleth of 24-Hour Ground Level NO_X from the Rice Mill Boiler (Scenario 1)

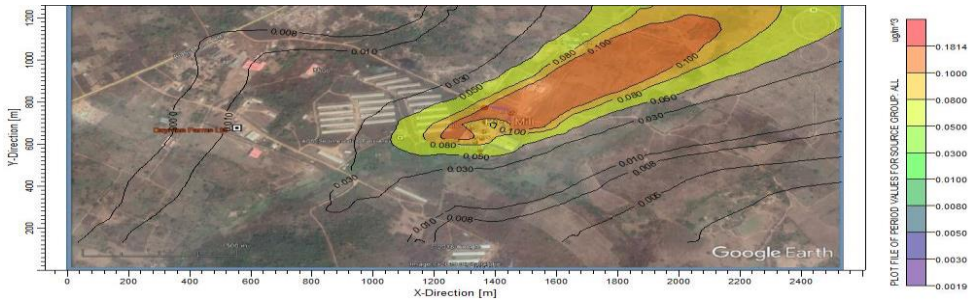

Figure 8: Isopleth of Annual Ground Level NO_X from the Rice Mill Boiler (Scenario 1)

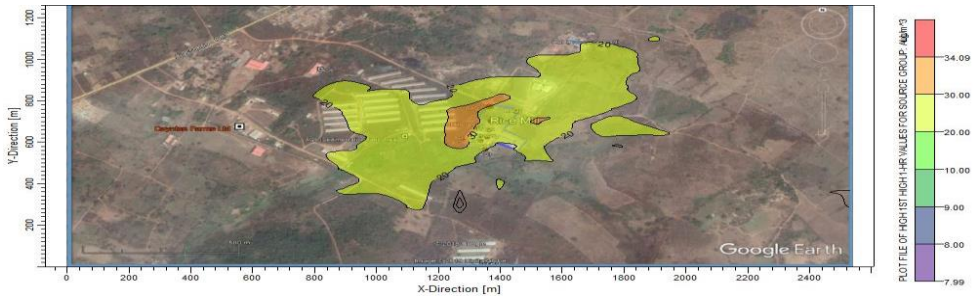

Figure 9: Isopleth of 1-Hour Ground Level SPM from the Rice Mill Boiler (Scenario 1)

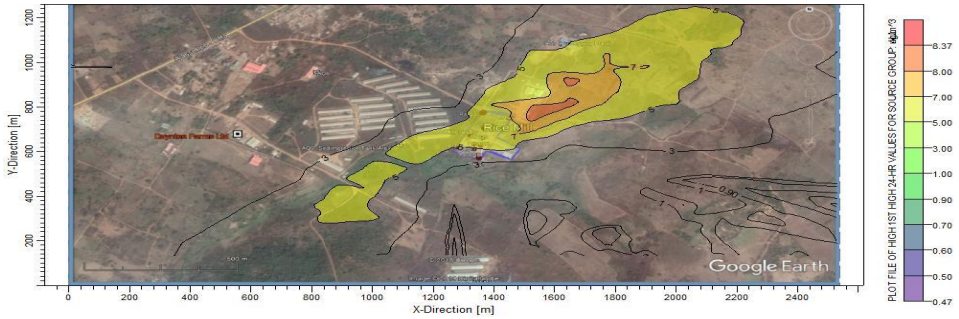

Figure 10: Isopleth of 24-Hour Ground Level SPM from the Rice Mill Boiler (Scenario 1)

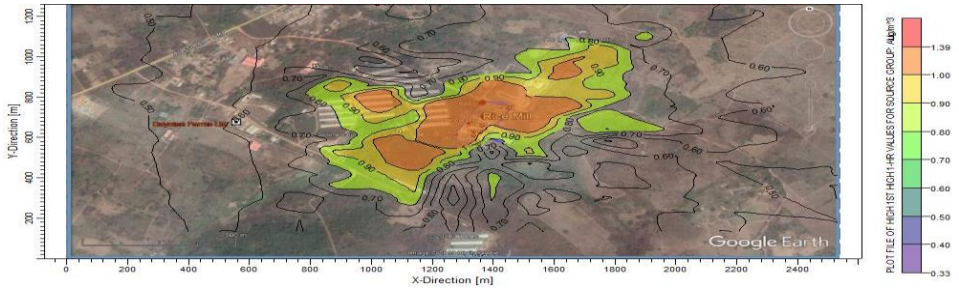

Figure 11: Isopleth of 1-Hour Ground Level SO_2 from the Rice Mill Boiler (Scenario 1)

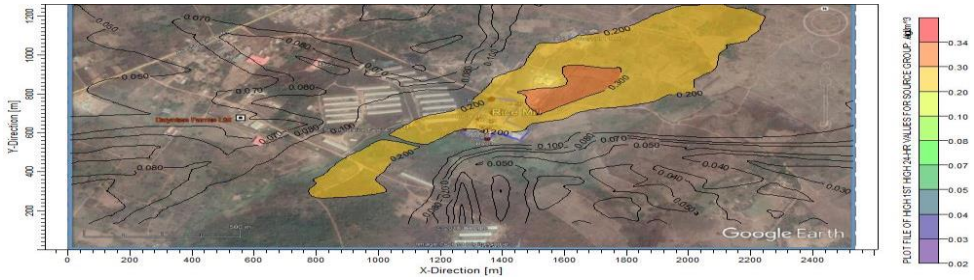

Figure 12: Isopleth of 24-Hour Ground Level SO_2 from the Rice Mill Boiler (Scenario 1)

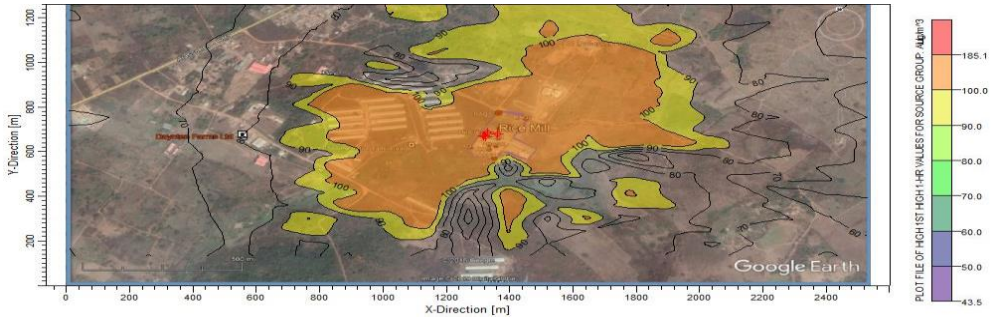

Figure 13: Isopleth of 1-Hour Ground Level CO from the Boiler and Power Generator (Scenario 2)

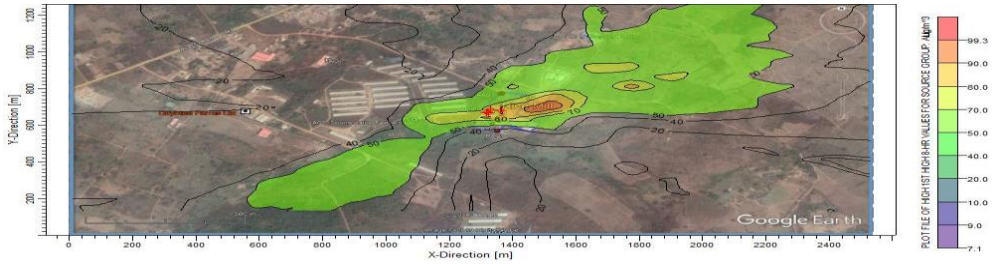

Figure 14: Isopleth of 8-Hour Ground Level CO from the Boiler and Power Generator (Scenario 2)

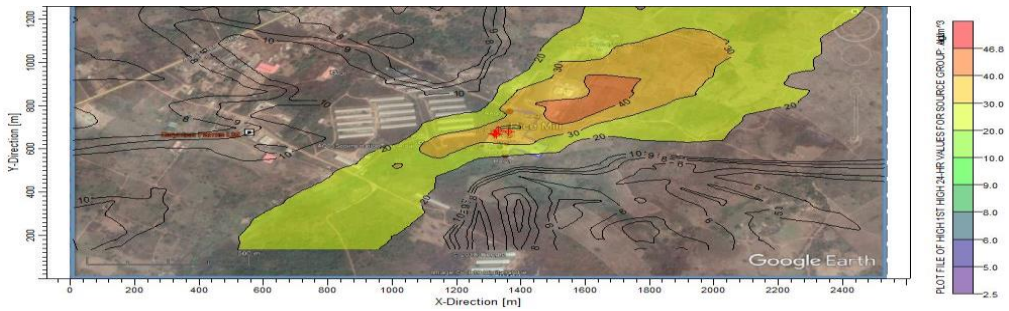

Figure 15: Isopleth of 24-Hour Ground Level CO from the Boiler and Power Generator (Scenario 2)

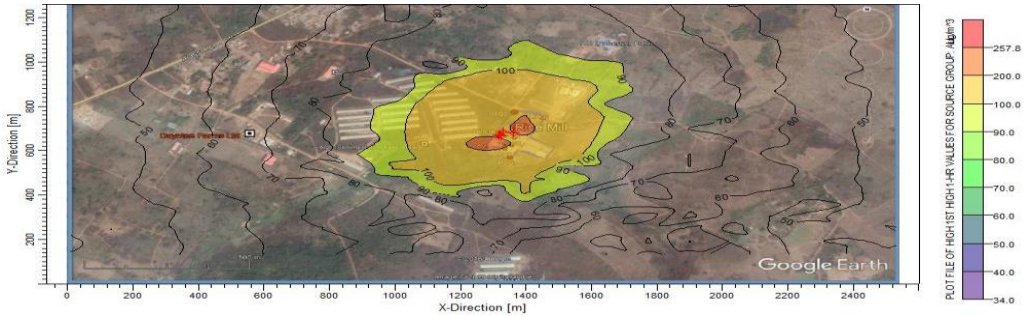

Figure 16: Isopleth of 1-Hour Ground Level NO_X from the Boiler and Power Generator (Scenario 2)

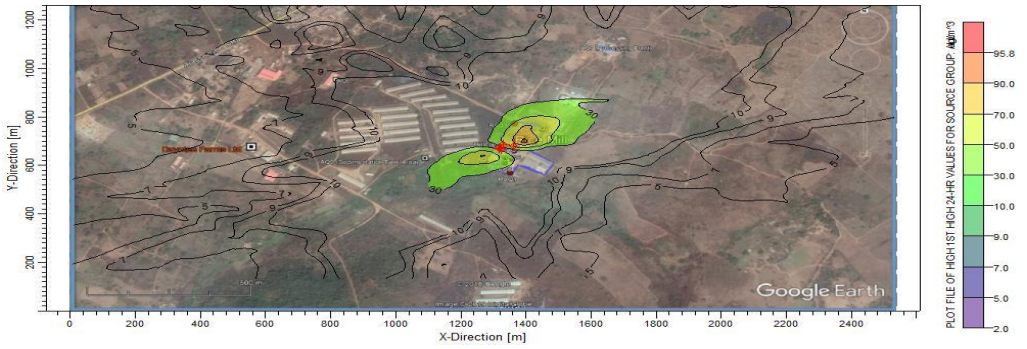

Figure 17: Isopleth of 24-Hour Ground Level NO_X from the Boiler and Power Generator (Scenario 2)

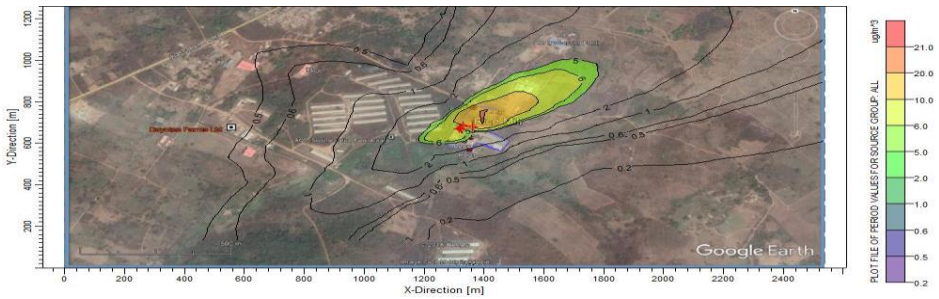

Figure 18: Isopleth of Annual Ground Level NO_X from the Boiler and Power Generator (Scenario 2)

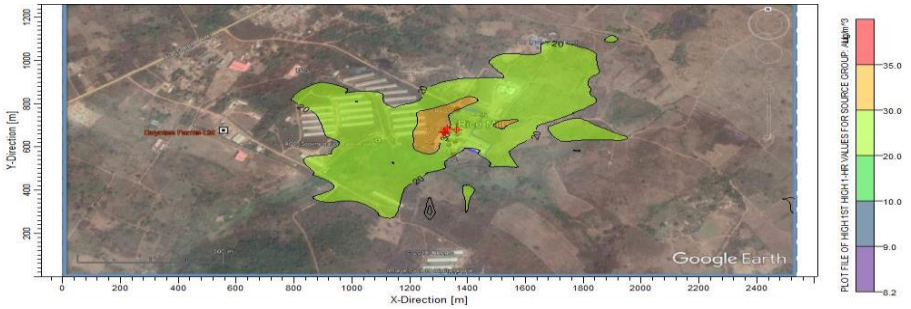

Figure 19: Isopleth of 1-Hour Ground Level SPM from the Boiler and Power Generator (Scenario 2)

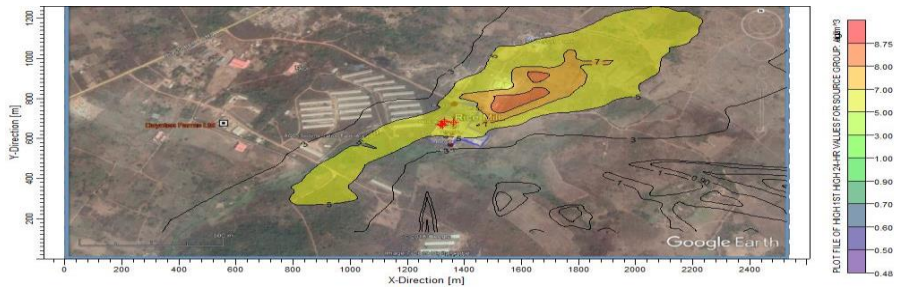

Figure 20: Isopleth of 24-Hour Ground Level SPM from the Boiler and Power Generator (Scenario 2)

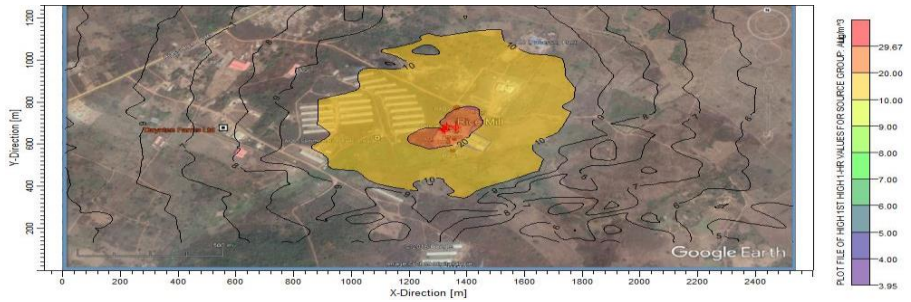

Figure 21: Isopleth of 1-Hour Ground Level SO_2 from the Boiler and Power Generator (Scenario 2)

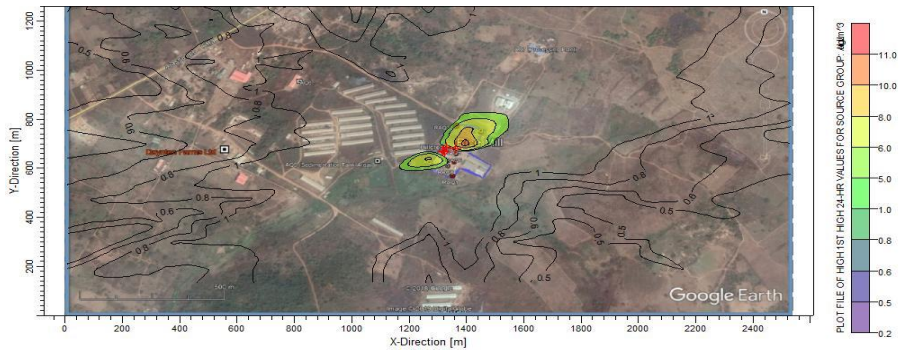

Figure 22: Isopleth of 24-Hour Ground Level SO_2 from the Boiler and Power Generator (Scenario 2)

3.2 Maximum Ground Level Concentrations Impact on Ambient Air Quality

Summarized in Table 3 are the maximum ground level concentrations of air pollutants presently emitted by the Rice Mill. From the steam boiler as investigated in scenario 1, the maximum 1-hour averaging period concentrations are 1.4 – 177.3 µg/m^3 with 24-hour averaging period maximum ground level concentrations of 0.3 – 43.5 µg/m^3 which are respectively 0.54 – 5.68% and 0.38 – 3.36% of their respective limits. While the minimum of these is from SO_2 the maximum is from CO. These maximum concentrations are around the boiler with the minimum in the northeast end of the Mill. The 1-hour averaging period cumulative maximum ground level concentrations of air pollutants from simultaneous operations of the steam boiler and the three diesel electric power generators as investigated in scenario 2 are 29.7 – 257.8 µg/m^3 with 24-hour levels of 8.8 – 95.8 µg/m^3 which are 0.62 – 11.42% and 0.41 – 84.78% of their respective limits. All these maximum concentrations of ground level air pollutants from the Rice Mill are within the set limit except in scenario 2 where the simultaneous operations of both the steam boiler and the diesel generator emits the 1-hour ground level NO_X concentrations of about 128% of the limit.

3.3 Impacts of the Rice Mill Project on the Host Airshed

As obtained from scenario 1, steam boiler of the Rice Mill presently adds about 0.38 – 5.68% of the respective investigated air pollutants limits to its host environment. Similarly simultaneous operations of the steam boiler and the electric power generators of the Rice Mill add about 0.41 – 84.78% of the respective investigated air pollutants limits to the ambient air quality of the host environment. Occasionally the daily NO_X limits from this ***scenario 2*** could breach the ambient limit.

Table 3: Maximum Ground Level Concentrations of Air Pollutants from the Rice Mill

Air Pollutant	Averaging Period	Concentration		Designation/Nearest Community
		Predicted (μg/m^3)	% of Standard	
Scenario 1 (Rice Mill Boiler)				
CO	1 – Hour	177.3	0.59	Within the Rice Mill
	8 – Hour	97.5	0.98	East End of the Rice Mill
	24 – Hour	43.5	0.38	Around the Boiler
NO_X	1 – Hour	2.4	1.20	Around the Boiler
	24 – Hour	0.59	0.52	East End of the Rice Mill
	Annual	0.18	0.45	Southwest End of the Mill
PM	1 – Hour	34.1	5.68	Southwest End of the Mill
	24-Hour	8.4	3.36	Northeast End of the Mill
SO_2	1 – Hour	1.4	0.54	Around the Boiler
	24-Hour	0.3	1.15	Northeast End of the Mill
Scenario 2 (Rice Mill Boiler and Diesel Generators)				
Air Pollutant	Averaging Period	Concentration		Designation/Nearest Community
		Predicted (μg/m^3)	% of Standard	
CO	1 – Hour	185.1	0.62	Generator House
	8 – Hour	99.3	0.99	Northeast End of Rice Mill
	24 – Hour	46.8	0.41	Northeast End of Rice Mill
NO_X	1 – Hour	257.8	128.90	Generator House
	24 – Hour	95.8	84.78	Northeast End of Rice Mill
	Annual	21.0	52.50	Generator House
PM	1 – Hour	35.0	5.83	Generator House
	24-Hour	8.8	3.52	Northeast End of Rice Mill
SO_2	1 – Hour	29.7	11.42	Generator House
	24-Hour	11.0	42.31	Northeast End of Rice Mill

CONCLUSIONS

The ISC-AERMOD View version 8.2.0 has been used in this study to determine the actual contribution of steam boilers and electric power generators in a Rice Mill to air pollutants of its host environment. Ground level concentrations of Carbon Monoxide (CO), Oxides of Nitrogen (NO_X), Particulate Matter (PM) and Sulphur Dioxide (SO_2) associated with the project were estimated. All the anticipated maximum ground level concentrations of air pollutant associated with the Rice Mill are within their respective limits except NO_X that could occasionally breach its limit. Continuous adherence of the Mill to its present attitude of keeping one of the electric power generators on standby will assist to keep the daily NO_X within its set standard.

REFERENCES

Adegun, I. K., Adepoju, S. A. and Aweda, J. A. (2012) A Mini Rice Processing Machine for Nigeria Farmer. Journal of Agricultural Technology 8(4): 1207 – 1216

FEPA. (1991). Guidelines to Standards for Environmental Pollution Control in Nigeria. Federal Environmental Protection Agency (FEPA), Lagos.

Irfan, M., Riaz, M., Afif, M.S., Shahzad, S.M., Saleem, F., Rahman, N., Berg. L.V.D and Abbas F. (2014) Estimation and characterization of gaseous pollutant emissions from agricultural crop residue combustion in industrial and household sectors of Pakistan. Atmospheric Environment, 189 - 197

Mantananont, N and Patumsawad, S (2016) Particulate matter and gaseous emission rate
from combustion of Thai lignite and agricultural residues in a fixed-bed combustor . Energy Sources, Part A: Recovery, Utilization, and Environmental Effects. 38:4, 478-484, DOI: 10.1080/15567036.2013.783655

NESREA (2007) National Environmental Standards and Regulations Enforcement Agency (Establishment) Act, 2007. Federal Republic of Nigeria.

NESREA (2013) National Environmental (Air Quality Control) Regulations, National Environmental Standards

and Regulations Enforcement Agency, Abuja.

Okeke, C. G. and Oluka, S. I. (2017) A Survey of Rice Production and Processing in Southeast Nigeria. Nigerian Journal of Technology. 36(1): 227 – 234

Poonam, D. (2014) Rice Milling. IOSR Journal of Engineering. 4(5): 34 – 42.

USEPA (2000) EPA. Compilation of Air Pollutant Emission Factors Volume I: Stationary Point and Area Sources, 5th ed. United States Environmental Protection Agency, Office of Air Quality Planning and Standards. Research Triangle Park NC 27711, USA, 1995.

WARDA (1996) West Africa Rice Development Association Annual Report.

World Bank (2007) Pollution Prevention and Abatement Handbook WORLD BANK GROUP, Washington DC.

World Bank (2016) Environmental, Health, and Safety Guidelines for Annual Crop Production. WORLD BANK GROUP, Washington DC.

IRON IMPREGNATED RICE HUSK ASH ADSORBENT FOR CYANIDE REMOVAL FROM CASSAVA PROCESSING EFLLUENT

Olakunle, M.S.[1], Ajayi, O. A. [2] and *Ajoge, H.S. [3]

[1,2]*Department of Chemical Engineering, Ahmadu Bello University, Zaria, Nigeria*
[3]*Department of Chemical Engineering, Kaduna Polytechnic, Kaduna, Nigeria*
[*]*Corresponding author E-mail address:* haruna.ajoge@gmail.com

ABSTRACT

Rice husk (RH) was calcined and the resultant ash (RHA) was impregnated with Fe, (Fe-RHA). Both were used to adsorb cyanide from simulated cyanide solution and effluent from cassava processing. X-ray fluorescence (XRF), Fourier-transform infrared spectroscopy (FTIR), and Scanning Electron Microscope (SEM) were used to characterize the RH, RHA and Fe-RHA, while UV spectrophotometer was used to monitor the cyanide concentrations. BET results for surface area, pore volume and pore width are 552 m^2/g, 0.625 cm^3/g, and 3.17 nm, respectively for RHA while those for Fe-RHA are 475.6 m^2/g, 0.2253 cm^3/g, and 2.128 nm respectively. The optimum conditions for the synthesis of Fe-RHA when response surface methodology was employed were 0.075 mol/L, 630 ^oC, and 11minutes respectively for impregnation ratio, calcination temperature, and calcination time. Batch adsorption processes for cyanide removal were carried out by contacting RHA and Fe-RHA adsorbents with effluents A (juice extracted from cassava tubers), B (effluent from cassava processing plant), and C (effluent from cassava processing plant after sedimentation). The adsorption efficiencies when RHA adsorbent was used were: 45.10%., 40.09% and 58.18% respectively for effluents A, B, and C. Similarly, 64.71%, 60.37%, and 63.03% respectively when Fe-RHA adsorbent was used. The analysis of the adsorption data using the Langmuir and Freundlich models showed that Langmuir model is suitable with adsorption capacity of 4.2 mg/g with a correlation coefficient (R^2) of 0.9924. Pseudo-second-order kinetic model has been found most applicable when first, second, and intra-particle kinetic models were used to fit the data.

Keywords: *Adsorption, Cyanide, Effluent, Impregnation, Calcination, Response Surface Methodology (RSM).*

INTRODUCTION

Wastes are generated in every facet of life including the industrial activities of man. Wastes emanating from local food processing industries; for instance cassava processing plants are becoming challenging, especially in developing countries where such activities are encouraged to alleviate poverty and provide food for the populace. The disposal of the wastes has followed varied routes from proper disposal to designated landfills and incinerators to indiscriminate disposal on streets, drainages and water bodies. Cassava (*Manihot esculenta Crantz*) is a very significant food crop in tropical countries and it is one of the most widely distributed food crops having high content of cyanogenic glycosides (Eletta *et al.*, 2016). According to Food and Agriculture Organization of the United Nations, cassava production in Nigeria is the largest in the World; it is a third more than the production in Brazil; it doubles that of Thailand and Indonesia and it feeds about 200 million people. Cassava is an important staple crop and in the tropical world it ranks fourth in importance after rice, wheat and maize. In Nigeria, '*garri*'- a grated, fermented and dehydrated cassava food product is one of the most popular staple foods produced from cassava, which provides some vital nutrients which may have health benefits. The increased importance of cassava in agricultural and economic development and in food security particularly in Africa has given its processing and waste handling a new attention (Okunade *et al.*, 2014).

The process of washing, grating and moisture extraction by pressing; results in the production of wastewater. There are environmental and human health implications of the whole '*garri*' processing procedure especially on the disposal of wastewater resulting therefrom (Okunade *et al.*, 2014).

Cassava processing, especially in areas where the industry is highly concentrated, is regarded as polluting and a burden on natural resources. Some forms of

processing, particularly for starch, have developed beyond traditional procedures and are now water intensive. By its nature, cassava processing for starch extraction produces large amounts of effluent high in organic content. If untreated this may be displayed in the form of stagnant effluent ponds from which strong odours originate. Other forms of processing, despite not requiring water, generate very visible dust waste. As a consequence of the visual display of pollution, cassava is often perceived by local populations as contributing significantly to environmental damage and water deficit (Okunade *et al.,* 2014). As an environmentally protective measure e.g control of discharge of industrial waste and prevention of contamination due to the use of chemical substance, the Environmental Protection Agency (EPA) has placed rigorous limitations on the permitted cyanide concentrations level in industrial wastewater effluent streams. The toxic effects of cyanide are so momentous to cause nerve damage and thyroid glands malfunctioning and the established toxicity level should be as low as 0.1mg/L. Adsorption and biodegradation are the effective methods of removal of cyanide ion from wastewater. The adsorption process is a well-founded and successful mechanism for curing municipal and industrial effluents. These two techniques are considerable methods for treatment of wastewater containing cyanide complexes to a tolerable level, operated either separately or simultaneously, but the choosing of the better treatment method is based on the benefit, cost and concentration of cyanide ion in wastewater (Mohammed *et al.*, 2014).

Rice is an important staple food for approximately half of the world population (Kumar *et al*, 2013). Rice husk is one of the most widely available agricultural wastes in many rice producing countries of the world. Rice hulls (or rice husks) are the hard protecting coverings of grains of rice and removed from rice seed as a by-product during the milling process. Rice husk used as a valued added raw material for different purposes. It possesses various properties that make them suitable for bioethanol production. Rice husk biomass is made up of three polymers like cellulose, hemicelluloses and lignin. Rice husk like other lignocellulosic biomass feedstock has been explored as the cheapest feedstock for bio-ethanol production. It is essentially free as waste product from agricultural sector and forest residues. Utilization of these wastes could solve the disposal problem and reduce the cost of waste treatment. When rice husk is incinerated, ash is obtained called rice husk ash. Rice husk contains 75-90% organic matter such as cellulose, lignin etc, and the rest being mineral components such as silica, alkalis and trace elements. Rice husk is usually high in ash compared to other biomass fuels in the range 10-20%. The ash is 87-97% silica, highly porous and light- weight, with a very high external surface area (Kumar *et al.*, 2013). Presence of high amount of silica makes it a valuable material for use in industrial application. Other constituents of Rice Husk Ash (RHA), such as K_2O, Al_2O_3, CaO, MgO, Na_2O, Fe_2O_3 are available in less than 1%. Rice husk also have bulk density of 96-160 kg/m^3, oxygen 31-37%, nitrogen 0.23- 0.32%, sulphur 0.04-0.08% (Kumar *et al.*, 2013).

Cyanide regardless of the sources, has been proven to be a toxicant to plant, animal and human. Most of the previous works reviewed on the remediation of this toxicant by adsorption process were primarily based on simulated water. Hence, the results obtained from the simulated experiments may not actually represent the reality. The long period of 20 days chemical remediation process carried out by Jideofor *et al.,* (2015) on real effluent remediation needs to be improved upon. Hence the essence of this research work is to harness the large availability of rice husk in Nigeria, synthesize the husk, and impregnate the ash with iron (Fe), and then used to remediate cyanide loaded cassava processing effluents (CPE) using batch adsorption method. The comparison between the real effluent (CPE) and simulated (cyanide simulated water) in terms of their adsorptions were also studied likewise the adsorption capacities of rice husk ash (RHA) and the iron loaded rice husk ash (Fe-RHA).

MATERIALS AND METHODS

Preparation of rice husk ash (RHA)

The rice husk was sourced from *Dariya* Rice processing mill *Kakuri*, Kaduna state. 100 g of the husk was weighed into 1000 mL measuring cylinder and mixed with 1 mole HCl. The content was heated to a temperature of 100 ^oC for 2 hours. After decanting, the content was then washed with deionized water. The pH was monitored using HANNA pocket-sized pH meter until pH of 7 was reached. The residue was then transferred into an electric oven (DHG9030 model) operated at a temperature of 110 ^oC for 5 hours. The dried chemically treated RH was calcined in a muffle furnace at a temperature of 700 ^oC for 2 hours. The result is the RHA which was cooled in a desiccator and packed in air-tight container.

Preparation of iron impregnated rice husk ash (Fe-RHA)

2 g of the RHA was weighed into a beaker and a known molar concentration (based on the design of experiment) of $FeSO_4.7H_2O$ was prepared and mixed with the RHA following impregnation process. This was thoroughly mixed and allowed for 24 hours before filtering with filter paper. The residue was then transferred into an electric oven set at a temperature of 110 ^oC for 30 minutes. The dried sample was then transferred into a muffle furnace and heated for a known temperature and time (based on the design of experiment). The resultant product, iron impregnated rice husk ash (Fe-RHA) was preserved and sent to analyses.

Design of experiment (DOE)

RSM is an approach to achieving optimum values for any method where multiple factors affect the response of interest (Dutta *et al.,* 2011). Three steps were followed to perform the optimization that is: perform the experiments that were designed statistically, estimate the coefficients using the mathematical model, predict the response, and study the model's effectiveness. An RSM model allows input (X_i) and output variable (Y) to be linked as shown in Eq. (1):

$$Y = f(X_1, X_2\ X_3, \dots\dots\dots\dots, X_n) \quad (1)$$

Central Composite Design (CCD) is an RSM design method, which was used to fit surface (quadratic) and thus optimize the active parameters with a minimum possible number of experiments. It also helps in studying the relationship between the parameters (Sen *et al.,* 2018). The CCD largely consists of 2^n factorial runs with 2n axial runs and n_c central runs (Chaterjee *et al.,* 2012). Experimental errors and the repeatability of the experiment were gotten with the aid of centre points. Therefore, the synthesis process having three numeric factors (impregnation temperature, calcination temperature and calcination time), the total experiments performed are given by Eq. (2):

$$N = 2^n + 2n + n_c = 2^3 + (2x3) + 6 = 20 \quad (2)$$

Design Expert software version 10; was used and the generated twenty set of runs is as shown in Table 3.Therefore, twenty sets of Fe-RHA were synthesized, and in order to determine the best sets of parameters (Impregnation ratio, calcination temperature and calcination time) each of the twenty sets of the Fe-RHA were subjected to adsorption process using 50 mL of simulated water prepared from sodium cyanide (NaCN) at a concentration of 80 mg/L, Fe-RHA dosage of 2 g, and pH of 8. To each of the set up; after 40 minutes and at room temperature the content was centrifuged operated at 4,500 revolutions per minute for 5 minutes. The content was then decanted and tested for final cyanide concentration using UV Spectrophotometer. The percentage cyanide removal was entered as response as shown also in Table 3.

Comparative study on cyanide removal using real effluent and simulated water

Three cassava effluents were sourced and tagged Samples A, B and C. Sample A was the juice extracted from cassava tubers purchased from *Kawo* market, Kaduna, while Sample B was the direct effluent from a cassava processing plant located at *Goningora*, Kaduna, and Sample C was the effluent obtained from the same plant but after sedimentation was carried out by the operators. The samples (A, B, and C) after ascertained their initial concentrations, were then subjected to adsorption process at the same conditions of 2 g adsorbents dosage (RHA and Fe-RHA) carried out separately, 50 mL of the sample solution, 40 minutes of contact time, and at room temperature. Then the set up in each case was centrifuged at 4,500 revolutions per minutes for a period of 5 minutes and then their final concentrations were determined. At the same stated adsorption conditions, simulated cyanide solutions were prepared from NaCN having the same initial concentrations as the real effluents (samples A, B, and C) and then contacted with RHA and Fe-RHA adsorbents. The adsorption efficiency or CN removal percentage in each case was calculated using Eq. (3) adopted from Eletta *et al.* (2016)

$$Adsorption\ Efficiency\ (\%) = \frac{C_t - C_t}{C_0} x100 \quad (3)$$

Where, C_o and C_t are initial and final cyanide concentrations respectively in mg/L.

RESULTS AND DISCUSSIONS

XRF analysis

The X-ray fluorescence was used to determine the metallic oxides in the Rice husk (RH), Rice husk ash (RHA), and Fe impregnated rice husk ash (Fe-RHA) as shown in Table 1. The percentage weight compositions of the oxides in RHA and Fe-RHA are lower compared with that of RH; the percentage weight compositions of the oxides in RHA and Fe-RHA are lower compared with that of RH; this is as a result of chemical and thermal treatments that RH was subjected to that reduced the impurities.

Table 1 XRF result of the samples

		PERCENTAGE COMPOSITION (wt. %)		
S/N	**COMPONENTS**	**RH**	**RHA**	**Fe-RHA**
1	CaO	6.21	0.529	0.528
2	SiO_2	52.4	94.873	92.043
3	Al_2O_3	4.72	0.101	0.115
4	Cr_2O	0.17	0.001	0.001
5	CuO	0.14	ND	ND
6	MgO	0.62	0.379	0.492
7	P_2O_3	0.51	0.214	0.22
8	NiO	0.18	ND	ND
9	SO_3	10.25	0.002	0.127
10	K_2O	5.12	0.22	0.22
11	TiO_2	0.41	0.087	0.093
12	MnO	0..31	0.04	0.04
13	Fe_2O_3	1.89	0.083	2.025
14	Na_2O	5.25	ND	ND
15	ZnO	0.14	0.05	0.047

ND= Not detected

This is in agreement with the finding of Gad *et al.*, (2012) which reported that acid treatment reduces the cellulose and hemicellulose as well as the traces of the metals in the husk. The silica content was improved as a result of thermal and chemical treatments. The impregnation of Fe onto the RHA was successful as shown in the table because it increased from 0.083 in RHA to 2.025 in Fe-RHA.

SEM analysis

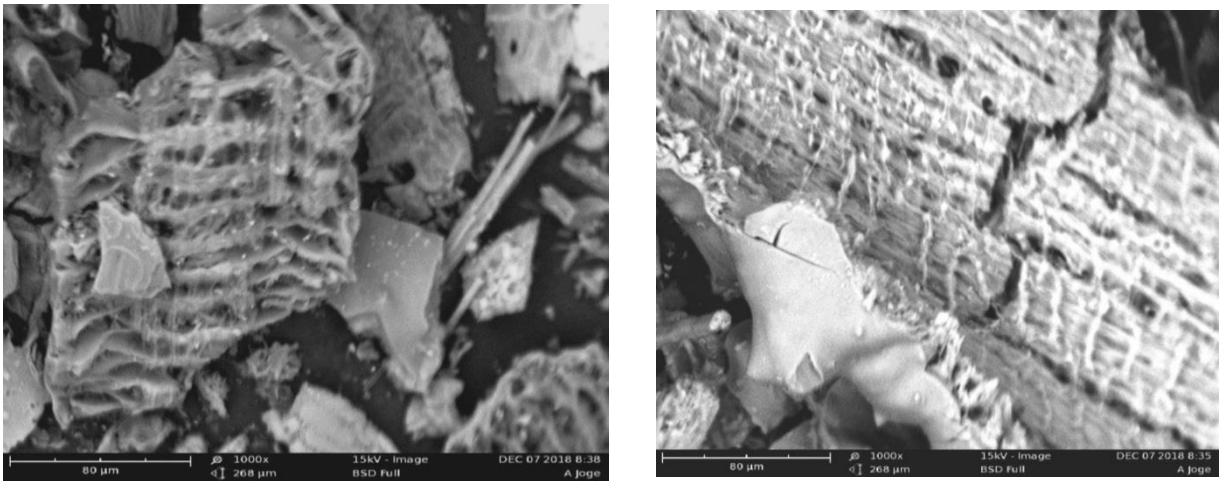

(a) (b)

Figure 1: SEM morphological image for (a) RHA and (b) Fe-RHA

Scan electron microscopic (SEM) analysis was carried out to establish the surface morphology of the samples; hence it revealed the surface texture and porosity. It showed that there are pores of varying sizes within the particles but much more pronounced in Figure 1a, and it is because of the anchoring of Fe on RHA which

reduced or clogged the pores and increased the surface roughness as shown in Figure 1b.

Fourier-transform infrared (FTIR) was also employed to establish phase conversions in the rice husk as well as the surface functional groups.

FTIR analysis

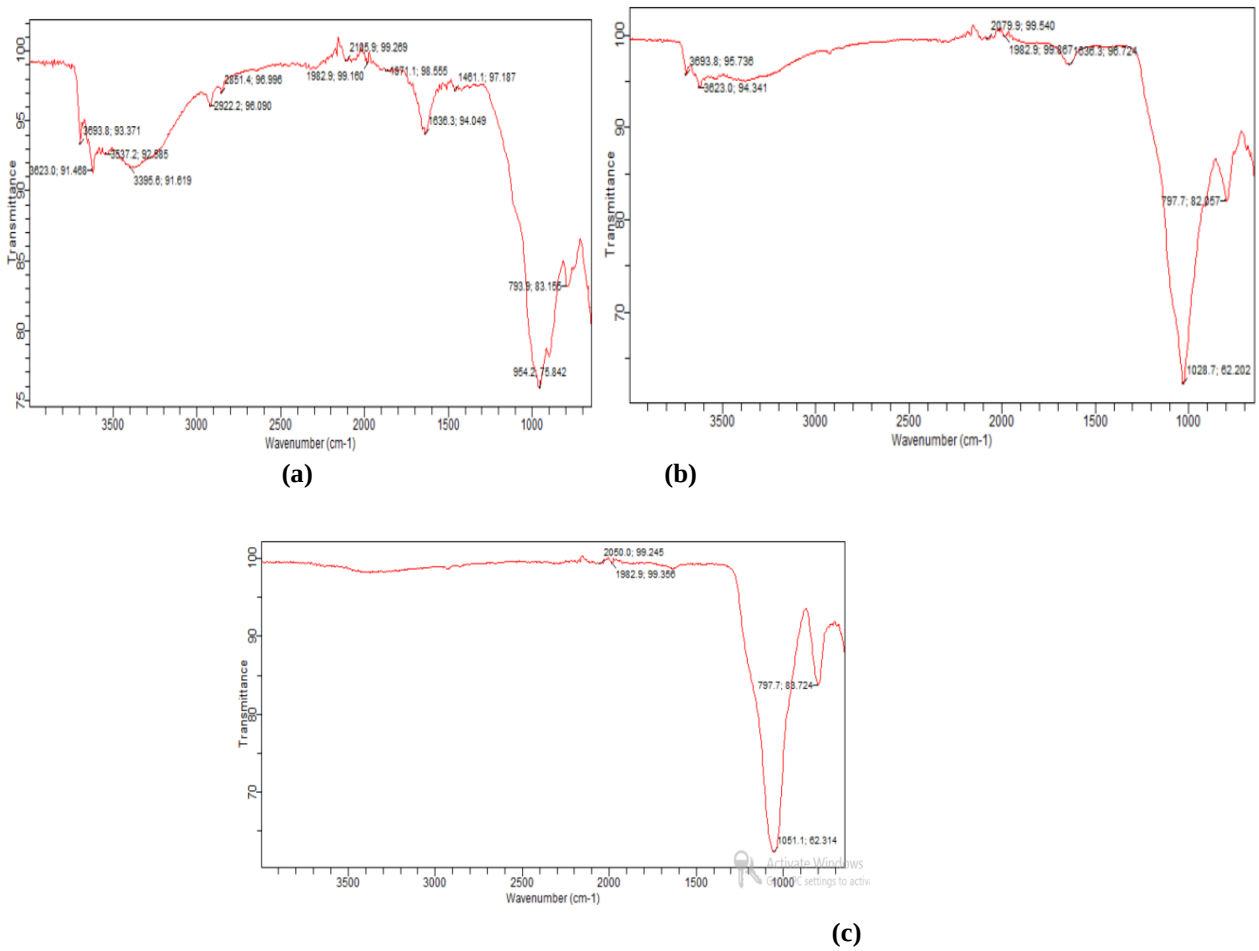

Figure 2: FTIR image for (a) RH, (b) RHA, and (c) Fe-RHA

The frequency ranges belonging to hydroxyl, carbonyl, and carboxyl are evident in the FTIR spectral shown in the Figure 2 a, b and c. The high content of silica present in ash necessitates the presence of Silanol functional group (Si-O-H) which is related to hydroxyl functional group(C-O-H).

BET analysis

Table 2 BET results

S/N	Parameters	Fe-RHA	RHA	Lit. Value (RHA)*
1	Surface area (m^2/g)	475.6	552.1	653
2	Pore volume (cm^3/g)	0.2253	0.625	0.64647
3	Pore width (nm)	2.128	3.17	1.98

(*Hassan *et al.*, 2013)

The pore size distribution and surface area analysis were carried out using BET (Brunauer - Emmett – Teller). The most extensively used technique for estimating surface area is the BET method (Naveen *et al*, 2014)

From Table 2, the analysis showed that the adsorbents (RHA and Fe-RHA) are mesoporous in nature, this is because according to International Union of Pure and Applied Chemistry (IUPAC) nomenclature, the pore

size classification range of 2-50 nm is a mesoporous material, if a particle size range is less than 2 nm, such material is microporous, and above 50 nm is macroporous material (Katsuhiko *et al*, 2012). The parameters for Fe-RHA is slightly lower than RHA, this is because the pores and the surface are slightly covered as a result of the deposition or anchoring of the impregnating chemical ($FeSO_4.7H_2O$). In comparison with Hassan *et al.*, (2013), there is relative discrepancies and agreement; this may be as a result of sol gel method employed for their RHA nano-silica powder production.

Experimental design & responses for Fe-RHA optimization

The percentage cyanide removals obtained from the experiments conducted using simulated water were inputted as response as shown in Table 3. Central Composite Design (CCD) was used for the Design of Experiment (DOE). The Response Surface Methodology (RSM) was applied to analyse these values leading to the quadratic model equation suggested by the software:

$$\%CN\ Removal = 85.83 + 11.07A + 6.42B + 4.61C + 2.79AB - 2.77AC - 2.00BC - 4.34A^2 - 1.54B^2 \quad (4)$$

Where; A is the impregnation ratio, B is the calcination temperature and C is the calcination time. The model equation signifies that impregnation ratio (A) having the highest coefficient is the dominant factor.

Table 3 CCD matrix and responses for Fe-RHA Optimization

S/No.	Impreg. Ratio (mol/l)	Calcination Temp. (^oC)	Calcination Time (min)	Cyanide Removal (%)
1	0.073	550	20	92.11
2	0.04	550	20	85.01
3	0.04	550	37	88.71
4	0.02	450	30	74.29
5	0.04	550	20	81.13
6	0.06	650	30	98.47
7	0.02	650	10	66.97
8	0.04	382	20	69.11
9	0.02	450	10	54.61
10	0.06	450	30	82.96
11	0.04	718	20	90.12
12	0.06	650	10	97.87
13	0.04	550	20	84.78
14	0.04	550	20	86.11
15	0.04	550	20	85.21
16	0.04	550	3	73.42
17	0.02	650	30	76.97
18	0.06	450	10	76.01
19	0.006	550	20	51.27
20	0.04	550	20	87.01

Analysis of variance (ANOVA)

The analysis of variance of the model shown in Table 4 indicated the significance values of the F- values which show the adequacy of the model. The square of the coefficient of regression of the model is 0.98 suggesting the accuracy of the model. All the parameters and their interactions as shown in the table are significant because their p-values are less than 0.05 except the C^2 which was screened out of the model equation. The predicted R^2 (0.9389) is in reasonable agreement with the adjusted R^2 (0.9745) because the difference is less than 0.2.

Table 4 ANOVA table

Source	**Sum of Squares**	**Df**	**Mean Square**	**F Value**	**p-Value Prob > F**	
Model	2975.80	9	330.64	81.81	< 0.0001	**Significant**
A-Imp. Ratio	1672.98	1	1672.98	413.93	< 0.0001	
B-Cal. temp.	563.75	1	563.75	139.48	< 0.0001	
C-Cal. Time	290.11	1	290.11	71.78	< 0.0001	
AB	62.33	1	62.33	15.42	0.0028	
AC	61.22	1	61.22	15.15	0.0030	
BC	32.12	1	32.12	7.95	0.0182	

A^2	271.76	1	271.76	67.24	< 0.0001	
B^2	34.20	1	34.20	8.46	0.0156	
C^2	15.23	1	15.23	3.77	0.0809	
Residual	40.42	10	4.04			
Lack of Fit	20.17	5	4.03	1.00	0.5017	**not significant**

Surface response plot (3D)

The conjugate effect of calcination temperature and impregnation ratio, calcination time and impregnation ratio (IR), calcination time and calcination temperature on percentage cyanide removal are displayed in Figures 3a, 3b, and 3c respectively.

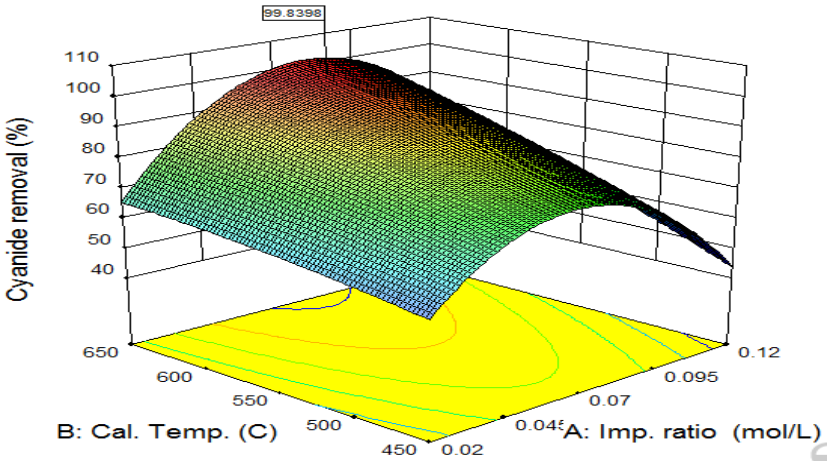

Figure 3a: 3D plot of calcination temperature and impregnation ratio on cyanide removal

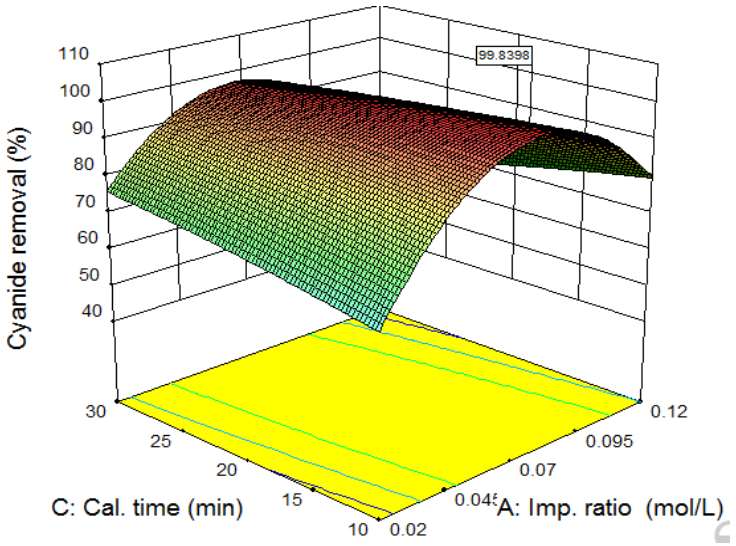

Figure 3b: 3D plot of calcination time and impregnation ratio on cyanide removal

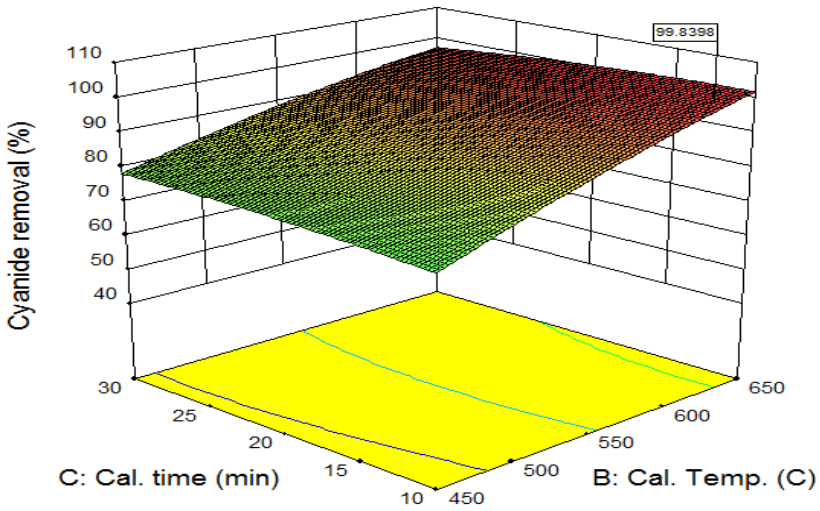

Figure 3c: 3D plot of calcination time and calcination temperature on cyanide removal

The experimental levels of each factor and the relationship were graphically represented using the response surface plots. Figure 3a shows increased cyanide removal with increasing calcination temperature and impregnation ratio values, however, further increase beyond the optimum of the impregnation ratio will cause decrease in the potency of the adsorbent produced and also in the cyanide removal. As the impregnation ratio increases beyond 0.075 mol/L, the cyanide removal began to drop at all calcination temperature values. This may as result of excess iron oxide blocking the pores of the adsorbent which make the adsorbate ions not having access to the active sites. Figure 3b show similar asymmetric relationship between the calcination time and impregnation ratio on the Fe-RHA adsorbent preparation and in turns its capacity for cyanide removal and Figure 3c show a linear relationship between the calcination time and temperature on the capacity of the adsorbent for cyanide removal.

Validation of predicted values

The numerical optimization technique was used whereby the goal of independent variables (Impregnation ratio, calcination temperature, and calcination time) were all set to their lower and upper limits respectively, however, the dependent variable (cyanide removal) was maximised. The result of the selected five predicted solutions (% removal predicted) and the validated results (% removal tested) are presented in Table 5

Table 5 Validation table

S/No	Impreg. Ratio (mol/L)	Calcination Temp. (^{o}C)	Calcination Time (min)	% Removal Predicted	% Removal Tested
1	0.067	648.563	25.901	99.403	99.38
2	0.072	638.505	20.475	99.782	99.74
3	0.065	637.682	14.770	99.491	99.33
4	0.071	631.813	18.076	99.532	99.51
5	0.075	630.478	10.778	99.840	99.81

As seen from Table 5, the experimental values obtained at the selected predicted values are very close; hence they are in agreement, and validated the findings of the optimization. Therefore; the optimal values are 0.075 mol/L, 630 ^{o}C, and 11 minutes respectively for impregnation ratio, calcination temperature and calcination time.

Comparative studies

The results of the batch adsorption experiments carried out on the three samples (A, B, and C) as well as simulated water using RHA and Fe-RHA adsorbents are presented in Figure 4. When the Sample A having the initial concentration of 1.02 mg/L was subjected to adsorption process, the percentage cyanide removal was observed to be 45.10% and 64.71% when RHA and

Fe-RHA adsorbent were used respectively. Similarly, when the adsorption was carried out on the simulated water of the same concentration with Sample A, the cyanide removal were 78.43% and 86.27% respectively when RHA and Fe-RHA adsorbents were used.

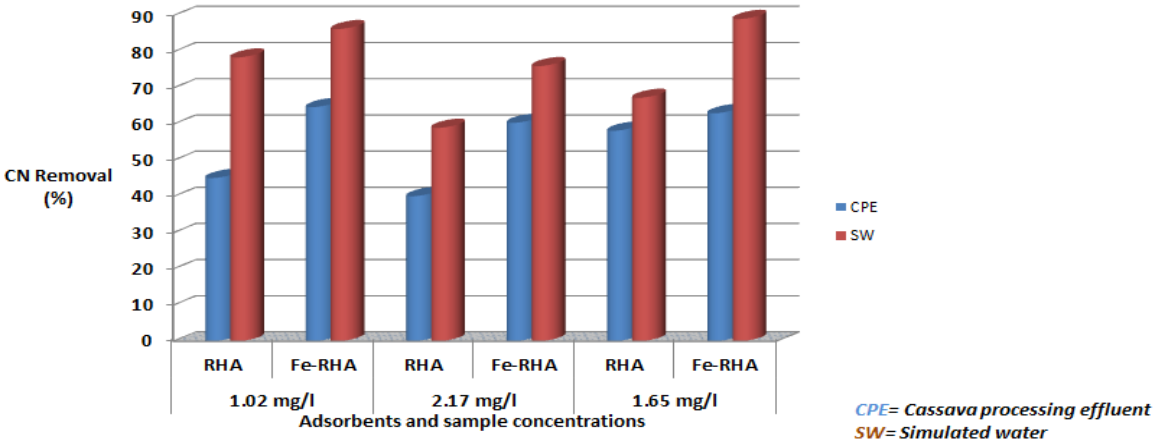

Figure 4: Comparative adsorption studies

The same trends were observed as seen in Figure 4 when the concentrations changed to 2.17 mg/L and 1.65 mg/L, that is, the percentage cyanide removal was higher in simulated water than in the real effluent, this may be because cassava effluent contains some other organic matters which compete with the capacity of the adsorbents. Correspondingly, the cyanide removal was also higher when Fe-RHA adsorbent was used. The improved adsorption efficiencies recorded while using Fe-RHA adsorbent against RHA adsorbent may be as a result of ferrous ions which react with free cyanide to form ferrocyanide complex. Therefore, with respect to this research work, the mechanism is surface adsorption as well as ionic exchange.

Adsorption isotherms for Fe-RHA

Isotherm is of significance to this research because it does not only reveals solute-surface relationship but also gives the idea about the extent of adsorbate accumulation on the surface of the adsorbent (Shelja *et al.*, 2019). The results obtained from the cyanide adsorption equilibrium experiments were fitted to Langmuir and Freundlich adsorption isotherm models. The linearized models were plotted as shown in Figure 5. The Langmuir isotherm model describes monolayer adsorption of adsorbate onto a homogeneous surface of the adsorbent, whereas Freundlich isotherm model describes multilayer adsorption of adsorbate onto the surface of the adsorbent and also assumes that the stronger binding sites are occupied first and that the binding strength decreases with the increasing degree of site occupation (Shelja *et al.*, 2019).

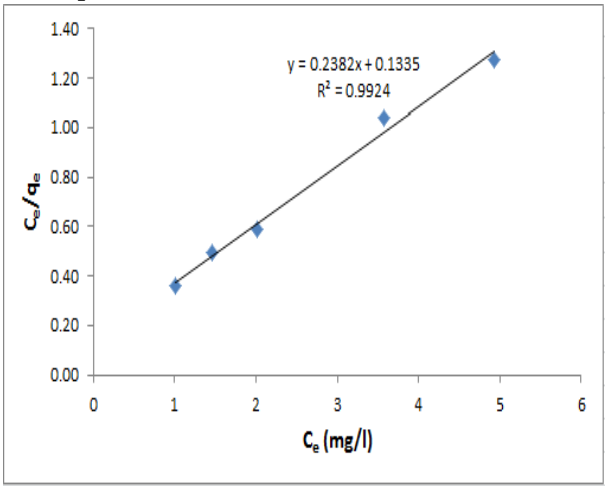

(a)

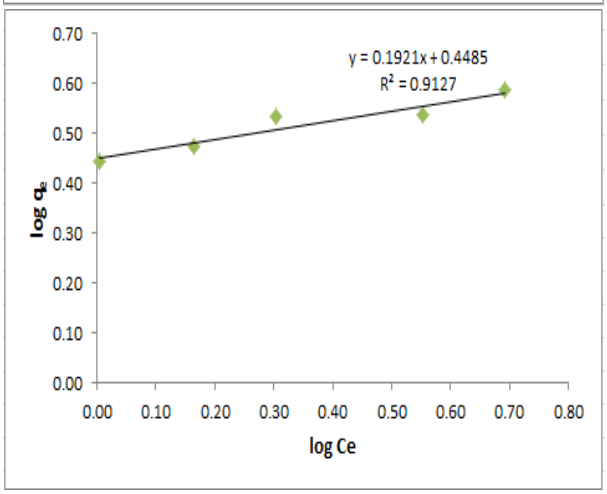

(b)

Figure 5: Adsorption Isotherms for (a) Langmuir and (b) Freundlich.

The Figure 5a (Langmuir isotherm) has a value of correlation coefficient (R^2=0.9924) with adsorption capacity of (q_m=4.2 mg/g) while that of Freundlich

isotherm model (Figure 5b) has correlation coefficient (R^2=0.9127). Therefore, with the K_F value of 1.5 mg/g and 1/n value of 0.1921 which is less than 1 indicates that Langmuir isotherm model fit the experimental data better.

Table 6 Adsorption isotherms parameters for Fe-RHA

Isotherm models	Equation	Parameter values
Langmuir	$\frac{1}{q_e} = \frac{1}{q_m K_L C_e} + \frac{1}{q_m}$	K_L= 1.784 L/mg, R_L= 0.0987, q_m= 4.2 mg/g R^2= 0.9924
Freundlich	$logq_e = logK_F + \frac{1}{n} logC_e$	1/n= 0.1921, n= 5.21, K_F= 1.57 mg/g R^2= 0.9127

R_L value indicates the isotherm shape and, R_L > 1 (unfavourable), R_L = 1 (linear adsorption), R_L = 0 (irreversible) and 0 < R_L< 1 (favourable) according to Mulu, 2013. The value of R_L in this study was found to be 0.0987, suggesting that adsorption of cyanide by Fe-RHA is favourable.

Adsorption kinetics

The pseudo-first-order, pseudo-second-order and intra-particle kinetic models were tested to investigate the rate of adsorption of cyanide ions by Fe-RHA adsorbent.

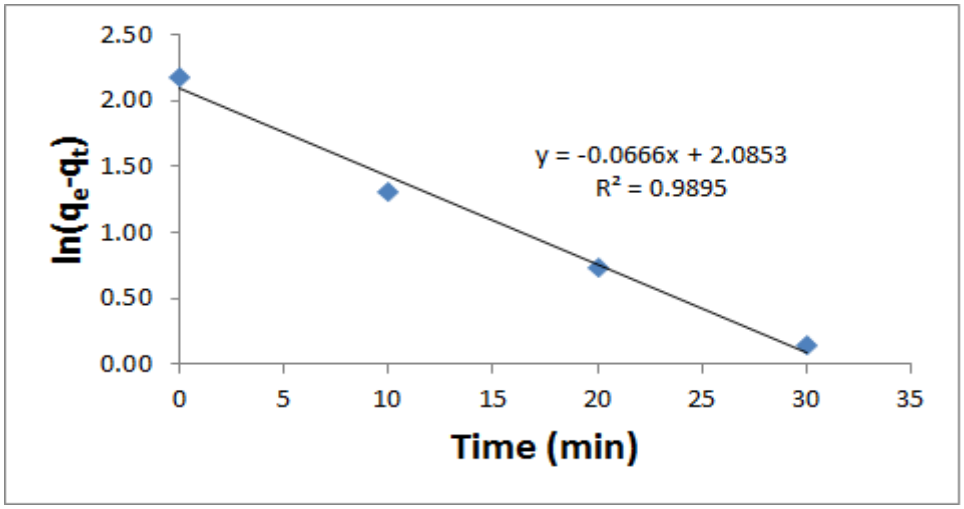

Figure 6a Pseudo-first-order kinetic model graph

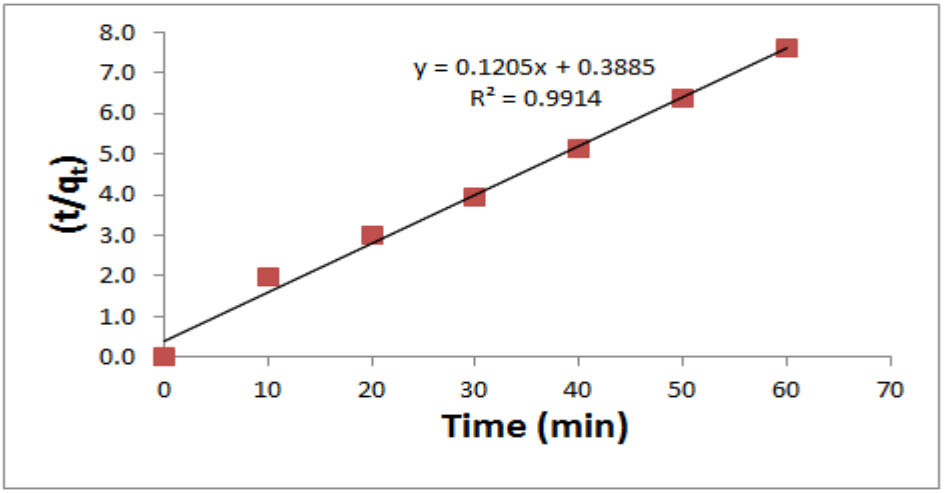

Figure 6b Pseudo-second-order kinetic model graph

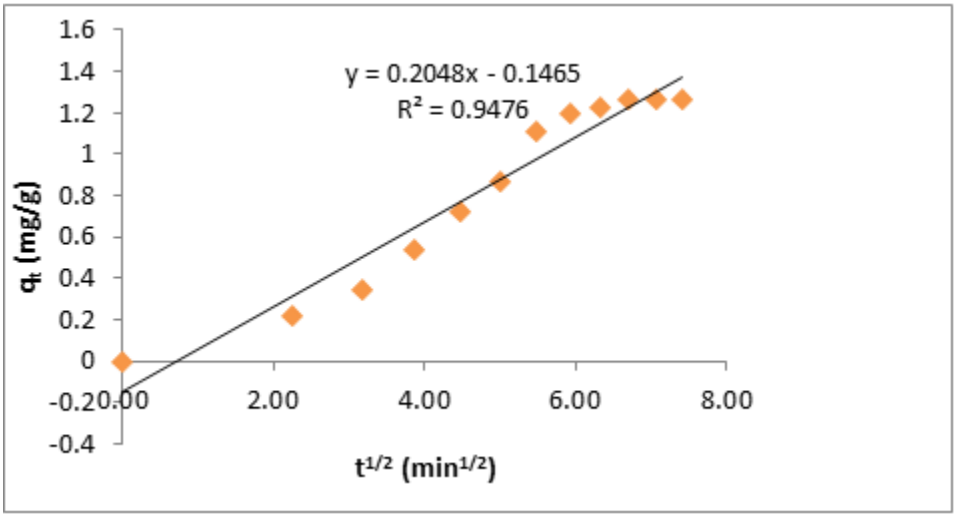

Figure 6c Intra-particle diffusion models graph

Table 7 Kinetic models and their parameter values

Kinetic models	Linear expression	Parameter values
Pseudo-first-order	$\ln(q_e - q_t) = lnq_e - k_1 t$	k_1= 0.067 min^{-1} q_e= 8.04 mg/g, R^2= 0.9895
Pseudo-second-order	$\frac{t}{q_t} = \frac{1}{k_2 q_e^2} + \frac{1}{q_e} t$	k_2= 0.037 g/mg.min q_e= 8.30 mg/g, R^2= 0.9914
Intraparticle diffusion (IPD)	$q_t = K_{id} t^{1/2} + C_i$	K_{id} = 0.2048 mg/g.$min^{1/2}$ C_i = -0.1465, R^2 = 0.9476

q_e exp. = 8.75 mg/g

The linearized form of adsorption kinetics adopted from Guo *et al.,* (2003) and their constants obtained from the plots are presented in Table 7. Therefore, the adsorption of cyanide ions from CPE using Fe-RHA adsorbent followed the pseudo-second order reaction and is shown in Figure 6b. The pseudo-second order model indicates that the adsorption of cyanide ions on the surface of the Fe-RHA adsorbent was due to physicochemical interactions between the two phases.

CONCLUSION

Rice husk was beneficiated and thermally treated to improve its properties needed for cyanide adsorption. Response surface methodology was used to synthesize the Fe-RHA and from the mathematical model developed the impregnation ratio showed the dominant factor. The characterizations carried out on the Fe-RHA prove its potential of its applicability. The Fe-RHA adsorbent was more efficient than RHA in each of the adsorption processes carried out; similarly, adsorption efficiencies were higher in simulated water than in the real effluent; which may be attributed to some organic matter that compete with the capacity of the adsorbent used. Equilibrium data were tested with Langmuir and Freundlich isotherm model equations and the adsorption of the cyanide followed Langmuir isotherm. Hence the prepared Fe-RHA adsorbent had homogeneous surfaces. The kinetic data were also tested with pseudo first order, pseudo second-order, and intra-particle diffusion models; it was concluded that the adsorption of the cyanide followed the pseudo second-order kinetics which indicates that the adsorption of cyanide ions on the surface of the Fe-RHA adsorbent was due to physicochemical interactions between the two phases. From this study, it can be concluded that the Fe-RHA can be effectively utilized for the adsorption of cyanide from cassava processing effluent, and more value addition to the rice husk waste generated from agricultural produce was achieved; which was proved to have great potential in environmental remediation processes.

REFERENCES

Chaterjee S, Kumar A, Basu S, Dutta S (2012)

''Application of response methodology for methylene blue dye removal from aqueous solution using low cost adsorbent''. *Chem Eng J* 181:289–299.

Dutta S, Bhattacharyya A, Ganguly A, Gupta S, Basu S (2011). ''Application of response surface methodology for preparation of low cost adsorbent from citrus fruit peel and for removal of methylene blue'' *Desalination* 275:26-31

Eletta O.A.A.A, Ajayi O. A, Ogunleye O.O, Akpan I.C. (2016) ''Adsorption of Cyanide from aqueous solution using calcinated eggshells: Equilibrium and Optimization Studies'' *Journal of environmental chemical engineering*. 4(2016):1367-1375.

Gad H.M, Borai E.H, & El-Khalafawy A.M. (2012) '' Sorption and Desorption of Strontium using Silica extracted from Acid Treated Rice Husk. I: Effect of pH and Interfering Ions'' *Arab Journal of Nuclear Sciences and Applications.* 45(2): 142-154

Kumar S., Sangwan P., Dhankhar R. Mor V., and Bidra S. (2013). ''Utilization of Rice Husk and Their Ash: A Review'' *Research Journal of Chemical and Environmental Sciences* 1 Issue 5.126-129

Mohammed N.A, Firas S. A, Suha I. (2014) '' Cyanide removal from wastewater by using banana peel'' *Journal of Asian Scientific Research* 4(5): 239-247

Naveen D., Chandrajit B.,and Prasenjit M. (2014) ''Study for the Treatment of Cyanide Bearing Wastewater using Bio-adsorbent Prunus Amygdalus (Almond Shell)'' *International Research Journal of Environment Sciences*. Volume 3(1) page 23-30

Okunade D. A. and Adekalu K.O. (2014) ''Characterization of Cassava-waste Effluents Contaminated Soils in Ile-Ife, Nigeria'' *European International Journal of Science and Technology Vol. 3 No. 4:173:182*

Sen S., and Nandi S, Dutta S (2018) ''Application of RSM and ANN for Optimization and modeling of biosorption of chromium (VI) using cyanobacterial biomass''. Appl Water Sci 8(5):148

Shelja A,, Sabyasachi P., Ajanur R., Kartik C., and Susmita D. (2019) ''A Cost-effective approach for abatement of cyanide using iron-impregnated activated carbon: Kinetic and Equilibrium study'' Journal of *Applied water science* (2019), 9:74

VALORISATION OF SUNFLOWER (TITHONIA DIVERSIFOLIA) STALKS FOR THE ADSORPTION OF PB(II) AND FE(II) FROM AQUEOUS MEDIA

Eletta, O. A. A[1], Ayandele, F. O.[1], Adeniyi, A. G[1], *Ighalo, J. O.[1]

[1]Chemical Engineering Department, Faculty of Engineering and Technology,
University of Ilorin, Ilorin, P. M. B. 1515, Nigeria
*Corresponding author, Email address: oshea.ighalo@yahoo.com

ABSTRACT

Sunflower (Tithonia diversifolia) stalk was harnessed as a precursor in preparing adsorbents for the removal of Pb(II) and Fe(II) from aqueous solutions. The biomass was acid activated by wet impregnation with phosphoric acid and carbonised at 500^{o}C. The adsorbent was characterised using Fourier Transform Infra-Red Spectroscopy (FTIR), Branueur Emmet and Teller analysis (BET) and Scanning Electron Microscopy with Energy-Dispersive X-ray Spectroscopy (SEM-EDS). The surface area of the adsorbent obtained was 325.375 m^2/g. The effect of metal ions concentration, adsorbent dosage and contact time was studied for both Pb(II) and Fe(II) uptake. The best fit isotherm model for Pb(II) and Fe(II) was Langmuir and Freundlich Models respectively. The monolayer adsorption capacity of the adsorbent to Pb(II) and Fe(II) was 31.55 mg/g and 35.84 mg/g respectively. The pseudo second order was the best fit kinetic model. The study was able to reveal that Sunflower (Tithonia diversifolia) stalk can be used to prepare low cost adsorbents for water treatment.

Keywords: *Adsorption, Tithonia diversifolia, Heavy metals, Kinetics, Isotherm, Valorisation*

1. INTRODUCTION

The treatment of polluted industrial wastewater remains an area of global concern among engineers and researchers since wastewater collected from municipalities, communities and industries must be returned to receiving waters or to the land (Eletta *et al.* 2019; Salam *et al.* 2011). Heavy metals are introduced into the environment majorly through anthropogenic activities. They are adulterant and their toxicity is a major problem from ecological, evolutionary, nutritional and environmental perspectives (Babatunde *et al.* 2019; Jaishankar *et al.* 2014). Heavy metals accumulate and persist in the ecosystems because they cannot be degraded or destroyed (Kano 2015; Pinho and Ladeiro 2012). Industrial waste water mostly contain heavy metals like arsenic, cadmium, chromium, iron, copper, lead, nickel, and zinc which could have adverse effect on human health (Jaishankar *et al.* 2014).

Various methods have been implemented in the treatment of wastewater among which are: chemical precipitation, solvent extraction, ion exchange, electrolytic techniques, coagulation, sedimentation, filtration, membrane process and adsorption techniques (Balcıoğlu and Ötker 2003; Kano 2015). Adsorption is a widely used technique for wastewater treatment and activated carbon is a commonly used adsorbent for the process. The usefulness of this method lies in the benefits of cleaner, easy controlled process, more efficient and cost-effective technology (Cherdchoo *et al.* 2019). Agricultural lignocellulosic based adsorbents have also been gaining worldwide attention as a result of their characteristics which includes renewability, biodegradability, environmentally friendliness, low cost and availability (Ling Pua *et al.* 2013). In recent times, activated carbons with very high surface area, high porosity, and high adsorptive capacity have been obtained by chemical activation method which have been extensively used for the removal of pollutants (Üner *et al.* 2015; Yahya *et al.* 2015).

Many studies have been carried out to utilise agricultural by-products as adsorbent material in wastewater treatment: peanut husk (Salam *et al.* 2011), rice husk (Hegazi 2013), *Delonix regia* (Babalola 2018), *Amaranthus hybridus* stalk (Egila *et al.* 2011), groundnut shell (Isah and Yusuf 2012), tea leaves and pumpkin seeds (Francis 2015), orange peel (Geremew 2017), almond shell (Largitte *et al.* 2016), mango peel (Foo and Hameed 2012), bamboo (Awoyale *et al.* 2013), coconut shell (Achaw 2012; Babarinde and Onyiaocha 2016), physic nut seed hull (Yakub *et al.* 2013), dates stone (Alhamed 2006), guava seeds (Largitte *et al.* 2016), sugarcane bagasse (Geremew 2017), watermelon rind (Üner *et al.* 2015), fox nut (Kumar and Jena 2016) and a host of others (Adeniyi and Ighalo 2019; Eletta and Ighalo 2019).

Figure 1. Sunflower plant

Sunflower (*Tithonia diversifolia*) is a plant that grows widely in Nigeria (shown in **Figure 1**) (Ayeni *et al.* 1997). It is regarded as a weed, with the stem/stalk having no major competitive use (Ayeni *et al.* 1997). The aim of this study is to evaluate the removal of Pb(II) and Fe(II) from wastewater by treating with a low cost adsorbent prepared from *Tithonia diversifolia*. The adsorbent was characterised using Fourier Transform Infra-Red Spectroscopy (FTIR), Branueur-Emmet-Teller analysis (BET) and Scanning Electron Microscopy with Energy-Dispersive X-ray Spectroscopy (SEM-EDS).

2. MATERIALS AND METHOD

2.1 Preparation of Adsorbent

Sun flower stalk (*Tithonia diversifolia*) was sourced from within the premises of the university of Ilorin, Kwara State, Nigeria. The stalks were rinsed with tap water and distilled water to remove dirt and dust and sundried for 24 h to reduce the moisture content prior to oven drying. It was then oven dried at 105^{o}C until no weight loss was observed (Bello and Ahmad 2011). The dried biomass was pulverized with a ball milling machine and sieved to 100 µm size (Odubiyi *et al.* 2012). H_3PO_4 was used for chemical activation with impregnation ratio of 1:2 acid-biomass. The mixture was stirred continuously using magnetic hot plate stirrer at ambient temperature for 1 hour and left to age for 24 h. The mixture was filtered and dried in the oven at 110^{o}C for 24 h. The sample was taken to a muffle furnace and heated at 500^{o}C for 1 h to produce activated carbon. Finally, the powdered sample was washed with 0.5 M of KOH and distilled water to remove residual acids until washing solution become neutral. The samples were then dried overnight at 100^{o}C and cool to room temperature to obtain H_3PO_4 activated carbon (Krishna 2014). The samples was grinded with mortar and pestle and sieved to obtain maximum particle size of 100 µm (Krishna 2014).

2.2 Adsorbent Characterisation

FTIR spectrometer used to identify the functional groups responsible for the heavy metals uptake and bonding present on the surface of the adsorbents. The scan range was set to 650-4000 cm^{-1}. The sample was placed on the sample holder and the sample was scanned to obtain the spectrum. BET analysis was employed to determine the surface area, pore size and pore volume of the adsorbent. The surface properties of the soot sample were done using Multipoint BET surface area and DR (Dubinin-Radushkevic) method for the pore volume and width (diameter) respectively. SEM was used for morphological structure such as size and shape of the adsorbent. The sample stub was placed on a charge reduction sample holder and introduced into the column of the SEM machine. On the SEM machine, it was viewed from a Navigation camera before being sent to SEM mode. Different magnifications were obtained after adjustment of brightness and contrast.

2.3 Batch Adsorption Experiments

The experiments were performed using 50 ml of synthetic wastewater (pH 6.4) at 30°C and 150 rpm for maximum of 180 mins. The choice of Pb(II) and Fe(II) for the experiments was based on an earlier characterisation of a real paint industry wastewater which highlighted the high levels of those metals. All adsorption experiments were performed in 250 ml conical flasks with 50 ml of wastewater, varying any one of the parameters and keeping the other parameters constant. The parameters studied were adsorbent dosage (1 – 6 g/l), initial Pb(II) and Fe(II) concentration (25 – 150 mg/l), contact time (30 – 180 minutes). The equilibrium isotherm experiments were done at 30^{o}C, initial metal concentration (C_i) was 25 – 150 mg/l and contact time of 60 minutes. The adsorbent dosage was 5 g/l. For the kinetic studies, the temperature was set at 30^{o}C, initial metal concentration (C_i) was set at 100 mg/l and dosage of 5 g/l and contact time was varied from 30-180 mins.

3. RESULTS AND DISCUSSION

3.1 Adsorbent Characterisation

3.1.1 Functional Groups

Figure 2 revealed that activated carbon from *Tithonia diversifolia* shows a weak N-H stretch of 3652.8 cm^{-1} which is assigned to amines group, it also shows a

strong band of C-H stretch of alkanes & alkyls at 2918.5 cm^{-1} which is similar to what was obtained by Cherdchoo *et al.* (2019). The band at 3123.5 cm^{-1} indicates weak medium =C-H stretch of alkenes group. The band at 2750.8 cm^{-1}, 3123.5 cm^{-1}, 2918.5 cm^{-1} are assigned to strong broad O–H stretching of hydroxyl groups from carboxylic acid (Kumar and Jena 2016). 2344.5 cm^{-1} indicates amino group (Cherdchoo *et al.* 2019). The bands at 805 cm^{-1} is assigned to strong C-H bend of aromatics compound group (Kumar and Jena 2016). The band region between 900 and 1300 cm^{-1} depicts the characteristic of phosphorous and phosphorous carbonaceous compounds present in the phosphoric acid activated carbon (Kumar and Jena 2016). N-H and O-H groups have been shown to be important functional groups for the sorption of heavy metals (Farhan *et al.* 2012) and especially Pb(II) (Fauzia *et al.* 2018).

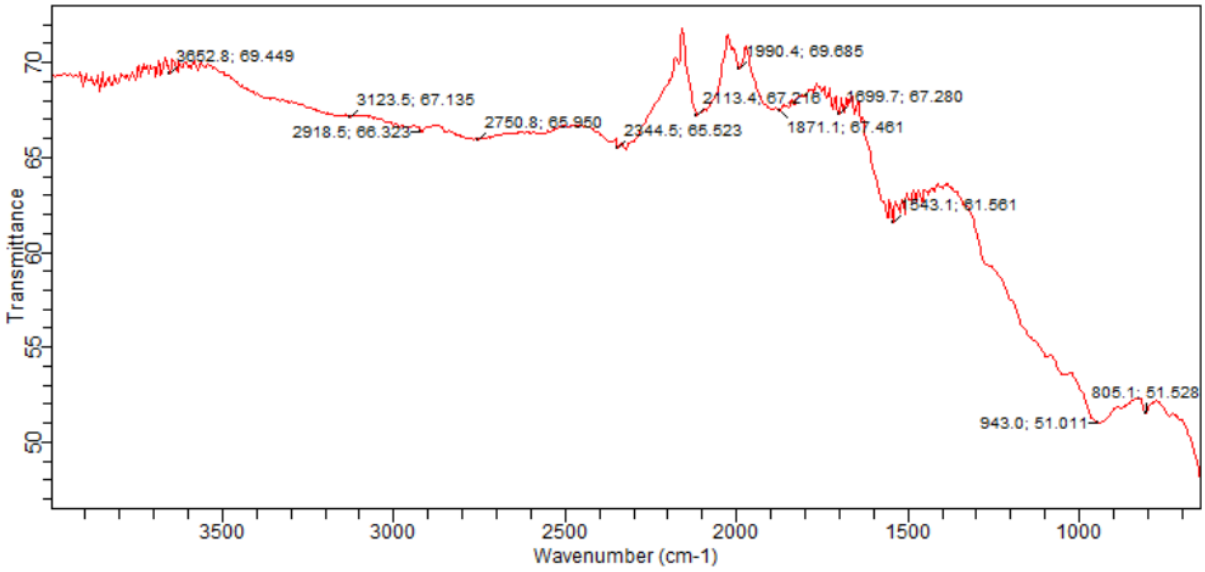

Figure 2. FTIR spectra of *Tithonia diversifolia* activated carbon

3.1.2 Porous Characteristics

The specific surface area of the *Tithonia diversifolia* AC was 325.375 m^2/g based on the Branueur-Emmett-Teller (BET) standard method which was higher when compared with peanut shell (Al-Othman *et al.* 2012), mixed waste tea and coffee ground (Cherdchoo *et al.* 2019). The total pore volume obtained was 0.136 m^3/g. The pore size width obtained was 5.749 nm suggesting a mesoporous structure (Cherdchoo *et al.* 2019). The prepared activated carbon has well-developed pores which can be attributed to the activation with H_3PO_4 during carbonisation of the adsorbent at 500^oC, H_3PO_4 also act as dehydrating agents that inhibit the formation of tar as well as volatile substances during the process, which enhance the yield from the process (Kumar and Jena 2016).

3.1.3 Surface Morphology

Figure 3 (a-b) showed small pieces and pores, this is due to the fact that during carbonisation, organic materials were volatilized from the biomass leading to the formation of many pores which led to higher BET surface area. The higher surface area can also be due to the interaction of H_3PO_4 during impregnation. *Tithonia diversifolia* (sunflower) activated carbon contained

59.43% carbon, 27.24% oxygen, 2.04% nitrogen, 10.01% phosphorous and others as shown in **Figure 4**. SEM image shows rough surface, some clouded white substances on the morphological surface of the sample and agglutinative flakes of *Tithonia diversifolia*, this suggests that the adsorbent has heterogeneous surface which makes it very suitable for use as an adsorbent.

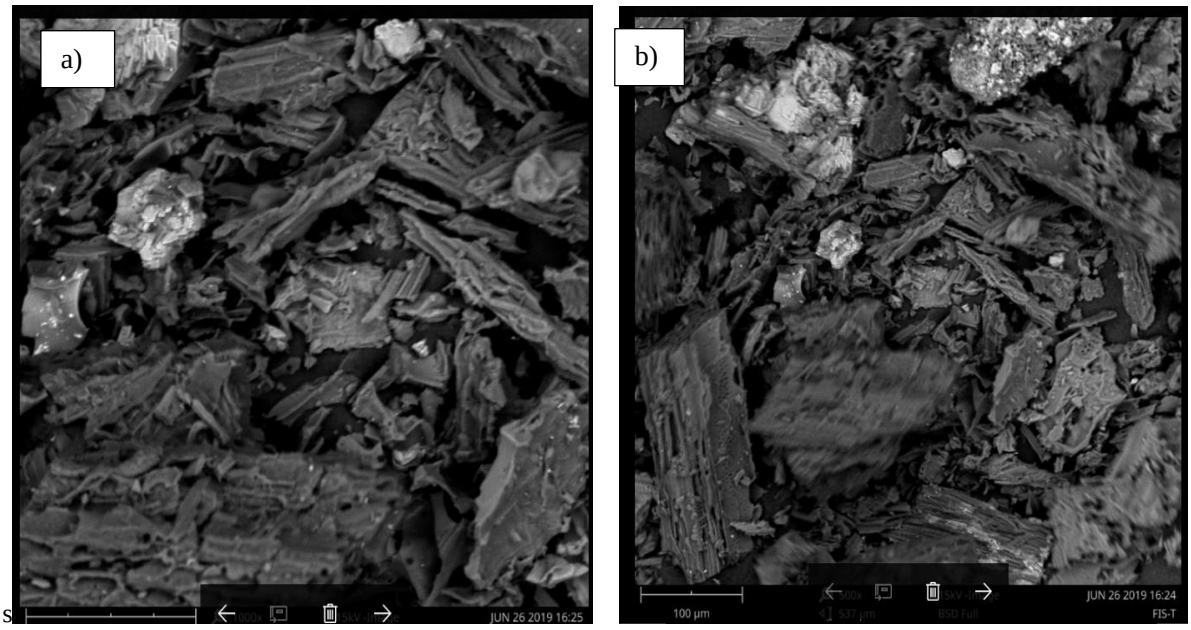

Figures 3 (a-b). SEM image of *Tithonia diversifolia* activated carbon (a) ×1,500 (b) ×1,000

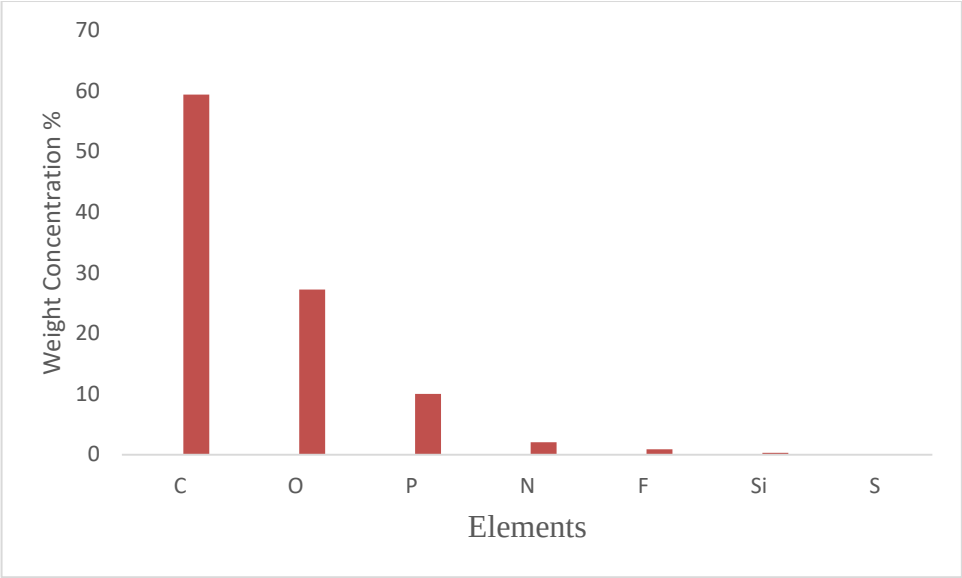

Figure 4. EDS plot of *Tithonia diversifolia* activated carbon

3.2 Parametric Studies

3.2.1 Effect of Initial Concentration

The effect of different initial concentrations of Fe(II) and Pb(II) was investigated and shown in **Figure 5**. It was observed that there was a decrease of adsorption of Pb(II) and Fe(II) with an increase in concentrations of Pb(II) and Fe(II) in the study. Adsorption efficiency decreased as metal ion concentrations increased which depicts saturation at the adsorbent surface site. The ratio of surface active sites to total amount of metal ions was higher in lower metal ion concentrations compared with higher metal ions. Rate of metal ion adsorption decreases when approaching equilibrium.

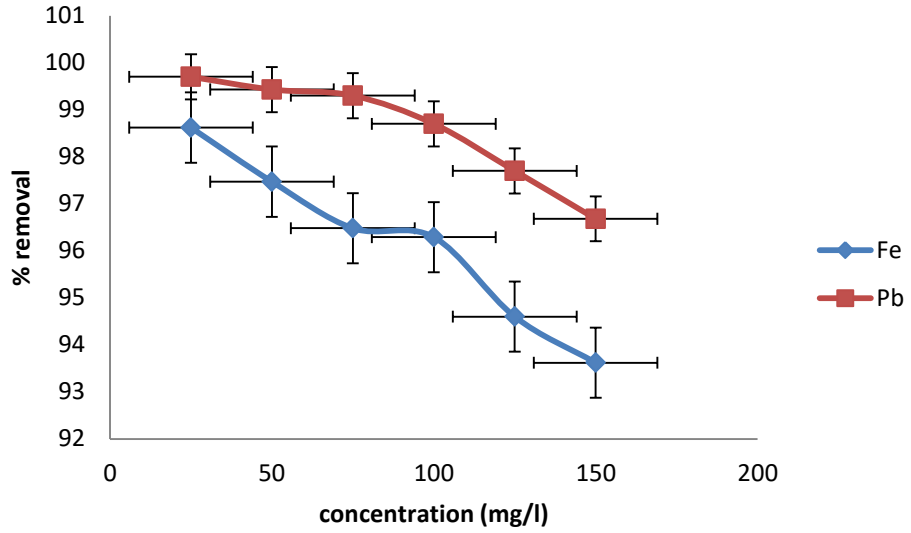

Figure 5. Effect of initial concentration on Pb(II) and Fe(II) adsorption onto *Tithonia diversifolia* activated carbon

3.2.2 Effect of Adsorbent Dosage

Different adsorbent doses (0.05–0.3 g/50 ml) on adsorption of Pb(II) and Fe(II) were analysed at a constant initial concentration of Pb(II) and Fe(II) solution (100 mg/l) under fixed parameters: pH = 6.4 and contact time 60 minutes. The percentage removal of Fe(II) and Pb(II) increased from 88.28 % to 98.04 % and 96.25 % to 99.38 % as shown in **Figure 6**. This showed that as adsorbent dose increased more surface area was available which exposed more active sites for binding metal ions.

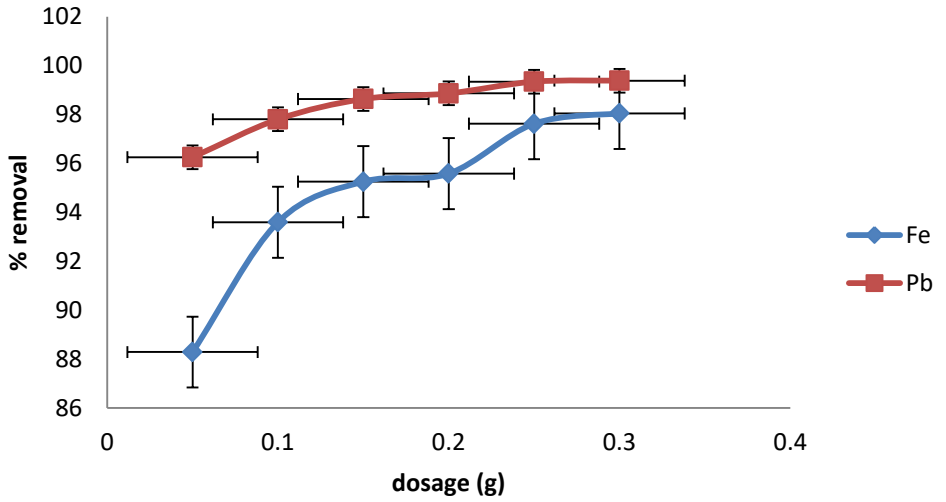

Figure 6. Effect of adsorbent dosage on Pb(II) and Fe(II) adsorption onto *Tithonia diversifolia* activated carbon

3.2.3 Effect of Contact Time

The effect of contact time on the adsorption of Fe(II) and Pb(II) was investigated. 93% of Fe(II) and 98.2% of Pb(II) was adsorbed at equilibrium, though the percentage removal increased from 90.15% to 95.28 and 96.78% to 99.2% between 30-180mins for Fe(II) and Pb(II) respectively. It can be seen from **Figure 7** that the adsorption rate increased rapidly because the adsorption sites are readily available on the adsorbent but adsorption approaches equilibrium as the sites becomes saturated after 60 and 120 minutes for Pb(II) and Fe(II) respectively (Odubiyi *et al.* 2012; Tao *et al.* 2015).

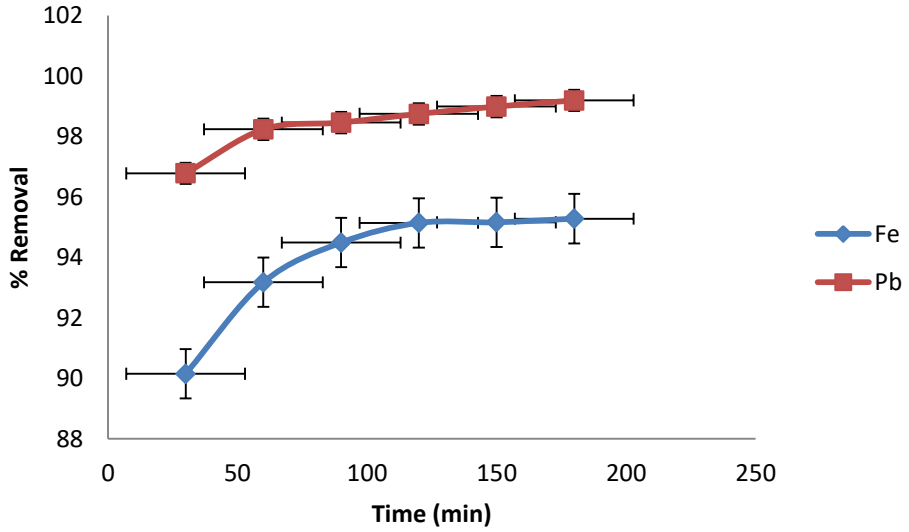

Figure 7. Effect of Contact Time on Pb(II) and Fe(II) Adsorption onto *Tithonia diversifolia* activated carbon

3.3 Equilibrium Isotherm Modelling

Adsorption isotherms are criteria used in optimising the use of adsorbents as they describe the nature of interaction between adsorbate and adsorbent. Langmuir, Freundlich and Temkin were used to study the adsorption of Pb(II) and Fe(II) under the conditions of 5 g/l dosage, 100 mg/l initial metal concentration, pH = 6.4, t = 60 mins. The results are shown in **Table 1**. The three models were in support of the study but Langmuir model fitted better than Freundlich and Temkin model for Pb(II) while Freundlich was the better fit for Fe(II). The main characteristic of Langmuir equation is a dimensionless constant called equilibrium parameter (R_L). The results obtained revealed R_L values of 0.1113 for Fe(II) and 0.00619 for Pb(II) which indicates a favourable adsorption (Albadarin *et al.* 2014; Cherdchoo *et al.* 2019). The maximum adsorption capacity was 31.55 mg/g for Pb(II) and 35.84 mg/g for Fe(II) while the maximum correlation coefficient is 0.9911 for Fe(II) and 0.9983 for Pb(II).

Table 1. Adsorption isotherm data for *Tithonia diversifolia* activated carbon

Model	Parameter	Metal ion	
		Pb(II)	**Fe(II)**
Langmuir	q_{max} (mg/g)	31.55	35.84
	b	0.6058	0.3195
	R_L	0.0062	0.1113
	R^2	0.9921	0.9691
Freundlich	K_F (L/mg)	16.49	8.7478
	n	2.402	1.8822
	1/n	0.4164	0.5313
	R^2	0.9635	0.995
Temkin	α (L/mg)	5.88	4.28
	β (kJ/mol)	6.9765	1.1043
	R^2	0.9478	0.7865

3.4 Adsorption Kinetics

The adsorption kinetics depends greatly on the physical and or chemical characteristics of the adsorbent and on the mass transfer process. The experimental data of adsorption of Pb(II) and Fe(II) onto the adsorbent at different time intervals were examined with pseudo-first-order and pseudo second-order models, using the plots of $Log\ (q_e - q_t)$ against t and t/q_t versus t, respectively. The results are shown in **Table 2**. The Pseudo second order gave a higher coefficient of determination >0.99, which implies that the basic adsorption is chemisorption involving sharing of electrons between the adsorbate and surface of the adsorbent. There is also a close range between $q_{e\,(\exp)}$ and $q_{e\,(calc)}$ which suggested that the adsorption of Pb(II) and Fe(II) was consistent with pseudo second order kinetic model.

Table 2. Adsorption kinetic data for *Tithonia diversifolia* activated carbon

Model	Parameters	Metal ion	
		Pb(II)	**Fe(II)**
	$q_{e\,(\exp)}$ (mg/g)	19.83	19.05
Pseudo first order	k_2 (min^{-1})	0.0341	0.0191
	$q_{e\,(calc)}$ (mg/g)	2.9	0.7619
	R^2	0.9593	0.9701
Pseudo second order	k_2 (g/mg.min)	0.0529	0.0261
	$q_{e\,(calc)}$ (mg/g)	19.92	19.31
	R^2	1.000	1.000

4. CONCLUSION

Sunflower (*Tithonia diversifolia*) stalk was harnessed as a precursor in preparing adsorbents for the removal of Pb(II) and Fe(II) from aqueous solutions. The biomass was acid activated by wet impregnation with phosphoric acid and carbonised at 500^{o}C. Transform Infra-Red Spectroscopy (FTIR) revealed the presence of several key functional groups needed for the adsorption of heavy metals such as N-H and O-H groups. Branueur Emmet and Teller analysis (BET) revealed that the adsorbent was mesoporous with and has a surface area of 325.375 m^2/g. Scanning Electron Microscopy with Energy-Dispersive X-ray Spectroscopy (SEM-EDS) revealed that the adsorbent has a highly heterogeneous surface which is favourable for adsorption. The effect of pollutant concentration, adsorbent dosage and contact time was studied for both Pb(II) and Fe(II) uptake. The best fit isotherm model for Pb(II) and Fe(II) was Langmuir and Freundlich Models respectively. The monolayer adsorption capacity of the adsorbent to Pb(II) and Fe(II) was 31.55 mg/g and 35.84 mg/g respectively. The pseudo second order was the best fit kinetic model. The study was able to reveal that Sunflower (*Tithonia diversifolia*) stalk can be used to prepare cost effective adsorbents for water treatment.

Disclosure Statement

Conflict of Interest: The authors declare that there are no conflicts of interest.

Compliance with Ethical Standards: This article does not contain any studies involving human or animal subjects.

REFERENCES

Achaw O-W (2012) A study of the porosity of activated carbons using the scanning electron microscope. In: Scanning Electron Microscopy. InTech,

Adeniyi AG, Ighalo JO (2019) Biosorption of Pollutants by Plant Leaves: An Empirical Review Journal of Environmental Chemical Engineering 7 doi:http://dx.doi.org/10.1016/j.jece.2019.103100

Al-Othman ZA, Ali R, Naushad M (2012) Hexavalent chromium removal from aqueous medium by activated carbon prepared from peanut shell: adsorption kinetics, equilibrium and thermodynamic studies Chemical Engineering Journal 184:238-247 doi:http://dx.doi.org/10.1016/j.cej.2012.01.048

Albadarin AB, Mo J, Glocheux Y, Allen S, Walker G, Mangwandi C (2014) Preliminary investigation of mixed adsorbents for the removal of copper and methylene blue from aqueous solutions Chemical engineering journal 255:525-534

Alhamed YA (2006) Activated carbon from dates' stone by ZnCl2 activation JKAU Eng Sci 17:75-100

Awoyale A, Eloka-Eboka A, Odubiyi A (2013) Production and experimental efficiency of activated carbon from local waste bamboo for wastewater treatment International Journal of Engineering and Applied Sciences 3:8-10

Ayeni A, Lordbanjou D, Majek B (1997) Tithonia diversifolia (Mexican sunflower) in south-western Nigeria: occurrence and growth habit Weed research 37:443-449

Babalola B (2018) Investigating adsorption characteristics of Delonix regia for heavy metals removal in wastewater and its potential for remediating contaminated soils. Lancaster University

Babarinde A, Onyiaocha GO (2016) Equilibrium sorption of divalent metal ions onto groundnut (Arachis hypogaea) shell: kinetics, isotherm and thermodynamics Chem Int 2

Babatunde EO, Akolo SA, Ighalo JO, Kovo AS (2019) Response Surface Optimisation of the Adsorption of Cu (II) from Aqueous Solution by Crab Shell Chitosan. Paper presented at the 3rd International Engineering Conference, Minna, Nigeria,

Balcıoğlu IA, Ötker M (2003) Treatment of pharmaceutical wastewater containing antibiotics by O3 and O3/H2O2 processes Chemosphere 50:85-95

Bello OS, Ahmad MA (2011) Adsorptive removal of a synthetic textile dye using cocoa pod husks Toxicological & Environmental Chemistry 93:1298–1308

Cherdchoo W, Nithettham S, Charoenpanich J (2019) Removal of Cr (VI) from synthetic wastewater by adsorption onto coffee ground and mixed waste tea Chemosphere 221:758-767

Egila J, Dauda B, Iyaka Y, Jimoh T (2011) Agricultural waste as a low cost adsorbent for heavy metal removal from wastewater International Journal of Physical Sciences 6:2152-2157

Eletta AAO, Adeniyi AG, Magaji MM, Ighalo JO A Mini-Review on the Application of Alumina Nano-Particles for Water Treatment. In: FUOYE science conference, Oye-ekiti, Nigeria, 2019. pp 4-8

Eletta AAO, Ighalo JO (2019) A Review of fish scales as a Source of Biosorbent for the Removal of Pollutants from Industrial Effluents Journal of Research Information in Civil Engineering 16:2479-2510

Farhan AM, Salem NM, Ahmad AL, Awwad AM (2012) Kinetic, Equilibrium and Thermodynamic Studies of the Biosorption of Heay Metals by Ceratonia Siliqua Bark American Journal of Chemistry 2:335-342

Fauzia S, Aziz H, Dahlan D, Zein R Study of equilibrium, kinetic and thermodynamic for removal of Pb(II) in aqueous solution using Sago bark (Metroxylon sago). In: Proceedings of the 3rd International Symposium on Current Progress in Mathematics and Sciences (ISCPMS2017), 2018. doi:http://dx.doi.org/10.1063/1.5064078

Foo K, Hameed B (2012) Factors affecting the carbon yield and adsorption capability of the mangosteen peel activated carbon prepared by microwave assisted K2CO3 activation Chemical engineering journal 180:66-74

Francis MM (2015) Aluminophosphates Derived From Tea Leaves And Pumpkin Seeds Ashes For Removal Of Selected Heavy Metals From Contaminated Water.

Geremew B (2017) A Review on Elimination of Heavy Metals from Wastewater Using Agricultural Wastes as Adsorbents Science Journal of Analytical Chemistry 5:72-75
doi:http://dx.doi.org/10.11648/j.sjac.20170505.12

Hegazi HA (2013) Removal of heavy metals from wastewater using agricultural and industrial wastes as adsorbents HBRC journal 9:276-282

Isah U, Yusuf A (2012) Adsorption of lead ions on groundnut shell activated carbon Der Chemica Sinica 3:1511-1515

Jaishankar M, Tseten T, Anbalagan N, Mathew BB, Beeregowda KN (2014) Toxicity, mechanism and health effects of some heavy metals Interdisciplinary toxicology 7:60-72

Kano N (2015) Adsorption of Heavy Metal onto the Materials Prepared by Biomass. In: Biomass Production and Uses. InTech,

Krishna C (2014) A Research On Cocoa Pod Husk Activated Carbon For Textile Industrial Wastewater Colour Removal International Journal of Research in Engineering and Technology 3:731-737

Kumar A, Jena HM (2016) Preparation and characterization of high surface area activated carbon from Fox nut (Euryale ferox) shell by chemical activation with H3PO4 Results in Physics 6:651-658

Largitte L, Brudey T, Tant T, Dumesnil PC, Lodewyckx P (2016) Comparison of the adsorption of lead by activated carbons from three lignocellulosic precursors Microporous and Mesoporous Materials 219:265-275

Ling Pua F, Sajab MS, Chia CH, Zakaria S, Rahman IA, Salit MS (2013) Alkaline-treated cocoa pod husk as adsorbent for removing methylene blue from aqueous solutions Journal of Environmental Chemical Engineering 1:460-465

Odubiyi OA, Awoyale AA, Eloka-Eboka AC (2012) Wastewater Treatment with Activated Charcoal Produced from Cocoa Pod Husk International Journal of Environment and Bioenergy 4:162-175

Pinho S, Ladeiro B (2012) Phytotoxicity by lead as heavy metal focus on oxidative stress Journal of Botany 2012

Salam OEA, Reiad NA, ElShafei MM (2011) A study of the removal characteristics of heavy metals from wastewater by low-cost adsorbents Journal of Advanced Research 2:297-303

Tao H-C, Zhang H-R, Li J-B, Ding W-Y (2015) Biomass based activated carbon obtained from sludge and sugarcane bagasse for removing lead ion from wastewater Bioresource Technology 192:611-617

Üner O, Geçgel Ü, Bayrak Y (2015) Preparation and characterization of mesoporous activated carbons from waste watermelon rind by using the chemical activation method with zinc chloride Arabian Journal of Chemistry

Yahya MA, Al-Qodah Z, Ngah CZ (2015) Agricultural bio-waste materials as potential sustainable precursors used for activated carbon production: A review Renewable and sustainable energy reviews 46:218-235

Yakub I, Mohammad M, Yaakob Z Effects of zinc chloride impregnation on the characteristics of activated carbon produced from physic nut seed hull. In: Advanced Materials Research, 2013. Trans Tech Publ, pp 751-755

MODEL PREDICTIVE CONTROL OF A TUBULAR AMMONIA REACTOR-HEAT EXCHANGER SYSTEM WITH SQUARE AND NON-SQUARE CONTROL STRUCTURES USING SINGULAR VALUE DECOMPOSITION (SVD) Part I: Development of the MPC Algorithm and SVD Computation

***Williams, A. O. F. and Adeniyi, V. O.**
Department of Chemical & Petroleum Engineering
University of Lagos, Akoka, Lagos
*Correspondence Author: bmnpsvg@gmail.com

ABSTRACT

This paper presents a multivariable model predictive control design strategy which incorporates manipulated variable blocking, and its computation using the singular value decomposition (SVD) approach. The attraction of the SVD approach is that it is a more reliable and transparent method of computing the solution of unconstrained least-squares optimization problems which often become ill-conditioned for typical tuning and design parameters employed in model predictive control. Guidelines for the application of the SVD approach are presented and discussed.

1 INTRODUCTION

Control system design involves two subtasks(Manousiothakis *et al.,* 1986):

1. selection of a control structure i.e. set of measurements and manipulated variables
2. decision on the structure interconnecting the measured and manipulated variables, along with the control law governing the interconnections.

Williams and Adeniyi (2018a) applied the dynamic resilience analysis technique for selection of the most promising control structures for a tubular ammonia reactor-heat exchanger system. This was undertaken as part of the task of advanced control design for the system. Improved control and operation of the ammonia reactor system is an industrially important goal since the Haber process for production of ammonia is the major process in the manufacture of nitrogenous fertilizers - a vital input for modern farming.

After selecting the most promising control structures, the next step in the controller design process is to decide on the controller structure i.e. the interconnections between the sets of inputs (manipulated variables) and outputs (controlled) variables. This is then followed by the actual design of the control laws based on the selected configuration.

For multi-input, multi-out (MIMO) systems, two choices exist for the controller structure: a *centralized* or *decentralized* controller structure. In the *centralized* controller structure, all the measurements are interconnected to all the manipulated variables and this allows the best achievable performance. In the *decentralized* approach, such as the multi-loop structure, one measurement is connected to only one input. This approach (when properly formulated) is more flexible, has lower communication cost, improved safety/fault tolerance, and easier monitoring and on-line tuning (Arkun, 1986; Manousiothakis *et al.,* 1986). Unfortunately, however, the *decentralized* controller structure is not applicable to non-square systems which is one of the requirements or conditions we wish to be able to address in this work. Furthermore, only the *centralized* controller structure allows the attainments of the best achievable performance. Consequently, we chose a *centralized* controller structure in this study.

In this final stage, the actual controller design i.e. derivation of the control law and selection of the tuning parameters, is to be carried out for the most promising control/measurement structure(s) previously identified in Williams and Adeniyi (2018a). The controller design technique should satisfy the following requirements, amongst others: (1) be easily computed so that undue computational burden is not placed on the process control computer, (2) be easily tuned on-line when necessary, (3) have multivariable features that allow a treatment of square as well as non-square systems, and (4) have excellent performance and robustness characteristics.

A technique that meets all the above criteria is Model Predictive Control (MPC) and is adopted for the actual controller design for the tubular ammonia reactor-heat exchanger system previously considered in Williams and Adeniyi (2018a).

Model Predictive Control (MPC) is used to describe the general class of the relatively new generation advanced control techniques which employ directly, a discrete convolution model of either impulse or step response elements for controller design. The underlying concept of MPC is that the future behaviour of a controlled variable is predicted from the present into the future, using a model of the process, and the value of manipulated variables (inputs) are determined such that the predicted values of the controlled variable is a best fit (in a given sense) to a desired value. For more detailed overview of general MPC, see Camacho and Bordons (1995), Lee (2011), Orukpe (2012) and more recently Levine (2019) and the references therein.

MPC has both feedforward and feedback control in its structure. The task of using the model to predict the changes in output and then determining the input to make the predicted output fit the desired value is the feedforward control of MPC. On the other hand, the task of making the observed output the new starting point is the feedback property of MPC. The effect of plant/model mismatch (which always exist in practice) is taken into account in the determination of the input by making the observed output the new starting point for subsequent prediction, and iteratively carrying out the determination of the input (Takamatsu *et al.*, 1988). Thus, MPC replaces the fixed-structure explicit control law (common in other control techniques) with on-line optimization. This makes it possible to deal easily with (1) square and non-square systems, (2) constraints on the manipulated or and controlled variables, and (3) the failure of actuators. While (2) and (3) are important properties/features of MPC, they are not explicitly addressed in our present study.

When input and other constraints are not addressed in an MPC formulation, the solution for the manipulated input becomes a least-squares optimization problem which can become ill-conditioned for typical design parameter values employed. In standard model predictive control (cf. Garcia and Morari, 1982, 1985; Marchetti et al., 1983), input penalty matrices are used for dealing with the ill-conditioning problem and for reducing the aggressiveness of manipulated variable moves. However, this approach has the principal disadvantage that the particular choice of input penalty matrices needed to properly condition the problem is not at all obvious and must therefore be chosen by trial and error. Thus, the motivation for using the singular value decomposition (SVD) is that it is a more reliable way of handling ill-conditioned or rank deficient least-squares optimization problems (cf. Forsythe *et al.*, 1977). Pan *et al*. (2016) have also employed the singular value decomposition to address the problem of ill-conditioned models in model predictive control problem formulation.

In this current paper (Part I), we present the development/formulation of the MPC problem starting from a state-space model, derivation of the control law and its computation using the Singular Value Decomposition (SVD), and then discuss some guidelines for its application. An abridged version of this work was presented in Williams and Adeniyi (2018b) and applied to the case of 2×2 control structures for a tubular ammonia reactor-heat exchanger system. This current work expands on this to include application to 2×3 (non-square) and 3×3 (square) control structures which are presented in the companion paper (Part II). Comparisons of the performance of the SVD-based model predictive controllers with mutli-loop PI controllers previously reported in the literature are also included in Part II.

2 METHODOLOGY

The design of a model predictive controller involves (Garcia and Prett, 1986; Prett and Garcia, 1988): (1) Identification of a linear dynamic (input/output) model relating the manipulated variables to the outputs of interest, (2) Statement of the control objective(s), and (3) Computation of the control law and closed loop implementation.

The development presented in this paper is concerned with only the unconstrained linear model predictive control problem. We assume that the model is open-loop stable. If this is not so, classical techniques such as proportional output feedback control may be used to first stabilize the system before carrying out the model predictive controller design. Also, it is assumed that the control algorithm is implemented in a sample-data system (such as is suitable for implementation on a digital process control computer) so that discrete-time model of the process is considered in which values are known only at discrete intervals of time k:

$$k\tau \le time \le (k+1)\tau$$

where τ is the sampling time of the system.

2.1 Identification of a Linear Input/Output Model of the Process

Based on the results of control structure analysis reported in Williams and Adeniyi (2018a), the linear systems

under consideration are all given by state-space equations of the form:

$$\dot{\mathbf{x}} = \mathbf{A}_1\mathbf{x} + \mathbf{B}_1\mathbf{u} + \mathbf{D}_m\mathbf{d}_m$$
$$\mathbf{y} = \mathbf{C}\mathbf{x} \qquad (1)$$

$\mathbf{x}_0 = \mathbf{0}$, where $\mathbf{x} \in \Re^s$, $\mathbf{u} \in \Re^m$, $\mathbf{d}_m \in \Re^r$, and $\mathbf{y} \in \Re^n$, are the vector of the state, manipulated, measurable disturbances and the output variables, respectively. $\mathbf{A}_1, \mathbf{B}_1, \mathbf{D}_m$, and $\mathbf{C}$ are matrices of appropriate dimensions.

2.1.1 Discretization of the continuous model

Since the model predictive control algorithm is normally implemented in a sample-data system, it is necessary to discretize Eq. (1) into the appropriate form. In a sample-data system such as digital computer control, the output of interest is sampled at finite intervals of time τ and the input applied to the system is constant over each interval. This produces a "stair case" input profile:

$$u(t) = u(k); \quad k\tau \le t \le (k+1)\tau$$

where $k = 0, 1, 2, \mathrm{K}$, represent discrete-time interval.

Based on the above, and through a process of simple integration, Eq. (1) can be represented at every discrete interval k, as:

$$\mathbf{x}(k+1) = \mathbf{F}\mathbf{x}(k) + \mathbf{G}\mathbf{u}(k) + \mathbf{G}'\mathbf{d}_m(k)$$
$$\mathbf{y}(k+1) = \mathbf{C}\mathbf{x}(k+1); \ \mathbf{x}(0) = \mathbf{0} \qquad (2)$$

where:

$$\mathbf{F} = e^{\mathbf{A}_1\tau}, \quad \mathbf{G} = \int_0^\tau e^{\mathbf{A}_1 t}\mathbf{B}_1 dt, \quad \mathbf{G}' = \int_0^\tau e^{\mathbf{A}_1 t}\mathbf{D}_m dt \qquad (3)$$

and τ is the sample time.

Let

$$\mathbf{H}_i = \mathbf{C}\mathbf{F}^{i-1}\mathbf{G}, \quad \mathbf{H}'_i = \mathbf{C}\mathbf{F}^{i-1}\mathbf{G}' \qquad (4)$$

$\mathbf{H}_i$ is the so-called impulse response coefficient that relates the effects of the manipulated variable (inputs) to the output variables; while $\mathbf{H}'_i$ is the impulse response coefficient that relates the effects of the measured disturbances to the outputs.

For N sufficiently large, $\mathbf{x}(k-N+1) \to \mathbf{x}(0) = \mathbf{0}$, it can easily be shown that:

$$\mathbf{y}(k+1) = \sum_{i=1}^{N}\mathbf{H}_i\mathbf{u}(k-i+1) + \sum_{i=1}^{N}\mathbf{H}'_i\mathbf{d}_m(k-i+1) \qquad (5)$$

For open-loop stable (or stabilised) systems, $\mathrm{H}_i \to 0$ as $i \to \infty$ so that a finite N samples is sufficient to describe the system.

An alternative input/output model using step response coefficients can also be used (Prett and Garcia, 1988; Maurath et al., 1988a,b) as is done in Dynamic Matrix Control (DMC), by defining a change in inputs as follows:

$$\Delta\mathbf{u}(k) = \mathbf{u}(k) - \mathbf{u}(k-1) \qquad (6)$$

$$\Delta\mathbf{d}_m(k) = \mathbf{d}_m(k) - \mathbf{d}_m(k-1) \qquad (7)$$

and substituting into Eq. (5). However, in this study, we shall make use of the impulse response model for the control computation.

Let $\mathbf{d}_u(k)$ represent process characteristics such as plant/model mismatch, unmeasurable disturbances (including noise) which are not accounted for in the outputs of the impulse response model; then the process output is given by

$$\mathbf{y}(k+1) = \sum_{i=1}^{N}\mathbf{H}_i\mathbf{u}(k-i+1) + \sum_{i=1}^{N}\mathbf{H}'_i\mathbf{d}_m(k-i+1) + \mathbf{d}_u(k) \qquad (8)$$

2.1.2 The prediction problem

.At time $\bar{k}$, we now use the impulse response model, Eq. (8) to predict future values of the outputs $\mathbf{y}(k)$ over a time horizon, P. Thus, for any future interval of time, the output prediction is given (for a non-zero initial condition, $\mathbf{y}_0$) by

$$\mathbf{y}(\bar{k}+l) = \mathbf{y}_0 + \mathbf{H}_1\mathbf{u}(\bar{k}+l-1) + \mathbf{H}_2\mathbf{u}(\bar{k}+l-2) + \cdots + \mathbf{H}_N\mathbf{u}(\bar{k}+l-N)$$
$$+ \mathbf{H}'_1\mathbf{d}_m(\bar{k}+l-1) + \mathbf{H}'_2\mathbf{d}_m(\bar{k}+l-2) + \cdots + \mathbf{H}'_N\mathbf{d}_m(\bar{k}+l-N)$$
$$+ \mathbf{d}_u(\bar{k}+l), \quad l = 1, 2, \ldots, P \qquad (9)$$

Let us assume that the measured disturbance variables $(\mathbf{d}_m(\bar{k}+l))$ do not change over the entire future time intervals $(l = 1, 2, \mathrm{K}, P)$, but may be measured at the current time, $\bar{k}$, i.e.

$$\mathbf{d}_m(\bar{k}) = \mathbf{d}_m(\bar{k}+1) = \cdots = \mathbf{d}_m(\bar{k}+P) \qquad (10)$$

then, Eq. (9) can be re-written as

$$\mathbf{y}(\bar{k}+l) = \sum_{j=1}^{l}\mathbf{H}_j\mathbf{u}(\bar{k}+l-j) + \mathbf{y}^{\mathring{a}}(\bar{k}+l) + \mathbf{d}_u(\bar{k}+l), \quad l = 1, 2, \ldots, P \qquad (11)$$

where the term $\mathbf{y}^{\mathring{a}}(\bar{k}+l)$ is given by

$$\mathbf{y}^{\mathring{a}}(\bar{k}+l) = \mathbf{y}_0 + \sum_{j=l+1}^{N}\mathbf{H}_j\mathbf{u}(\bar{k}+l-j) + \sum_{j=l+1}^{N}\mathbf{H}'_j\mathbf{d}_m(\bar{k}+l-j) + \sum_{j=1}^{l}\mathbf{H}'_j\mathbf{d}_m(\bar{k}) \qquad (12)$$

and is the contribution to the future values $(l = 1, 2, \mathrm{K}, P)$ of the outputs due to past inputs (both

manipulated and measured disturbance variables) up to time $\bar{k}-1$, and the most recent measured disturbance, $\mathbf{d}_m(\bar{k})$.

In Eq. (11), future unmodelled effects $\mathbf{d}_u(\bar{k}+l)$ are unknown at the present time, $\bar{k}$, and must therefore be estimated. This is done as follows:

For $l=0$ (present-time prediction, $\bar{k}$), Eq. (11) becomes:

$$\mathbf{y}(\bar{k}) = \mathbf{y}^{\text{å}}(\bar{k}) + \mathbf{d}_u(\bar{k}) \tag{13}$$

At present time $\bar{k}$, the process output measurement, $y_m(\bar{k})$ is available. Thus, $d_u(\bar{k})$ can be estimated as

$$\mathbf{d}_u(\bar{k}) = \mathbf{y}_m(\bar{k}) - \mathbf{y}^{\text{å}}(\bar{k}) \tag{14}$$

where

$$\mathbf{y}^{\text{å}}(\bar{k}) = y_0 + \sum_{j=1}^{N}\mathbf{H}_j\mathbf{u}(\bar{k}-j) + \sum_{j=1}^{N}\mathbf{H}'_j\mathbf{d}_m(\bar{k}-j) \tag{15}$$

is obtained from Eq. (12) by setting $l=0$. Although $\mathbf{d}_u(\bar{k}+l), l=1,2,\ldots,P$ may now be estimated by filtering theory (provided that there is additional knowledge about the noise statistics), the simplest approach is to set (cf. Garcia, 1984; Garcia and Prett, 1986; Prett and Garcia, 1988):

$$\mathbf{d}_u(\bar{k}+l) = \mathbf{d}_u(\bar{k}), \quad l=1,2,\ldots,P \tag{16}$$

which essentially matches the prediction at $\bar{k}$ to the present measurement, $\mathbf{y}_m$.

Substituting Eq. (16) into Eq. (11) we have

$$\mathbf{y}(\bar{k}+l) = \sum_{j=1}^{l}\mathbf{H}_j\mathbf{u}(\bar{k}+l-j) + \mathbf{y}^{\text{å}}(\bar{k}+l) + \mathbf{d}_u(\bar{k}), \quad l=1,2,\ldots,P \tag{17}$$

2.2 Statement of the Control Objective

Qualitatively, the control problem to be solved at time $\bar{k}$, is to determine the present [$u(\bar{k})$] and future values of the manipulated variables:[$\mathbf{u}(\bar{k}+l), l=1,2,\ldots,P-1$] such that the predicted future values of the outputs: $\mathbf{y}(\bar{k}+l), l=1,2,\ldots,P$ track the corresponding future set points, $\mathbf{y}_s(\bar{k}+l), l=1,2,\ldots,P$ in an optimal manner.

Mathematically, the present and future values of the manipulated inputs, $\mathbf{u}(\bar{k}+l), l=1,2,\ldots,P-1$ are to be determined by solving the following optimization problem:

$$\min_{\mathbf{u}(\bar{k}+l),l=1,2,\ldots,P-1}\sum_{l=1}^{P}\left[\left\|\mathbf{y}_s(\bar{k}+l)-\mathbf{y}(\bar{k}+l)\right\|^2_{\Gamma_l^T\Gamma_l} + \left\|\mathbf{u}(\bar{k}+l-1)\right\|^2_{\Lambda_l^T\Lambda_l}\right] \tag{18}$$

subject to Eq. (17); in which

$$\mathrm{P}\mathbf{z}\mathrm{P}_R^2 = \mathbf{z}^T\mathbf{R}\mathbf{z}$$

$\mathbf{\Gamma}_l$ and $\mathbf{\Lambda}_l$ are positive semi-definite weighting matrices which are taken to be diagonal in our present study.

If Eq. (17) is written for all future times from $(\bar{k}+1),(\bar{k}+2),\mathrm{K},(\bar{k}+P)$, we obtain the following values of the predicted outputs (after rearrangement into vector-matrix form):

$$\mathbf{Y} = \mathbf{X}\mathbf{U} + \mathbf{Y}^{\text{å}} + \mathbf{D}_u \tag{19}$$

where

$$\mathbf{Y} = \left[\mathbf{y}(\bar{k}+1)\ \ \mathbf{y}(\bar{k}+2)\cdots\mathbf{y}(\bar{k}+P)\right]^T;\ \mathbf{Y}\in\Re^{np};$$

$$\mathbf{U} = \left[\mathbf{u}(\bar{k})\ \ \mathbf{u}(\bar{k}+1)\cdots\mathbf{u}(\bar{k}+P-1)\right]^T,\quad \mathbf{U}\in\Re^{mp}$$

$$\mathbf{Y}^{\text{å}} = \left[\mathbf{y}^{\text{å}}(\bar{k}+1)\ \ \mathbf{y}^{\text{å}}(\bar{k}+2)\cdots\mathbf{y}^{\text{å}}(\bar{k}+P)\right]^T,$$

$$\mathbf{Y}^{\text{å}}\in\Re^{np};\quad \mathbf{D}_u = \left[\mathbf{d}_u(\bar{k})\ \ \mathbf{d}_u(\bar{k})\cdots\ \mathbf{d}_u(\bar{k})\right]^T\in\Re^{np}$$

and $\mathbf{X}$ is a lower block-triangular matrix, given by

$$\mathbf{X} = \begin{bmatrix}\mathbf{H}_1 & \mathbf{0} & \\ \mathbf{H}_2 & \mathbf{H}_1 & \mathbf{0} \\ \vdots & \vdots & \ddots \\ \mathbf{H}_P & \mathbf{H}_{P-1} & \ldots\mathbf{H}_1\end{bmatrix};\ \mathbf{X}\in\Re^{np\times mp} \tag{20}$$

If we define

$$\mathbf{Y}_s = \left[\mathbf{y}_s(\bar{k}+1)\ \ \mathbf{y}_s(\bar{k}+2),\ldots\mathbf{y}_s(\bar{k}+P)\right]^T,\ \mathbf{Y}_s\in\Re^{np}$$

then we can write the following unconstrained quadratic optimization problem

$$\min_{\mathbf{U}}\left[\left\|\mathbf{Y}_s-(\mathbf{X}\mathbf{U}+\mathbf{Y}^{\text{å}}+\mathbf{D}_u)\right\|^2_{\Gamma^T\Gamma} + \left\|\mathbf{U}\right\|^2_{\Lambda^T\Lambda}\right] \tag{21}$$

If we consider blocking of manipulated variables in the formulation of the model predictive control problem (cf. Reid *et al.*, 1980; Mehra *et al.*, 1981; Ricker, 1985), in which we constrain $\mathbf{U}$ by specifying that the manipulated variables are to be held constant over a block of sampling intervals, allowed to change, and then held constant over another block, and so on, then only the first element of U in each block is retained in the definition of $\mathbf{U}$ which now becomes (cf. Ricker, 1985):

$$\mathbf{U}_B^T = \left[\mathbf{U}_{k_1}^T\ \ \mathbf{U}_{k_2}^T\cdots\mathbf{U}_{k_q}^T\right] \tag{22}$$

where $k_1, k_2, \mathrm{K}, k_q$ indicate the sampling intervals at which each block starts, and are chosen such that

$$k_1 = 0$$
$$k_j < k_{j+1},\ j = 1, 2, \mathrm{K}, q-1,$$
$$k_q \le P-1$$

Eq. (22) indicates, for example, that

$$\mathbf{U}_{k_1} = \mathbf{U}_{k_1+1} = \cdots = \mathbf{U}_{k_2-1}$$

with the effect that the size of the X matrix will reduce because the columns representing each block must be added together for consistency with the blocked form of $\mathbf{U}$. For example, if $k_2 = 4$ and $k_3 = 7$, the first four columns of matrix $\mathbf{X}$ [Eq. (20)] would be added together, the next three would be added together, etc.

Based on the foregoing considerations, we can formulate our general model predictive control optimization problem as

$$\min_{\mathbf{u}_{k_1}, \mathbf{u}_{k_2}, \ldots, \mathbf{u}_{k_q}} \sum_{l=1}^{P} \left[\begin{array}{l} \left\| \mathbf{y}_s(\bar{k}+l) - \mathbf{y}(\bar{k}+l) \right\|^2_{\mathbf{\Gamma}_l^T \mathbf{\Gamma}_l} \\ + \left\| \mathbf{u}(\bar{k}+l-1) \right\|^2_{\mathbf{\Lambda}_l^T \mathbf{\Lambda}_l} \end{array} \right] \quad (24)$$

subject to Eq. (17) and

$$u_{k_1} = u_{k_1+1} = \mathrm{L} = u_{k_2-1}$$
$$u_{k_2} = u_{k_2+1} = \cdots = u_{k_3-1}$$
$$\mathrm{M}$$
$$u_{k_q} = u_{k_q+1} = \mathrm{L} = u_{k_P-1} \quad (25)$$

As pointed out by Ricker (1985), there are at least two potential advantages to blocking: (1) the dimensionality of the optimization problem can be greatly reduced by the elimination of variables from $\mathbf{U}$, while still retaining a large prediction horizon, P; (2) since blocking affects the form of $\mathbf{X}$, it represents an additional way to tune the controller. The blocking of the manipulated inputs $\mathbf{U}$ (but not the outputs $\mathbf{Y}$) is said to be analogous to using a state-deadbeat controller rather than an output-deadbeat controller which is likely to cause large fluctuations in the manipulated variables, especially for higher-order systems — such as lumped parameter approximants of DPS. Blocking can resolve such a problem. As noted by Ricker (1985, 1990), blocking is a generalization of the manipulated variable suppression parameter used for examples, by Garcia and Morari (1985a,b) and in DMC (Prett and Garcia, 1988). Cagienard *et al.* (2007), Shekhar and Manzie (2015) and Schwickart *et al.* (2016) present some more recent discussions of the benefits and strategies for move blocking in model predictive control.

Let there be q blocks of the manipulated variables at the samples periods: $k_1, k_2, \mathrm{K}, k_q$ according to Eq. (23). Then the blocked manipulated variables can be collected together in the vector $\mathbf{U}_b \in \Re^{mq}$ which is related to $\mathbf{U}$ according to the equation (23)

$$\mathbf{U} = \mathbf{T}_b \mathbf{U}_b \quad (26)$$

where $\mathbf{T}_b \in \Re^{mp \times mq}$ is a matrix of zeros and ones.

2.3 Computation of the Control Law and Implementation

The optimization problem given above is a standard linear least squares problem for which it is possible to easily obtain an analytical solution from the following development.

In terms of the blocked variables, $\mathbf{U}$ is related to $\mathbf{U}_b$ according to Eq. (26), thus, Eq. (19) can be re-written as

$$\mathbf{Y} = \mathbf{X}\mathbf{T}_b\mathbf{U}_b + \mathbf{Y}^{\mathring{a}} + \mathbf{D}_u \quad (27)$$

in which

$$\mathbf{U}_b = \left[\mathbf{u}_{k_1}^T \ \ \mathbf{u}_{k_2}^T \cdots \mathbf{u}_{k_q}^T \right] \in \Re^{mq}$$

Then in terms of the blocked manipulated inputs $\mathbf{U}_b$, Eq. (21) is equivalent to the following unconstrained quadratic optimization problem

$$\min_{\mathbf{U}_b} \left[\left\| \mathbf{E} - \mathbf{X}\mathbf{T}_b\mathbf{U}_b \right\|^2_{\mathbf{\Gamma}^T\mathbf{\Gamma}} + \left\| \mathbf{T}_b\mathbf{U}_b \right\|^2_{\mathbf{\Lambda}^T\mathbf{\Lambda}} \right] \quad (28)$$

where

$$\mathbf{E}(\bar{k}+1) = \mathbf{Y}_s - \mathbf{D}_u - \mathbf{Y}^{\mathring{a}} = \left[\mathbf{Y}_s - \mathbf{D}_u \right] - \left[\mathbf{Y}^{\mathring{a}} \right] \quad (29)$$

Eq.(28) has the well-known least-squares solution given by

$$\mathbf{U}_b = \left[\mathbf{T}_b^T \mathbf{X}^T \mathbf{\Gamma}^T \mathbf{\Gamma} \mathbf{X} \mathbf{T}_b + \mathbf{T}_b^T \mathbf{\Lambda}^T \mathbf{\Lambda} \mathbf{T}_b \right]^{-1} \mathbf{T}_b^T \mathbf{X}^T \mathbf{\Gamma}^T \mathbf{\Gamma} \mathbf{E}(\bar{k}+1) \quad (30)$$

$$= \left[\mathbf{X}_b^T \mathbf{X}_b + \mathbf{T}_b^T \mathbf{\Lambda}^T \mathbf{\Lambda} \mathbf{T}_b \right]^{-1} \mathbf{X}_b^T \mathbf{E}(\bar{k}+1) \quad (31)$$

where $\mathbf{X}_b = \mathbf{\Gamma}\mathbf{X}\mathbf{T}_b$.

In the above equations/expressions, n is the number of output variables; m is the number of manipulated inputs, and P is the controller prediction horizon. We note that in this formulation, the number of inputs (m) may not necessarily be equal to the number of output variables (n).

2.3.1 Computation of control law using the singular Value decomposition (SVD)

If the matrix $\mathbf{X}_b$ has full rank i.e. Rank$[\mathbf{X}_b] = mq$ (where $mq \le np$) then the solution to the optimization problem is unique and can be reliably computed using Eq. (31). The assumption that $\mathbf{X}_b$ has full rank has been implicitly made in writing the solution as Eq. (31). However, when matrix $\mathbf{X}_b$ is rank deficient (i.e. Rank $[\mathbf{X}_b] = k < mq$) or nearly so, the solution $\mathbf{U}_b$ cannot be reliably computed using Eq. (31) because of ill-conditioning i.e. small changes in the elements of matrix $\mathbf{X}_b$ can result in large changes in the elements of the solution, $\mathbf{U}_b$. Furthermore, the solution $\mathbf{U}_b$ is then not unique. However, uniqueness is obtained by picking the shortest such solution (Forsythe *et al.*, 1977). The ill-conditioning problem occurs as the dimensions of the matrix $\mathbf{X}_b$ increases, especially for values of P and q parameters usually used for predictive controller designs.

The input penalty matrices, $\mathbf{\Lambda}_l, l = 1, 2, \ldots, P$ are used in standard model predictive control (cf. Garcia and Morari, 1982, 1985; Marchetti *et al.*, 1983) for dealing with the ill-conditioning problem and for reducing the manipulated variable moves much similar to the way the ridge parameter is used in ridge regression for statistical parameter estimation problems (Ogunnaike, 1983; 1986). However, this approach has the principal disadvantage that the particular choice of Λ_l needed to properly condition the problem is not at all obvious and must therefore be chosen by trial and error. For this reason, we set $\mathbf{\Lambda}_l = 0, l = 1, 2, \ldots, P$.

A more reliable way of handling ill-conditioned or rank deficient least-squares optimization problems is through the application of the singular value decomposition, SVD (cf. Forsythe *et al.*, 1977).

By employing the singular value decomposition (SVD) of a real matrix $\mathbf{X}_b \in \Re^{nP \times mq}$ defined as follows (cf. Forsythe *et al.*, 1977; Garbow *et al.*, 1977; Dongarra *et al.*, 1979; Klema and Laub, 1980)

$$\mathbf{X}_b = \mathbf{Q}_1 \mathbf{\Sigma} \mathbf{Q}_2^T \tag{32}$$

where $\mathbf{Q}_1 \in \Re^{nP \times nP}$, $\mathbf{Q}_2 \in \Re^{mq \times mq}$ are orthogonal matrices, and $\mathbf{\Sigma} \in \Re^{nP \times mq}$ is a matrix with entries $\sigma_{ij} = 0$ if $i \ne j$ and $\sigma_{ii} = \sigma_i \ge 0$, in which the quantities σ_i are the singular values of $\mathbf{X}_b$, and the columns of $\mathbf{Q}_1$ and $\mathbf{Q}_2$ are the *left and right singular vectors*, the solution of Eq. (28) can be put in the following form after some rearrangement:

$$\mathbf{U}_b = \mathbf{Q}_2 \mathbf{\Sigma}^+ \mathbf{Q}_1^T \Gamma \left[\mathbf{Y}_s - \mathbf{D}_u - \mathbf{Y}^{\text{å}} \right] \tag{33}$$

where $\mathbf{\Sigma}^+ \in \Re^{mq \times nP}$ is a matrix with entries $\sigma_{ij}^+ = 0$ if $i \ne j$ and $\sigma_{ii} = \sigma_i^+ \ge 0$, in which

$$\sigma_i^+ = \begin{cases} 1/\sigma_i & i = 1, 2, \text{K}, L \\ 0 & i = L+1, L+2, \text{K}, mq \end{cases}$$

With the moving horizon concept, only the first m values of the mq manipulated inputs computed from Eq. (33) are implemented on the actual process. When the next feedback measurement becomes available [i.e. new $\mathbf{D}_u(\bar{k}+1)$] the problem is solved again. In this regard, we should particularly note that only the vector $\mathbf{E}(\bar{k}+1) = [\mathbf{Y}_s - \mathbf{D}_u - \mathbf{Y}^{\text{å}}]$ in Eq. (33) changes at every sample time.

2.3.2 Controller Tuning and Stability

For systems where $m < n$, or for constrained systems where $m \ge n$, it may not be possible to achieve the desired control objective.

Garcia and Morari (1982, 1985a,b), and several other authors (Ricker, 1985; Maurath *et al.*, 1988a,b; Prett and Garcia, 1988; Erickson and Otto, 1991) have discussed the tuning and stability analysis of model predictive control algorithms. Because model predictive controllers have an internal model control structure (Garcia and Morari, 1982), stability of the controller is sufficient for closed-loop stability, provided the model is perfect and open-loop stable.

2.3.3 Computation of Multivariable Off-set Compensator

Finally, it should be pointed out that as fewer number of singular values are retained in the control law given by Eq. (33), the closed-loop system response becomes more sluggish and a point is latter reached when the controller is not able to eliminate offsets. Since integral action is achieved automatically (within the IMC framework) by making the steady-state controller gain the inverse of the model gain (Garcia and Morari, 1982, 1985a,b), it implies that offsets will result when

$$\mathbf{G}(1)\mathbf{G}_I(1) \ne \mathbf{I}$$

where $\mathbf{G}(1)$ is the steady-state gain of the model

z-transfer function, while $\mathbf{G}_I(1)$ is the steady-state gain of the controller z-transfer function. This problem is corrected by the use of the multivariable offset compensator proposed by Garcia and Morari (1985b):

$$\mathbf{G}_{OFF} = \left[\mathbf{G}(1)\mathbf{G}_I(1)\right]^{-1} \tag{34}$$

2.4 SVD Application Guidelines to MPC Controller Design

Most applications of the SVD require the specification of a tolerance or zero threshold, $\sigma^{å}$ for which Garbow *et al.* (1977) and Forsythe *et al.* (1977) recommend the following:

1. In problems involving experimental or inexact data

$$\sigma^{å} \geq \max_{i,j} |\Delta_{ij}| \tag{35}$$

where Δ_{ij} are errors in the elements of the matrix whose SVD is being computed.

2. For problems whose matrix elements are known exactly, or are contaminated only by round-off error:

$$\sigma^{å} \geq \sqrt{nP \times mq}\, ò \max_j \sigma_j \tag{36}$$

where $ò$ is the relative accuracy of the floating point arithmetic on the machine being used.

Following the specification of $\sigma^{å}$, the *effective rank* of the matrix $\mathbf{X}_b \in \Re^{nP\times mq}$ is the number of singular values which are greater than $\sigma^{å}$. If the effective rank of $\mathbf{X}_b$ is mq, then the matrix is of "full rank".

The SVD can be applied directly to the optimization problem as follows:

$$\rho(\mathbf{U}_b) = \min_{\mathbf{U}_b} \left\|\mathbf{E} - \mathbf{X}\mathbf{T}_b\mathbf{U}_b\right\|^2_{\mathbf{\Gamma}^T\mathbf{\Gamma}} \tag{37}$$

$$= \min_{\mathbf{U}_b} \left\|\mathbf{X}_b\mathbf{U}_b - \mathbf{\Gamma}\mathbf{E}\right\|^2 \tag{38}$$

$$= \min_{\mathbf{U}_b} \left\|\mathbf{Q}_1\mathbf{\Sigma}\mathbf{Q}_2^T\mathbf{U}_b - \mathbf{\Gamma}\mathbf{E}\right\|^2 \tag{39}$$

where $\mathbf{E}(\bar{k}+1)$ has been replaced with $\mathbf{E}$ for notational convenience only; and $\mathbf{X}_b = \mathbf{\Gamma}\mathbf{X}\mathbf{T}_b$ has been replaced by its SVD in Eq. (39).

Since orthogonal matrices preserve norm i.e.

$$\mathrm{P}\mathbf{Q}_1^T\mathbf{x}\mathrm{P}=\mathrm{P}\mathbf{x}\mathrm{P}$$

We can multiply Eq. (39) by $\mathbf{Q}_1^T$ without changing its norm, to obtain

$$\rho(\mathbf{U}_b) = \min_{\mathbf{U}_b} \left\|\mathbf{Q}_1^T\mathbf{Q}_1\mathbf{\Sigma}\mathbf{Q}_2^T\mathbf{U}_b - \mathbf{Q}_1^T\mathbf{\Gamma}\mathbf{E}\right\|^2 \tag{40}$$

$$= \min_{\mathbf{U}_b} \left\|\mathbf{\Sigma}\mathbf{Q}_2^T\mathbf{U}_b - \mathbf{Q}_1^T\mathbf{\Gamma}\mathbf{E}\right\|^2 \tag{41}$$

If we define the following:

$$\mathbf{w} = \mathbf{Q}_2^T\mathbf{U}_b \tag{42}$$

$$\mathbf{g} = \mathbf{Q}_1^T\mathbf{\Gamma}\mathbf{E} \tag{43}$$

Eq. (41) becomes

$$\rho(\mathbf{U}_b) = \min_{\mathbf{U}_b} \left\|\mathbf{\Sigma}\mathbf{w} - \mathbf{g}\right\|^2$$

$$= \min_{\mathbf{U}_b} \left\|\mathbf{\Sigma}\mathbf{w} - \mathbf{g}\right\| \tag{44}$$

since minimizing the square of the length is equivalent to minimizing the length itself. The vector $\mathbf{w}$ is known as the principal components in the literature (cf. Maurath *et al.*, 1988; Callaghan and Lee, 1988).

Thus, the application of the SVD reduces the least-squares problem to one involving an essentially diagonal matrix, $\mathbf{\Sigma}$.

When $\mathbf{X}_b$ is of rank k relative to $\sigma^{å}$, the *minimal norm* vector w, that solves the optimization problem [Eq. (44)] is given by (cf. Forsythe *et al.*, 1977):

$$w_j = \frac{g_j}{\sigma_j},\ \sigma_j \neq 0,\ j = 1,2,\mathrm{K}\,,k$$

$$w_j = 0,\ \sigma_j < \sigma^{å},\ j = k+1, k+2, \mathrm{K}\,, mq \tag{45}$$

Then, $\mathbf{U}_b$ is obtained from

$$\mathbf{U}_b = \mathbf{Q}_2\mathbf{w} \tag{46}$$

Eq. (45) shows that $w_j,\ j = 1,2,\mathrm{K}\,,k$, are solved exactly. The remaining ones lead to a possibly non-zero residual given by

$$\rho_k = \sum_{j=k+1}^{nP} g_j^2 = \sum_{j=1}^{nP} g_j^2 - \sum_{j=1}^{k} g_j^2 \tag{47}$$

Or, equivalently,

$$\bar{\rho}_k = \frac{\sum_{j=k+1}^{nP} g_j^2}{\sum_{j=1}^{nP} g_j^2} = 1 - \frac{\sum_{j=1}^{k} g_j^2}{\sum_{j=1}^{nP} g_j^2} \tag{48}$$

where ρ_k has been normalized to $\bar{\rho}_k$ by the largest possible residual which would occur if no singular value is included in the solution vector i.e. $\sum_{j=1}^{nP} g_j^2$, which is

the largest possible residual if all the solution components w_j, $j = 1,2,\mathrm{K},mq$ are set to zero.

To compute ρ_k (or equivalently, $\bar{\rho}_k$), it is necessary to specify $\mathbf{E}$. Under closed-loop control, $\mathbf{E}$ changes at every sample time and this change cannot be determined apriori. Hence, for the purpose of computing ρ_k (or $\bar{\rho}_k$), we assume a simultaneous unit step change in all the outputs i.e. $\mathbf{E}$ is taken as

$$\mathbf{E} = (1\ 1\cdots 1\ 1\ 1\cdots 1\cdots 1\ 1\cdots 1)^T \in \Re^{nP\times 1} \quad (49)$$

The sensitivity of the solution ($\mathbf{U}_b$) to errors in X_b is well known to be given by

$$\eta_L(X_b) = \frac{\sigma_1}{\sigma_L} \quad (50)$$

where σ_1 is the maximum singular value, and σ_L is the smallest singular value of the matrix $\mathbf{X}_b$ with effective rank, L.

The quantities, η_L and $\bar{\rho}_L, L = 1,2,\mathrm{K},k$, can be readily computed from the SVD matrices, and on the basis of their values, the designer may decide on the number of singular values to retain in the solution. A table can be constructed to aid the designer by listing the following:

1. The singular values of $\mathbf{X}_b$, $\sigma_i, i = 1,2,\mathrm{K},k$, where k is the effective rank of $\mathbf{X}_b$.
2. The condition number, η_L, assuming L number of singular values (arranged in descending order of magnitude) are retained in the solution i.e. $\eta_L = \sigma_1 / \sigma_L$.
3. The residual, ρ_L or $\bar{\rho}_L$, assuming L number of singular values (arranged in descending order of magnitude) are retained in the solution and the rest discarded.

3 DISCUSSIONS

The above completes the controller design strategy. To round up, let us state as follows: Joseph and Brosilow (1975) have earlier used the condition number and the residual ($\bar{\rho}$) as criteria for the selection of secondary measurements for inferential control of processes, for which a least-squares problem was formulated. They recommend a residual, $\bar{\rho} \le 0.05$, and a condition number, $\eta < 100$. However, they did not use the SVD technique as we have proposed here. Let us also state that Maurath *et al.* (1988b) have presented a principal component analysis (PCA) method for the design of a model predictive controller (such as DMC) using the SVD technique. The approach presented in this work, while similar to the approach of Maurath *al.* (1988b) in the use of the SVD technique, is entirely different and more straightforward.

4 CONCLUSION

This paper presented a multivaiable model predictive control design strategy which incorporated a general manipulated variable blocking and its computation using the singular value decomposition (SVD) approach. Guidelines for the application of the SVD approach were presented and discussed. The approach has been successfully applied to evaluate various 2×2, 2×3 and 3×3 control structures for a tubular ammonia reactor-heat exchanger system under nominal, additive plant/model mismatch and measurement noise. The results are presented in the companion paper (Part II) of this work.

REFERENCES

Arkun, Y. (1986).Dynamic Process Operability. Important Problems, Recent Results and New Challenges. *Proc. Chemical Process Control, CPC III*, Morari, M., and McAvoy, J. J., (Eds.), CACHE and Elsevier, Amsterdam.

Cagienard, R., Grieder, P., Kerrigan, E. and Morari, M.(2007). Move Blocking Strategies in Receding Horizon Control, *Journal of Process Control*, **17**, pp. 563-570.

Callaghan, P. J., and Lee, P. L.(1988). An Experimental Investigation of Predictive ControllerDesign By Principal Component Analysis, *Chem. Eng. Res. Des.*, **Vol. 66**, July, pp. 345-356.

Camacho, E. F., Bordons, C. (1995). *Model Predictive Control in the Process Industry*, Springer-Verlag London.

Dongarra, J. J., Moler, C. B., Bunch, B. R., and Stewart, G. W. (1979). *LINPACK User's Guide*, SIAM, Philadelphia.

Erickson, K. T., and Otto, R. E. (1991). Development of a Multivariable Forward Modeling Controller, *Ind. Eng. Chem. Res.*, **Vol. 30**, pp. 482-490.

Forsythe, G. E., Malcolm, M. A. and Moler, C. B. (1977).

Computer Methods for Mathematical Computations, Prentice-Hall, Inc., Englewood Cliffs, N. J.

Garbow, B. S., Boyle, F. M., Dongarra, J. J., and Moler, C. B. (1977). *Matrix Eigensystem Routine - EISPACK Guide Extension*, Lecture Notes in Computer Science **No. 51**, Springer, Berlin.

Garcia, C. E. (1984). Quadratic Dynamic Matrix Control of Nonlinear Processes: An Application to a Batch Reactor Process, AIChE Annual mtg. San Francisco, CA.

Garcia, C. E., and Morari, M. (1982). Internal Model Control. 1. A Unifying Review and Some New Results, *Ind. Eng. Chem. Process Des. Dev.*, **Vol. 21**, pp. 308‑323.

Garcia, C. E., and Morari, M.(1985a). Internal Model Control 2. Design Procedure for Multivariable Systems, *Ind. Eng. Chem. Process Des. Dev.*, **Vol. 24**, pp. 472‑484.

Garcia, C. E., and Morari, M. (1985b). Internal Model Control. 3. Multivariable Control Law Computation and Tuning Guidelines, *Ind. Eng. Chem. Process Des. Dev.*, **Vol. 24**, pp. 484‑494.

Garcia, C. E. and Prett, D. M. (1986). Advances in Industrial Model Predictive Control, *Proc.Chem. Process Control, CPC III*, Morari, M. and McAvoy, T. J., (Eds.); Elsevier, New York, pp. 245‑293.

Joseph, B., and Brosilow, C. B. (1970). Inferential Control of Processes, *AIChE J.*, **Vol. 24**, No. 3, pp. 485‑491.

Klema, V. C. and Laub, A. J. (1980). The singular value Decomposi- tion: Its Computation and some Applications, *IEEE Trans. Autom. Control*, **AC-25**, pp. 164‑176.

Lee, J. H., (2011). Model Predictive Control: Review of the Three Decades of Development, *Journal of Control Automation and Systems*, **Vol. 9**, No. 3, pp. 415-424.

Levine, W.S. (2019). The Essentials of Model Predictive Control. In: Rakovi´c S., Levine W. (eds) *Handbook of Model Predictive Control*, Control Engineering. Birkh¨auser, Cham., pp. 3‑27.

Manousiothakis, V., Savage, R., and Arkun, Y. (1986).Synthesis of Decentralized Process Control Structures Using the Concept of Block Relative Gain, *AIChE J.*, **Vol. 32**, No. 6, pp. 991‑1003.

Marchetti, J. L., Mellichamp, D. A., and Seborg, D. E. (1983). Predictive Control Based on Discrete Convolution Models, *Ind. Eng. Chem. Process Des. Dev.*, **Vol. 22**, pp. 488‑495.

Maurath, P. R., Mellichamp, D. A., and Seborg, D. E. (1988a). Predictive Controller Design for Single-Input/Single-Output (SISO) Systems, *Ind. Eng. Chem. Res.*, **Vol. 27**, pp. 956‑963.

Maurath, P. R., Laub, A. J. Seborg, D. E., and Mellichamp,D. A. (1988b). Predictive Controller Design by Principal Component Analysis, *Ind. Eng. Chem. Res.*, **Vol. 27**, pp. 1204‑1212.

Mehra, R. K., Rouhani, R., Eterno, J., Richalet, J.,and Rault, A.(1981). Model Algorithmic Control: Review and Recent Developments, *Proc. Chemical Process Control II Conference*, Seborg, D. E., and Edgar, T. F., (eds.), p. 287.

Ogunnaike, B. A. (1983). A Statistical Appreciation of Dynamic Matrix Control, *Proc. American Control Conference*, San Francisco, pp. 1126‑1131.

Ogunaike, B. A. (1986). Dynamic Matrix Control: A Non-Stochastic, Industrial Process Control Technique with Parallels in Applied Statistics, *Ind. Eng. Chem. Fundam.*, **Vol. 25**, No. 4, pp. 712‑718.

Orukpe, P. E. (2012). Model Predictive Control Fundamentals, *Nigerian Journal of Technology*, **Vol. 31**, No. 2, pp. 139-148.

Pan, H., Zou, T., Yu, H-b. and Du, D-w. (2016). Analysis and correction of ill-conditioned model in multivariable model predictive control, *Int. J. Modelling, Identification and Control*, **Vol. 26**, No. 2, pp.130‑139.

Prett, D. M., and Garcia, C. E. (1988). *Fundamental Process Control*, Butterworths: Stoneham, MA.

Reid, J. G. Chaffin, D. A., and Silverthorn, J, T. (1980). Output Predictive Algorithmic Control: Precision Tracking with Application to Terrain Following, *Proc. of Joint Automatic Control Conference*, p. FA 9-F.

Ricker, N. L. (1985). Use of Quadratic Programming for Constrained Internal Model Control, *Ind. Eng. Chem. Process Des. Dev*, **Vol. 24**, pp. 925‑936.

Ricker, N. L. (1990). Model Predictive Control with State Estimation, *Ind. Eng. Chem. Res.*, **Vol. 29**, pp. 374‑382.

Schwickart, T., Voos, H., Darouach, M., Bezzaoucha Reba ¨ ı, S. (2016). A Flexible Move Blocking Strategy to Speed up Model-Predictive Control while Retaining a High Tracking Performance, *Proc. Eur Control Conf.*, 29 Jun - 1 Jul, Aalborg, Denmark, pp. 764-769.

Shekhar, R. and Manzie, C. (2015). Optimal Move

Blocking Strategies for Model Predictive Control. *Automatica*, **61**, pp. 27-34.

Takamatsu, T., Hashimoto, I., Ohshima, M., and Ohno, H., A. (1988). study of Model Predictive Control (MPC) in Terms of it' s Structure and Degrees of Freedom, *Int. Chem. Eng.*, **Vol. 28**, No. 4, pp. 661‑668.

Williams , A. O. F. and Adeniyi, V. O. (2018a). Identification of New Control Structures for a Tubular Ammonia Reactor-Heat Exchanger System Using Dynamic Resilience Analysis, *Journal of the Nig. Soc. of Chem. Engrs.*, **Vol. 33**, No 1, pp. 116- 128.

Williams , A. O. F. and Adeniyi, V. O. (2018b). Model Predictive Control of a Tubular Ammonia Reactor System: Closed-Loop Evaluation of Alternate 2 x 2 Control structures, *Proc. 48th. Annual Conf. of Nig. Soc. of Chem. Engrs.*, Abeokuta, 8-10 Nov. 2018, pp. 474-485.

MODEL PREDICTIVE CONTROL OF A TUBULAR AMMONIA REACTOR-HEAT EXCHANGER SYSTEM WITH SQUARE AND NON-SQUARE CONTROL STRUCTURES USING SINGULAR VALUE DECOMPOSITION (SVD)

Part II: Application to an Ammonia Reactor-Heat Exchanger System

***Williams, A. O. F. and Adeniyi, V. O.**
Department of Chemical & Petroleum Engineering
University of Lagos, Akoka, Lagos
*Correspondence Author: bmnpsvg@gmail.com

ABSTRACT

In this paper, we present the application of a model predictive control (MPC) strategy to a tubular ammonia reactor-heat exchanger system based on the singular value decomposition (SVD) approach to computation of the control law. The SVD-based MPC controller was used to evaluate various 2×2, 2×3 *and structures under nominal, additive plant/model mismatch, and measurement noise. The closed-loop simulation results validated the previously reported outcome of the selection of the most promising* 2×2 *and* 2×3 *control structures, and rejection of the* 3×3 *control structures based on dynamic resilience analysis. The designed SVD-based MPC controllers performed better than a decentralized PI controller previously reported in the literature*.

.

1 INTRODUCTION

Improved control and operation of an ammonia reactor system is an industrially important goal since the Haber process for production of ammonia is the major process in the manufacture of nitrogenous fertilizers - a vital input for modern agricultural farming.

Williams and Adeniyi (2018a) applied the dynamic resilience analysis technique for selection of the most promising control structures for a tubular ammonia reactor-heat exchanger system rom the literature. This was undertaken as part of the task of advanced control design for the system such as model predictive control (MPC).

In a companion paper (Part I), the formulation of the MPC problem starting from a state-space model, derivation of the control law and its computation using the Singular Value Decomposition (SVD) was presented. In the present paper (Part II), the SVD-based MPC is applied to a series of previously selected control structures of the tubular ammonia reactor-heat exchanger system and assessed using closed-loop computer simulations.

An abridged version of this work which considered only 2×2 control structures was presented in Williams and Adeniyi (2018b). This current work expands on this to include 2×3 (non-square) and 3×3 (square) control structures, along with presentation of essential details that could not be included in the abridged paper. Comparisons of the performance of the SVD-based model predictive controllers with mutli-loop PI controllers previously reported in the literature are also presented.

2 THE AMMONIA TUBULAR-REACTOR HEAT EXCHANGER SYSTEM

A schematic diagram of the ammonia synthesis reactor-heat exchanger system under consideration as presented by Patnaik *et al.* (1980a,b) and Viswanadham *et al.*, 1979) is shown in Figure 1. The inlet gaseous mixture is split into three separate streams: (i) the main stream called the heat exchanger flow, $F_1(u_1)$; (ii) the second stream called the heat exchanger by pass flow, $F_2(u_2)$; and (iii) the third stream called the direct by pass flow, $F_3(u_3)$.

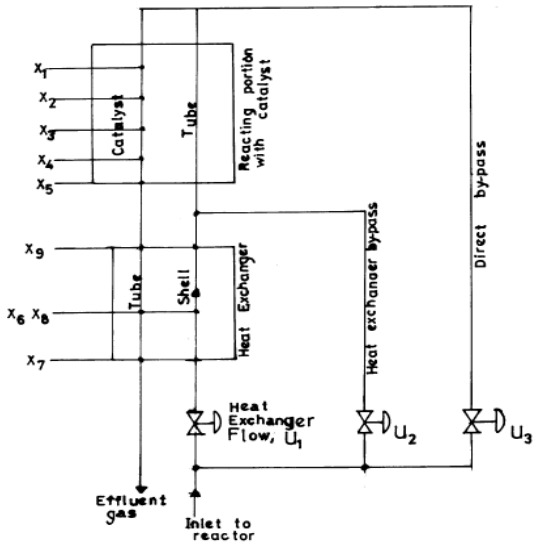

Figure 1: Schematic of ammonia synthesis reactor (Patnaik *et al.*, 1980a,b; Viswanadham *et al.*, 1979)

3 CONTROL STRUCTURES IDENTIFIED FROM DYNAMIC RESILIENCE ANALYSIS

Various control structures identified for the ammonia reactor-heat exchanger system using dynamic resilience analysis (Williams and Adeniyi, 2018a) which shall be considered in the SVD-based MPC design and closed-loop simulation evaluation are as follows:

- 2×2 control structures

(a) structure D i.e. control x_1 and x_5 with u_1 and u_2 .

(b) structure P i.e. control x_1 and x_9 with u_1 and u_2.

(c) structure X i.e. control x_1 and x_5 with u_1 and u_3 .

(d) structure AR i.e. control x_1 and x_5 with u_2 and u_3.

- 2×3 Control Structures.

(a) structure BL i.e. control x_1 and x_5 with u_1, u_2, and u_3.

(b) structure BN i.e. control x_1 and x_9 with u_1, u_2, and u_3.

(c) structure BQ i.e. control x_2 and x_5 with u_1, u_2, and u_3

(d) structure BU i.e. control x_3 and x_5 with u_1, u_2, and u_3

- 3×3 Control Structure: structure CL i.e. control x_1, x_4 and x_5 with the three control variables u_1, u_2, and u_3

4 APPLICATION OF MPC-SVD DESIGN TO THE TUBULAR-AMMONIA REACTOR-HEAT EXCHANGER SYSTEM

The model predictive controller designs for the ammonia reactor-heat exchanger system is based on the SVD technique presented in the companion paper (Part I). We considered design and closed-loop simulation evaluation for a number of 2×2, 2×3 and 3×3 control structures of the ammonia reactor system.

Preliminary designs/closed-loop simulations to assess the effect of design/tuning parameters on performance were first carried out for a 2×2 system using the control structure D, based on a perfect model assumption. The design and closed-loop simulations to determine the best control structures for the 2×2, 2×3 and 3×3 systems under nominal and plant/model mismatch conditions are then carried out. Following these, comparisons are made between the performance of the multivariable model predictive controller, and the decentralized (single-loop) PI controllers of Viswanadham *et al.*, 1979 in order to establish which one is superior.

5 RESULTS AND DISCUSSION

5.1 Preliminary Designs and Simulations

The initial design and closed-loop simulation evaluation of the model predictive controller to aid in proper selection of "fixed" tuning parameters was carried out for the ammonia reactor system with control structure D. After some trials, we chose a sampling time, $\tau = 0.4$, and a model horizon, $N = 80$. We chose the controller horizon, $q = 10$ to guarantee flexibility in the tuning of the controller. The following values of prediction horizon (P) and manipulated input blocking strategy were considered for the preliminary designs and closed-loop simulations:

1. $P = 10$, k_q = 0, 1, 2, 3, 4, 5, 6, 7, 8, 9
2. $P = 30$, k_q = 0, 1, 2, 3, 4, 5, 6, 7, 8, 9
3. $P = 20$, k_q = 0, 2, 4, 6, 8, 10, 12, 14, 16, 18
4. $P = 30$, k_q = 0, 3, 6, 9, 12, 15, 18, 21, 24, 27

Table 1 shows the results of the SVD analysis of the model predictive controller design (with control structure D) using various values of P and k_q given above. This table shows the computed singular values (σ_i), the condition numbers (η_i), and the normalized performance ($\bar{\rho}_i$) when $k = 1, 2, \ldots, i$ singular values are retained in the controller solution and others are discarded.

It is seen from Table 1 that the controller design based on this structure should be fairly robust as the η_{20} values lie between 6.90 to 44.5 for the four values of P and k_q shown. We also see that heavier blocking of the control input significantly reduces η_{20}, especially as the P/q ratio increases. This also suggests better robustness of the controller with heavier blocking of the control inputs. As expected, Table 1 shows that the closed-loop system performance (as measured by $\bar{\rho}_i$) improves (i.e. lower $\bar{\rho}_i$) as more singular values are retained in the controller solution.

Table 1: Results of SVD analysis of model predictive controller design for various values of P, q, and k_q. (Ammonia reactor system system with control structure D)

S/N.	Set (a)			Set (b)		
	σ_i	η_i	$\bar{\rho}_i$	σ_i	η_i	$\bar{\rho}_i$
1	0.0138	1.0000	0.9939	0.0631	1.0000	0.9922
2	0.0135	1.0206	0.9889	0.0495	1.2747	0.3342
3	0.0134	1.0334	0.9885	0.0138	4.5572	0.3342
4	0.0132	1.0436	0.9784	0.0135	4.6589	0.3237
5	0.0131	1.0545	0.9741	0.0134	4.7103	0.3147
6	0.0130	1.0616	0.9445	0.0133	4.7504	0.3089
7	0.0129	1.0693	0.9134	0.0131	4.8022	0.3070
8	0.0129	1.0723	0.8364	0.0130	4.8441	0.3062
9	0.0128	1.0761	0.7911	0.0129	4.8806	0.3059
10	0.0128	1.0778	0.7865	0.0129	4.9058	0.3058
11	0.0082	1.6822	0.0410	0.0128	4.9214	0.3057
12	0.0042	3.3136	0.0284	0.0090	7.0311	0.0176
13	0.0029	4.8375	0.0091	0.0044	14.3507	0.0084
14	0.0023	6.0884	0.0060	0.0029	22.0965	0.0031
15	0.0019	7.1098	0.0024	0.0022	28.4590	0.0016
16	0.0017	7.9490	0.0015	0.0019	33.5525	0.0007
17	0.0016	8.6305	0.0005	0.0017	37.6394	0.0003
18	0.0015	9.1625	0.0002	0.0015	40.8300	0.0001
19	0.0014	9.5454	0.0000	0.0015	43.1370	0.0000
20	0.0014	9.7767	0.0000	0.0014	44.5376	0.0000
S/N.	Set (c)			Set (d)		
	σ_i	η_i	$\bar{\rho}_i$	σ_i	η_i	$\bar{\rho}_i$
1	0.0208	1.0000	0.9014	0.0270	1.0000	0.7857
2	0.0195	1.0646	0.8975	0.0244	1.1039	0.7809
3	0.0192	1.0794	0.8974	0.0238	1.1314	0.7804
4	0.0191	1.0887	0.8959	0.0236	1.1434	0.7794
5	0.0189	1.0967	0.8959	0.0234	1.1514	0.7794
6	0.0188	1.1037	0.8946	0.0233	1.1578	0.7789
7	0.0187	1.1098	0.8945	0.0232	1.1628	0.7789
8	0.0186	1.1143	0.8938	0.0231	1.1666	0.7787
9	0.0186	1.1173	0.8938	0.0231	1.1690	0.7787
10	0.0182	1.1416	0.7921	0.0223	1.2090	0.7146
11	0.0148	1.3994	0.0467	0.0193	1.3983	0.0537
12	0.0095	2.1762	0.0440	0.0148	1.8242	0.0537
13	0.0066	3.1473	0.0154	0.0108	2.4902	0.0184
14	0.0050	4.1150	0.0128	0.0084	3.2298	0.0168
15	0.0041	5.0300	0.0069	0.0068	3.9877	0.0091
16	0.0035	5.8755	0.0058	0.0057	4.7363	0.0082
17	0.0031	6.6370	0.0041	0.0050	5.4485	0.0058
18	0.0028	7.2898	0.0037	0.0044	6.0866	0.0055
19	0.0027	7.7983	0.0034	0.0041	6.6002	0.0050
20	0.0026	8.1237	0.0033	0.0039	6.9354	0.0049

Plots in Figure 2 show the closed-loop simulation performance of the model predictive controller in the regulation of temperatures x_1 and x_5 for a 5^oC step change disturbance in the reactor feed temperature, with various numbers of singular values retained in the controller solution, and different tuning parameters. The corresponding control inputs (u_1, u_2) are shown in Figures 3.

When the foregoing plots are closely examined, one is able to make the following observations:

1. For different numbers of singular values (2 or more) retained in the controller solution, fast regulation of temperatures x_1 and x_5 without offsets is obtained.
2. The performance (settling time, overshoots, etc.) of temperature x_5 seem not to be affected by the values of P and k_q considered. However, the performance of temperature x_1 is slightly affected by values of P and k_q used. From Figure 2, it appears that $P = 10, q = 10$ and $k_q = 0,1,\ldots,9$ give the best performance for variable x_1 using feedback control alone.
3. From the plots of the control inputs (u_1, u_2), it is clear that it is not desirable to retain many singular values in the controller solution because it results in large and sudden changes in the controller outputs which might not be realizable in practice. It was generally found that retaining only 5 or less singular values in the controller solution seem to provide a more gradual change in the controller output which may be more readily achieved in practice.

On the basis of the foregoing observations, the following may be recommended in the tuning of the model predictive controller for the ammonia reactor system:

1. With no blocking of the manipulated variable i.e. $k_q = 0,1,2,\ldots,9$, using $P = q = 10$ gives the best closed-loop performance. However, if better robustness is desired, it seems one should use $P = 30$, $q = 10$, and $k_q = 0,3,6,\ldots,27$.
2. The number of singular values retained in the controller solution should lie between 2 and 5 in order for the controller to yield practically realizable control inputs.

5.2 Closed-loop Simulation of Different Control Structures

We now present the results of the model predictive controller design and closed-loop simulation for the ammonia reactor-heat exchanger system using different

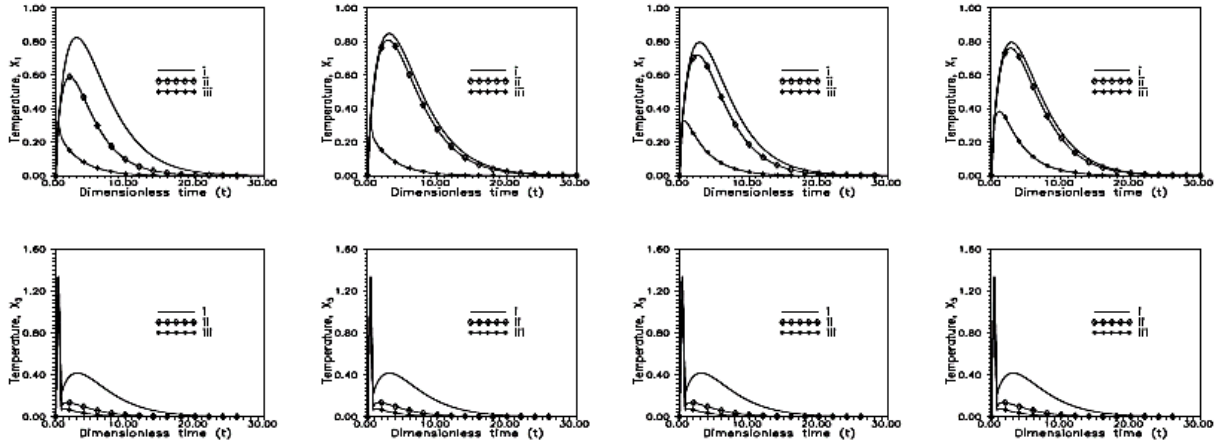

Figure 2: Closed-loop simulation responses of temperature x_1 (Top) and x_5 (Bottom) for a 5 ^{o} C step change disturbance in reactor feed temperature under MPC. 1st, 2nd, 3rd & 4th column plots from left to right are for the tuning parameter sets (a), (b), (c) and (d), respectively. Legend: i, ii, iii for 2, 11, and 20 singular values retained in controller solution.

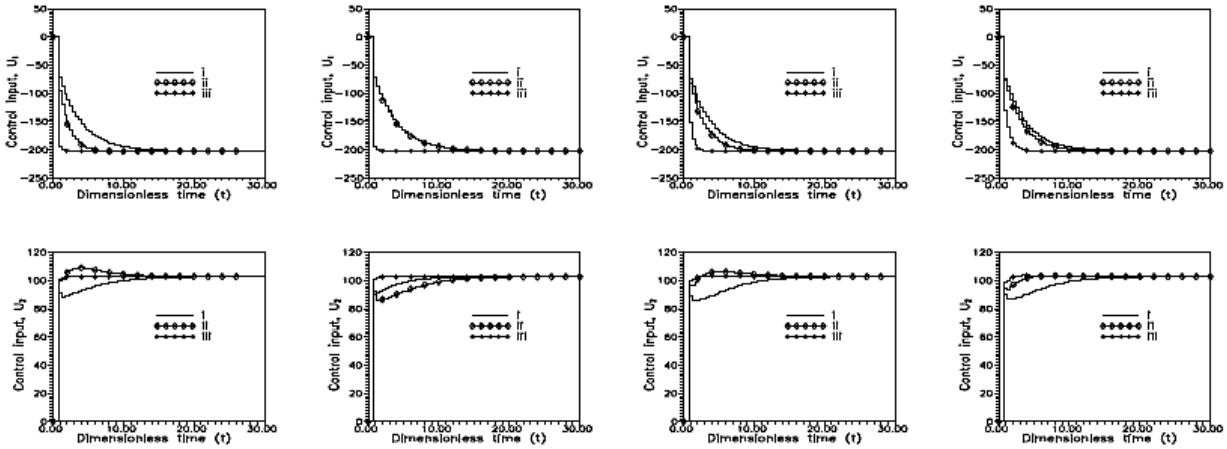

Figure 3: Manipulated control inputs: u_1 (Top) and u_2 (Bottom) for the response plots of Figure 2 1st, 2nd, 3rd & 4th column plots from left to right are for the tuning parameter sets (a), (b), (c) and (d), respectively. Legend: i, ii, iii for 2, 11, and 20 singular values retained in controller solution.

control structures. Closed-loop simulations were carried-out under nominal (perfect model assumptions) and model/plant mismatch conditions in the presence of significant noise in the temperature measurements. Model/plant mismatch conditions were created by assuming that the actual, linear plant matrices to be given by the following:

$$A_p = (1.+\Delta_e)A,\ B_p = (1.+\Delta_e)B,\ D_p = (1.+\Delta_e)D,$$

where A, B, and D are the linear model matrices employed in the model predictive controller designs.

The simulation results to be presented are for $\Delta_e = -0.9, 0$ and 0.9 in the case of the 2×2, 2×3, and 3×3 control structures with $\Delta_e = 0$ being the nominal case in which there is no model/plant mismatch. In all cases, temperature measurement noise was simulated by adding independent, zero-mean, normally distributed random numbers, each with a variance of 0.025 to the states x_1 to x_9 to produce the measured temperatures, two of which are fed back for control. The zero-mean, normally distributed random numbers were generated using a random number generator based on the algorithm presented in Forsythe *et al.* (1977). For the simulation results which follow, only feedback control was employed in the model predictive controller i.e. there

is no feedforward of the measurable, reactor feed temperature disturbance. The following tuning parameters were used for all the simulations: $\tau = 0.4$, $N = 80$, $P = 10$, $q = 10$, and $k_q = 0,1,2,\ldots,9$.

5.2.1 2×2 Control Structures

The following 2×2 control structures were selected for controller design and closed-loop simulation testings (a) structure D i.e. control x_1 and x_5 with u_1 and u_2, (b) structure P i.e. control x_1 and x_9 with u_1 and u_2, (c) structure X i.e. control x_1 and x_5 with u_1 and u_3, and (d) structure AR i.e. control x_1 and x_5 with u_2 and u_3. Note that structures D and AR were identified as the best structures according to the dynamic resilience analysis earlier reported in Williams and Adeniyi (2018a) so we have have included structures P and X only for the purpose of comparisons.

For a 5^{o}C step change disturbance in reactor feed temperature, Figure 4 shows the closed-loop simulated responses of the five temperatures (x_1 to x_5) along the reactor length for the four control structures, with only four (4) singular values retained in the controller solution. The plots show the closed-loop responses (of x_1 to x_5) for the nominal and the two model/plant mismatch cases. The corresponding control inputs are shown in Figures 5.

When the plots of x_1 to x_5 are examined, we can see that on the whole, structure AR gives the best performance in terms of how well the variables are regulated about the origin, magnitude of steady-state offsets (where these occur), magnitude of control efforts, and sensitivity to model/plant mismatch. This is then followed by structure D, while it is difficult to rank the overall performance of structures P and X. This is because, structure X has better closed-loop responses (of x_1 to x_5) than structure P. However, structure X requires much larger magnitudes of control input u_1 (than for structure P), which may be impossible to implement practically.

Although the closed-loop responses (of x_1 to x_5) for structure X are clearly better than those of structure D, we have ranked those of the latter to be better based on the magnitudes of control inputs necessary to achieve the regulatory task. It is of course clear, that the closed-loop responses (of x_1 to x_5) for structure D are, on the whole better than those of structure P since that of the latter exhibits large offsets in variables x_3, x_4, and x_5; and also requires considerably larger control inputs (u_1 and u_2).

From the foregoing simulation results, we see that the closed-loop simulation results confirm the outcome of our earlier work for the selection of the most promising 2×2 control structures (Williams and Adeniyi, 2018a) based on dynamic resilience analysis i.e. structure AR is indeed the best followed by structure D.

5.2.2 2×3 Control Structures

The following control structures were selected for controller design and closed-loop simulation assessments: (a) structure BL i.e. control x_1 and x_5 with u_1, u_2, and u_3, (b) structure BN i.e. control x_1 and x_9 with u_1, u_2, and u_3, (c) structure BQ i.e. control x_2 and x_5 with u_1, u_2, and u_3, and (d) structure BU i.e. control x_3 and x_5 with u_1, u_2, and u_3. Again, it should be noted that structures BL and BQ were identified as the best structures according to the dynamic resilience analysis outcome reported in Williams and Adeniyi (2018a); we have included structures BN and BU only for the purpose of comparisons.

For a 5^{o}C step change disturbance in reactor feed temperature, Figure 6 shows the closed-loop simulated responses of the five temperatures (x_1 to x_5) along the reactor length for the four control structures, with only four (4) singular values retained in the controller solution. The plots show the closed-loop responses (of x_1 to x_5) for the nominal, and the two model/plant mismatch cases. The plots of the corresponding control inputs u_1, u_2, and u_3 are shown in Figure 7.

When the plots of x_1 to x_5 are examined, we can see that on the whole, structure BL gives the best performance in terms of how well the variables are regulated about the origin, magnitude of steady-state offsets (where these occur), magnitude of control efforts, and sensitivity to model/plant mismatch. This is.

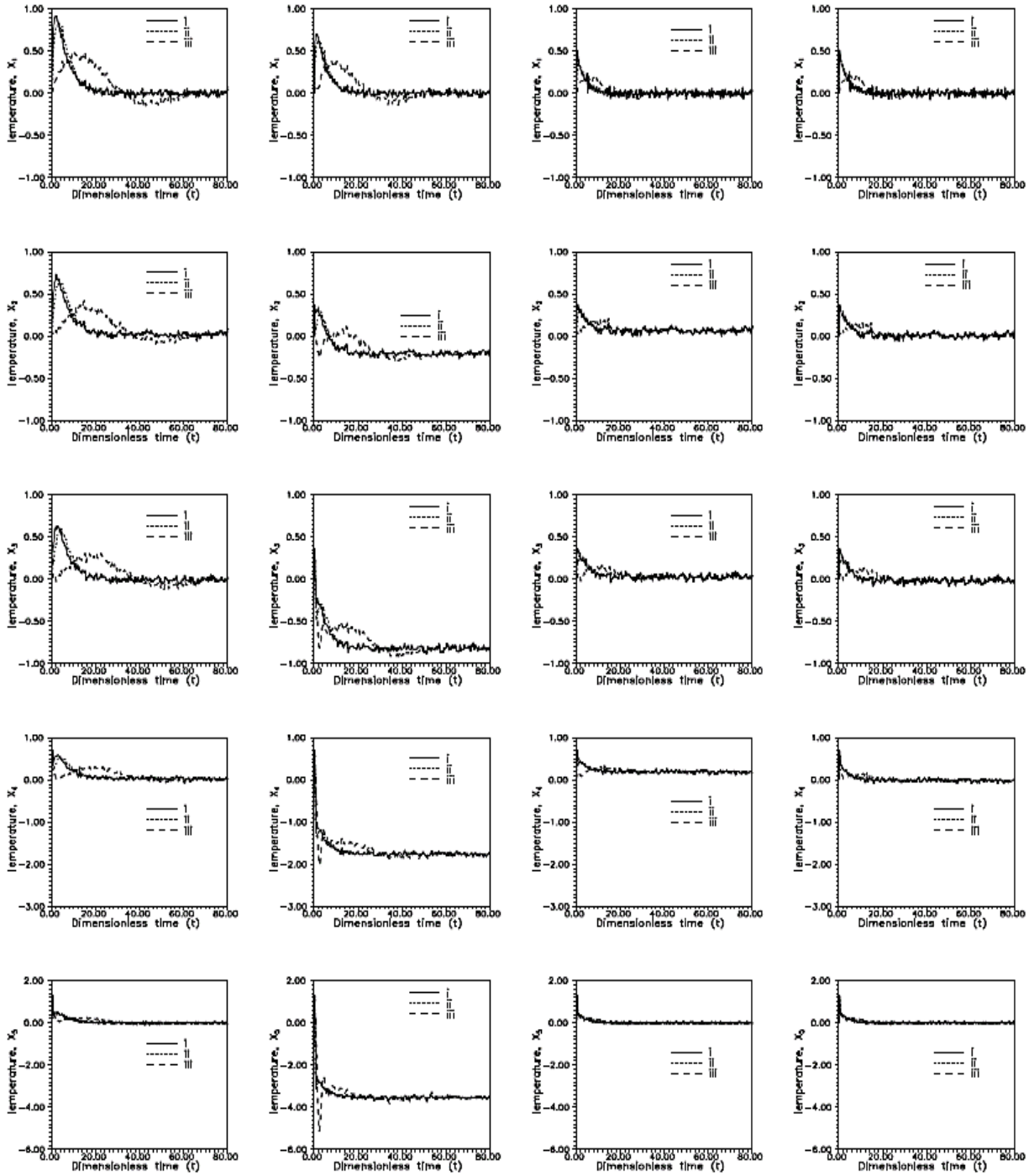

Figure 4: Closed-loop simulation responses of temperatures along the tubular reactor length (x_1, x_2, x_3, x_4 & x_5 for a 5 ^{o} C step change disturbance in reactor feed temperature under MPC with 4 singular values retained. 1st, 2nd, 3rd & 4th column plots from left to right: 2×2 control structures D, P, X, and AR, respectively. Legend: i, ii, iii for Δ_e = 0.9, 0, -0.9, respectively.

then followed by structures BQ, BN and BU, in that order. Note the high sensitivity of structure BU especially for the model/plant mismatch case with $\Delta_e = -0.9$. This kind of high sensitivity was predicted by the dynamic resilience analysis and is clearly not desirable for practical implementation purposes. It is for this reason that the performance of structure BN (even though it leads to offsets) was ranked better than that of structure BU

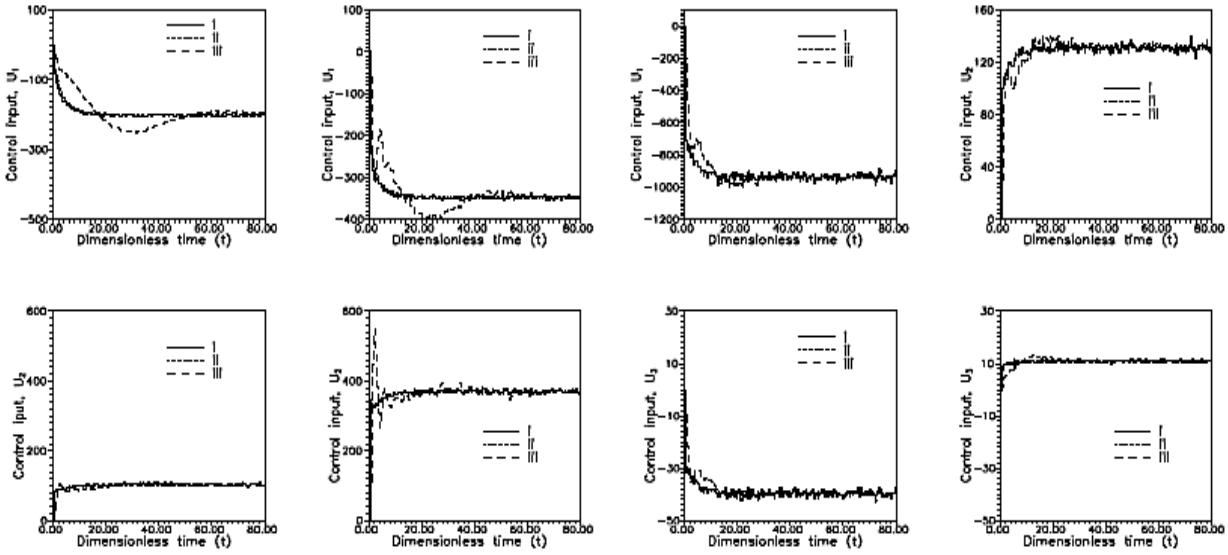

Figure 5: Control inputs for the response plots of Figure 4. 1st (u_1, u_2), 2nd (u_1, u_2), 3rd (u_1, u_3) & 4th (u_2, u_3) column plots from left to right: 2×2 control structures D, P, X, and AR, respectively. Legend: i, ii, iii for Δ_e = 0.9, 0, -0.9, respectively.

Again, we see that the closed-loop simulation results also confirm the outcome of our earlier work for the selection of the most promising 2×3 control structures (Williams and Adeniyi, 2018a) based on dynamic resilience analysis. As expected from the results of dynamic resilience analysis, and physical reasoning, comparison of the closed-loop simulation responses and the control inputs for the 2×2 and the 2×3 control structures show the latter to be generally better.

5.2.3 3×3 Control structures

The results of dynamic resilience analysis reported in Williams and Adeniyi (2018a) indicated that only the 2×2 and 2×3 control structures can be used for practically useful controller designs, while the 3×3 would not lead to a useful controller design. To confirm this, we selected the best 3×3 structure i.e. structure CL, which is to control x_1, x_4 and x_5 with the three control variables u_1, u_2, and u_3, for control design and closed-loop simulation testing under nominal, and model/plant mismatch conditions.

For a 5^o C step change disturbance in reactor feed temperature, Figure 8 shows the closed-loop simulated responses of temperatures x_1, x_2, x_3 and x_5 with only four (4) singular values retained in the controller solution. The plots show the closed-loop responses for the nominal and the two model/plant mismatch cases. The corresponding control inputs are also shown in Figure 8. Without making any comments, these plots clearly demonstrate the point that this structure is not suitable for carrying out any practically useful control system design for the ammonia reactor system. This is also in consonance with the outcome of the dynamic resilience analysis of the 3×3 control structures earlier reported in Williams and Adeniyi (2018a)

5.3 Comparison with decentralized PI controllers

Figure 9 shows the comparisons of the closed-loop simulated responses of the model predictive controllers (designed with the 2×2 and 2×3 control structures AR and BL, respectively), and those of the two single-loop PI controllers of Viswanadham *et al.* (1979), which were extensively tuned for best performance using closed-loop simulations, based on the 2×2 control structure AR. These figures respectively show the closed-loop simulated responses of temperatures x_1 and x_5 following a 5^o C step change disturbance in the reactor feed temperature under nominal (i.e. perfect model, no noise), measurement noise, and two cases of model/plant mismatch plus measurement noise conditions. The measurement noise and the two cases of model/plant mismatch were as previously described. The corresponding control inputs for the plots in Figure 9 are shown in Figure 10

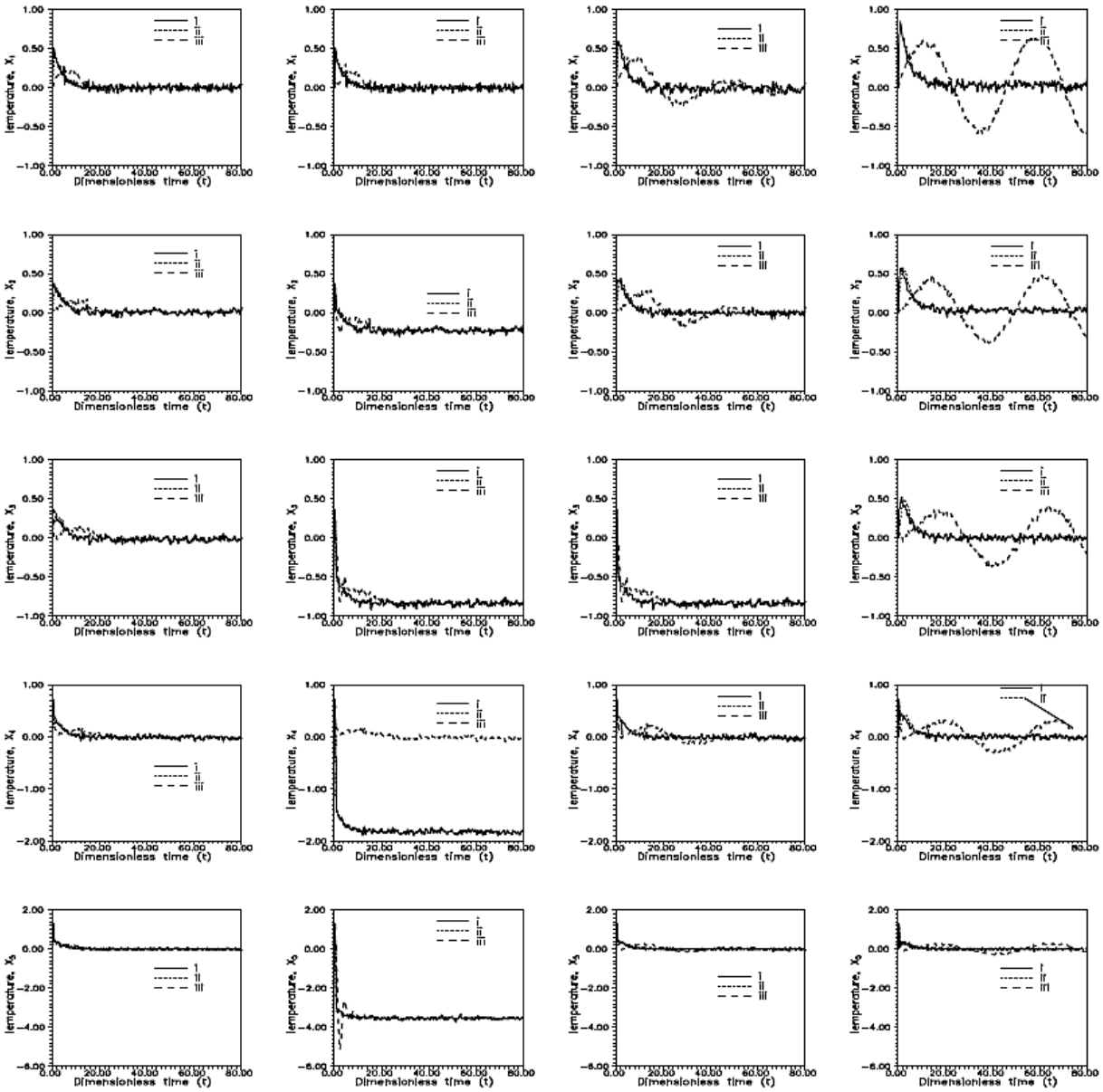

Figure 6: Closed-loop simulation responses of temperatures along the tubular reactor length (x_1, x_2, x_3, x_4 & x_5 for a 5 ^{o}C step change disturbance in reactor feed temperature under MPC with 4 singular values retained. 1st, 2nd, 3rd & 4th column plots from left to right: are for 2×3 control structures BL, BN, BQ, and BU, respectively. Legend: i, ii, iii for Δ_e = 0.9, 0, -0.9, respectively.

It can be seen from the foregoing figures that the model predictive controllers give better regulation of the temperatures x_1 and x_5 about the origin than the two single-loop PI controllers in all cases. Furthermore, the two single-loop PI controllers display larger sensitivity to the effect of measurement noise and model/plant mismatch as evident by the jagged movement of the control inputs. Such jagged movements are clearly undesirable as they will lead to rapid wear and tear of the final control element such as a control valve. Although the closed-loop responses of x_1 and x_5 are practically the same for the 2×2 and 2×3 MPC, we can see that latter requires smaller inputs in u_2 and u_3 than the former, since u_1 is also moved. This clearly suggests, as previously predicted by dynamic resilience analysis (Williams and Adeniyi, 2018a), that the 2×3 structure is superior as it can handle disturbances of larger magnitudes (without saturation) than the 2×2 structure

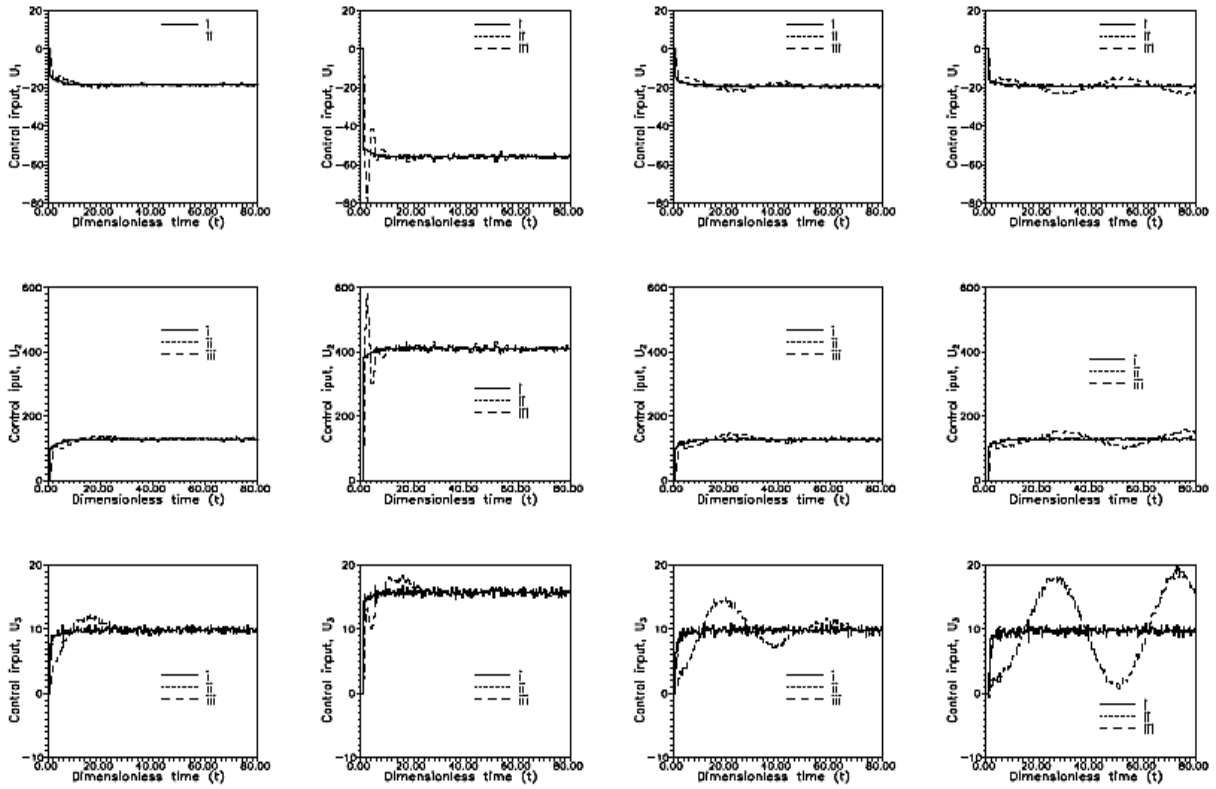

Figure 7: Control inputs (u_1, u_2, u_3) for the response plots of Figure 6. 1st, 2nd, 3rd & 4th column plots from left to right are for the 2×3 control structures BL, BN, BQ, and BU, respectively. Legend: i, ii, iii for Δ_e = 0.9, 0, -0.9, respectively.

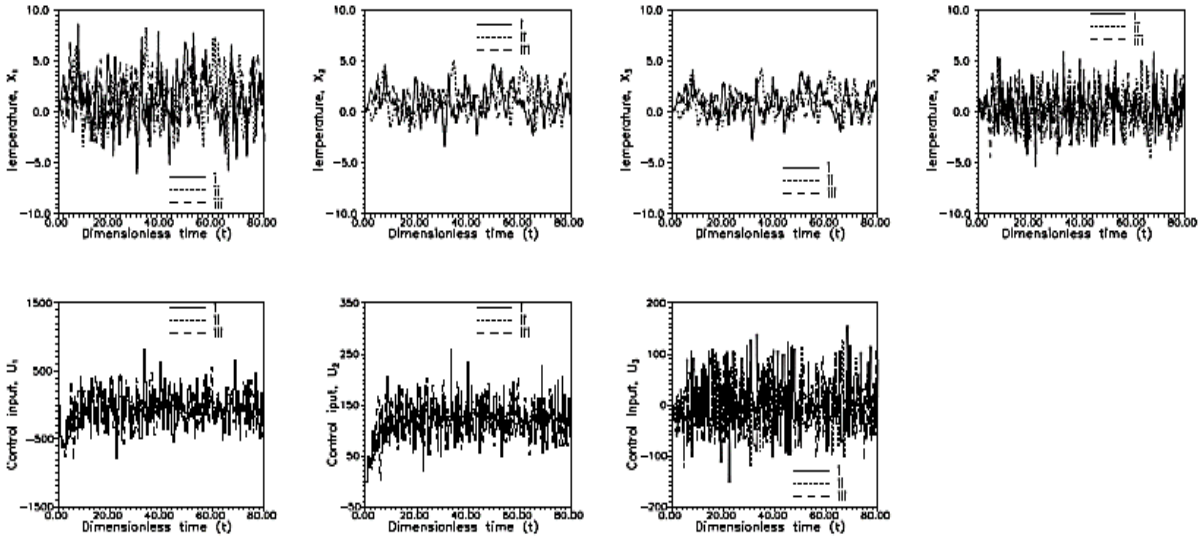

Figure 8: Top figures: Closed-loop simulation responses of temperatures x_1, x_2, x_3, and x_5 for a 5 ^{o} C step change disturbance in reactor feed temperature under MPC with 4 singular values retained. Bottom figures: corresponding control inputs, u_1, u_2, u_3 (for 3×3 structure CL). Legend: i, ii, iii for Δ_e = 0.1, 0, -0.1, respectively. (Feedback configuration).

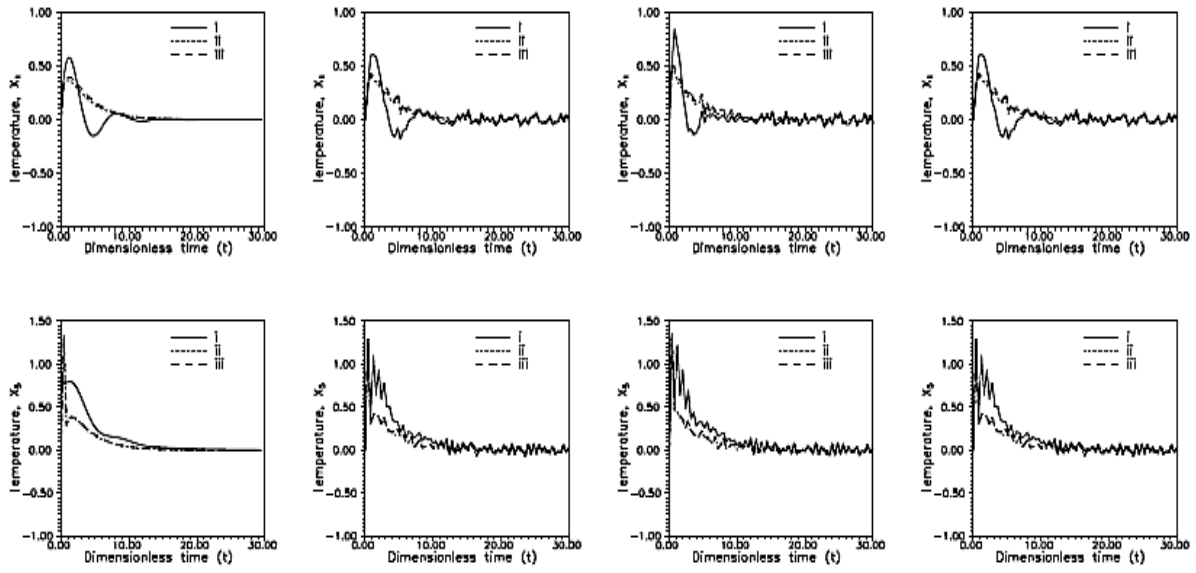

Figure 9: Comparisons of closed-loop simulation responses of temperatures for a 5 ^{o} C step change disturbance in reactor feed temperature. Top: x_1, Bottom: x_5 1st, 2nd, 3rd & 4th column plots from left to right are for the nominal, noise + Δ_e = 0, noise + Δ_e =0.9, and noise + Δ_e = -0.9, respectively. Legend: i, two single-loop PI controllers; ii, & iii 2×2 and 2×3 MPC, respectively.

.

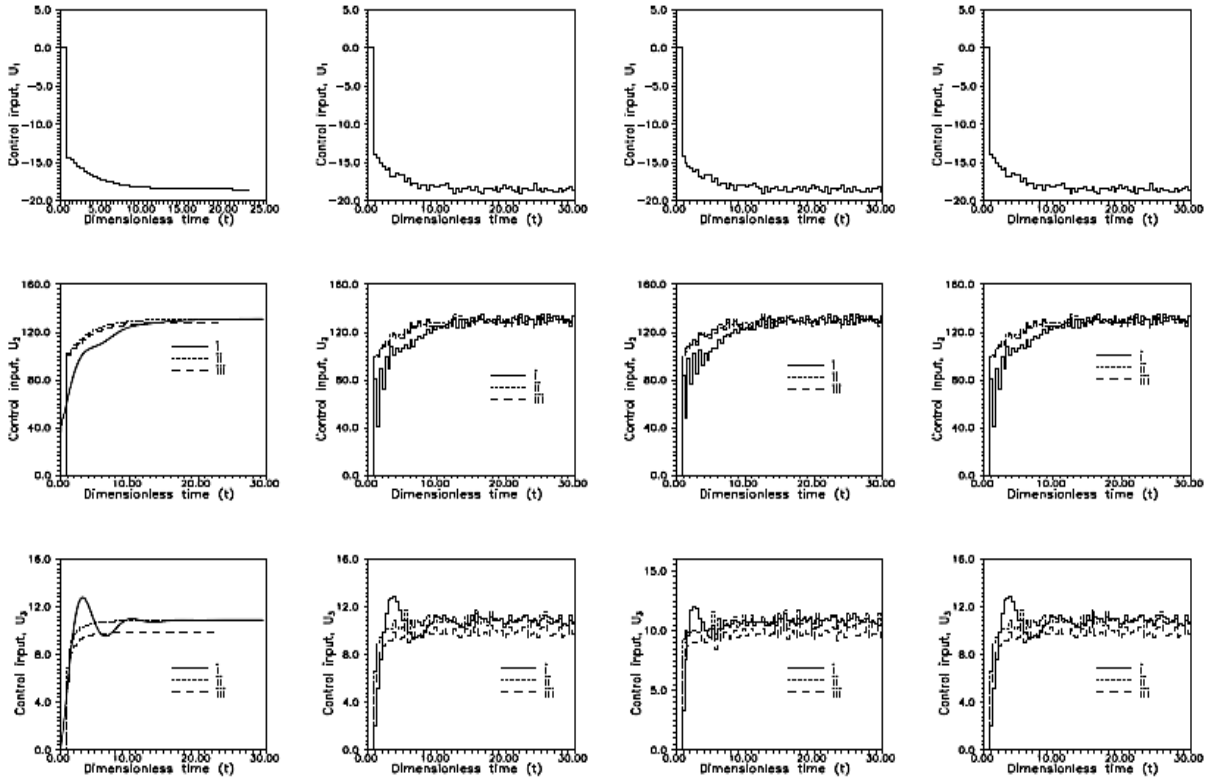

Figure 10: Control inputs for the 2×3 MPC with 4 singular values retained. Top: u_1, Middle : u_2, Bottom: u_3. 1st, 2nd, 3rd & 4th column plots from left to right are for the nominal, noise + Δ_e = 0, noise + Δ_e =0.9, and noise + Δ_e = -0.9, respectively.

6 CONCLUSION

This paper presented the design of a model predictive

controller for a tubular ammonia reactor-heat exchanger system using the singular value decomposition (SVD) approach to computation of the control law. The SVD-based model predictive controller was used to evaluate various 2×2 , 2×3 and 3×3 control structures under additive plant/model mismatch and measurement noise.

The closed-loop simulation results validated the previously reported outcome of the selection of the most promising 2×2 and 2×3 using dynamic resilience by the authors. Closed-loop simulations also confirmed that no practically useful controllers can be designed for the system using any of the 3×3 control structures. The designed SVD-based MPC controllers based on the selected 2×2 and 2×3 control structures performed better than a decentralized PI controller previously reported in the literature.

This method of using the SVD to compute the control law in model predictive control has also been successfully applied to another multivariable system under set point control. This shall be presented in a future paper
.

REFERENCES

Forsythe, G. E., Malcolm, M. A. and Moler, C. B. (1977). *Computer Methods for Mathematical Computations*, Prentice-Hall, Inc., Englewood Cliffs, N. J.

Patnaik , L. M. Viswanadham, N., and Sarma, I. G. (1980a). State Space Formulation of Ammonia Reactor Dynamics, *Comput. & Chem. Eng.*, **Vol. 4**, pp. 215‑222.

Patnaik , L. M., Viswanandham and Sarma, I. G. (1980b). Computer Control Algorithms for a Tubular Ammonia Reactor, *IEEE Trans. Autom. Control.*, **AC-25**, No. 4, August, pp. 642‑651.

Viswanadham , N., Patnaik, L. M., and Sarma I. G. (1979). Robust Multivariable Controllers for a Tubular Ammonia Reactor, *ASME J. Dynamic Syst. Meas. & Control*, **Vol. 101**, p. 290, Dec., (1979).

Williams , A. O. F. and Adeniyi, V. O. (2018a). Identification of New Control Structures for a Tubular Ammonia Reactor-Heat Exchanger System Using Dynamic Resilience Analysis, *Journal of the Nig. Soc. of Chem. Engrs.*, **Vol. 33**, No 1, pp. 116- 128.

Williams , A. O. F. and Adeniyi, V. O. (2018b). Model Predictive Control of a Tubular Ammonia Reactor System: Closed-Loop Evaluation of Alternate 2 x 2 Control structures, *Proc. 48th. Annual Conf. of Nig. Soc. of Chem. Engrs.*, Abeokuta, 8-10 Nov. 2018, pp. 474-485.

JOURNAL OF THE NIGERIAN SOCIETY OF CHEMICALENGINEERS INSTRUCTION TO AUTHORS

1. TYPES OF PUBLICATION

The Journal of the Nigerian Society of Chemical Engineers will publish articles on the original research on the Science and Technology of Chemical Engineering. Preference will be given to articles on new processes or innovative adaptation of existing processes. Critical reviews on current topics of Chemical Engineering are encouraged and may be solicited by the Editorial Board. The following types of articles will be considered for publication:

a. Full length **articles or review papers**.
b. **Communication** – a preliminary report on research findings.
c. **Note** – a short paper describing a research finding not sufficiently completed to warrant a full article.
d. **Letter to the Editor** – comments or remarks by readers and/or authors on previously published materials.

The authors are entirely responsible for the accuracy of data and statements. It is also the responsibility of authors to seek ethical clearance and written permission from persons or agencies concerned, whenever copyrighted material is used.

2. MANUSCRIPT REQUIREMENTS

a. The **Manuscript** should be written in clear and concise English and typed in Microsoft Word using double spacing on A4-size paper, Times New Romans font and 12 point. A full length article or review should not exceed 15 pages. Margin should be Normal (i.e. 2.54cm for Top, Bottom, Left & Right margins).
b. The **Manuscript** should be prepared in the following format: Abstract, Introduction, Materials and Methods, Results, Discussion, Conclusion, Acknowledgements, and References..
c. The **Manuscript** must contain the full names, address and emails of the authors. In the case of multiple authorship, the person to whom correspondence should be addressed must be indicated with functional email address. As an examples, authors' names should be in this format:
Momoh, S. O., Adisa, A. A. and **Abubakar, A. S.**
If the addresses of authors are different, use the following format:
***Momoh, S. O.[1], Adisa, A. A.[2]** and **Abubakar, A. S.[3]**
Use star * to indicate the corresponding author.

d. **Symbols** should conform to America Standard Association. An abridged set of acceptable symbols is available in the fourth edition of Perry's Chemical Engineering Handbook. Greek letters, subscripts and superscripts should be carefully typed. A list of all symbols used in the paper should be included after the main text as **Nomenclature**.
e. All **Units** must be in the SI units (kg, m, s, N, etc).
f. The **Abstract** should be in English and should not be more than 200 words. The Abstract should state briefly the purpose of the research, methodology, results, major findings and major conclusions. Abstracts are not required for Communications, Notes or Letters.
g. **Citation** must be in the Harvard Format i.e. (Author, Date). Examples are (Smith, 1990) or (Jones et al, 2011). (Kemp, 2000) demonstrated that …..; (Mbuk, 1985; Boma, 1999; Sani, 2000) if more than two authors. (Telma, 2001a), (Telma, 2001b); etc if the citation have the same author and year of publication.
For more information on **Harvard Referencing: Guide** visit
http://www.citethisforme.com/harvard-referencing
h. **References** must also be in the Harvard Format i.e. (Author, Date, Title, Publication Information). References are listed in alphabetical order. Examples are shown below:
Haghi, A. K. and Ghanadzadeh, H. (2005). A Study of Thermal Drying Process. *Indian Journal of Chemical Technology*, Vol. 12, November 2005, pp. 654-663
Kemp, I.C., Fyhr, C. B., Laurent, S., Roques, M. A., Groenewold, C. E., Tsotsas, E., Sereno, A. A., Bonazzi, C. B., Bimbernet, J. J. and Kind M.(2001). Methods for Processing Experimental Drying Kinetic Data. *Drying Technology*, 19: 15-34.
i. **Tables** should contain a minimum of descriptive materials. Tables should be numbered in Arabic numerals (1, 2, 3, etc), and should be placed at the referenced point with captions (centralised) placed at the top of the table.
j. **Figures**, charts, graphs and all illustrations should be placed at the referenced point, numbered in Arabic numerals (1, 2, 3, etc) and incorporated in the text. Caption for Figures should be placed at the bottom of the Figure (centralised). Lettering set or symbols should be used for all labels on the figures, graphs, charts, photographs even when drawn in colours. (Note that figures drawn in colours may be unreadable if printed in black and white).
k. **Equations** should be typed using MS Word Equation Editor and should be centred with number (in Arabic numeral) at the right margin.
l. Wherever possible, **Fractions** should be shown using the oblique slash. E.g. x/y
m. **Footnotes** should not be incorporated in the text.
n. **Acknowledgements** should appear at the end of the paper, before the list of references.

3. SUBMISSION OF MANUSCRIPTS

Manuscripts should be submitted by sending a Microsoft Word document (taking into account the Manuscript Requirements described in section 2 above) to the following email address: **nschejournal@yahoo.com** and copy **stevmomoh@yahoo.com.**
All correspondences are directed to the Editor-in-Chief using the submission emails addresses: nschejournal@yahoo.com and copy stevmomoh@yahoo.com.

4. ACCEPTED PAPERS

On acceptance, authors will be required to submit a copy of their manuscripts using Microsoft Word by emails to **nschejournal@yahoo.com** and copy **stevmomoh@yahoo.com**.

The following additional information should be observed for accepted papers: (i) Typed in Microsoft Word using 1.15 spacing on A4-size paper, Times New Romans font and 10 point; (ii) Margin should be 2.54cm for Top & Bottom; 2.20cm for Left & Right margins; (iii) The abstract should be one column document while the body of the manuscript should be double columns with 0.5cm gutter spacing except some tables and figures that may have to go in for one column document.

5. PUBLICATION

Full NSChE Journal edition in hard copy will be published twice annually.

6. REPRINT

Reprints are available on request at a moderate fee per page. Orders must be placed before the paper appears in Print.

7. READER'S INFORMATION

The papers are wholly the view of their author(s) and therefore the publishers and the editors bear no responsibility for such views.

8. SUBSCRIPTION INFORMATION

The subscription price per volume is as follows:

a. Individual Reader - ₦3,000.00
b. Institutions, Libraries, etc. - ₦5,000.00
c. Overseas Subscription - $100.00

Request for information or subscription should be sent to the Editor-in-Chief through the following emails addresses: nschejournal@yahoo.com and copy stevmomoh@yahoo.com.

9. COPYRIGHT NOTICE

Copyright of published material belongs to the journal

10. PRIVACY STATEMENT

The names and email addresses entered in this journal site will be used exclusively for the stated purposes of this journal and will not be made available for any other purpose or to any other party.

GENERAL ANNOUNCEMENT

Fees charged for paper review and publication are as follows:

1. **Manuscript Review charges = ₦6,500 payable by both Members and Non-Member.**
2. **Publication Charges = ₦10,000 payable by Non-Members and Members who are not financially up-to-date.**
3. **Members would only get one (1) Journal free and buy the other if they so wish.**
4. **Corresponding Author whose paper is published on a particular edition would get one (1) free copy on behalf of all the co-authors. Other co-authors will buy if they so wish.**
5. **These payments shall be payable to the following account:**
   - **Name of account: Nigerian Society of Chemical Engineers**
   - **UBA account No:1001730178**
   - **or**
   - **GTB account No 0139519728**
6. **Make your payments and send a proof to Editor's email address: stevmomoh@yahoo.com.**
7. **These charges may be reviewed by the Council from time to time.**